

Copyright Notice

Notice 1

Under the Copyright Act 1968, this thesis must be used only under the normal conditions of scholarly fair dealing. In particular no results or conclusions should be extracted from it, nor should it be copied or closely paraphrased in whole or in part without the written consent of the author. Proper written acknowledgment should be made for any assistance obtained from this thesis.

Notice 2

I certify that I have made all reasonable efforts to secure copyright permissions for third-party content included in this thesis and have not knowingly added copyright content to my work without the owner's permission.

ADDENDUM

Page 3 first sentence :“If this transition results in a change in dipole moment a molecule can be excited by an infrared photon”

Should read as:

“If this vibration results in an oscillating dipole moment it can be excited by an infrared photon”

Page 3: Equation 4 should be:

$$p_{a \rightarrow b} = \left(\frac{8\pi^3}{3h^2} \right) [|(a|\mu_x|b)|^2 + |(a|\mu_y|b)|^2 + |(a|\mu_z|b)|^2] \rho(\nu_{ab})$$

Where:

$$(a|\mu_F|b) = \int \psi_a^* \mu_F \psi_b d\tau$$

where $\mu_F = (\mu_x, \mu_y, \mu_z)$ represents the vector for the electric dipole moment of the molecule with components along each Cartesian axis.

Page 5 equation 11 should be:

$$A = \frac{h}{8\pi^2 I_a}, B = \frac{h}{8\pi^2 I_b}, C = \frac{h}{8\pi^2 I_c}$$

Page 6 line 6: the expression $(I_c > I_b = I_a)$ should be $(I_c = I_b > I_a)$

Page 8 note: K_a and K_c are no longer ‘good’ quantum numbers however they are useful in facilitating calculations.

Page 9 note the term $F_{\pm}(K, J)$ that is used in equations 19, 20, 21 and 25 is:

$$F_{\pm}(K, J) = \sqrt{J(J+1) - K(K \pm 1)}$$

Page 10 equations 22 should be:

$$\langle \nu_s, \nu_{s'} | \hat{H} | \nu_s + 1, \nu_{s'} - 1 \rangle = i \zeta_{\nu\nu'}^a \hat{J}_\alpha$$

And equation 23:

$$\langle \nu_s, \nu_{s'} | \hat{H} | \nu_s + 1, \nu_{s'} - 1 \rangle = \eta_{\nu\nu'}^{\beta\gamma} \{ \hat{J}_\beta, \hat{J}_\gamma \}_+$$

Page 16 line 6: should read as: “a linear combination of the Hartree-Fock exact exchange functional”

Page 17 Note: Double resonance microwave or millimetre wave techniques can provide extremely precise information on excited vibrational states. This technique uses a high power laser to pump a significant population of molecules into an excited vibrational state and then uses microwave or millimetre-wave spectroscopy to measure rotational transitions within this vibrational state. This does have the disadvantage of requiring a transition be co-incident with a laser emission frequency.

Page 21: equation 36 note:

d_{max} is in mm and ν is in cm^{-1} this makes the constant 36.63 have the units $\text{mm}\cdot\text{cm}^{-1/2}$

Page 29 equation 39, note that:

Optical acceptance or etendue (θ) is a product of the area of the optical beam and the solid angle at the limiting aperture of the system.

The optical efficiency (ξ) is the fraction of light which makes it through the system.

Detectivity (D^*) is a constant related to the specific detector in use. It is given by:

$$D^* = \frac{\sqrt{A_D}}{NEP}$$

Where A_D is the area of the detector and NEP is the *Noise Equivalent Power* which is given by the ratio of the rms noise voltage ($V \cdot \text{Hz}^{-1/2}$) and the responsiveness of the detector ($V \cdot W^{-1}$)

Page 32 line before equation 42 should read as:

“If τ is the average time between collisions the line broadening due to collisions is given by:”

Page 37, 4th line from bottom. "aides" should be "aids".

Page 46: Note, mirrors M1 and M2 refer to mirrors D and F in figure 27.

Page 127: Add “as phase III” after the line: “A less ordered orthorhombic phase (II) above 98.4K, where the Cl atoms are located in the same positions”

INFRARED SPECTROSCOPY OF COLD MOLECULES

Christopher Michael Medcraft, B.Sc (Honours)

School of Chemistry, Monash University

December 2012

ABSTRACT

A long path collisional cooling cell has been installed at the Far-Infrared beamline at the Australian Synchrotron to study the infrared spectrum of molecules at cryogenic temperatures. New transfer optics and vacuum chambers were designed in order to allow study in the far infrared region where the synchrotron source provides the most advantage. Experiments using this cooling cell can be divided into two themes: rotationally resolved high resolution spectroscopy and low resolution spectroscopy of aerosols (solid or liquid particles suspended in a gas).

Chapter 1 contains the background information and theory important to high resolution spectroscopy. This chapter also contains details of the instrumentation used and the modifications to the optics of the cooling cell.

Chapter 2.1 is the first publication, a report on the performance of the Far-IR beamline and the optical modifications to the cooling cell. This paper also contains examples of the data obtained with the new arrangement. The far-IR spectrum of carbon dioxide aerosols and the high resolution spectrum of 1,1-difluoroethane recorded at room temperature and at 154 K, showing the advantages of cooling for high resolution FTIR spectroscopy.

Prior to the completion of the optical modifications the mid-IR spectrum of carbon-13 enriched C_2F_4 was measured in the cooling cell at 150 K. Chapter 2.2 contains the structural, vibrational and rovibrational analysis of this molecule. The ground state rotational constants for $^{12}C^{13}CF_4$ and $^{13}C_2F_4$ were determined and used to compute a semi-experimental equilibrium geometry. Upper state rotational constants were also determined.

Chapter 2.3 contains a publication where the pure rotational spectrum of the important interstellar molecule oxirane (cyclic- C_2H_4O) was measured between 15 and 73 cm^{-1} (0.4-2.2 THz).

Chapter 2.4 contains the high resolution analysis of ketenimine. It involved the pyrolysis of a precursor molecule and recording the IR spectrum of the transient product. The analysis and writing of the paper were performed by Dr. Michael Bane.

Chapter 3 is concerned with the use of the cooling cell to generate aerosols. This type of cell is in use in a number of laboratories for the study of aerosols; however they are all limited to the mid-infrared region. Chapter 3.1 is a brief introduction to the aspects that are unique to infrared spectroscopy of particles.

Chapter 3.2 presents the first far-IR spectrum of water ice in the aerosol phase. These experiments were initially intended as a simple test with the presumption that it was a well understood system. However absorption features of the particles we produced did not agree with literature data. By repeating the same experiments in the mid infrared (chapter 3.3) we were able to determine the size of the particles to be 3-200 nm in diameter and attribute the discrepancies to the effects of scattering in previous studies.

Chapter 3.4 is a study on droplets of pure and binary aerosol particles of solid HCl and liquid ozone. Chapter 3.5 is a study on particles of HCl and NH₃ which showed a competition between the physical process of the freezing of the pure compounds and the chemical reaction between the two to form ammonium chloride.

General Declaration

In accordance with Monash University Doctorate Regulation 17 Doctor of Philosophy and Research Master's regulations the following declarations are made:

I hereby declare that this thesis contains no material which has been accepted for the award of any other degree or diploma at any university or equivalent institution and that, to the best of my knowledge and belief, this thesis contains no material previously published or written by another person, except where due reference is made in the text of the thesis.

The data used in Chapters 3.4 and 3.5 were obtained during my undergraduate degree, however the analysis and writing of the papers was done during this degree.

This thesis includes **six** original papers published in peer reviewed journals and **two** unpublished publications. The core theme of the thesis is Gas Phase Infrared Spectroscopy. The ideas, development and writing up of all the papers in the thesis were the principal responsibility of myself, the candidate, working within the School of Chemistry under the supervision of Professor Don McNaughton

In the case of chapters 3 and 4 my contribution to the work involved the following:

Thesis chapter	Publication title	Publication status*	Nature and extent of candidate's contribution
2.1	Low Temperature Gas-phase IR Spectroscopy at the Australian Synchrotron	Yet to be Submitted	Initiation, key ideas, experimental, development and writing up (80%)
2.2	Structural, vibrational, and rovibrational analysis of tetrafluoroethylene	Published	Initiation, key ideas, experimental, development and writing up (80%)
2.3	The Far-Infrared Spectrum of Ethylene Oxide	Published	Initiation, key ideas, experimental, development and writing up (80%)
2.4	High-resolution Fourier-transform infrared spectroscopy of the Coriolis coupled ground state and ν_7 mode of ketenimine	Published	Experimental Assistance (5%)
3.2	Size and Temperature Dependence in the Far-IR spectra of water ice particles	Published	Initiation, key ideas, experimental, development and writing up (80%)
3.3	Water ice nanoparticles: size and temperature effects on the mid-infrared spectrum	Submitted	Initiation, key ideas, experimental, development and writing up (80%)
3.4	Infrared spectroscopy of ozone and hydrogen chloride aerosols	Published	Initiation, key ideas, experimental, development and writing up (80%)
3.5	IR spectroscopy of physical and chemical transformations in cold hydrogen chloride and ammonia aerosols	Published	Initiation, key ideas, experimental, development and writing up (60%)

I have not renumbered sections of submitted or published papers in order to generate a consistent presentation within the thesis.

Signed: Date:

ACKNOWLEDGEMENTS

This work could not have been completed without the support and guidance of a number of people. Firstly to my supervisors. Don, your guidance and experience were invaluable motivators. Evan, thanks for all the hard work and patience in getting the papers over the line. And Dom for being consistently available at all hours to solve Bruker's problems. Crispy thanks for the unofficial supervision, the friendship and the invitations to watch you hang out with musicians.

I would like to thank Sigurd Bauerecker, the extension of the optics would not have been possible without his invaluable advice and expertise. And to John Taylor who actually built the vacuum chambers and provided fantastic advice in their design. All the engineers and technical staff at the Australia Synchrotron who helped and advised through countless vacuum and electronic problems. Particularly to Danielle and Ruth, thanks for going above and beyond the call of duty.

To my office mates, it was a joy to spend time in and out of the office with you. Mot, your quiet hard work was a motivator for me. Michael, you showed me that if a physicist could do chemistry a chemist could do physics...even if they show up at midday. David, whenever I was having trouble with the instrument I could always see what you were doing (or not doing) and see that it could be much worse. Andy, I hand over protection of the EFC cell to you. Treat her well and she will treat you well.

Last but not least, my family, the emotional and financial support was invaluable. Being able to come home and forget about problems at work was vital. Likewise, to my non-uni mates, being able to have a quite beer or three and not talk about quantum mechanics or vacuum leaks was important.

TABLE OF CONTENTS

Abstract	i
Acknowledgements	iv
1.0 Background Theory and Instrumentation	1
1.1 Quantum Mechanics	2
1.1.2 Vibrational	2
1.1.3 Rotational	5
1.1.4 Vibration/Rotation interactions	10
1.1.5 Analysis Techniques	11
1.1.6 Ground State Combination Differences	13
1.1.7 Structural determination	14
1.1.8 Computational Methods	16
1.2 Instrumentation	17
1.2.1 Molecular Spectroscopy Techniques	17
1.2.2 FTIR Theory	18
1.2.3 Instrumental line shape	19
1.2.4 Zero Fill Factor	20
1.2.5 Aperture	21
1.3 Synchrotrons	22
1.3.2 Australian Synchrotron	23
1.3.3 Coherent Synchrotron Emission	23
1.3.4 Free Electron Lasers	24
1.3.5 Far-IR Beamline	24
1.4 Bruker IFS125HR FTIR Spectrometer	27
1.4.2 Signal to Noise	29
1.4.3 Natural Line Shape	31
1.4.4 Doppler Width	31
1.4.5 Pressure broadening	32

1.4.6	Long Path Gas cells	33
1.4.7	Cooled Spectra	34
1.4.8	Translational Temperature	35
1.4.9	Vibrational Temperature	36
1.4.10	Rotational Temperature	37
1.4.11	Equilibrium Cooling	38
1.4.12	Supersonic Jets	38
1.4.13	Collisional Cooling	39
1.5	Enclosive Flow Cooling Cell	40
1.5.2	Cooling Modes	42
1.6	Optical Modifications	45
1.6.1	Far-Infrared region	45
1.6.2	Cell Windows	48
1.7	References	50
2.0	Publications on High Resolution FTIR Spectroscopy	52
2.1	“Infrared Spectroscopy of Gases and Condensates at the Australian Synchrotron”	53
2.2	“Structural, vibrational, and rovibrational analysis of tetrafluoroethylene”	69
2.3	“The Far-Infrared Spectrum of Ethylene Oxide”	81
2.4	“The High-resolution Fourier-transform infrared spectroscopy of the Coriolis coupled ground state and ν_7 mode of ketenimine”	85
3.0	FTIR Spectroscopy Of Aerosols	92
3.1	Introduction	93
3.1.2	Infrared Absorption	97
3.1.3	Refractive index	99
3.1.4	References	101
3.2	“Size and Temperature Dependence in the Far-IR spectra of water ice particles”	104

3.3	“Water ice nanoparticles: size and temperature effects on the mid-infrared spectrum”	111
3.4	“Infrared spectroscopy of ozone and hydrogen chloride aerosols”	120
3.5	“IR spectroscopy of physical and chemical transformations in cold hydrogen chloride and ammonia aerosols”	126
4.0	Conclusions	135

Measure what is measurable and make measurable what is not

- Galileo

CHAPTER 1.0

BACKGROUND THEORY AND INSTRUMENTATION

1.1 QUANTUM MECHANICS

A photon can interact with a molecule by being absorbed, transmitted or scattered depending on the molecule and the energy of the photon. If a molecule has two states ψ_a and ψ_b separated in energy by $E_a - E_b$ then photon of energy $h\nu_{ab}$ may be absorbed. The determination of these states is aided by the Born-Oppenheimer approximation which posits that molecular vibrations, rotations and electronic dynamics have little influence on each other and can therefore be treated separately. The total wavefunction (Ψ) can be represented as a product of each component:

$$\Psi_{\text{total}} = \Psi_{\text{elec}} \Psi_{\text{vib}} \Psi_{\text{rot}} \quad 1$$

And therefore at stationary states:

$$\hat{H}_{\text{total}} = \hat{H}_{\text{elec}} + \hat{H}_{\text{vib}} + \hat{H}_{\text{rot}} \quad 2$$

$$E_{\text{total}} = E_{\text{elec}} + E_{\text{vib}} + E_{\text{rot}} \quad 3$$

All work in this thesis was conducted within the electronic ground states and therefore the electronic component of the wavefunction is not needed.

1.1.2 VIBRATIONAL

Within the ground electronic state a molecule can transition from one vibrational energy level to another, the possible transitions of two vibrations ν_a and ν_b are shown in Figure 1.

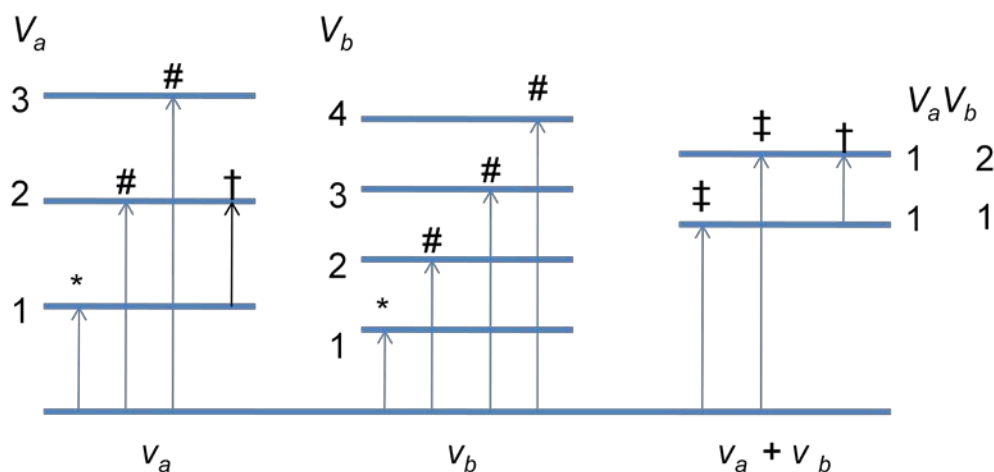


Figure 1: Possible vibrational transitions of ν_a and ν_b . Showing fundamentals (*), overtones (#), combination bands of both vibrations (‡) and hot bands (†).

If this transition results in a change in dipole moment a molecule can be excited by an infrared photon. This can be deduced by symmetry considerations; if the symmetry species of the vibrational mode possess a linear translation it will be infrared allowed.

More explicitly the probability of absorption occurring is given by:

$$(a|\hat{\mu}_F|b) = \int \psi_a^* \hat{\mu}_F \psi_b d\tau \quad 4$$

Where $F = x, y, z$ represents the matrix elements of the electric dipole moment (μ) of the molecule along each Cartesian axis.

The vibrational motion of the atomic nuclei in a diatomic molecule can be approximated by a harmonic potential, shown in Figure 2.

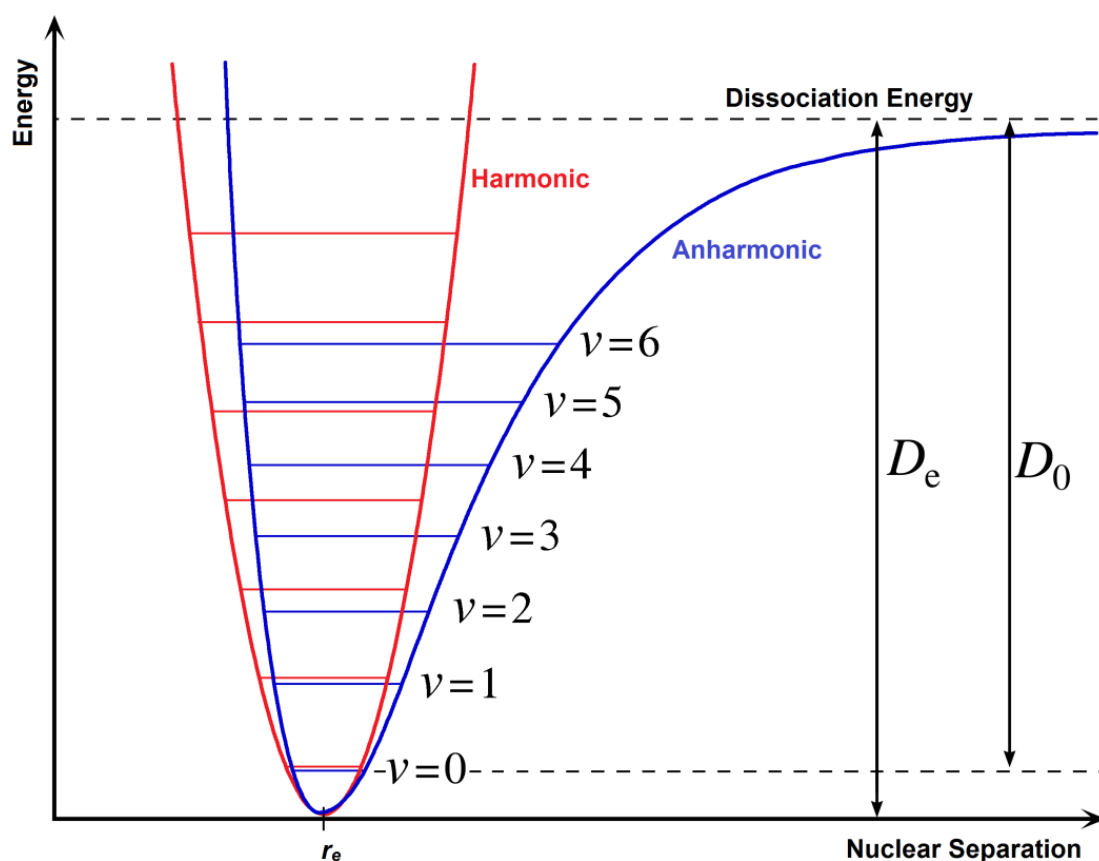


Figure 2: One dimensional potential energy surfaces for a harmonic (red) and anharmonic oscillator

The harmonic energy levels are given by:

$$E_v = h\omega\left(v + \frac{1}{2}\right) \quad 5$$

Where $v = 0,1,2,3 \dots$ is the vibrational quantum number, h is the Planck constant and ω is the angular vibrational frequency.

While the harmonic potential is adequate for small oscillations it cannot explain a number of important molecular properties such as vibrational overtones, hot bands, dissociation energy or vibrations with large amplitudes. An anharmonic Morse potential is needed to explain these and the spacing between anharmonic energy levels are given by:

$$E(v) = \omega_e \left(v + \frac{1}{2}\right) - \omega_e x_e \left(v + \frac{1}{2}\right)^2 + \omega_e y_e \left(v + \frac{1}{2}\right)^3 + \dots \quad 6$$

Where $\omega_e x_e$ and $\omega_e y_e$ are the anharmonic constants

When molecules are in the condensed phase the vibrational motion of one molecule can influence that of a neighbouring molecule. The treatment of these vibrations is important to the work presented in chapter 3 of this thesis which is concerned with IR spectroscopy of gases condensed into the aerosol phase. The special considerations related to aerosols are presented in an introduction to that section. In the current section molecules will be assumed to be in the gas phase and at low pressure, i.e. each molecule behaves independently.

1.1.3 ROTATIONAL

The distribution of mass in a molecule can be described by the moments of inertia (I) about the Cartesian axes (x, y, z):

$$I_x = \sum_i m_i (y_i^2 + z_i^2) \quad \mathbf{7}$$

$$I_y = \sum_i m_i (x_i^2 + z_i^2) \quad \mathbf{8}$$

$$I_z = \sum_i m_i (x_i^2 + y_i^2) \quad \mathbf{9}$$

Another set of axes are chosen such that the products of inertia (I_{xy}, I_{yz}, I_{xz}) equal zero, these axes (a, b, c) are the principal inertial axes. The most commonly used convention is the I^r representation where $(x, y, z) \equiv (b, c, a)$, the other possible representations are shown in Table 1.

Table 1 Identification of molecular axes						
	I^r	II^r	III^r	I^I	II^I	III^I
x	b	c	a	c	a	b
y	c	a	b	b	c	a
z	a	b	c	a	b	c

By convention the axes are chosen such that:

$$I_c \geq I_b \geq I_a \quad \mathbf{10}$$

In both upper and lower vibrational states a gas phase molecule has rotational angular momentum. It is often useful to use rotational constants (A, B, C) which are defined as:

$$A = \frac{\hbar^2}{2I_a}, B = \frac{\hbar^2}{2I_b}, C = \frac{\hbar^2}{2I_c} \quad \mathbf{11}$$

In diatomic or linear molecules ($I_c = I_b > I_a = 0$) the rotational energy levels can be described by the total angular momentum quantum number, J and the rotational energy levels are given by:

$$E_J = BJ(J + 1) - Dj^2(J + 1)^2 + HJ^3(J + 1)^3 \dots \quad 12$$

Where, D the quartic centrifugal distortion constant and H the sextic centrifugal distortion constant (all in units of frequency).

For symmetric tops all three moments of inertia are non-zero ($I_c > I_b = I_a$) and a second quantum number, K , is required which is the projection of the total angular momentum along the symmetry axis, thus $K \leq J$. There are also two rotational constants, A and B . The term equation of a symmetric top is given by:

$$\begin{aligned} E_{J,K} = & BJ(J + 1) + (A - B)K^2 - D_J[J(J + 1)]^2 - D_{JK}[J(J + 1)]K^2 \\ & - D_K K^4 + H_{JJ}[J(J + 1)]^3 + H_{JK}[J(J + 1)]^2 K^2 \quad 13 \\ & + H_{KK}[J(J + 1)]K^4 + H_{KKK}K^6 + \dots \end{aligned}$$

The degree of asymmetry in an asymmetric top ($I_c \neq I_b \neq I_a$) can be given by κ which can vary between -1 for a prolate symmetric top and +1 for an oblate symmetric top.

$$\kappa = \frac{2B - A - C}{A - C} \quad 14$$

And the K quantum number is replaced by K_a and K_c which are projections of K about the a and c inertial axis at the prolate and oblate limits of κ . Between these two limits K_a and K_c are no longer 'good' quantum numbers as the rotational momentum is no longer equal along any symmetry axis. The selection rules for K_a and K_c depend on the symmetry axis that the change in dipole moment occurs along; these are listed in Table 2.

Table 2: Ro-vibrational selection rules

Transition Dipole	Band Type	Selection Rules ($K_a K_c$)	ΔJ	ΔK_a	ΔK_c	Parity Change
a-axis	A-type	$ee \leftrightarrow eo$ $oe \leftrightarrow oo$	$0, \pm 1$	$0, \pm 2, \pm 4 \dots$	$\pm 1, \pm 3 \dots$	K_c
b-axis	B-type	$ee \leftrightarrow oo$ $oe \leftrightarrow eo$	$0, \pm 1$	$\pm 1, \pm 3 \dots$	$\pm 1, \pm 3 \dots$	K_a, K_c
c-axis	C-type	$ee \leftrightarrow oe$ $eo \leftrightarrow oo$	$0, \pm 1$	$\pm 1, \pm 3 \dots$	$0, \pm 2, \pm 4$	K_a

The transitions are grouped into the P -branch ($\Delta J = -1$), Q -branch ($\Delta J = 0$) and the R -branch ($\Delta J = +1$) and are shown in Figure 3. Transitions where $\Delta K_a/K_c \geq 2$ are typically not observable as they are substantially less likely.

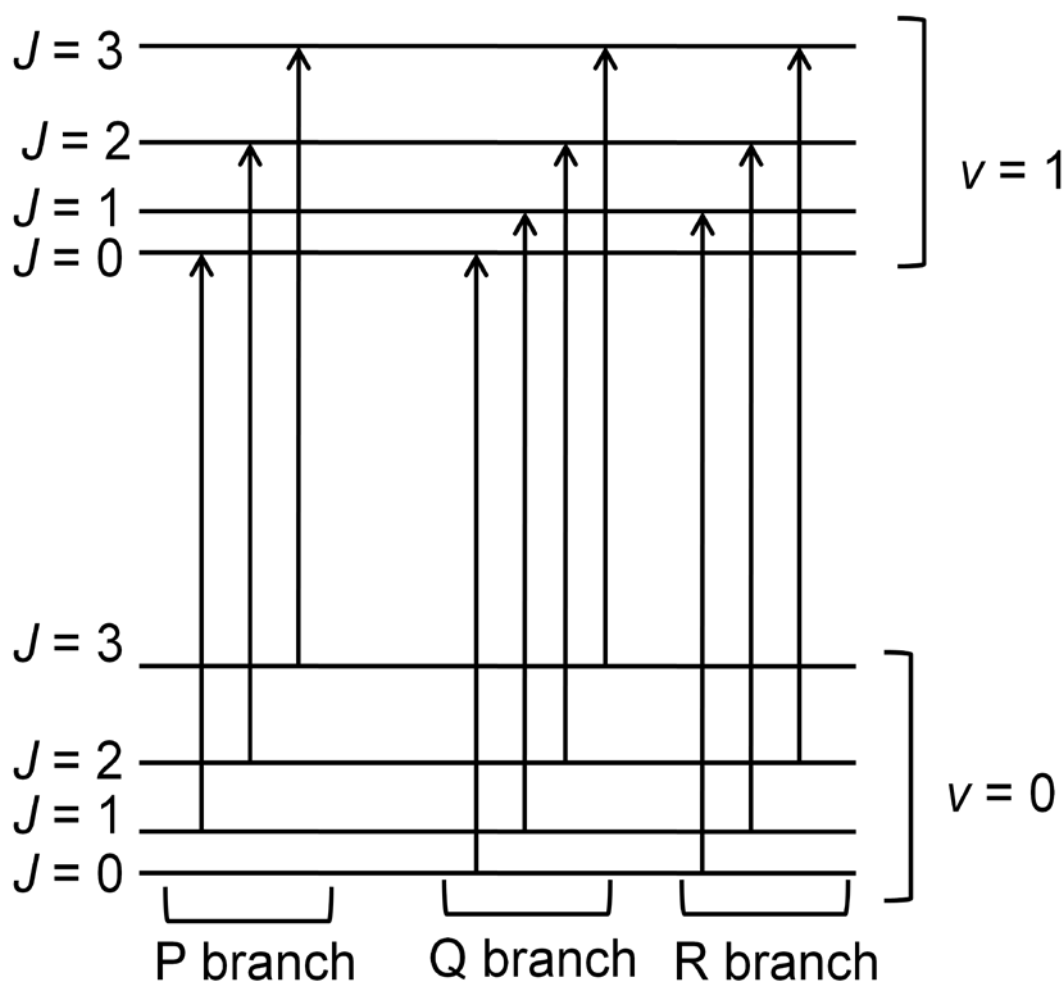


Figure 3: Possible rotational transitions within a vibrational transition. P branch $\Delta J = -1$, Q branch (not always allowed) $\Delta J = 0$, R branch $\Delta J = +1$.

Whereas the rotational energy levels of linear or symmetric rotors can be expressed as term equations, the matrix representation of the molecular Hamiltonian needs to be evaluated in order to determine the rotational energy levels of an asymmetric top. The general form of this Hamiltonian is very complex; however the number of terms can be reduced significantly by taking into account symmetry properties. Two common forms are Watson's S (symmetrically) and A (asymmetrically) -reduced Hamiltonians, these use wavefunctions of a symmetric top $\Psi^S = |J, K\rangle$ and K_a is substituted for K . When expressed in terms of the quantum mechanical operators the Watson S-reduced Hamiltonian takes the form:

$$\begin{aligned}
\hat{H} = & \frac{1}{2}(B_x + B_y)\hat{J}^2 + [B_z - \frac{1}{2}(B_x + B_y)]\hat{J}_z^2 \\
& + \frac{1}{4}(B_x - B_y)(\hat{J}_+^2 + \hat{J}_-^2) - D_J\hat{J}^4 - D_{JK}\hat{J}^2\hat{J}_z^2 - D_K\hat{J}_z^4 \\
& + d_1\hat{J}^2(\hat{J}_+^2 + \hat{J}_-^2) + d_2(\hat{J}_+^4 + \hat{J}_-^4) + H_{JJJ}\hat{J}^6 + H_{JJK}\hat{J}^4\hat{J}_z^2 \\
& + H_{JKK}\hat{J}^2\hat{J}_z^4 + H_{KKK}\hat{J}^6 + h_1\hat{J}^4(\hat{J}_+^2 + \hat{J}_-^2) + h_2\hat{J}^2(\hat{J}_+^4 + \hat{J}_-^4) \quad 15 \\
& + h_3(\hat{J}_+^6 + \hat{J}_-^6) - L_{JJJJ}\hat{J}^8 - L_{JJJK}\hat{J}^6\hat{J}_z^2 - L_{JJKK}\hat{J}^4\hat{J}_z^4 \\
& - L_{JKKK}\hat{J}^2\hat{J}_z^6 - L_{KKKK}\hat{J}_z^8 + l_1\hat{J}^6(\hat{J}_+^2 + \hat{J}_-^2) + l_2\hat{J}^4(\hat{J}_+^4 + \hat{J}_-^4) \\
& + l_3\hat{J}^2(\hat{J}_+^6 + \hat{J}_-^6) + l_4(\hat{J}_+^8 + \hat{J}_-^8) \dots
\end{aligned}$$

Where \hat{J} is the total angular momentum vector and $\hat{J}_x, \hat{J}_y, \hat{J}_z$ are the angular momentum vectors along the x, y, z molecular axis and \hat{J}^2 and \hat{J}_\pm^2 are:

$$\hat{J}^2 = \hat{J}_x^2 + \hat{J}_y^2 + \hat{J}_z^2 \quad 16$$

$$\hat{J}_\pm^2 = \hat{J}_x \pm i\hat{J}_y \quad 17$$

Specific rotational energy levels can be grouped into four Wang sub-groups: E⁺, E⁻, O⁺ and O⁻ where the parity of K_a is denoted by E (even) or O (odd) and the superscript '+' denotes $J - K_a + K_c = 0$ while '-' denotes $K_a + K_c - J = 1$. The matrix elements for the S-reduced Hamiltonian up to the 8th order are shown below (equations 18-21) in the I' representation. Each of these elements can be solved separately for each value of J and each of the Wang sub-groups.

$$\begin{aligned}
\langle v_s; J, K | \hat{H} | v_s; J, K \rangle = & \overline{\mathbf{v}}_s^0 + \overline{\mathbf{B}}_s J(J+1) + (A_s - \overline{\mathbf{B}}_s) K^2 - D_J J^2 (J+1)^2 - \\
& D_{JK} J(J+1) K^2 - D_K K^4 + H_{JJJ} J^3 (J+1)^3 + H_{JJK} J^2 (J+1)^2 K^2 + \\
& H_{JKK} J(J+1) K^4 + H_{KKK} K^6 - L_{JJJJ} J^4 (J+1)^4 - L_{JJJK} J^3 (J+1)^3 K^2 - \\
& L_{JJKK} J^2 (J+1)^2 K^4 - L_{JKKK} J(J+1) K^6 - L_{KKKK} K^8 \dots
\end{aligned} \tag{18}$$

$$\begin{aligned}
\langle v_s; J, K | \hat{H} | v_s; J, K \pm 2 \rangle = & [1/4 (B - C) + d_1 J(J+1) + h_1 J^2 (J+1)^2 + \\
& l_1 J^4 (J+1)^4 \dots] F_{\pm}(J, K) F_{\pm}(J, K \pm 1)
\end{aligned} \tag{19}$$

$$\begin{aligned}
\langle v_s; J, K | \hat{H} | v_s; J, K \pm 4 \rangle = & [d_2 + h_2 J(J+1) \dots] F_{\pm}(J, K) F_{\pm}(J, K \pm 1) \\
& F_{\pm}(J, \pm 2) F_{\pm}(J, K \pm 3)
\end{aligned} \tag{20}$$

$$\begin{aligned}
\langle v_s; J, K | \hat{H} | v_s; J, K \pm 6 \rangle = & \\
& h_3 F_{\pm}(J, K) F_{\pm}(J, K \pm 1) F_{\pm}(J, \pm 2) F_{\pm}(J, K \pm 3) F_{\pm}(J, K \pm 4) F_{\pm}(J, K \pm 5)
\end{aligned} \tag{21}$$

1.1.4 VIBRATION/ROTATION INTERACTIONS

A Coriolis interaction is a breakdown of the Born-Oppenheimer approximation where molecular vibrations can influence the rotational energy levels. A Coriolis interaction can exist between vibrational states ν_s and $\nu_{s'}$, if the product of the symmetry species contains a rotational term R_α , where α is the axis along which the Coriolis interaction occurs. This represents a breakdown in the Born-Oppenheimer approximation and the vibrations and rotations can no longer be treated independently. The matrix elements for the Coriolis interactions were derived by [1]:

$$\text{1st Order: } \langle \nu_s, \nu_{s'} | \hat{H} | \nu_s + 1, \nu_{s'}, -1 \rangle = i \xi_{\nu\nu'}^\alpha \hat{J}_\alpha \quad \mathbf{22}$$

$$\text{2nd Order: } \langle \nu_s, \nu_{s'} | \hat{H} | \nu_s + 1, \nu_{s'}, -1 \rangle = \eta_{\nu\nu'}^{\beta\gamma} \{ \hat{J}_\beta, \hat{J}_\gamma \}_+ \quad \mathbf{23}$$

The Coriolis interaction occurs between different Wang sub-blocks in each vibrational level as shown in Table 3.

Table 3: Linked Wang sub-blocks in Coriolis and Fermi interactions

Interaction	Linked sub-blocks
<i>a</i> -axis Coriolis	$E^+ \leftrightarrow E^-, O^+ \leftrightarrow O^-$
<i>b</i> -axis Coriolis	$E^+ \leftrightarrow O^-, E^- \leftrightarrow O^+$
<i>c</i> -axis Coriolis	$E^+ \leftrightarrow O^+, E^- \leftrightarrow O^-$
Fermi	$E^+ \leftrightarrow E^+, E^- \leftrightarrow E^-,$ $O^+ \leftrightarrow O^+, O^- \leftrightarrow O^-,$

Fermi resonances occur between vibrational modes that possess the same symmetry, the matrix terms are shown below and the linked Wang-sub blocks are shown in Table 3.

$$\langle \nu; J, K | \hat{H} | \nu; J, K \rangle = F_{\nu\nu'} + F_{\nu\nu'}^J J(J+1) + F_{\nu\nu'}^K K^2 \quad \mathbf{24}$$

$$\langle \nu; J, K | \hat{H} | \nu; J, K \pm 2 \rangle = \pm F_{\nu\nu'}^\alpha F_\pm(J, K) F_\pm(J, K \pm 1) \quad \mathbf{25}$$

1.1.5 ANALYSIS TECHNIQUES

The analysis of high resolution spectra begins with the processing of the raw spectra in order to produce a list of peak positions. The interferogram is post zero-filled so that the peak positions are precisely determined. The spectrum is then calibrated by comparing with the known position of vibration-rotation lines, typically residual atmospheric molecules (H₂O or CO₂) with absorptions in the region of interest.

A peak list of the absorptions in the region of interest is then generated and inputted into a Loomis-Wood spectral analysis program. Our group normally uses MACLOOMIS[2], however there are a number of other programs such as LOOMIS-WOOD FOR WINDOWS[3], PGOPHER[4]. All these programs operate on the principal of splitting the spectrum into sections of equal length and stacking them vertically so that patterns in the vibration-rotation lines emerge and can be used to assign quantum numbers to the transitions.

The length of these sections is based on the spacing of transitions in linear rotors:

$$E_J - E_{J-1} = BJ(J + 1) - BJ(J - 1) = 2BJ \quad 26$$

Thus if each spectral section is $2B \text{ cm}^{-1}$ in length then transitions of successive values of J will stack vertically. A similar pattern is observed for symmetric and asymmetric tops however there are multiple vertical stacks with successive values of K fanning horizontally as shown in left side of Figure 4.

In order to stack the transitions correctly an informed choice of band origin, rotational and centrifugal distortion constants must be made. This initial choice is based on either ground state rotational constants or constants determined from *ab initio* calculations and a band centre estimated from the raw spectrum. If this choice is close enough a pattern should be evident and peaks can be selected and fitted to an equation similar to equation 26.

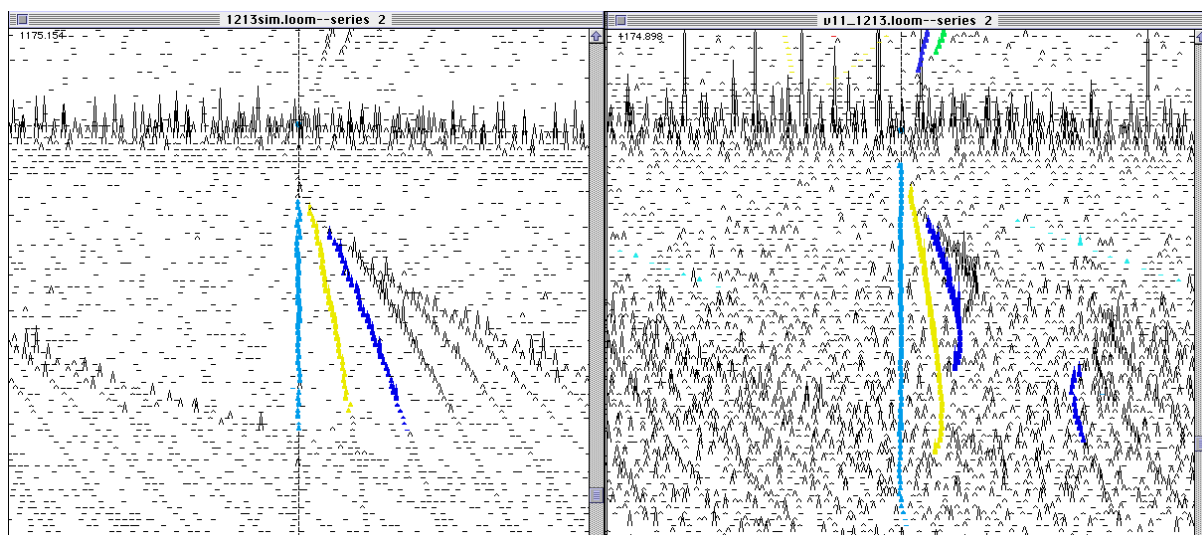


Figure 4: MacLoomis plots of the a-type ν_{11} mode of $^{12}\text{C}^{13}\text{CF}_4$, from a simulation using parameters from $^{12}\text{C}_2\text{F}_4$ (left) and from an experimental spectrum (right)

At this point the Loomis-Wood plot should appear somewhat like Figure 4 with a series of transitions arranged vertically. The next step is to assign quantum numbers to each of these transitions. Initially this is aided by examining a similar Loomis-Wood plot of peaks from a predicted line positions generated from an initial 'guess' of rotational and centrifugal distortion constants. If ground vibrational state constants are known an initial approximation that $B' = B''$ may predict transitions close enough for correct assignment to be possible. An *ab initio* calculated change in rotational constants may be used to provide a better prediction. If ground vibrational state rotational constants are lacking the initial prediction would rely solely on *ab initio* calculations or on the ground state constants for a similar molecule.

Figure 4 shows the MACLOOMIS plots of an a-type band of $^{12}\text{C}^{13}\text{CF}_4$, the left panel is a simulation based on constants of the $^{12}\text{C}_2\text{F}_4$ isotopologue while the right panel is the experimental spectrum of a similar band of the $^{12}\text{C}^{13}\text{CF}_4$ isotopologue. It can be seen that while the patterns are not identical they are sufficiently close enough so as to enable an initial assignment. The assigned transitions are then used as an input for SPFIT, a least squares fitting program that fits rotational constants to the assigned transitions [5]. These assignments can be confirmed by using ground state combination differences.

1.1.6 GROUND STATE COMBINATION DIFFERENCES

Assigned rovibrational transitions can be used to generate a set of pseudo-transitions that depend only on the lower vibrational state. If two transitions originate from different lower state energy levels but go to the same upper state energy level the difference in energy between the two transitions will be equal to a hypothetical transition within the lower vibrational state (see Figure 5). These ground state combination differences can be used to determine ground vibrational state rotational and centrifugal distortion constants where pure rotational data is unavailable (no permanent dipole moment) or incomplete. Alternatively they can be used to check the veracity of assignments.

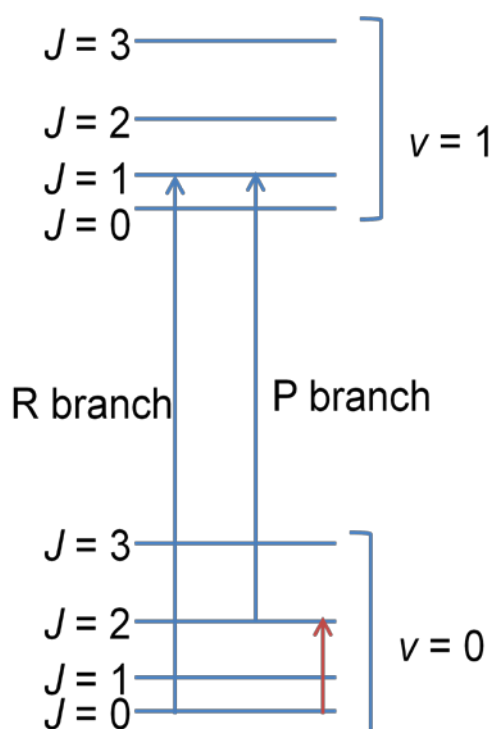


Figure 5: Calculation of a ground state combination difference pseudo transition (red) from two observed transitions (blue)

The rotational constants can be used to accurately predict rotational and rovibrational line positions which can then be used to aid the remote identification and quantification of molecules in a wide range of environments. Accurate quantification also requires an accurate prediction of line shapes which are a function of the Doppler and pressure broadening.

1.1.7 STRUCTURAL DETERMINATION

Since rotational constants are the reciprocal of the moments of inertia they describe the mass distribution in a molecule and can be used to determine the gas phase molecular structure. A first approximation involves using the ground state rotational constants to find a ground vibrational state structure. This can be done by fitting the structural parameters of a molecule (bond lengths and angles) to the ground state constants which results in an r_0 structure. This structure includes the effects of the zero point motions of the molecule and can be significantly different to the equilibrium structure..

If the rotational constants for the upper vibrational state are known for all vibrational modes the vibration-rotation interaction parameters (α) can be determined and can be subtracted from the ground vibrational state rotational constants to produce equilibrium rotational constants.

$$A_v = A_e - \sum_i \alpha_i^A \left(\nu_i + \frac{1}{2} \right) \quad 27$$

$$B_v = B_e - \sum_i \alpha_i^B \left(\nu_i + \frac{1}{2} \right) \quad 28$$

$$C_v = C_e - \sum_i \alpha_i^C \left(\nu_i + \frac{1}{2} \right) \quad 29$$

Apart from the simplest of molecules it is only possible to determine the rotational constants for a small proportion of the vibrational modes. However an important feature of vibrational potential wells is that the equilibrium point does not change with isotopic substitution. This can be exploited via the substitution method to produce an r_s molecular structure. If ground state rotational constants for two isotopologues of a molecule are known then the Cartesian coordinates of the substituted atom, in relation to the centre of mass, can be determined. For a planar asymmetric top (such as C_2F_4):

$$|x| = \left[\frac{1}{\mu} \frac{(I'_Y - I_Y)(I'_X - I_X)}{I_X - I_Y} \right]^{\frac{1}{2}} \quad \mathbf{30}$$

$$|y| = \left[\frac{1}{\mu} \frac{(I'_X - I_X)(I'_Y - I_Y)}{I_Y - I_X} \right]^{\frac{1}{2}} \quad \mathbf{31}$$

Where I_X is the moment of inertia about the x Cartesian axis of the parent species and I'_X is the moment of inertia of the substituted species and $\mu = M\Delta m/(M + \Delta m)$ and M is the mass of the parent species, Δm is the change in mass of the molecule upon isotopic substitution.

This is usually closer to the equilibrium structure than the r_0 structure as the vibrational contributions to the zero point energy tend to cancel out between isotopologues. However this is not perfect and a number of structural determination methods have been developed to achieve greater compatibility with the equilibrium structure. These include r_c [6] r_m [7] and $r_m^{(2)}$. [8] However with the increasing availability of high level *ab initio* computational methods it has become possible to calculate the vibration-rotation interaction parameters accurately. This can be used to convert the ground state rotational constants into equilibrium constants which can then be used to fit the structural parameters r_e^{SE} . This semi-experimental method can produce molecule geometries that are very close to full experimental structures.

1.1.8 COMPUTATIONAL METHODS

While computational chemistry was not a large focus of this thesis it was used a number of times to aide spectroscopic measurements. A full description of the methods is beyond the scope of this thesis however the methods used are briefly described below.

Density function theory describes the molecule using functions describing the distribution electron density. Hybrid functionals, such as B3LYP (Becke, three-parameter, Lee-Yang-Parr) approximate the electron-electron exchange-correlation functional by using a linear combination of the exact Hartree-Fock functional.

Møller-Plesset perturbation theory extends the Hartree-Fock method by including electron-electron correlation effects using Rayleigh-Schrödinger perturbation theory.[9] Second order (MP2) calculations are the most common form as they are relatively inexpensive and provide good agreement to experiment.

Coupled Cluster is a numerical technique that also extends the Hartree-Fock method by constructing multi-electron wavefunctions and using an exponential cluster operation to include electron correlation effects. These cluster operations use an excitation operator to produce a linear combination of Slater determinants and can be performed at singly, doubly etc excitation levels.

Each level of theory also requires the use of a basis sets which are linear combinations of functions used to create the molecular orbitals, typically in the form of Gaussian functions. The main basis sets that were used in this work can be divided into three groups: Pople's triple split (6-311)[10], the Dunning-type correlation consistent (cc-pVnZ)[11] and Ahlrich's contracted Gaussians (nZV)[12]. Each of these can be augmented by adding diffuse functions which attempt to model the orbitals at distances far from the nuclei.

1.2 INSTRUMENTATION

1.2.1 MOLECULAR SPECTROSCOPY TECHNIQUES

There are a number of experimental techniques that can provide information on molecule vibrations and/or rotations. Raman spectroscopy measures vibrational modes that are complimentary to infrared spectroscopy. Raman is generally not sensitive enough to provide information on molecular rotations as only a small fraction of scattered photons are Raman scattered (≈ 1 in 10 million). Techniques such as surface or tip enhanced Raman spectroscopy can improve the sensitivity by factors up to 10^{10} , however they are not useful for rotational spectroscopy.

Microwave and millimetre wave spectroscopy provides valuable information on vibrational ground state rotational constants. This is a very mature field and the sensitivity and resolution of modern instruments is extremely competitive. These techniques only have a limited ability to probe excited vibrational states via vibrational satellites. Only low lying modes that can be thermally populated are accessible to pure rotational spectroscopy. Molecules must also possess a significant permanent dipole moment to be detectable by these methods.

Laser based spectroscopic techniques such as tunable diode laser absorption or cavity ring down spectroscopy can be extremely sensitive with detection limits of parts per billion to trillion. These methods are often limited to measuring small spectral slices as the available lasers cannot be tuned over a wide range. More modern lasers, such as quantum cascade lasers, make new spectral ranges accessible with greater tunability however they cannot yet match the range of broadband FTIR spectroscopy.

1.2.2 FTIR THEORY

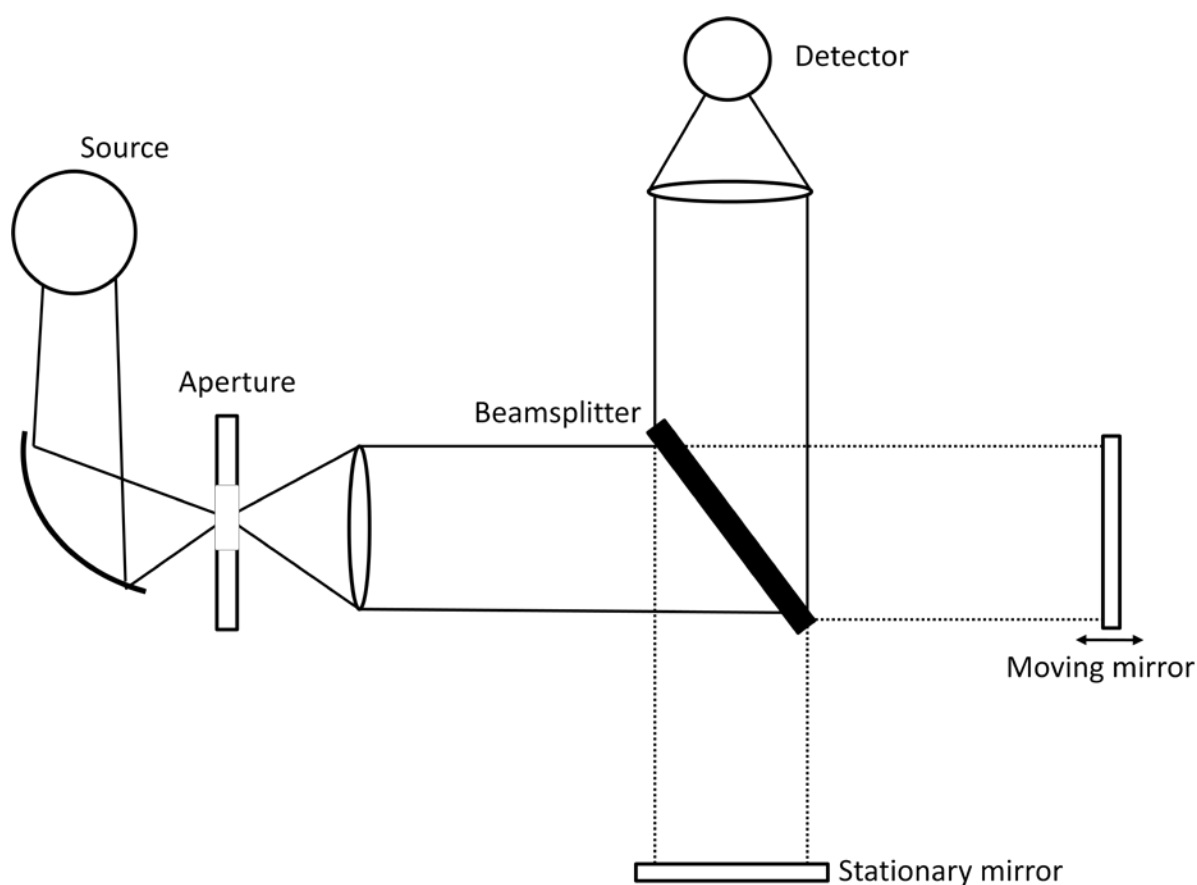


Figure 6: Schematic of a Michelson interferometer

Unlike dispersive spectrometers that use a grating or prism to divide the spectrum into discrete sections Fourier transform (FT) spectrometers use a Michelson interferometer (Figure 6) to obtain a spectrum. The beamsplitter splits the source beam and sends half the beam to the stationary mirror and the other half to a moving mirror; creating a difference in path length between the two beams. When the beam is recombined constructive and destructive interference occurs, this interference pattern is recorded as intensity (I) at the detector as a function of the path length difference or optical retardation (δ). The resultant interferogram is then Fourier transformed to produce the energy-spectrum.

1.2.3 INSTRUMENTAL LINE SHAPE

The interferogram of a monochromatic line is given by:

$$I(\delta) = 0.5I(\nu) \cos(2\pi\nu\delta) \quad 32$$

The Fourier transform is performed to obtain the energy spectrum:

$$B(\tilde{\nu}) = \int_{-\infty}^{+\infty} I(\delta) \cos 2\pi \tilde{\nu} \delta \, d\delta$$

This implies that the interferogram needs to be measured for an optical difference between $-\infty$ and $+\infty$ to avoid this the measured interferogram is convolved with a second function $D(\delta)$:

$$B(\tilde{\nu}) = \int_{-\infty}^{+\infty} I(\delta) D(\delta) \cos 2\pi \tilde{\nu} \delta \, d\delta \quad 33$$

In its simplest form $D(\delta)$ is equal to one for the range where the interferogram was measured and is zero outside of this range. This is referred to as a box car function and for the idealised monochromatic line the Fourier transformation produces the sinc function:

$$f(\nu) = 2\Delta \text{sinc}(2\pi\nu\Delta) \quad 34$$

This produces a spectrum (Figure 7) that with a central peak of width $0.605/\Delta$ and with side lobes that are up to 22% of the amplitude of the main peak.

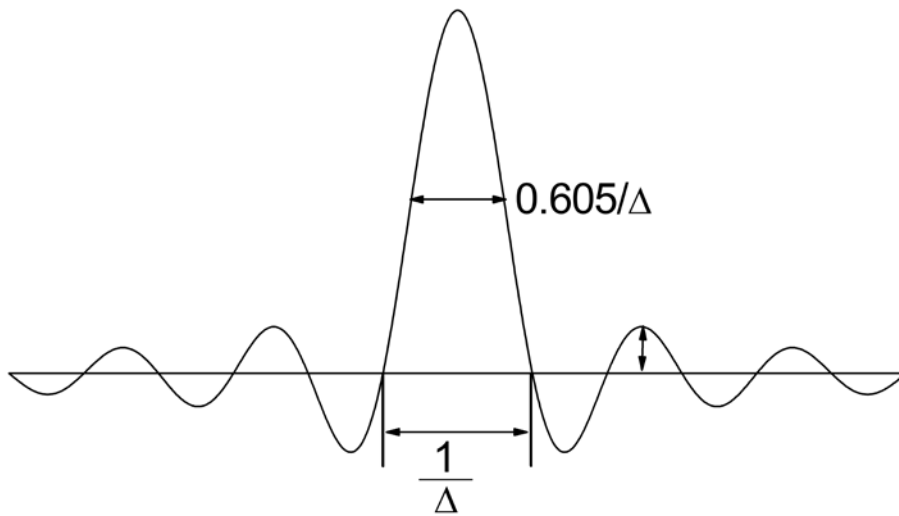


Figure 7: Spectral line shape of a monochromatic line from a Fourier transform with the Boxcar function

These side lobes can be minimised by using a different function for $D(\delta)$, these so called apodisation functions truncate the interferogram less abruptly than the box car function and reduce the side lobes at the expense of resolution. For high resolution spectroscopy the signal at maximum optical path difference is very close to zero and the interferogram is effectively self apodised. However 3 or 4 point apodisation functions can still be helpful in reducing the intensity of side lobes. These functions use the last few points of the interferogram to gradually reduce the intensity to zero.

1.2.4 ZERO FILL FACTOR

A consequence of only measuring a finite number of points is the picket fence effect where absorption lines appear to be clipped. This can be overcome by adding zeros to the end of the interferogram, in effect interpolating the spectrum. A zero fill factor of 2 doubles the number of points in the interferogram, typically a fill factor of at least 8 is used to ensure peak positions are precise.

1.2.5 APERTURE

The idealised case above requires a perfectly collimated beam that produces complete interference however an infinitely small source is required to produce such a beam. The light produced from a source of finite size will produce a divergent beam and it can be shown that a divergent beam will produce an interference pattern with the form of concentric rings of intensity with a spacing that becomes shorter with greater optical retardation.[13] If these concentric rings are measured by the detector it will have the effect of further apodising the interferogram thus limiting resolution. An aperture is required so that only the central maximum of the image is sampled by the detector. The size of the aperture required for a thermal source is given by:

$$d_{max} = 2\sqrt{2}F \sqrt{\frac{\Delta\tilde{\nu}}{\tilde{\nu}}} \quad 35$$

Where d is the diameter of the aperture and F is the focal length of the collimating mirror, for the Bruker 125HR this is 418 mm. When operating at full resolution (0.00096 cm^{-1}) the aperture required is:

$$d_{max} \approx \frac{36.63}{\sqrt{\tilde{\nu}}} \quad 36$$

1.3 SYNCHROTRONS

The above equation (36) is only true for thermal sources that emit in all directions from a relatively large area. The source point of synchrotron radiation is the electron beam in the storage ring which, for normal operation at the Australia Synchrotron, is $\approx 300 \mu\text{m}$ in diameter (FWHH). Due to relativistic effects the synchrotron radiation is emitted into a narrow angle and for most infrared wavelengths the physical size of the source is often diffraction limited (fig 6 in ref [14]). This allows the source to be imaged as a near point source and the beam can therefore be well collimated without the need for an aperture.[15] These effects give synchrotron radiation sources a large advantage in brightness over blackbody sources as shown in Figure 8.

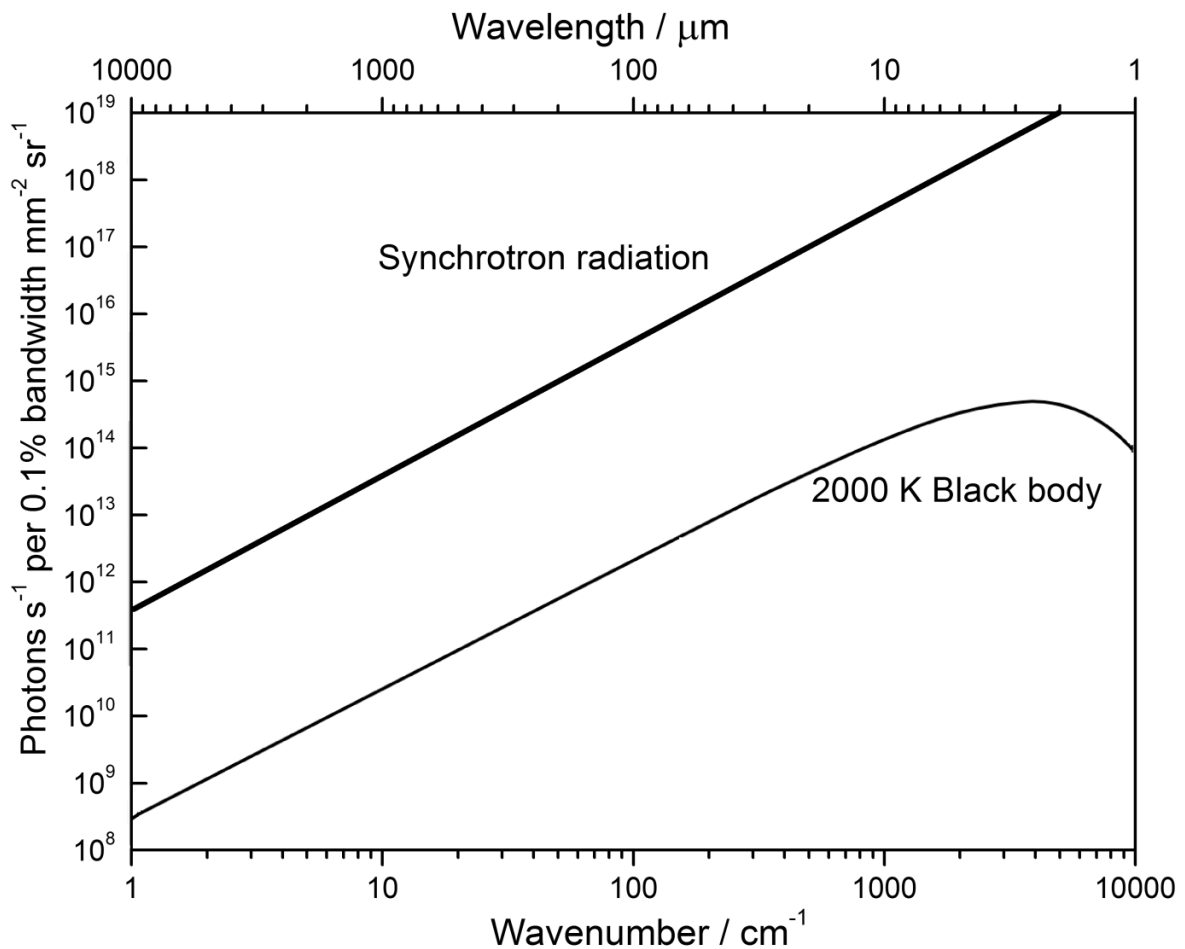


Figure 8: Brightness of a 1 A synchrotron source compared to a 2000 K black body source

The brightness of a black body source is given by the Planck equation:

$$B_{bb} = 2hc^2\tilde{\nu}^3 \frac{1}{e^{hc\tilde{\nu}/(k_B T)} - 1} \quad 37$$

While the brightness of a synchrotron source in the infrared can be approximated [16] by:

$$B_{sr}(\nu) = 10^{-8} I \tilde{\nu}^2 \quad 38$$

A full treatment of relativistic effects of an accelerated charged particle can be found in Ebashi et al.[17], and the advantages of synchrotron light specific to infrared spectroscopy were explored by Duncan & Williams.[14]

1.3.2 AUSTRALIAN SYNCHROTRON

The Australian Synchrotron is a 3rd generation light source which first uses a linear accelerator followed by a booster ring to inject relativistic electrons into a storage ring. The electrons orbit the storage ring at 3.0 GeV and emit radiation as they are accelerated by the bending magnets or one of the insertion devices located in the straight sections of the ring. Since May 2012 the ring has operated in ‘top-up mode’ where electrons are periodically injected into the storage ring to maintain a beam current of 200 mA. Most of the work in this thesis was performed when the ring was operated in a decay mode whereby an injection was made twice daily topping the current up to 200 mA which would decay to ≈ 150 mA over 12 hours.

1.3.3 COHERENT SYNCHROTRON EMISSION

Coherent synchrotron emission occurs when the electron bunches in the storage ring are of the same physical size as the emitted photons. This can, theoretically, occur at any wavelength however it is limited in practice to the very far-infrared region as for wavelengths smaller than ≈ 0.1 mm the electron-electron repulsion within the bunch becomes too great and beam stability cannot be maintained.

1.3.4 FREE ELECTRON LASERS

Free electron lasers emit light using a similar principle to coherent synchrotron emission. Instead of a storage ring a large linear accelerator and a long undulator are used to periodically accelerate an electron bunch perpendicular to the direction of travel. The periodicity of this acceleration is such that the motion of the electrons matches the electric field of the emitted radiation and adds coherently, greatly enhancing the intensity of the radiation. This intensity is unmatched by almost all other radiation sources, however the production mechanism makes the emission bandwidth very narrow. While the emission wavelength is tunable it is limited by the design of the machine, particularly the number of magnets and their strength.

1.3.5 FAR-IR BEAMLINER

The infrared beamlines at the Australian synchrotron extract a 58 mrad (horizontal) by 17 mrad (vertical) beam containing both bending magnet and edge radiation from the storage ring. This optical arrangement is described by Creagh et al. [18] and a schematic is shown in Figure 9. The first mirror is planar and has a 3 mm slot that allows X-Rays and UV radiation to pass through, greatly reducing heat load on the mirror. The collected visible and infrared light is then focused near to the diamond window which separates the ultra high vacuum of the storage ring from the high vacuum of the beamline. The bending magnet radiation is directed to the Infrared Microscopy beamline while the edge radiation is directed to the Far-IR High Resolution FTIR beamline.

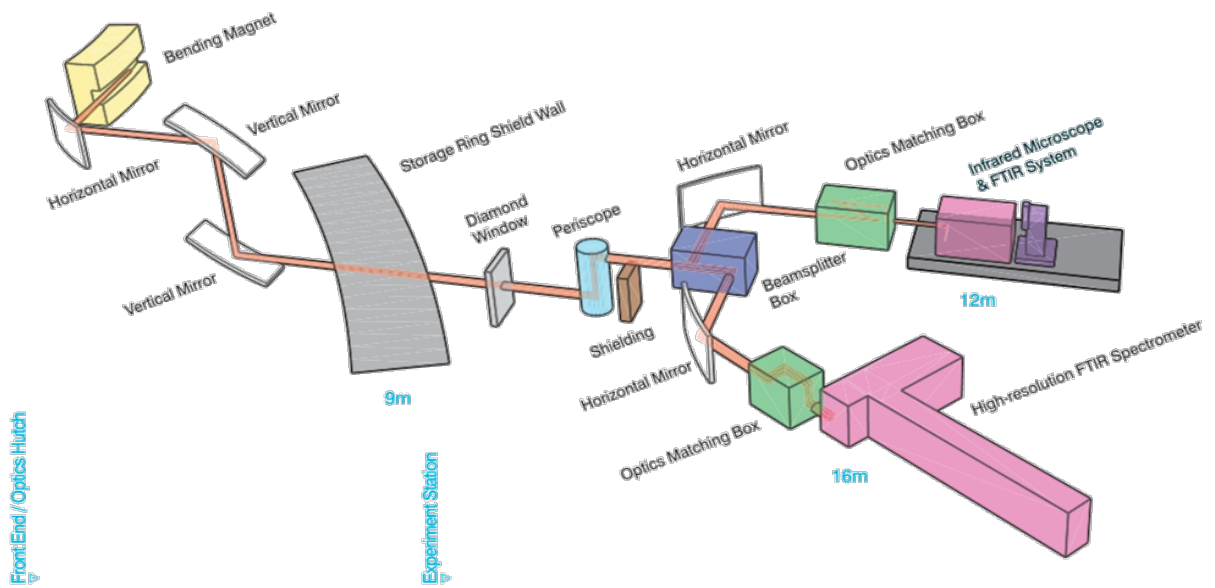


Figure 9: Schematic diagram of the infrared beamlines at the Australian Synchrotron

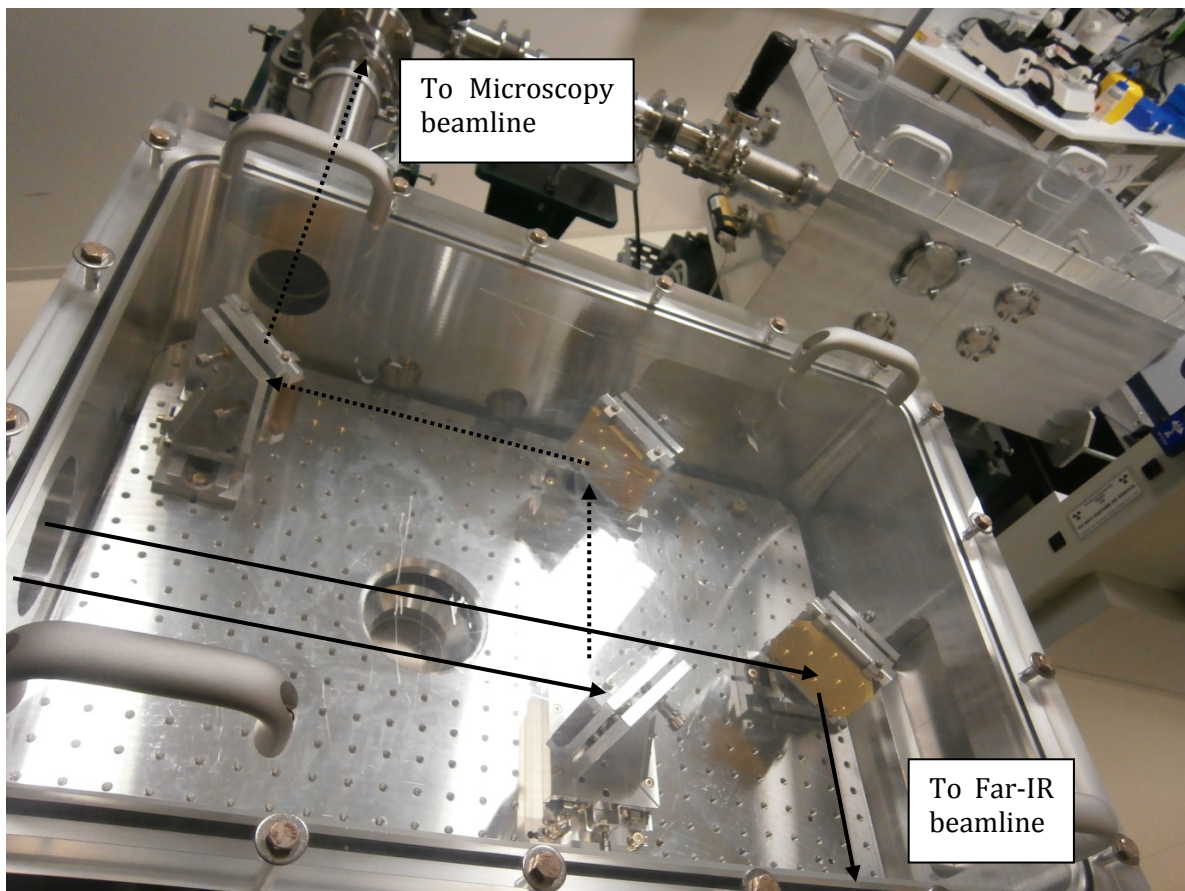


Figure 10: Optical path within the beamsplitter box of the IR beamlines

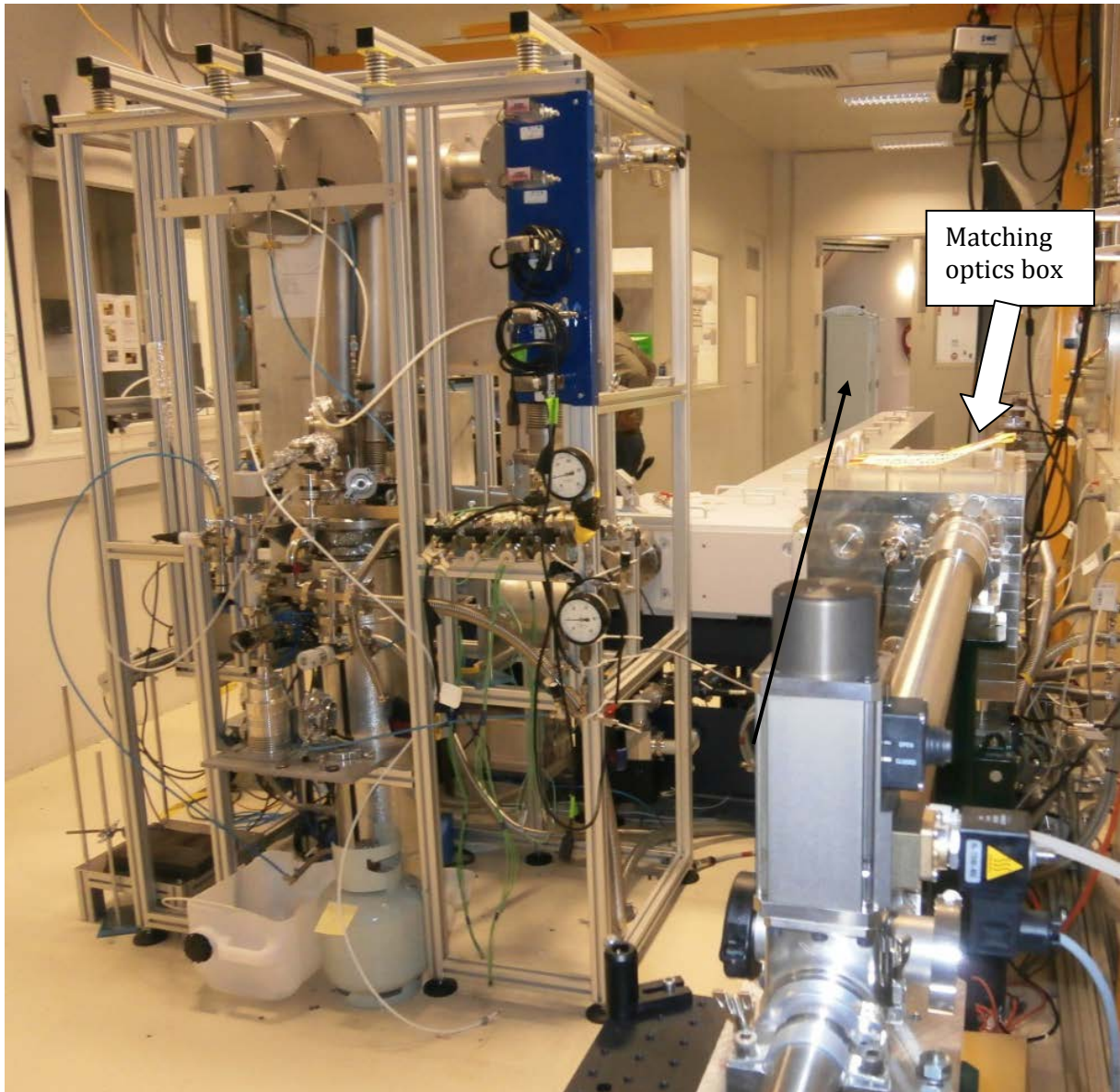


Figure 11: View of the Far-IR beamline from the horizontal mirror after the beamsplitter box. The spectrometer can be seen in the background, with the EFC cell in the foreground on the left.

1.4.1 BRUKER IFS125HR FTIR SPECTROMETER

From the beamsplitter box (Figure 10) the synchrotron beam is then collimated in the matching optics box (Figure 11) and passes into the source compartment of a Bruker IFS125HR spectrometer (see Figure 13) where it is focussed onto an aperture wheel. From this point the synchrotron beam uses the same optical path as the internal sources which can be selected via software. As discussed earlier (section 1.3) the synchrotron source does not require an aperture stop to improve the collimation so when the synchrotron source is used the aperture can be set to its largest setting (12.5 mm).



Figure 12: Interferometer arm of the Bruker IFS125HR

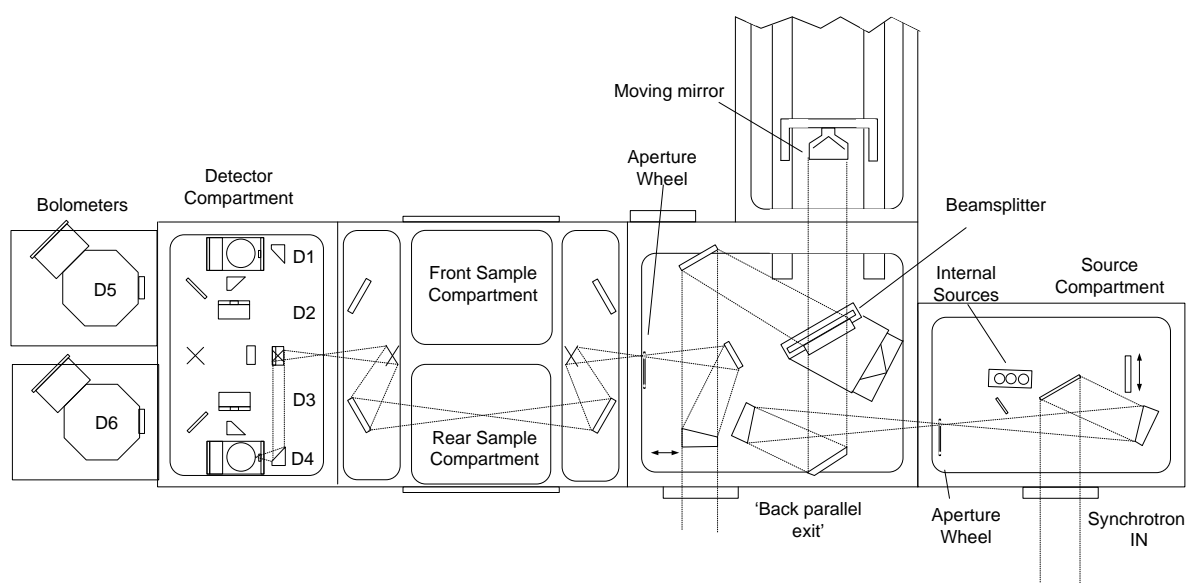


Figure 13: Schematic diagram of the Bruker IFS125HR. Detectors labelled as D1-D6

After the light passes through the aperture it enters the beamsplitter compartment. It is first collimated and then goes through the beamsplitter. Once recombined after the beamsplitter the parallel beam can be directed out of the spectrometer via the 'back parallel exit' or it can be focussed on a secondary aperture wheel and directed into the front or back sample compartments. From here any one of six detector positions can be selected. The various beamsplitters and detectors that are available are listed in Table 4 according to their useful spectral regions.

Table 4: Optimal optical configurations for various spectral ranges

Lower Limit (cm ⁻¹)	Upper Limit (cm ⁻¹)	Beamsplitter	Detector	Filter
5	95	125 mm Mylar	Si-Bolometer	CF=2
15	110	75 mm Mylar	Si-Bolometer	CF=2
110	380	6 mm Mylar	Si-Bolometer	CF=1
380	650	6 mm Mylar	Si:B Photo	CF=1
650	750	KBr	Si:B Photo	CF=1
750	1300	KBr	MCT-mid	4
1300	2850	KBr	MCT-narrow	6

1.4.2 SIGNAL TO NOISE

The advantage in brightness of the synchrotron source is key to FTIR spectroscopy because for systems limited by noise from the detector the signal to noise ratio of a FTIR spectrum can be described by:

$$\text{SNR} = \frac{B\theta\xi\Delta\nu t^{1/2}D^*}{A_D^{1/2}} \quad 39$$

Where B is the brightness of the source, θ is the optical acceptance, ξ is the optical efficiency, $\Delta\nu$ is the resolution, t is the measurement time, D^* and A_D is the detectivity and the surface area of the detector respectively.

Experimentally the signal to noise ratio can be increased by recording for a longer time, using a detector with greater detectivity, increasing the light reaching it or by increasing the brightness of the source. Since the SNR only scales with the square root of measurement time it is desirable to increase the other factors. The best available detectors are chosen for a particular experiment and the optical setup and alignment is optimised, leaving the source brightness as the remaining factor. For the same optical arrangement the $\approx 10^3$ enhancement in brightness offered by synchrotron radiation should increase SNR by a similar factor.

However, the above equation (39) is true for detector noise limited systems which is generally the case when a thermal source is used whereas when Synchrotron radiation is used noise inherent in the source usually dominates. The actual signal to noise advantage that the synchrotron source has over the internal sources was investigated at a number of positions throughout the infrared spectrum using the appropriate optical components. The SNR of the each source was calculated by ratioing two successive spectra to produce a 100% transmission curve which was then used to calculate signal to noise ratio using the inbuilt feature in Bruker's OPUS software package. The ratio of the SNR of the synchrotron source to the internal source is shown in is shown in Figure 14, also shown is the single channel intensity of the synchrotron source.

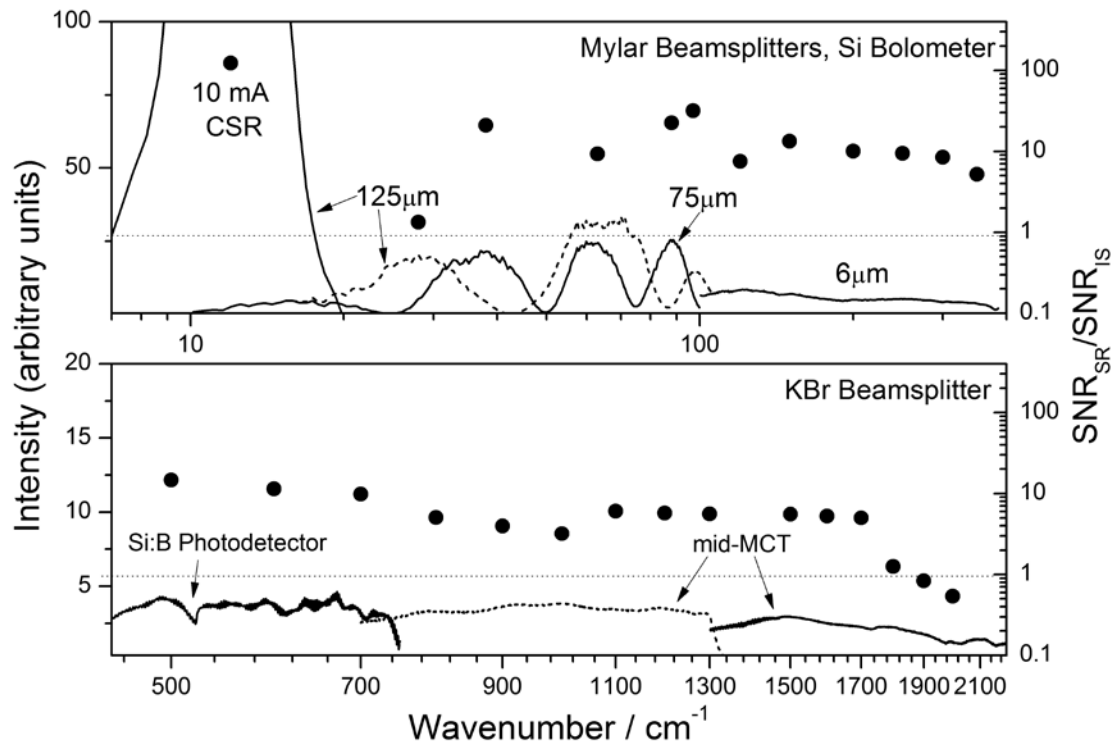


Figure 14: Ratios of the SNR of the synchrotron and internal sources (circles) and the single channel intensities of the synchrotron source in various optical configurations.

It can be seen that while the synchrotron source does have a large advantage over internal sources it is not as dramatic as the brightness advantage shown in Figure 8. The increased noise is largely due to the complexity of the accelerator with noise contributions from the various magnets, power supplies and vacuum equipment. This noise can be extremely severe at particular frequencies or ranges of frequencies. If these sources of noise cannot be eliminated their impact on the resultant spectrum can be minimised by changing the velocity of the spectrometer's scanning mirror thus moving the spectral location of the noise spikes.

It has been found that much of the noise is located on the outer edges of the beam profile. It is hypothesised that this may be due to slight movements in the electron beam creating instabilities in the light reaching the beam splitter box (see Figure 10) of the beamline. The mirror that directs part of the beam toward the microscopy beamline effectively casts a shadow on the mirror sending the beam to the high resolution beamline. Slight horizontal movements in the beam may cause more or less photons to reach the second mirror which may manifest as noise in the spectrum. Although this has not been fully confirmed as a noise source it has been seen that reducing the aperture inside the spectrometer improves the signal to noise ratio.

1.4.3 NATURAL LINE SHAPE

At maximum resolution the instrumental line width of the IFS125HR is $\approx 0.00096\text{cm}^{-1}$, depending on the apodisation function. Along with this the measured line width of an absorption is composed of a natural line width that is intrinsic to the molecule. The most fundamental contribution to natural line shape is due to the Heisenberg uncertainty principle. Where ΔE is the width of the energy distribution, i.e. the line width of the transition, while Δt is its lifetime.

$$\Delta E \Delta t \geq \frac{\hbar}{2} \quad 40$$

Typical values of this line broadening process are 10^{-7}cm^{-1} for vibrational transitions and 10^{-15}cm^{-1} for rotational transitions which are well below the measurement capabilities of FTIR spectroscopy however it does become important in other techniques such as Lamp dip spectroscopy.[19] Much more significant to FTIR spectroscopy is the Doppler broadened line width.

1.4.4 DOPPLER WIDTH

Doppler broadening of rotational lines occurs as a result of the random velocities of the gas molecules toward and away from the detector. Molecules moving away from the detector will absorb light at slightly lower frequencies and molecules moving toward the detector will absorb light at slightly higher frequencies. The degree of Doppler broadening is dependent on wavenumber.[20]

$$FWHH = \frac{\tilde{\nu}}{c} \sqrt{\frac{8NkT \ln 2}{M}} \quad 41$$

$\tilde{\nu}$ is in cm^{-1} , T in Kelvin and M is molecular mass in atomic mass units, N is Avogadro's constant and k is the Boltzmann constant.

Figure 15 shows the room temperature Doppler width of four molecules with different masses as a function of wavenumber. The arrows show the wavenumber at which the Doppler width of

each molecule becomes greater than the instrumental line width of the nine chamber Bruker IFS125HR.

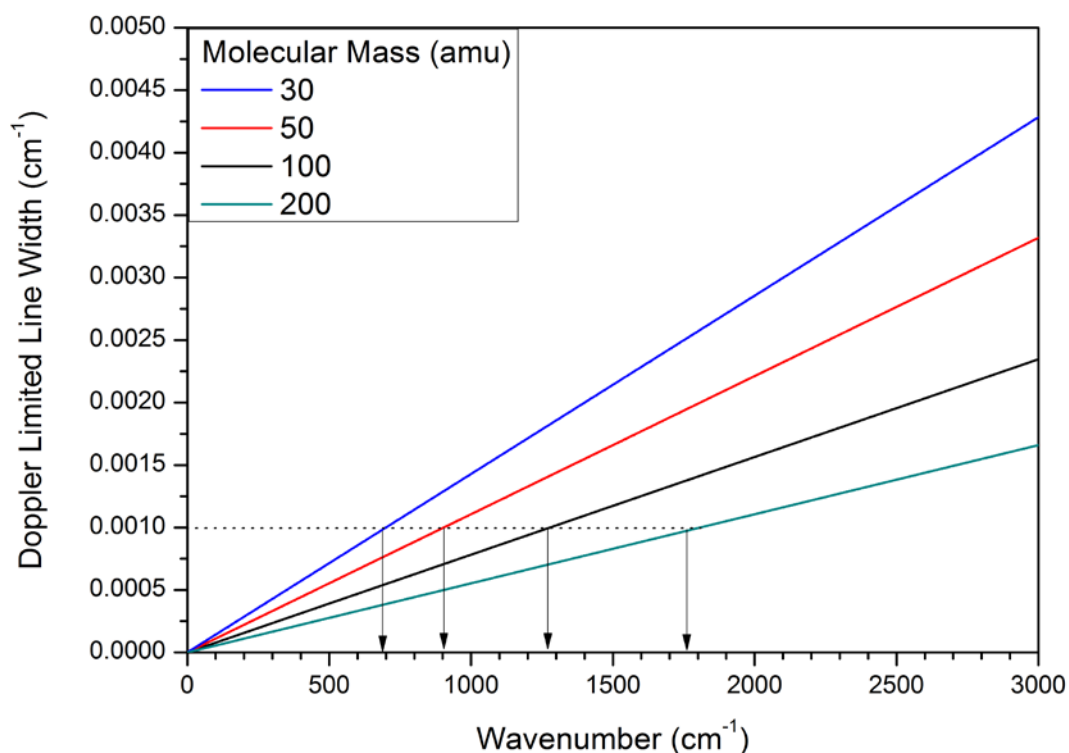


Figure 15: Doppler width at 298 K for four molecular masses as a function of wavenumber. The arrows show the wavenumber above which the resolution is limited by the Doppler width, not the instrumental line width.

1.4.5 PRESSURE BROADENING

Pressure broadening occurs when a collision between molecules results in a transition occurring at shifted frequency. If τ is the average time between transitions the line broadening due to collisions is given by:

$$\Delta\nu = \frac{1}{2\pi\tau} \quad 42$$

Given that the frequency of collisions is dependent on molecular velocity (temperature and molecular mass) as well as the size of the molecule (cross sectional area) the average time between collisions varies between molecules. An entire field of study is devoted to the determination of collision broadening coefficients for each rovibrational line; the HITRAN molecular spectroscopy database contains line width parameters for a number of small

molecules [21]. As a general rule of thumb pressure broadening is negligible if pressures are maintained below 1 Torr (133 Pa) [20].

1.4.6 LONG PATH GAS CELLS

Given that the pressure of a gas sample must be low in order to maintain resolution the measurement path length must be long enough to maintain sufficient sensitivity. In laboratory settings long path lengths are obtained using a gas cell with multiple optical traversals. The most common optical schematic is the White type cell that was first designed in 1942 [22]. These cells have three spherical mirrors as shown in Figure 16. An expanding beam is directed onto the first focussing mirror (or 'D-mirror') which focuses a beam onto the field mirror ('T-mirror').

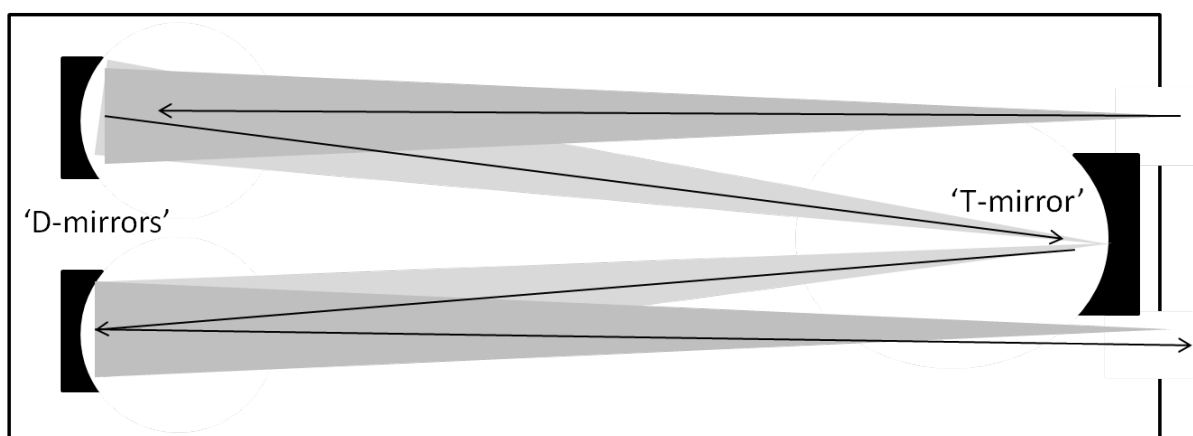


Figure 16: Optical path of a White cell set to four passes

The beam is reflected onto the second focussing mirror which, depending on the angle it is set to, will direct the beam out of the cell or back onto the field mirror for another series of traversals. For n number of passes the field mirror will have $\frac{n}{2} - 1$ images arranged in a pattern as shown in Figure 17. The maximum number of passes is determined by the location of the first image (labelled '2' in Figure 17) because the next image (4) will be symmetrically opposite it; if image '2' is walked to the right of Figure 17 image '4' will exit the cell through the entrance window. A modification of this type of cell is possible by positioning retro-reflecting mirrors at the entry and exit ports, this creates four or more rows of images on the field mirror.

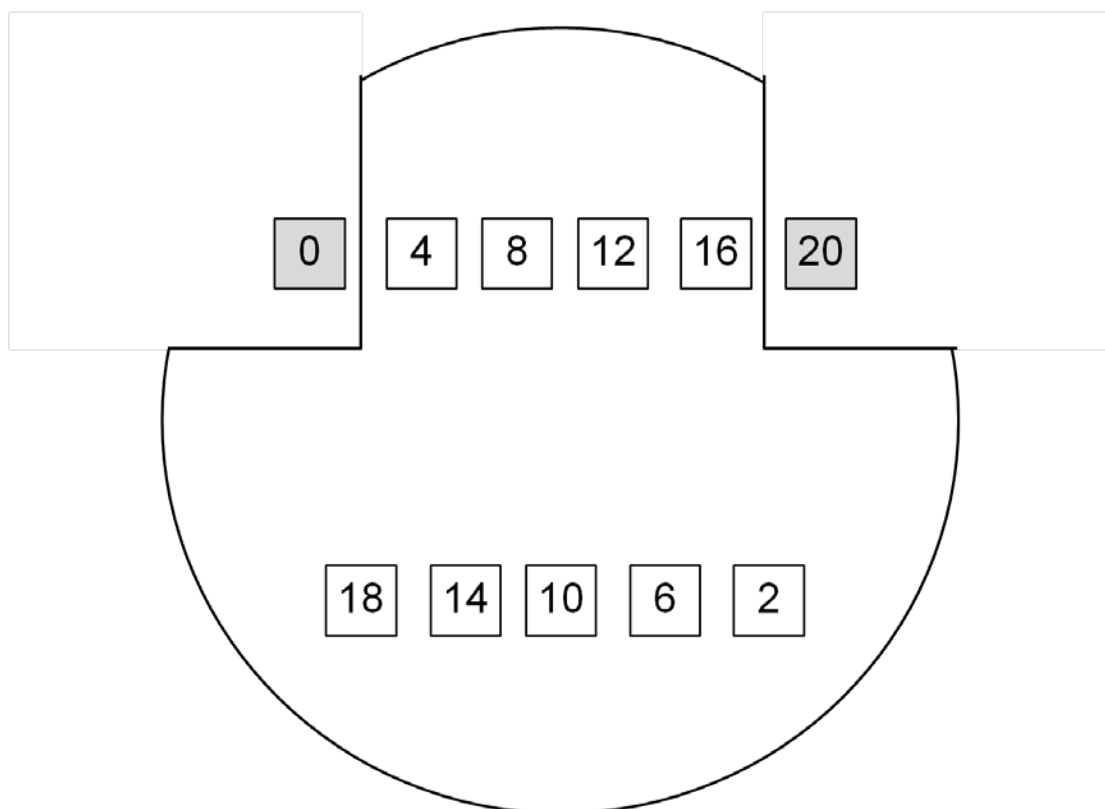


Figure 17: Images on a field mirror of a White cell numbered by the number of passes through the cell

1.4.7 COOLED SPECTRA

The spectral effects of cooling gas samples can be separated and described in terms of translational, rotational and vibrational temperatures. The rate at which the equilibrium temperature is reached is not the same for each of these and in some systems, such as supersonic expansions, the measured temperatures will be different. Generally, translational temperatures equilibrate faster than rotational temperatures while vibrational temperatures reduce slower than either:

$$T_{trans} < T_{rot} < T_{vib}$$

43

The experimental results reported in this thesis are all in a near equilibrium state and translational, rotational and vibrational temperatures are assumed to be equal. The benefits of cooling these degrees of freedom for rovibrational spectroscopy are outlined in the following sections.

1.4.8 TRANSLATIONAL TEMPERATURE

Figure 15 shows that the Doppler width of a molecule can often limit the maximum achievable resolution. Translational temperature can be reduced by cooling the sample gas or by only sampling molecules with low relative velocities (e.g. supersonic jet expansions or Lamb dip spectroscopy). Figure 18 shows simulated rovibrational lines of the ν_{11} band of C_2F_4 ($M=100$) near 1153 cm^{-1} at three different peak widths corresponding to the Doppler widths at 65 K, 150 K and 300 K. It is quite clear that as the Doppler width is reduced more peaks are resolved and are therefore amenable to analysis.

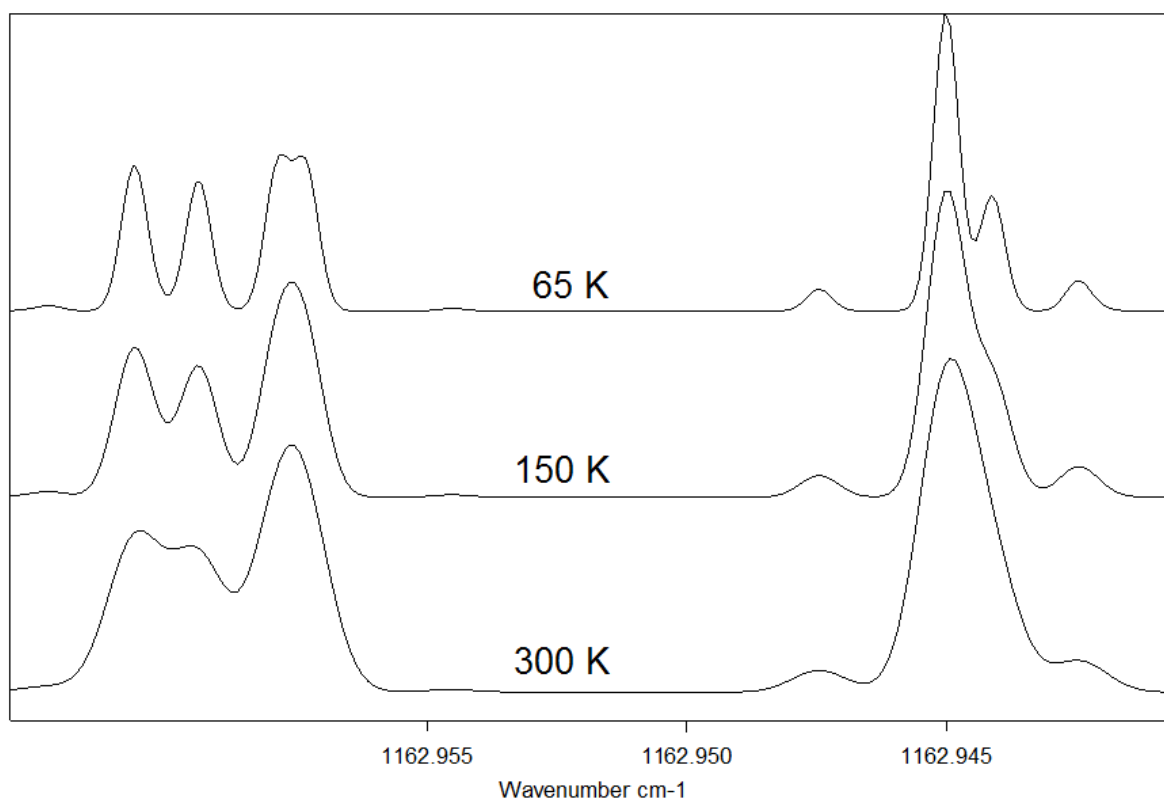


Figure 18 Simulated Doppler line width of C_2F_4 at three different temperatures.

1.4.9 VIBRATIONAL TEMPERATURE

The vibrational energy levels of a molecule will be populated according to the Boltzmann distribution:

$$\frac{N_i}{N_0} = d_i e^{-E_i/kT} \quad 44$$

Low lying vibrational modes will be significantly populated at room temperature. Molecules in these excited states can then absorb a photon to produce a hot band (Figure 1). These modes overlap with fundamental modes and interfere with the assignment of the fundamental rovibrational transitions (Figure 20). This also means the population of molecules in the ground vibrational state are reduced at high temperatures. The proportion of molecules in the ground vibrational state of tetrafluoroethylene is shown as a function of temperature in Figure 19.

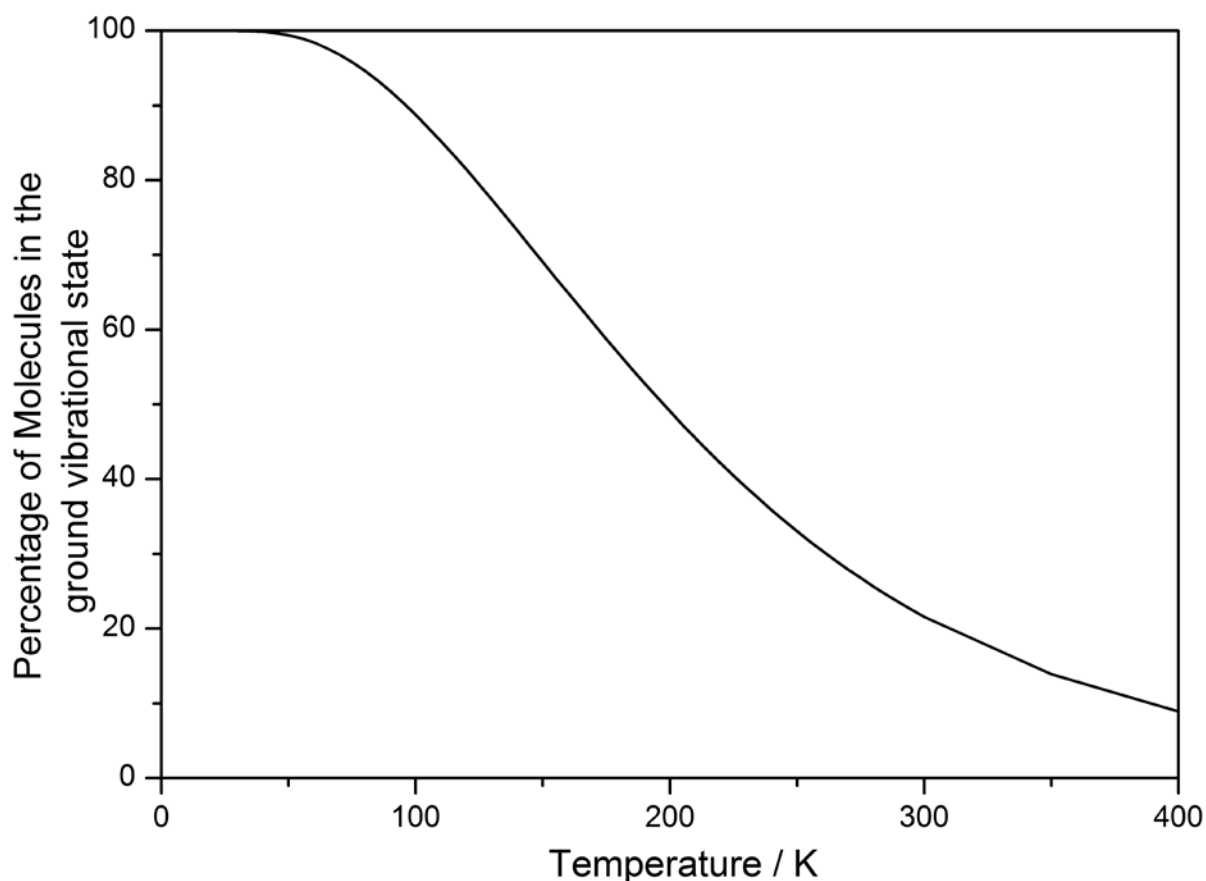


Figure 19: Population of the ground vibrational state of C₂F₄ as a function of temperature

1.4.10 ROTATIONAL TEMPERATURE

The rotational energy levels of a molecule will also be populated according to a Boltzmann distribution:

$$\frac{N_i}{N_o} = d_i e^{-E_r/kT} \quad 45$$

Where E_r is the energy of level i and d_i is the degeneracy.

Reducing the rotational temperature has the effect of compressing the rotational envelope toward the band centre by reducing the intensity of many lines with high rotational quantum numbers (Figure 20).

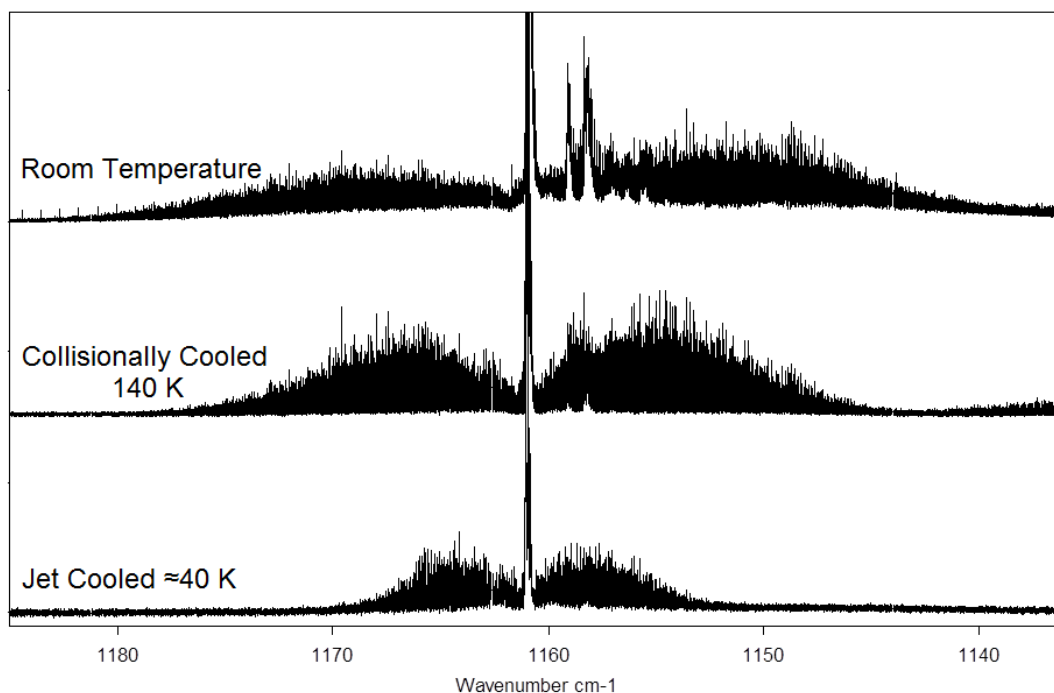


Figure 20: High resolution FTIR spectra of R-12 (dichlorodifluoromethane) at various temperatures. The Jet cooled spectrum was provided by Evan Robertson

Figure 20 depicts the ν_8 region of dichlorodifluoromethane at three different temperatures showing how reducing the rotational and vibrational temperature simplifies the spectrum. While cooling aids in the assignment of lower rotational levels in fundamental bands it also reduces the sensitivity to transitions with high values of J . Ideally any experiment would be conducted over a range of temperatures so that an initial analysis is simplified by using the low temperature spectrum and rovibrational transitions with high values of J subsequently can be

included in the analysis using the high temperature spectrum. An analysis of low temperature spectra can also allow for the simulation and subtraction of the fundamental band from a warm spectrum in order to aid in the assignment of hot bands.

1.4.11 EQUILIBRIUM COOLING

A common way to cool a gas sample for high resolution FTIR spectroscopy is simply to cool the entire gas cell. This can provide a very stable, equilibrium temperature this is valuable since spectra often need to be recorded over many hours in order to obtain a spectrum with sufficient signal-to-noise. The limitation with this method is that the sample must retain a vapour pressure high enough for measurements to be adequately sensitive.

1.4.12 SUPERSONIC JETS

Adiabatic cooling in jet expansions is another commonly used technique wherein a high pressure mixture of sample and carrier gas is expanded through a small nozzle to intersect with the beam of an FTIR instrument.[23-24] Rotational temperatures of less than 10 K are achievable with this method however a single optical pass of the millimetre sized expansion from a pinhole nozzle often provides insufficient sensitivity. Due to the small size of pin-hole nozzle expansions optics that allow for multiple passes through the jet can be complex as each pass must be coincident with the expansion at the same location. [25-26]

Another technique to increase the optical interaction is to make the size of the expansion larger by using multiple nozzles [27] or a slit nozzle [28-29] however both these introduce additional optical constraints. Ideally a multi-nozzle or slit jet expansion would be optically sampled with a small parallel beam; however shaping the large parallel beam output from a commercial spectrometer into an appropriate size is difficult. Typically the parallel beam is focussed onto the expansion using mirrors with long focal lengths so the optical divergence within the expansion is minimised.[27, 30] The high collimation of a synchrotron source may prove to be advantageous over conventional sources in this regard as a small parallel beam can be readily produced.[31]

The larger area of these nozzles can also increase the already large sample and pumping requirements of jet expansions, these can be somewhat reduced by using a pulsed nozzle which allows the pump a recovery time between pulses.[32] Such systems can also be useful in the study of molecular clusters.[33-34]

1.4.13 COLLISIONAL COOLING

Collisional cooling or diffuse trapping [35] is another method to overcome the vapour pressure limit of the sample gas by using a non-condensing buffer gas to cool the sample via inelastic collisions. This can be accomplished in a typical coolable long path gas cell by introducing small amounts of sample gas into the cell which contains precooled buffer gas. A typical arrangement will have the sample introduced perpendicular to the optical axis of the gas cell in order to avoid condensation on the mirrors. The cold buffer gas cools the sample gas as it enters and small amounts of sample gas are periodically added to replace that which condenses on the cell walls. This method relies on the rate of cooling being faster than the rate of diffusion out of the optical path.

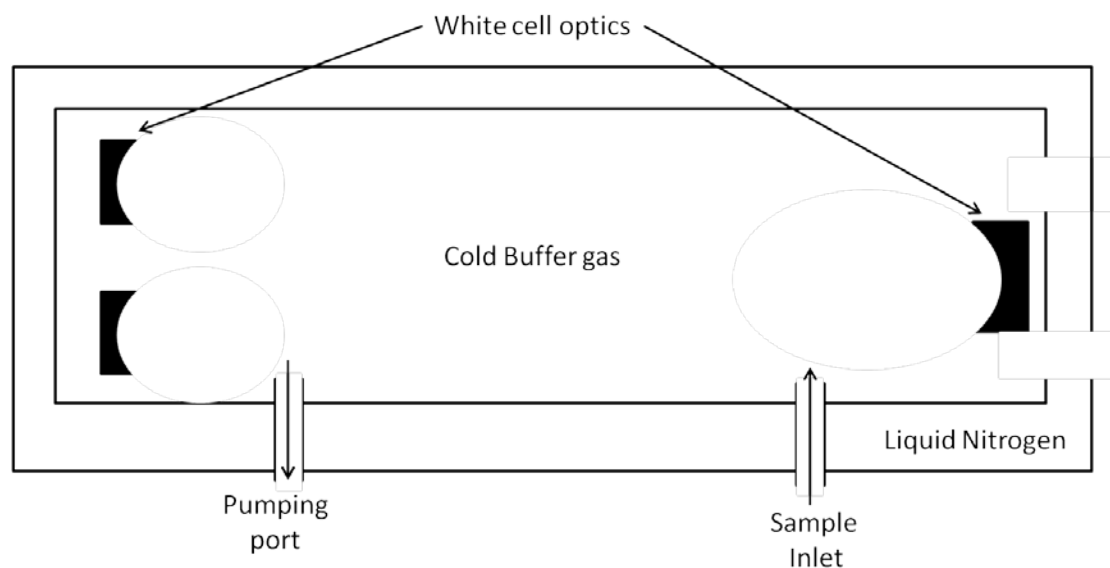


Figure 21: Schematic of a typical collisional cooling cell

1.5 ENCLOSIVE FLOW COOLING CELL

The EFC cell (Figure 22) is a White-type long path gas cell that consists of a cylindrical stainless steel vacuum chamber inside a large glass Dewar. This Dewar can be filled with liquid nitrogen to cool the cell to 77 K; to achieve intermediate temperatures (100 K – 270 K) cold nitrogen gas can be set to flow through the Dewar. Liquid helium can also be used to cool the cell down further.

Inside the vacuum chamber is a cylindrical colander that houses the White-type optics. This colander has small holes in it to allow a flow of buffer gas (N_2 or He) to envelope and cool a sample gas that is injected into the centre of the colander. On the outside of the colander are three zones of heating coils that allow the temperature of the cooling gas to be finely controlled, near each heater is a thermocouple which is used to monitor and inform the control of the heating. The colander also houses the mirrors, each of which has a heater and thermocouple.

This cell was constructed by Sigurd Bauerecker and co-workers [36], a number of research groups have identical cells. Our cell was previously installed on a Bruker IFS120 spectrometer at Monash University and was moved to the Australian Synchrotron in late 2008.

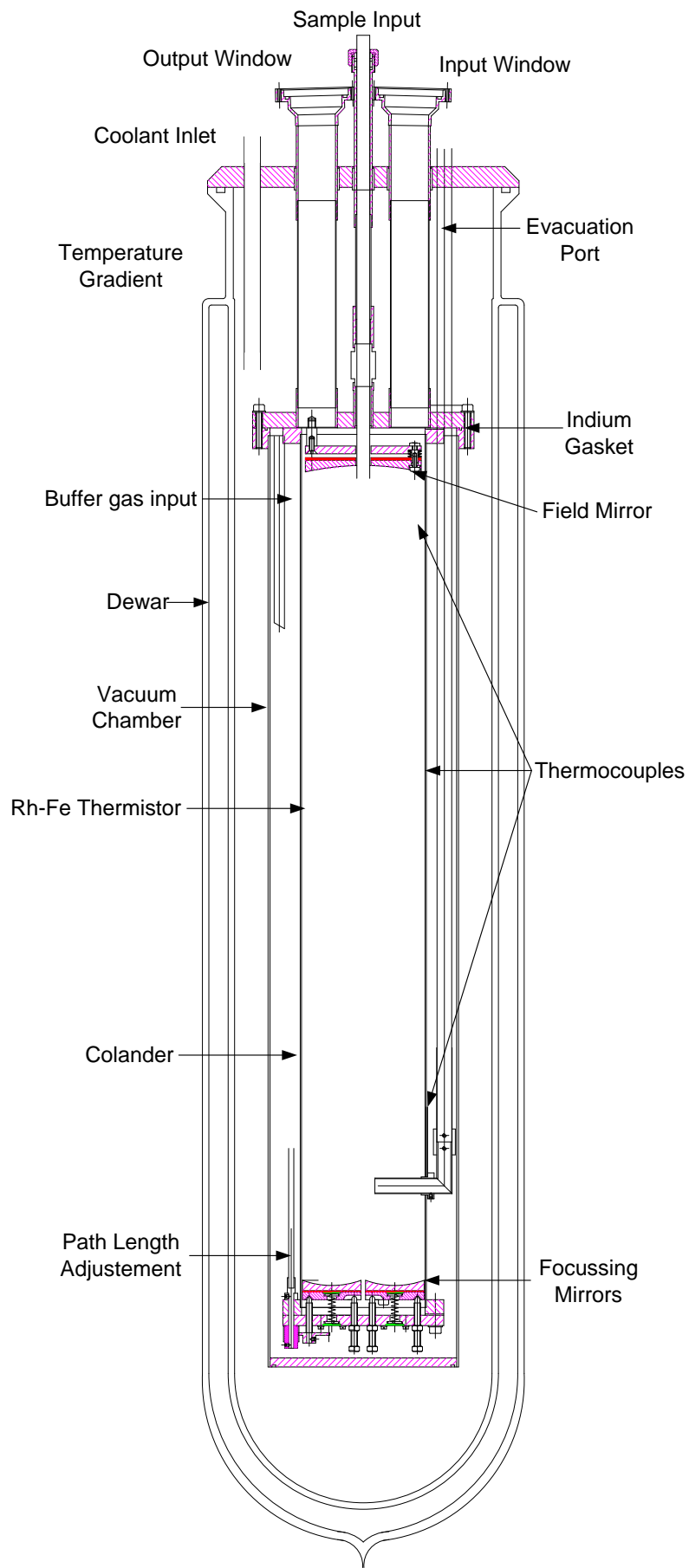


Figure 22: Schematic of the Enclosive Flow Cooling Cell

1.5.2 COOLING MODES

The EFC cell can be operated in a number of different experimental modes depending on the specific needs of the experiment. For high resolution measurements the most useful mode involves flowing cold nitrogen gas through the Dewar (Figure 23). The flow of cold gas is generated and controlled by a heater submerged in liquid nitrogen, this gas flows through vacuum insulated tubing into a heater that is used to set the final temperature of the gas. The cold gas then flows around the outside of the vacuum chamber cooling the cell and sample gas. In order to achieve the desired temperature faster the Dewar is precooled using a small amount of liquid nitrogen and the EFC cell is filled with a small pressure of helium gas to facilitate heat transfer.

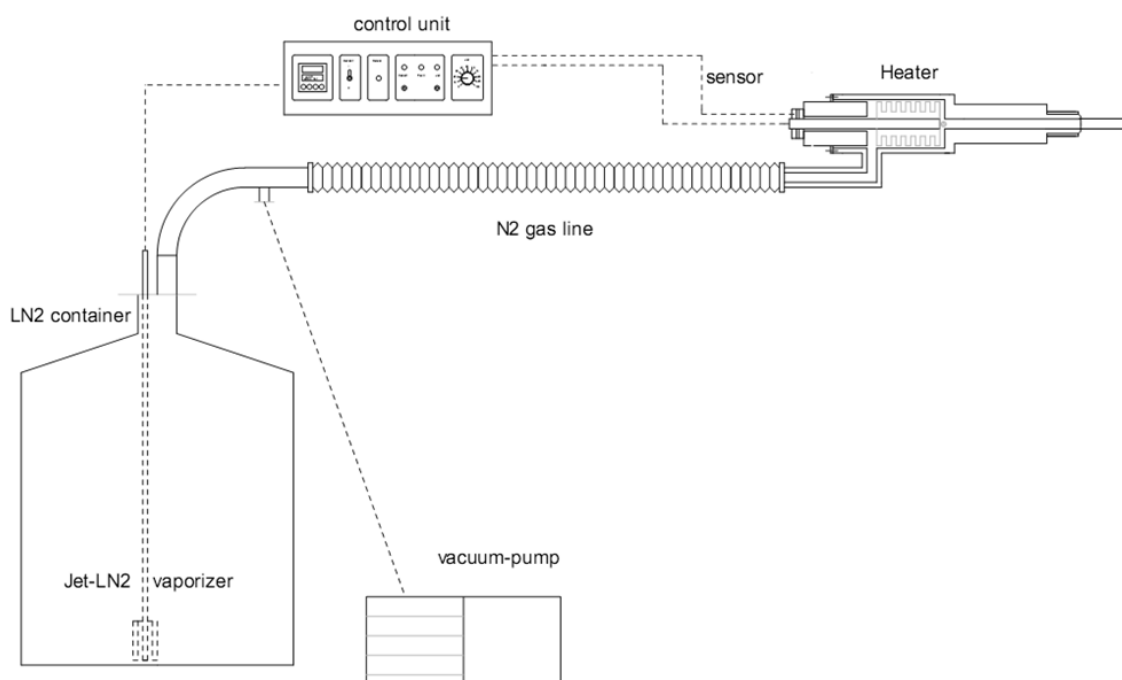


Figure 23: Schematic of the cold gas cooling unit, modified from the operating manual [37]

This method can be used to achieve temperatures down to 100 K with a stability of ± 0.5 K over a number of hours (Figure 24). Spectra recorded with this method have a near equilibrium temperature thus making simulation and subtraction of major components to reveal the minor components (e.g. isotopologues) relatively easy. However, the lowest practical temperature in

this mode of operation is limited by the sample's vapour pressure. For some species, particularly large molecules, the achievable temperature may not be cold enough to simplify the spectrum sufficiently.

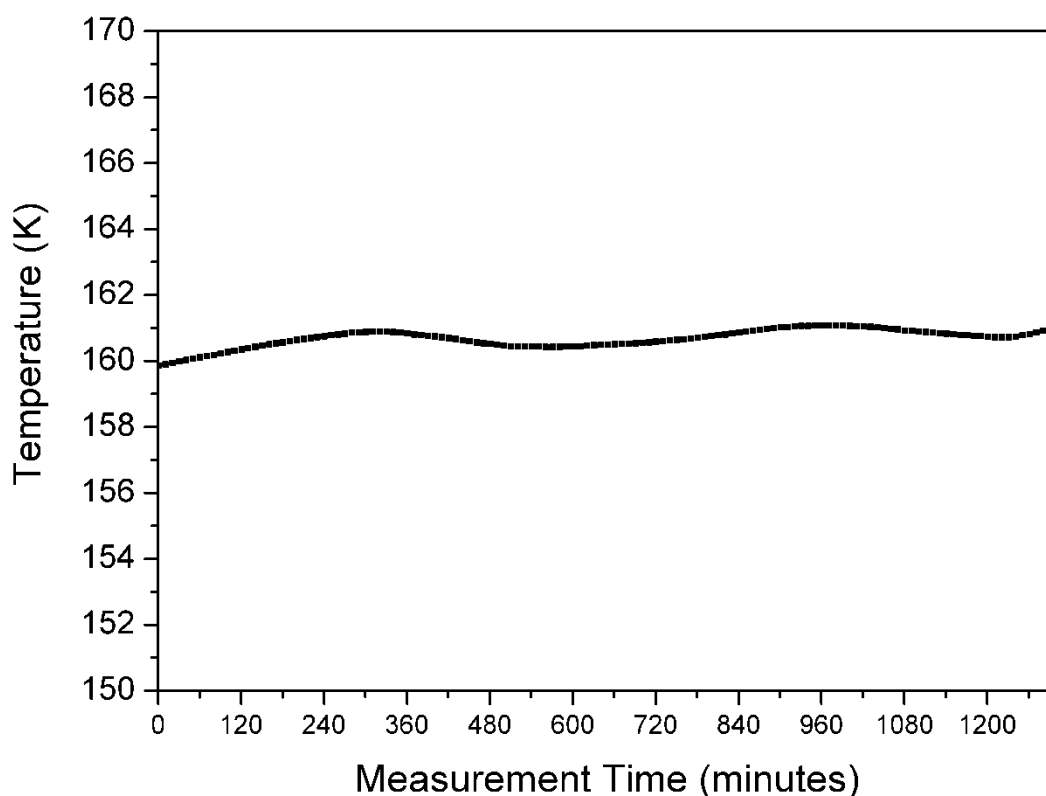


Figure 24: Temperature stability when using the cold gas flow as measured by a rhodium-iron thermistor on the colander (Figure 22)

If extra cooling of a sample is required the cell can be operated in the enclosive flow cooling mode. The concept of enclosive flow cooling can be thought of as an extension of collisional cooling. Rather than adding sample gas to replace that which is lost to condensation, sample and buffer gas is continuously pumped through the optical path. The sample gas enters through the centre of the top mirror while the buffer gas will enter on the outside of the colander and flow through the holes. The Dewar is filled with a liquid cryogen which quickly cools the buffer gas which in turn cools the sample gas as it enters the central portion of the cell. This mode has the advantage of being able to cool the sample below its freezing point further reducing hot bands and Doppler widths. However this method requires large amounts of sample and may not be suitable for expensive or toxic samples although it may improve the lifetimes of unstable or reactive compounds.

Figure 25 shows a room temperature spectrum of N_2O flowing through the cell at a constant rate (blue) and then flowing through the cell with an ‘enclosive flow’ of nitrogen buffer gas (red). The increase in absorbance when the flow of buffer gas was present is the result of the sample gas being enveloped in the nitrogen gas and being contained inside the smaller volume at the centre of the colander in the infrared path rather than distributed over the entire vacuum chamber.

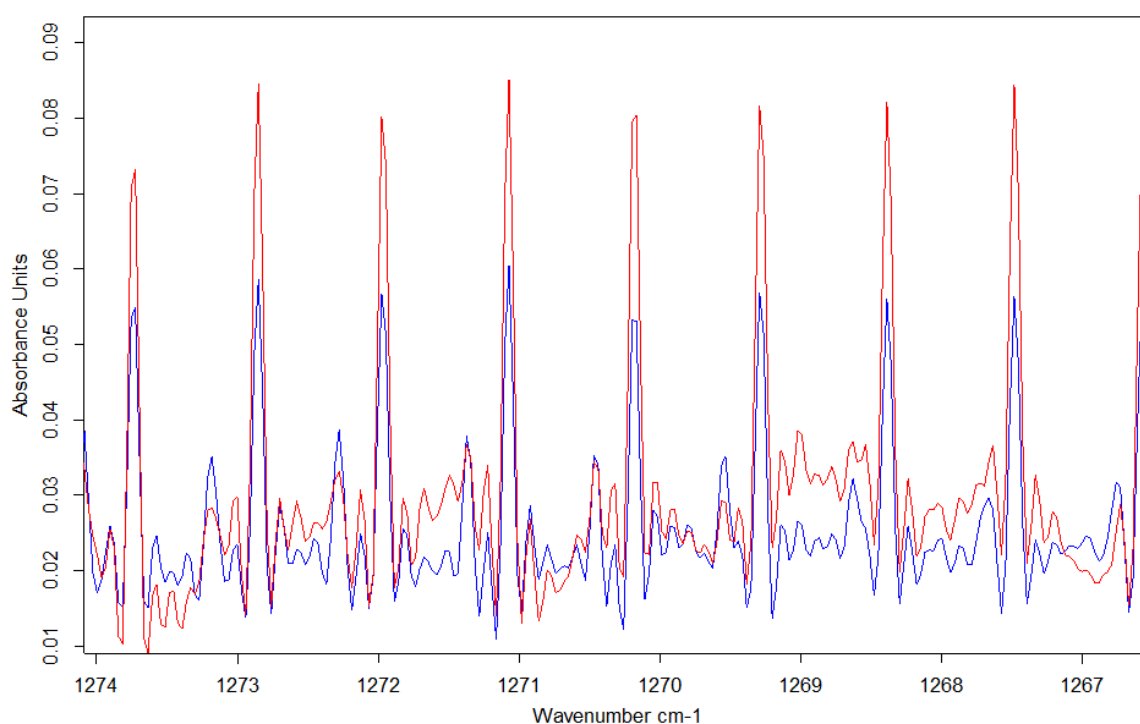


Figure 25: Room temperature mid-IR Spectrum of nitrous oxide with enclosive flow of nitrogen (red) and without (blue)

In addition to cooling gas samples the EFC cell can be used to generate aerosol particles and observe their behaviour over a wide range of formation conditions. A typical experiment involves filling the cell with a pressure of inert buffer gas, 1-1000 mbar of N_2 or He and cooling it to a desired temperature. A short pulse (10-1000 ms) of sample gas at moderate pressures ($\approx 2-3$ bar) is then introduced into the cell. When the sample gas encounters the cold buffer gas it is rapidly cooled via inelastic collisions becoming supersaturated and thence nucleation and particle growth occurs. Chapter 3 of this thesis deals exclusively with this aspect.

1.6 OPTICAL MODIFICATIONS

1.6.1 FAR-INFRARED REGION

The original optical scheme for the EFC cell is shown in Figure 26, the beam exiting the spectrometer from the back parallel exit (see Figure 13) is directed up and then across to a toroidal mirror. This focuses the beam at the level of the field mirror of the White cell optics, the beam then traverses the cell multiple times then exiting and being focused onto a detector by an elliptical mirror. The vacuum chamber for this detector was designed to hold the standard liquid nitrogen Dewar of mid-IR detectors (mercury-cadmium telluride or indium-antimonide). The cell was therefore effectively limited in its wavenumber range by the detector cut off; $\approx 450 \text{ cm}^{-1}$ for a wide band MCT detector. In order to allow for the cell to operate in the far-infrared a new optical scheme was needed. The finalised optical design is presented in chapter 2.1, below is an expanded discussion on logic behind the design and problems that were encountered.

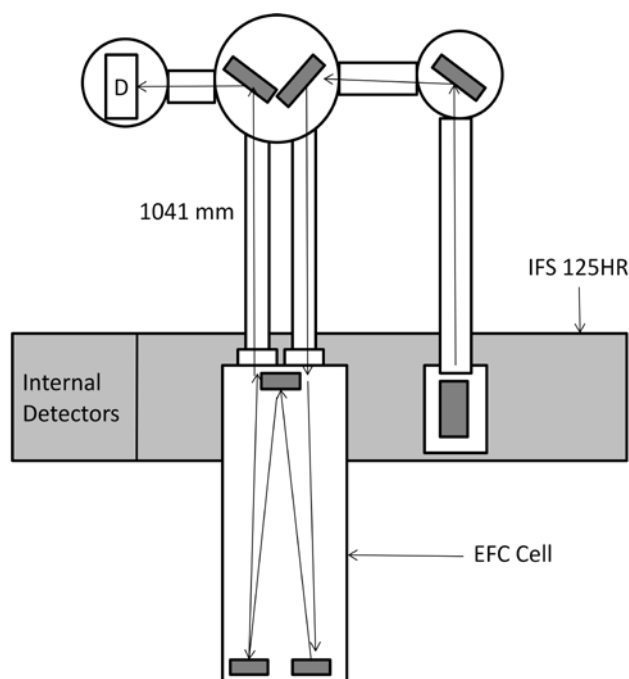


Figure 26: Schematic of original optics (left) and a photograph of the system (right)

The simplest scheme of modifying the external detector compartment to accommodate a far-IR bolometer was considered, however this would require a new bolometer or removing an existing one from the spectrometer, limiting experiments to the EFC cell. This detector compartment is approximately 2.5 m off the ground so even if a system to fill it with liquid helium could have been designed it likely it would have involved some significant hazards.

It was decided that the best option was to send the beam that exits the EFC cell back into the spectrometer via the back sample compartment. This was done by first directing the beam backwards with a flat mirror, rather than upwards, (Figure 27 D) towards an off-axis parabolic mirror (F) that collimates the beam. The third mirror in the set up (G) then directs the parallel beam into the sample compartment of the spectrometer.

The first mirror inside the spectrometer (J in Figure 28) is another off axis parabolic mirror that is used to bring the parallel beam to a focus. The last two mirrors (K and M) are located on translation stages and are used to direct the beam focus to the spectrometers focal point. At this point the light passes through the spectrometers existing mirrors and onto a choice of detectors.

One design constraint was that the original optics be left in a usable condition so experiments could continue using the mid-IR detectors as work on the new optics progressed. This left only a very small amount of space for the first mirror and its vacuum chamber. An early design placed a flexible bellows between the window and the M1 mirror chamber. This was to allow a small amount of adjustment in the vertical position of M1 and ensure proper alignment with M2. This would also have absorbed the small angles of the window flange. Due to the small gap between the window surface and the original transfer optics vacuum chamber the bellows had to be removed from the design and replaced with a small section of solid tubing. This has proved troublesome during alignment and window replacements. Note that the mirror that sends the beam into the EFC cell is housed in the same chamber as the original output (detector) mirror and the necks that run down to the EFC cell are welded in place and are not easily removable.

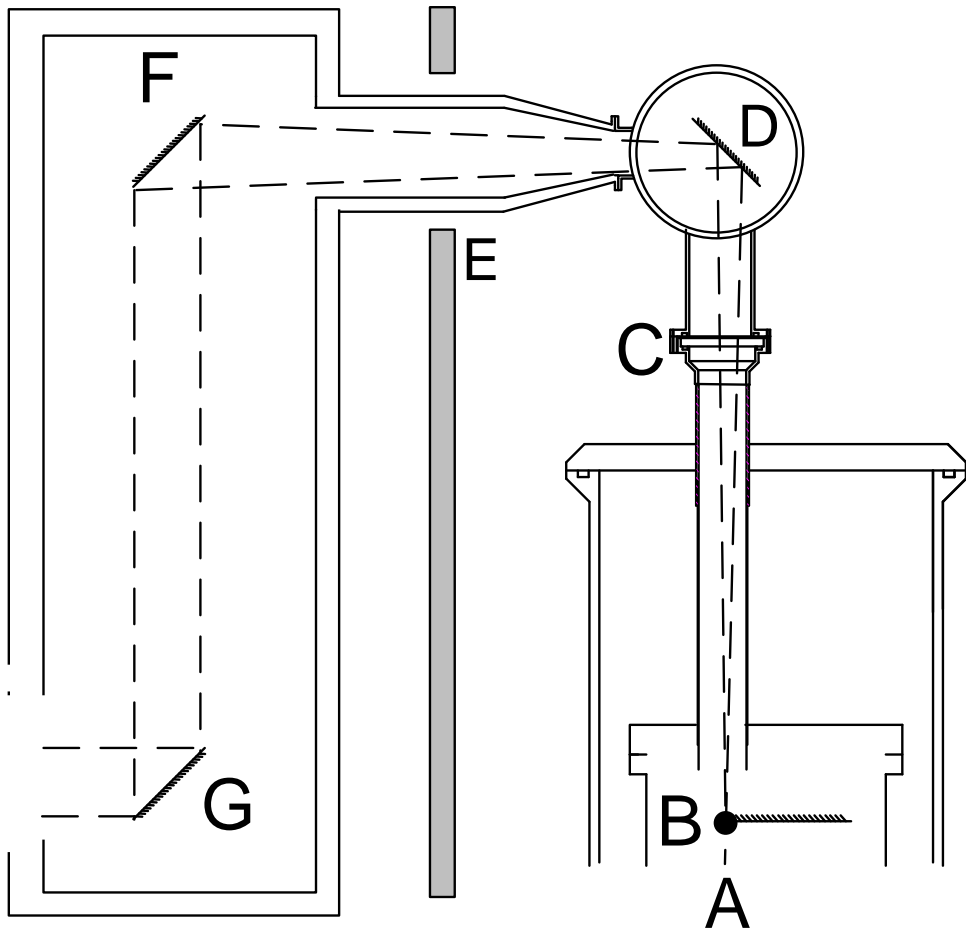


Figure 27: Schematic (top) and photographs (bottom) of the new optics

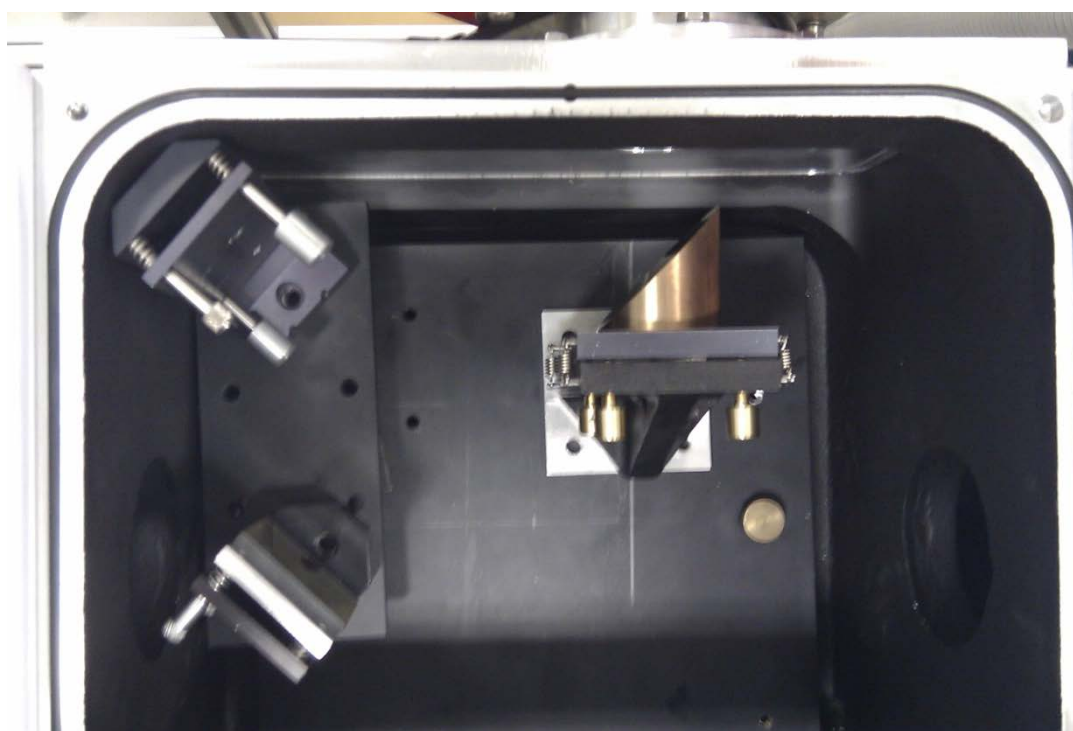
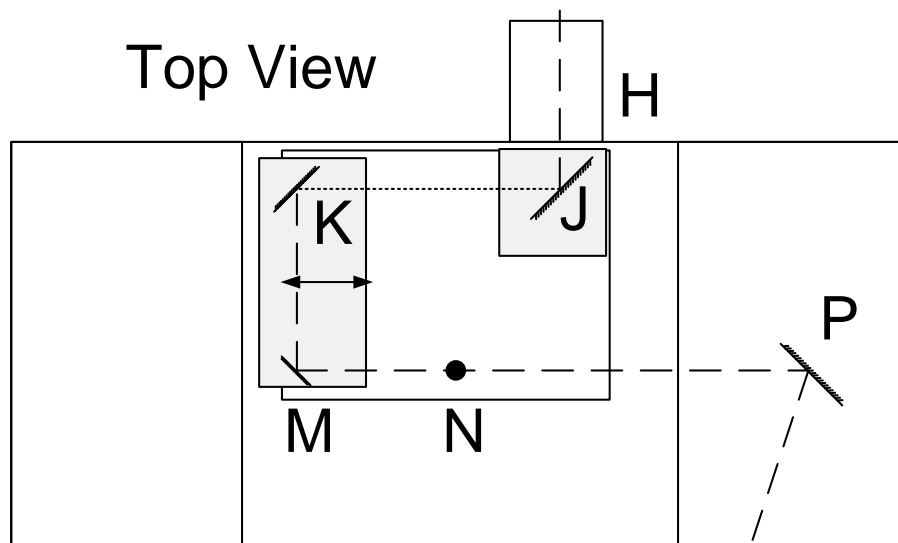


Figure 28: Schematic of optics inside the sample compartment (top) and a photograph of them (bottom)

1.6.2 CELL WINDOWS

In addition, far-infrared windows that separate the cooling cell from the rest of the optical path were required to access the far-infrared region. The primary requirement of new windows was good far-infrared transmission; secondary to this was visible transmission in order to aid alignment. Experiments on the formation of aerosols require an internal cell pressure up to one atmosphere so the windows would need to be able to withstand pressure of at least one atmosphere differential.

The existing windows were 5 mm thick, 50 mm diameter wedged potassium bromide and calcium fluoride windows. The new windows were chosen to match these dimensions so that new flanges were not needed. A number of other salts offer slightly increased range such as KRS-5 (thallium bromiodide) and CsI however KRS-5 is extremely toxic and CsI is very soft and hygroscopic. Most importantly these windows did not allow access to the very far infrared (<100 cm⁻¹) where the synchrotron source is most advantageous.

In terms of far-infrared and visible throughput the ideal window material would have been diamond, however these would have cost more than €3000 each and would require a redesign of the window flanges in order to protect them from mechanical stress. The remaining options were between three different polymers: high density polyethylene (HDPE), polypropylene (PP) and polymethylpentene (PMP or TPX®). Polypropylene is typically used as a thin film (<1 mm) stretched across the window flange and this would not suit aerosol experiments. Ultimately two sets of windows were purchased, one TPX set for alignment and very far infrared throughput (<100 cm⁻¹) and one HDPE set which has better transmission in the region 100-400 cm⁻¹.

Table 5: Common infrared window materials

Material	Throughput	Visible	Physical Characteristics	
	(cm ⁻¹)	transmission		
KBr	400+	Moderate	Hygroscopic	Soft
CaF₂	1000+	Very Good	Brittle	Hard
KRS-5	250+	Poor	Very toxic	Soft
CsI	175+	Good	Hygroscopic	Very soft
Diamond	0-40,000	Very Good	Expensive	Very hard
HDPE	0-600	None	Cheap	
PP	0-800	Good	Cheap	Flexible
TPX	0-250	Good	Cheap	

1.7 REFERENCES

1. Nakagawa, T. and Y. Morino, *Coriolis interactions in the $[nu]$ 4 and $[nu]$ 6 bands of formaldehyde*. Journal of Molecular Spectroscopy, 1971. **38**(1): p. 84-106.
2. McNaughton, D., D. McGilvery, and F. Shanks, *High resolution FTIR analysis of the ν_1 band of tricarbon monoxide: Production of tricarbon monoxide and chloroacetylenes by pyrolysis of fumaroyl dichloride*. Journal of Molecular Spectroscopy, 1991. **149**(2): p. 458-473.
3. Lodyga, W., M. Kreglewski, P. Pracna, and S. Urban, *Advanced graphical software for assignments of transitions in rovibrational spectra*. Journal of Molecular Spectroscopy, 2007. **243**(2): p. 182-188.
4. Western, C.M., *PGOPHER, a Program for Simulating Rotational Structure*, University of Bristol, <http://pgopher.chm.bris.ac.uk>.
5. Pickett, H.M., *The fitting and prediction of vibration-rotation spectra with spin interactions*. Journal of Molecular Spectroscopy, 1991. **148**(2): p. 371-377.
6. Nakata, M. and K. Kuchitsu, *Estimation of the equilibrium structures of polyatomic molecules using isotopic differences in vibrationally averaged structures*. Journal of Molecular Structure, 1994. **320**(0): p. 179-192.
7. Watson, J.K.G., *The estimation of equilibrium molecular structures from zero-point rotational constants*. Journal of Molecular Spectroscopy, 1973. **48**(3): p. 479-502.
8. Watson, J.K.G., A. Roytburg, and W. Ulrich, *Least-Squares Mass-Dependence Molecular Structures*. Journal of Molecular Spectroscopy, 1999. **196**(1): p. 102-119.
9. Schrödinger, E., *Quantisierung als eigenwertproblem*. Annalen der physik, 1926. **385**(13): p. 437-490.
10. Krishnan, R., J. Binkley, R. Seeger, and J.A. Pople, *Self-consistent molecular orbital methods. XX. A basis set for correlated wave functions*. The Journal of Chemical Physics, 1980. **72**: p. 650.
11. Dunning Jr, T.H., *Gaussian basis sets for use in correlated molecular calculations. I. The atoms boron through neon and hydrogen*. The Journal of Chemical Physics, 1989. **90**: p. 1007.
12. Schäfer, A., H. Horn, and R. Ahlrichs, *Fully optimized contracted Gaussian basis sets for atoms Li to Kr*. The Journal of Chemical Physics, 1992. **97**: p. 2571.
13. Griffiths, P.R. and J.A. De Haseth, *Fourier Transform Infrared Spectrometry*. 1986, New York: Wiley Interscience.
14. Duncan, W.D. and G.P. Williams, *Infrared synchrotron radiation from electron storage rings*. Appl. Opt., 1983. **22**(18): p. 2914-2923.
15. Brubach, J.-B., L. Manceron, M. Rouzies, O. Pirali, D. Balcon, F.K. Tchana, V. Boudon, M. Tudorie, T. Huet, A. Cuisset, and P. Roy, *Performance of the AILES THz-Infrared beamline at SOLEIL for High resolution spectroscopy*. AIP Conference Proceedings, 2010. **1214**(1): p. 81-84.
16. Williams, G., *Synchrotron and Free Electron Laser Sources of Infrared Radiation*. Handbook of Vibrational Spectroscopy, 2002.
17. Ebashi, S., M. Koch, and E. Rubenstein, *Handbook on synchrotron radiation*. 1991.
18. Creagh, D., M. Tobin, A. Broadbent, and J. McKinlay, *An Infrared Beamline at the Australian Synchrotron*. AIP Conference Proceedings, 2007. **879**(1): p. 615-618.
19. Hollas, J.M., *High Resolution Spectroscopy*. 2nd ed. 1998, Chichester: John Wiley & Sons.
20. McNaughton, D., *Instrumentation and Methods for High-Resolution Gas-Phase Spectroscopy*, in *Handbook of Vibrational Spectroscopy*, P. Griffiths, Editor. 2002, John Wiley & Sons: Hoboken.
21. Rothman, L.S., I. Gordon, A. Barbe, D.C. Benner, P. Bernath, M. Birk, V. Boudon, L. Brown, A. Campargue, and J.P. Champion, *The HITRAN 2008 molecular spectroscopic database*.

- Journal of Quantitative Spectroscopy and Radiative Transfer, 2009. **110**(9-10): p. 533-572.
22. White, J.U., *Long Optical Paths of Large Aperture*. J. Opt. Soc. Am., 1942. **32**(5): p. 285-285.
 23. Herman, M., R. Georges, M. Hepp, and D. Hurtmans, *High resolution Fourier transform spectroscopy of jet-cooled molecules*. International Reviews in Physical Chemistry, 2000. **19**(2): p. 277-325.
 24. Snels, M., V. Horká-Zelenková, H. Hollenstein, and M. Quack, *High-Resolution FTIR and Diode Laser Spectroscopy of Supersonic Jets*, in *Handbook of High-resolution Spectroscopy*. 2011, John Wiley & Sons, Ltd.
 25. McNaughton, D., D. McGilvery, and E.G. Robertson, *High-resolution FTIR-jet spectroscopy of CCl₂F₂*. J. Chem. Soc., Faraday Trans., 1994. **90**(8): p. 1055-1060.
 26. Petry, R., S. Klee, M. Lock, B.P. Winnewisser, and M. Winnewisser, *Spherical mirror multipass system for FTIR jet spectroscopy: application to the rovibrationally resolved spectrum of OC₅O*. Journal of Molecular Structure, 2002. **612**(2): p. 369-381.
 27. Georges, R., G. Durry, M. Bach, R. Pétrisse, R. Jost, and M. Herman, *Multinozzle supersonic expansion for Fourier transform absorption spectroscopy*. Chemical Physics Letters, 1995. **246**(6): p. 601-606.
 28. Amrein, A., M. Quack, and U. Schmitt, *High-resolution interferometric Fourier transform infrared absorption spectroscopy in supersonic free jet expansions: carbon monoxide, nitric oxide, methane, ethyne, propyne, and trifluoromethane*. The Journal of Physical Chemistry, 1988. **92**(19): p. 5455-5466.
 29. Barnes, J.A. and T.E. Gough, *Fourier transform infrared spectroscopy of supersonic jets: observation of clusters containing sulphur hexafluoride*. Chemical Physics Letters, 1986. **130**(4): p. 297-300.
 30. Arno, J. and J.W. Bevan, *Jet Spectroscopy and Molecular Dynamics*, ed. J.M. Hollas and D. Phillips. 1995, Edinburgh: Blackie.
 31. Chandrasekaran, V., L. Biennier, E. Arunan, D. Talbi, and R. Georges, *Direct Infrared Absorption Spectroscopy of Benzene Dimer*. The Journal of Physical Chemistry A, 2011. **115**(41): p. 11263-11268.
 32. Luckhaus, D., M. Quack, U. Schmitt, and M.A. Suhm, *On FTIR Spectroscopy in Asynchronously Pulsed Supersonic Free Jet Expansions and on the Interpretation of Stretching Spectra of HF Clusters*. Berichte der Bunsengesellschaft für physikalische Chemie, 1995. **99**(3): p. 457-468.
 33. Devlin, J.P., M. Farnik, M.A. Suhm, and V. Buch, *Comparative FTIR spectroscopy of HX adsorbed on solid water: Ragout-jet water clusters vs ice nanocrystal arrays*. Journal of Physical Chemistry A, 2005. **109**(6): p. 955-958.
 34. Häber, T., U. Schmitt, and M.A. Suhm, *FTIR-spectroscopy of molecular clusters in pulsed supersonic slit-jet expansions*. Phys. Chem. Chem. Phys., 1999. **1**(24): p. 5573-5582.
 35. Barnes, J., T. Gough, and M. Stoer, *Diffusive trapping: An alternative to supersonic jet cooling for spectroscopic experiments?* Review of Scientific Instruments, 1989. **60**(3): p. 406-409.
 36. Bauerecker, S., M. Taraschewski, C. Weitkamp, and H.K. Cammenga, *Liquid-helium temperature long-path infrared spectroscopy of molecular clusters and supercooled molecules*. Review of Scientific Instruments, 2001. **72**(10): p. 3946-3955.
 37. KGW-Isotherm. *Kaltgas System Operating Manual*. Available from: http://www.kgw-isotherm.com/downloads/kgas_manual_en.pdf.

CHAPTER 2.0

PUBLICATIONS ON HIGH RESOLUTION FTIR SPECTROSCOPY

Declaration for Thesis Chapter 2.1

Declaration by candidate

In the case of Chapter 2.1, the nature and extent of my contribution to the work was the following:

Nature of contribution	Extent of contribution (%)
Initiation, key ideas, experimental, development and writing up	80%

The following co-authors contributed to the work. Co-authors who are students at Monash University must also indicate the extent of their contribution in percentage terms:

Name	Nature of contribution	Extent of contribution (%) for student co-authors only
E.G. Robertson	Initiation and key ideas	
A. Wong	Experimental assistance	5%
Ruth Plathe	Experimental assistance	
D. McNaughton	Initiation and key ideas	
D.R.T. Appadoo	Initiation, key ideas and experimental assistance	

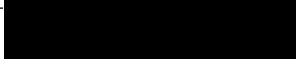
Candidate's Signature		Date
-----------------------	--	------

Declaration by co-authors

The undersigned hereby certify that:

- (1) the above declaration correctly reflects the nature and extent of the candidate's contribution to this work, and the nature of the contribution of each of the co-authors.
- (2) they meet the criteria for authorship in that they have participated in the conception, execution, or interpretation, of at least that part of the publication in their field of expertise;
- (3) they take public responsibility for their part of the publication, except for the responsible author who accepts overall responsibility for the publication;
- (4) there are no other authors of the publication according to these criteria;
- (5) potential conflicts of interest have been disclosed to (a) granting bodies, (b) the editor or publisher of journals or other publications, and (c) the head of the responsible academic unit; and
- (6) the original data are stored at the following location(s) and will be held for at least five years from the date indicated below:

Location(s) Monash University, School of Chemistry

Signature 1		3-12-2012
Signature 2		
Signature 3		
Signature 4		
Signature 5		

Infrared Spectroscopy of Gases and Condensates at the Australian Synchrotron

Chris Medcraft¹, Evan G. Robertson², Don McNaughton¹, Andy Wong¹, Ruth Plathe³ and Dominique R.T. Appadoo³

¹ School of Chemistry, Monash University, Wellington Rd., Clayton, Victoria 3800, Australia

² Department of Chemistry & La Trobe Institute of Molecular Sciences, La Trobe University, Bundoora, Victoria 3086, Australia

³ Australian Synchrotron, 800 Blackburn Rd, Clayton, Victoria 3168, Australia

Abstract

The Far-IR/THz beamline at the Australian Synchrotron is coupled to a Bruker IFS125/HR FT spectrometer offering an unapodized resolution of 0.00064 cm^{-1} . The intrinsic high brightness of the synchrotron light source provides a signal to noise advantage over conventional thermal sources from the THz region up to 1700 cm^{-1} for high spectral resolution studies. The beamline is equipped with multi-traversal gas-cells which have been used to successfully study a variety of gases of atmospheric and astrophysical importance. One of the cells is a vertically mounted cryogenic cell which can be operated as a collisional cooling cell to study cold gases and aerosols of molecular ices, or as an enclosive flow cooling cell enabling the study of gases below their freezing point. The cryogenic cell has been optically coupled to the FT spectrometer, and the far infrared lattice modes of carbon dioxide have been recorded between 7 K and 102 K for the first time.

Introduction

Third generation electron storage rings have intrinsically low emittance (small size and low angular divergence), as a result, can be considered as point sources, which allows for high-collimation. Although electron storage rings are most often used as a source for x-ray and UV experiments the high brightness (flux per unit solid angle) persists in the infrared region providing an advantage over conventional, thermal sources used in bench-top infrared spectrometers. This increased brightness and high collimation are most useful for infrared spectroscopy at high-spectral resolution (or high-spatial resolution for IR microscopy) as small apertures are required when using standard diffuse thermal light sources such as a globar or a mercury-arc lamp (large apertures can be used with the synchrotron light). In general, this advantage increases with the wavelength and there is also a significant raw flux advantage in the far-infrared ($<400\text{ cm}^{-1}$) [1].

The first beamline dedicated to high spectral resolution far-infrared spectroscopy was built at MAX-lab in Lund, Sweden [2]. As of 2012, there are only four other high resolution far-infrared beamlines in operation at synchrotron facilities around the world: Synchrotron SOLEIL in France [3], Canadian Light Source [4], Swiss Light Source [5] and the Australian Synchrotron [6]. All these beamlines use commercial high resolution FTIR spectrometers, and a comprehensive review of capabilities and results from these beamlines was compiled recently by McKellar[1].

The Australian Synchrotron (AS) is 3rd generation 3 GeV electron storage ring with a circumference of 216 m.[7] Built in 2007, the AS had been operating in 12-hr decay mode until May 2012 when it moved to top-up injection mode where electrons are injected into the storage ring approximately every 4 minutes to maintain a minimum beam current of 200 mA. The infrared beamlines at the AS extract a portion of the synchrotron radiation measuring 58 mrad horizontally and 17 mrad vertically emitted by a bending magnet; this portion of the synchrotron light is caused by the electron beam being subjected to both a changing and constant magnetic-field giving rise to edge and bend magnet radiation respectively. The bend magnet radiation is directed to the Infrared Microscopy beamline while the edge radiation to the Far-IR beamline; this

optical arrangement is described by Creagh *et al.*[6]. Both beamlines use Bruker FT spectrometers and the synchrotron light is simply treated as an alternative light source to the internal thermal sources.

In this paper, we present the optical components available at the beamline used to cover the spectral range between 10 and 2850 cm^{-1} , the apparatus used to study gases, the performance of the Far-IR beamline for high spectral resolution studies and some applications. We also describe a gas cell for the study of cold gases and clusters of molecular ices, and how the cryogenic cell has been optically coupled to the FT spectrometer, and present an application on the far infrared lattice modes of carbon dioxide between 7 K and 102 K.

Far-Infrared Beamline instrumentation & Performance

The high resolution far-IR/THz beamline at the Australian Synchrotron is coupled to a Bruker IFS125HR FT spectrometer which has a maximum optical path difference of 942 cm and has three internal sources: tungsten filament source (for $>3000 \text{ cm}^{-1}$) a silicon carbide Globar and a high pressure mercury discharge lamp for the far-infrared region (for $<150 \text{ cm}^{-1}$). The spectrometer is equipped with a variety of detectors and beamsplitters to cover the spectral range from 10 cm^{-1} to 2850 cm^{-1} (see Table 1.).

Table 1. Optimal optical configurations for various spectral ranges

$\nu_{\text{Lo}}/\text{cm}^{-1}$	$\nu_{\text{Hi}}/\text{cm}^{-1}$	Beamsplitter	Detector	Filter	Graph
10	95	125 mm Mylar	Si bolometer	CF=2 ¹	A
10	105	75 mm Mylar	Si bolometer	CF=2 ¹	B
105	380	6 mm Mylar	Si bolometer	CF=1 ²	C
380	610	6 mm Mylar	Si:B Photodetector	CF=1 ³	D
610	730	KBr	Si:B Photodetector	CF=1 ³	E
730	1300	KBr	MCT-mid	4 ⁴	F
1300	2850	KBr	MCT-narrow	6 ⁵	G

ν_{Lo} is the lower wavenumber limit of the spectral range and ν_{Hi} the higher limit. The Si bolometer is equipped with 2 Cold Filters (CF) the Si:B photodetector has one: ¹ 12.7 mm thick white PE film, overlaid on one face with 4-8 mm diamond scatter layer, ² 1 mm thick diamond wedged crystal Qz with Garnet powder on one face, ³ Silicon crystal, ⁴ 1340 cm^{-1} long-wave pass optical filter on a KBr substrate, ⁵ 1125-2950 cm^{-1} band pass optical filter on a CaF_2 substrate.

The curves shown in Figure 1 are the single channel intensity for the various beamsplitter, detector and filter combinations covering the spectral range from 10 – 2850 cm^{-1} . The most intense curve, centred near 12 cm^{-1} is from coherent synchrotron emission, an accelerator operating mode whereby the electron bunches are compressed longitudinally. When the electron bunches are near the physical size of the wavelength they begin to emit light coherently, the intensity of which scales with the square of the number of electrons rather than linearly.[8] The Far-IR beamlines at the Canadian Light Source [9] and SOLEIL [10] have also measured spectra in this operating mode. Despite significant dynamics of the electron bunches manipulation of storage ring parameters can produce a stable source for high resolution spectroscopy.[11]

Users have a choice of 3 gas cells to study gases: 2 room temperature cells, M24V and M35V, and a cryogenic EFC cell (shown in Figure 2). The M35-V gas cell (Figure 2 a) is dedicated to the study of non-reactive gases at room temperature; the M24-V cell (Figure 2 b) has been designed to be coupled to a furnace ($< 1150 \text{ }^\circ\text{C}$ or 1425 K), and is used to study short-lived radicals generated by pyrolysis; while the EFC cell (Figure 2 c) is

used to generate cold gases which helps simplify their spectra, and it can also be used to generate clusters of molecular ice. The cell properties and parameters are listed in Table 2. Wedged TPX®, PE and KBr windows are available for this cell to cover the THz-mid-IR spectral range.

There is also a custom built 10 cm long steel gas-cell. It is designed to study strongly absorbing gaseous molecules which do not require long-path interaction with the synchrotron light. The 10 gas cell was designed with vacuum ports for electrical feed-through and vacuum ports to enable in-situ change of sample concentration or gas-mixture composition. The cell can be equipped with a heater to study gases at different temperatures. This should allow the study of line-width changes with pressure and temperature and therefore may be of interest to atmospheric scientists.

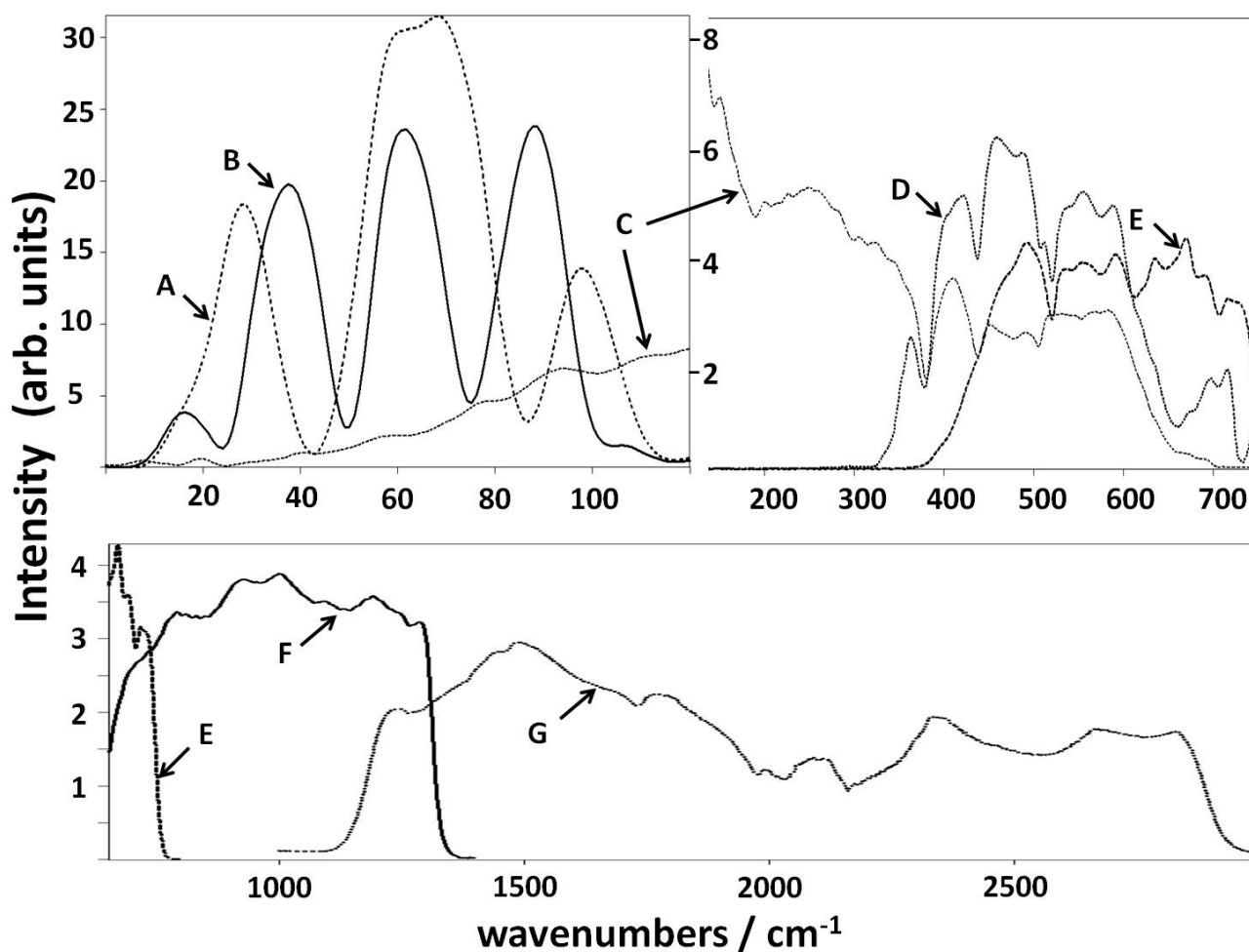


Figure 1 Graphs showing the energy curves of the optimal optical configurations listed in Table 1.

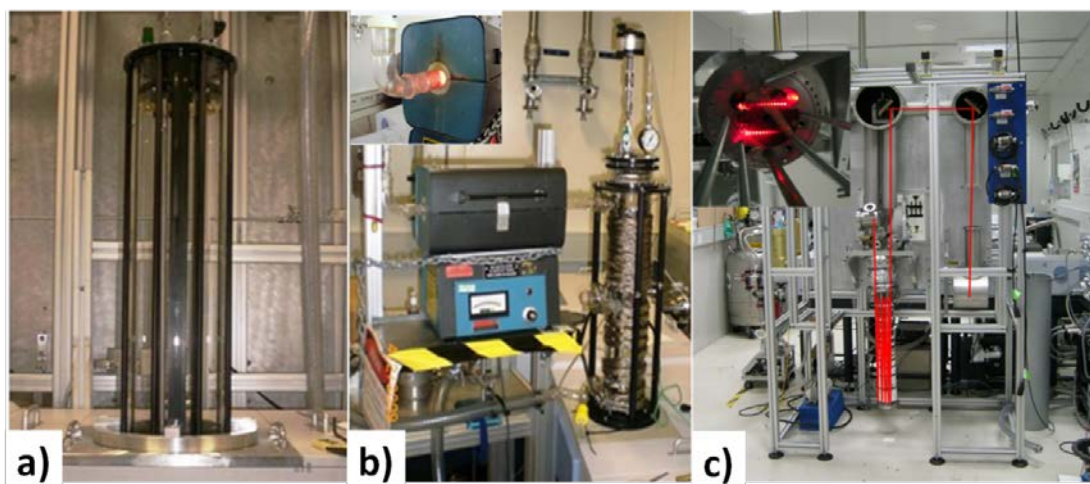


Figure 2. Pictures of the M35-V (a), M24-V & its furnace (b), and the EFC (c) setups at the Far-IR beamline.

Table 2. List of vacuum chambers for gas-phase applications available at the beamline.

Name	Diam/cm – Vol/L	Base path- length/cm	# passes-path- length/m	Applications	Operating Temperature
M35-V	15-11.5	55	40-22	Stable gases	Room temp
M24-V	10-5	55	24-13	Radicals	300-370 K
EFC	15-14	80	24-15	Stable gases, Radicals, aerosols	77K or 4.8K
10cm cell	2.5-0.05	10		Strong absorbers	Room temp

The signal amplitude & noise of the synchrotron source and internal sources were measured at a number of points throughout the spectrum with appropriate optical configurations (detectors, filters, and beamsplitters); at each point an aperture was chosen for the internal source that would allow the full resolution of the instrument. The ratio of the RMS signal to noise of the synchrotron radiation (SR) to that of the internal sources (IS) was then calculated and are presented in Figure 3 (circles, right axis). Near 2000 cm^{-1} there is an absorption (see Figure 1) due to the diamond window of the beamline, from the onset of this absorption $\approx 1800\text{ cm}^{-1}$ the signal to noise ratio of the internal source is greater than that of the synchrotron source for high-spectral resolution applications. In the very low wavenumber region ($< 50\text{ cm}^{-1}$) measurements are highly influenced by mechanical and electrical noises that are inherent in the beam. Due to the high complexity of the accelerator there are many possible sources of noise, a recent collaboration between the Far-IR beamlines at SOLEIL and SLS identified a number of difference sources including various high voltage power supplies [12].

Five years ago at the 2007 IRMMWTHz conference in Cardiff, it was announced that there were a few planned missions to study the earth's atmosphere as well as interstellar media and the atmospheres of other planets by a variety of agencies based in the US, Canada, Chile, Germany, Europe and Asia: these missions are SOFIA, ALMA, Herschel and JWST. In the last 3 years, the Herschel Space Observatory (formerly called Far Infrared and Sub-millimetre Telescope or FIRST), the large telescope SOFIA (mounted in a modified Boeing 747-SP aircraft) and the Atacama Large Millimeter/sub-millimeter Array (ALMA) missions have been launched. These 3 missions will be collecting high-quality data from the high-end of the far-infrared region down to the millimetre spectral region in order to study the formation of galaxies and stars in the Universe and examine

their molecular chemistry, to observe the chemical composition of the atmospheres and surfaces of comets, planets and satellites in our Solar System, also to help astronomers understand sulfur and water chemistry in the interstellar medium, the chemistry of interstellar dust, and the role of large and complex molecules, such as PAHs in the interstellar medium.

With this new influx of high quality spectral data, there would be a need for supporting laboratory spectral data of the highest quality to help better understand the molecules present in the spectra collected in the missions. Ever since the Far-IR beamline of the Australian Synchrotron welcomed its first synchrotron users in 2008, gas-phase researchers in Australia have been taking advantage of this unique facility outside Europe and Canada (which combines the bright synchrotron light with an ultra-high resolution FT spectrometer) to contribute to the high-quality laboratory spectra needed for these missions. The 2 main research areas of the gas-phase program have been the far-ir studies of short-lived gaseous molecular species of astrophysical interest and refrigerant-replacement gases of atmospheric importance, both at room-temperature using the M24V and M35V multi-pass gas-cell.[13-19]

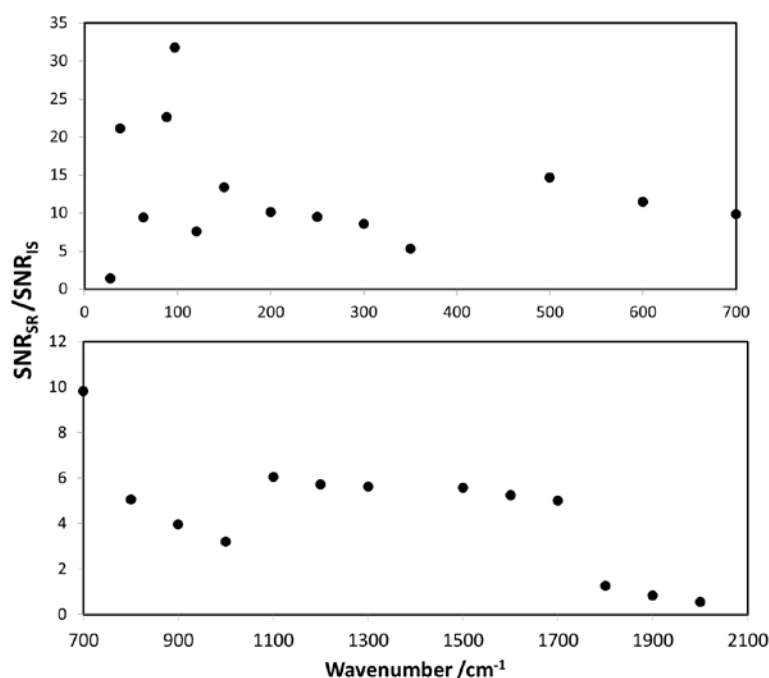


Figure 3: Signal to noise advantage of the Australia Synchrotron source for high resolution studies. Filled circles represent the signal to noise ratio of the Synchrotron source divided by that of the internal sources (Globar or Mercury lamp) at the appropriate aperture. Data in the top panel uses a Silicon bolometer and Mylar beamsplitters, below 100 cm⁻¹ a quartz low pass filter is used. The lower panel has data that uses a KBr beamsplitter and either a boron doped silicon photodetector or a mid band MCT detector, high pass filters were used in this region.

Low Temperature Spectroscopy

Cooling gas samples for high resolution FTIR spectroscopy simplifies the spectrum in a number of ways; firstly, the reduction in rotational temperatures concentrate the rotational envelope of a vibrational transition toward its band centre by increasing the population in energy levels with low rotational quantum numbers and dramatically decreasing the population in energy levels with high rotational quantum numbers. Secondly, there is also a reduced vibrational temperature which increases the population of the ground vibrational energy level thus increasing the signal strength of fundamental modes; this also has the effect of eliminating overlapping 'hot bands' (transitions from the thermally excited vibrational state). Cooling can be particularly useful in the study of halocarbons which often have low wavenumber vibrational modes and isotopologues with significant natural abundance.[20]

Cooling of gas samples can be accomplished by simple thermal control of a long path gas cell and sample to the desired temperature, however sample vapour pressure constrains the minimum practical temperature. This method was used to produce the spectrum in Figure 6, and it can be seen that although the intensity of the hot bands have been reduced significantly, they have not been eliminated and further reduction in temperature will lead to sample condensation. A method to overcome this limitation is ‘collisional cooling’ whereby a small amount of buffer gas (N₂ or He) is cooled to below the sample’s freezing point and the sample gas is continuously added to the cell, the buffer gas cools the sample via inelastic collisions.[21-22]

Adiabatic cooling in jet expansions is another commonly used technique wherein a high pressure mixture of sample and carrier gas is expanded through a small nozzle to intersect with the beam of an FTIR instrument.[23-24] Rotational temperatures of less than 10 K are achievable with this method however a single optical pass of the millimetre sized expansion from a pinhole nozzle often provides insufficient sensitivity. Optics that allow for multiple optical passes of the jet are possible, although complex since each pass must be coincident with the expansion at the same location. [25-26] Another technique to increase the optical interaction is to make the size of the expansion larger by using multiple nozzles [27] or a slit nozzle [28-29] however both these introduce additional optical constraints. Ideally a multi-nozzle or slit jet expansion would be optically sampled with a small parallel beam; however shaping the large parallel beam output from a commercial spectrometer into an appropriate size is difficult. Typically the parallel beam is focussed onto the expansion using mirrors with long focal lengths so the divergence is minimised.[27, 30] The high collimation of a synchrotron source may prove to be advantageous over conventional sources in this regard.[31] The larger area of these nozzles can also increase the already large sample and pumping requirements of jet expansions, these can be somewhat reduced by using a pulsed nozzle which allows the pump a recovery time between pulses.[32] Such systems can also be useful in the study of molecular clusters.[33-34]

Most Far-IR synchrotron beamlines have or are acquiring accessories to cool gas samples, these are summarised in Table 4. At Max-Lab, they use a stainless steel long pass White-type absorption cell that is surrounded by a liquid nitrogen container; temperature control is achieved by using low pressure helium gas to transfer heat from the cell to the cryogen [35]; this cell has been modified to allow less volatile samples to be continuously flowed through the cell after being diluted in a buffer gas [36]. A similar cell is under construction at the AILES beamline at SOLEIL, however this uses Chernin [37] type optics which use three objective mirrors in order to obtain a higher optical path length with a cell of smaller physical dimensions. The Far-IR beamline at the Canadian Light Source has a long path White cell that is cooled by passing cold liquid or gas through copper tubes that surround the cell, a methanol refrigerator is typically used to achieve temperatures of ≈100 K, liquid nitrogen could also be used to achieve temperatures near 80 K. The beamline at the Swiss Light Source has access to a cooling cell identical to the one described in the next section, however it does not appear to have been attached to the beam line yet.[38]

Table 3: Cooling methods at high resolution FTIR beamlines

Facility	Min Temp (K)	Max Path length (m)	Cooling modes	Status
MAX-LAB	80	150	Helium gas transfers heat to liquid N ₂	Operational
SOLEIL	80	150?	Helium gas transfers heat to liquid N ₂	Near completion
	<15K	<1	Jet expansion	?
CLS	~80K	80	Cold gas or liquid in copper tubing around cell	Operational
Swiss light source	4	40	(As below)	Unknown...?

			i. Equilibrium cooling - cold gas or liquid surrounds cell.	
AS	4	40	ii. Collisional cooling – bath gas inside of cell transfers heat to coolant	Operational
			iii. Enclosive flow cooling – flow of buffer gas envelopes and cools a flow of sample gas	

Collisional and Enclosive Flow Cooling

For low temperature gas phase experiments we have recently coupled a cooling cell (Figure 4) to the beamline that can be used in collisional cooling mode or enclosive flow cooling mode. The cooling cell has been described thoroughly elsewhere [39], in brief it consists of an inner cylinder made of Invar steel that houses the White cell optics, heaters and thermocouples. This cylinder has a large number of holes in its wall that allow for a flow of buffer gas to enter from an outer cylinder. The outer cylinder seals the vacuum with an indium gasket and infrared windows that are kept at room temperature. This cylinder sits inside a large glass Dewar where the coolant resides. A flow of cold nitrogen gas in the volume between the outer cylinder and the Dewar can be used to achieve stable equilibrium temperatures from ≈ 100 K to 250 K. This mode of operation is particularly useful for high resolution studies where spectra may need to be recorded over a number of days and temperature stability is crucial. This mode can maintain the temperature of the sample to ± 0.5 K for days.

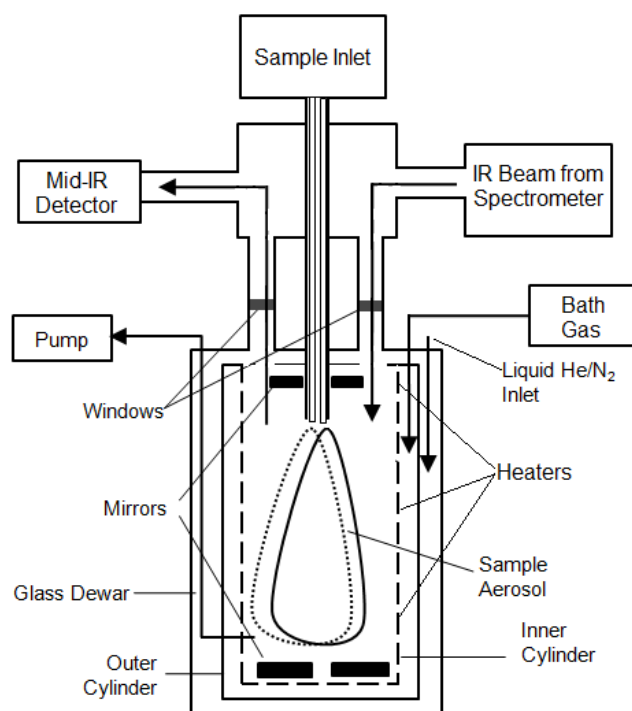


Figure 4: Schematic of the original optical setup of the enclosive flow cooling cell.

The cell can also be cooled with liquid cryogen (N_2 or He) in the Dewar; in combination with the internal heaters temperatures of ≈ 5 -150 K are achievable. In this mode the cell can be operated as a traditional collisional cooling cell by adding small amounts sample gas to a small pressure of buffer gas (He or N_2). The concept of enclosive flow cooling is an extension of this mode whereby a slow flow of buffer gas is

continuously pumped through the cell. The buffer gas flows from the outer cylinder into the inner one via the holes in its wall and forms an envelope of gas that surrounds the sample gas which enters directly into the centre of the cell. This mode allows for further super cooling of the gas sample by keeping the sample from condensing on the cell walls and mirrors [40-41].

The condensation of gas phase molecules into an aerosol can also be studied with this cell. Typically these experiments are performed by filling the cell with a pressure of inert bath gas (10-1000 mbar) which is cooled to a desired temperature by the coolant on the outside of the cell and controlled by heaters on the inside. A high pressure (≈ 2 atm) of sample gas (often diluted) is then allowed to enter the cell. This plume of sample gas expands into the optical volume and is cooled by the bath gas thus becoming supersaturated and then nucleating to form particles (see Figure 4). The spectral effects of changing formation conditions (bath gas temperature & pressure, and sample gas concentration & pressure) can be used to infer structural changes in the particles. Multiple inlet tubes can be used to study how different gases nucleate, to see if they form pure or mixed particles or if they form a mantle around existing particles.

Cooling Cell Transfer Optics

In its original optical design the enclosive flow cooling cell (Figure 5) was coupled to the IFS125 spectrometer via its parallel exit port, and the IR beam was then steered through the cell onto an MCT or InSb detector mounted in the optical vacuum chamber of the EFC cell system. The latter was not designed to handle liquid helium bolometers (which are conventionally used in the Far-IR) thus, limiting studies to the mid infrared region ($>700\text{ cm}^{-1}$).

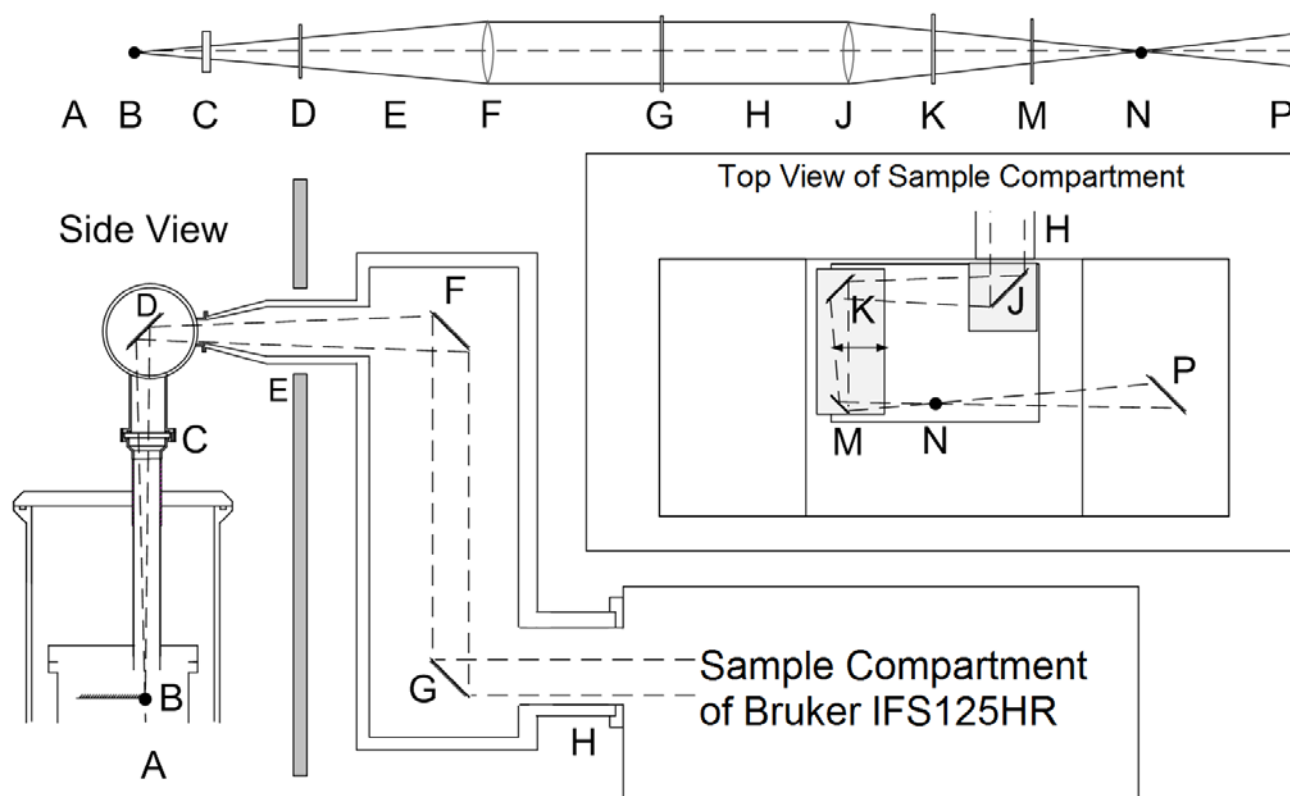


Figure 5: Optical schematic of EFC cell transfer optics, not to scale. A: EFC Cell optics, B: Focal point of white cell optics, $f/16$. C: EFC cell window, D: Plane mirror. E= supporting plate for EFC cell. F: Collimating mirror, off axis parabolic mirror, $f/16$. G: Plane mirror.

H: entrance into spectrometer. J: Focussing mirror (Off axis parabolic mirror, $f/6.5$. K & M: Plane mirrors on translation stage .N: Spectrometer focus location. P: Spectrometer optics, beam goes onward to detector compartment.

In order to access the far infrared region where the synchrotron is most advantageous the optics for the beam exiting the EFC were modified to steer the beam back into the spectrometer to access the far-infrared detectors (as well as mid-IR) mounted directly in the vacuum chamber of the IFS125. The new optical setup is illustrated in Figure 5 where the expanding beam that exits the cell is directed to an off axis parabolic mirror (F); the collimated beam is then steered into the sample compartment of the spectrometer (as shown in the top view of Figure 5) and focused with another off axis parabolic mirror (J) and two flat mirrors (K, M) which can be translated to bring the beam to a focal point coincidental with the spectrometers focus (N). The beam then passes into the detector compartment of the spectrometer where any one of 5 infrared detectors can be selected.

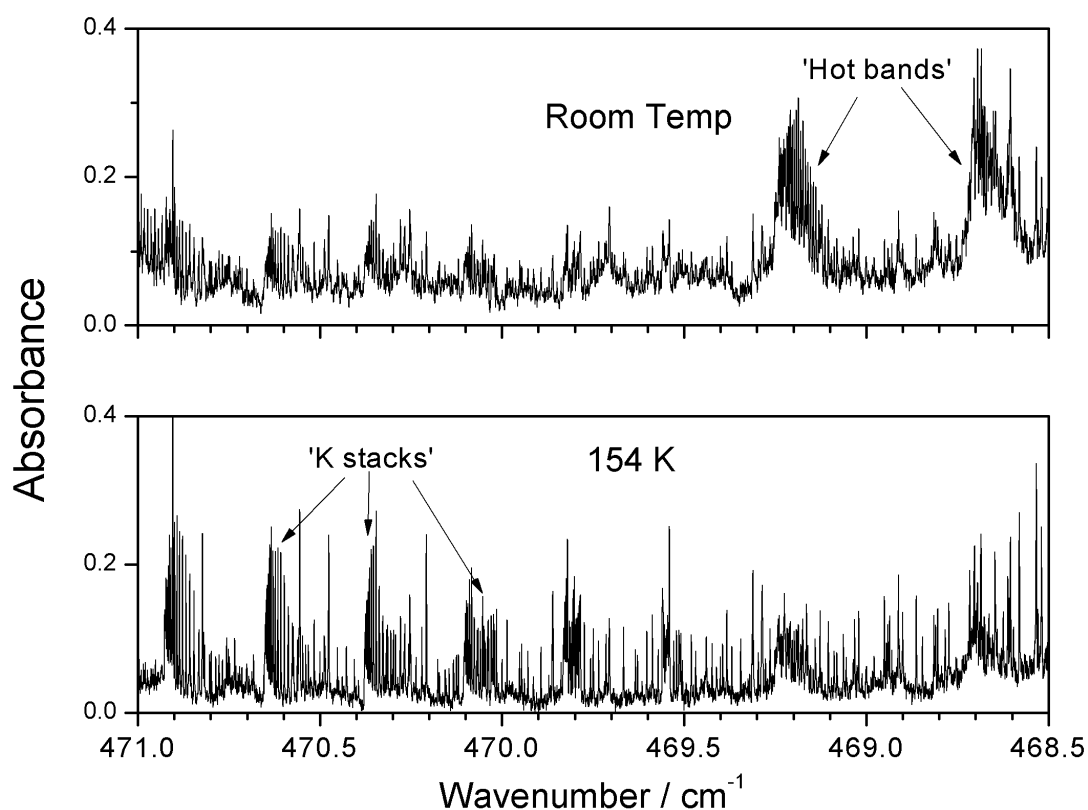


Figure 6: The ν_{11} band of R152a (1,1,-Difluoroethane) at a nominal resolution of 0.00096 cm^{-1} , the top trace was recorded in a room temperature cell at 66 Pa and a path length of 2.2 m. The lower trace was recorded in the EFC cell at 154 K with a path length of 2.5 m, pressure of 28 Pa. These spectra were recorded with the storage ring in decay mode whereby the injections were made two times per day up to a current of 202 mA which decayed over 12 hours to $\approx 150 \text{ mA}$.

Figure 6 shows the spectral effects of reduced temperature on a sample of 1,1,-Difluoroethane (R152a), the cooled spectrum was recorded at 154 K using the Enclosive Flow Cooling (EFC) cell in collisional cooling mode while the warm spectrum was obtained in a room temperature gas cell. Although the effective path length† and sample pressures of the two spectra are approximately equal, the cold spectrum shows an increased intensity of the fundamental mode due to the decreased vibrational temperatures. The intensity is also increased by the reduced Doppler line width due to the lower rotational temperature.

$$\dagger \frac{\text{Pressure}}{\text{Temperature}} * \text{Path length} = \frac{66 \text{ Pa}}{300 \text{ K}} * 2.2 \text{ m} \approx \frac{28 \text{ Pa}}{154 \text{ K}} * 2.5 \text{ m}$$

Carbon Dioxide Aerosols

Numerous studies have used similar cells to examine aerosols of various small molecules and mixtures in the mid-infrared [42-53], including a number of studies on carbon dioxide [49, 54-57]. However, our group is the first to adapt it for use in the far-infrared where the intermolecular lattice modes can be interrogated.[58] In the present study we have measured the far infrared spectrum of CO_2 aerosols which consists of two absorptions due to translational lattice modes near 114 cm^{-1} and 68 cm^{-1} .

Carbon dioxide ice is of great interest in a number of fields, carbon dioxide clouds have been detected on Mars with average particle radii of 4-22 μm [59]. At these sizes, the particles strongly scatter mid-infrared light and are thought to have strongly influenced the climate of the planet [60-61]. Solid carbon dioxide is also a major component of interstellar dust [62], these dust grains typically include a silicate core with an icy mantle. While aerosol phase spectra are not directly analogous to these systems it is important to have knowledge of the spectrum of the pure compound to fully understand how substrates and impurities influence

the spectrum. At present, there appears to be no spectroscopic studies on the far infrared spectrum of CO₂ in the aerosol phase in the literature, and only a few studies on thin films [63-66]

The aerosols were formed by introducing a sample of CO₂ (<99.8% pure, approximately 60 mL at 270 kPa) into the cell which contained helium bath gas at $\approx 15 \text{ mol/m}^3$ precooled to each of the temperatures shown in Figure 7 (7-102 K). Pressure was measured with a BOC active strain gauge and temperature was recorded via a rhodium-iron thermistor located in the centre of the gas cell. A background spectrum was taken once the bath gas reached the desired temperature and then the sample spectra were recorded whilst the sample was injected. The absorbance was seen to reach a maximum after approximately 5 seconds and then slowly decay over the next few minutes as the particles diffused out of the optical path. The spectra in Figure 7 were measured at a resolution of 1 cm^{-1} ; an average was taken from the spectra recorded after the maximum was reached. At this resolution the brightness of the synchrotron source is of no advantage; however the flux in this region is approximately five times greater than that of a mercury arc lamp.

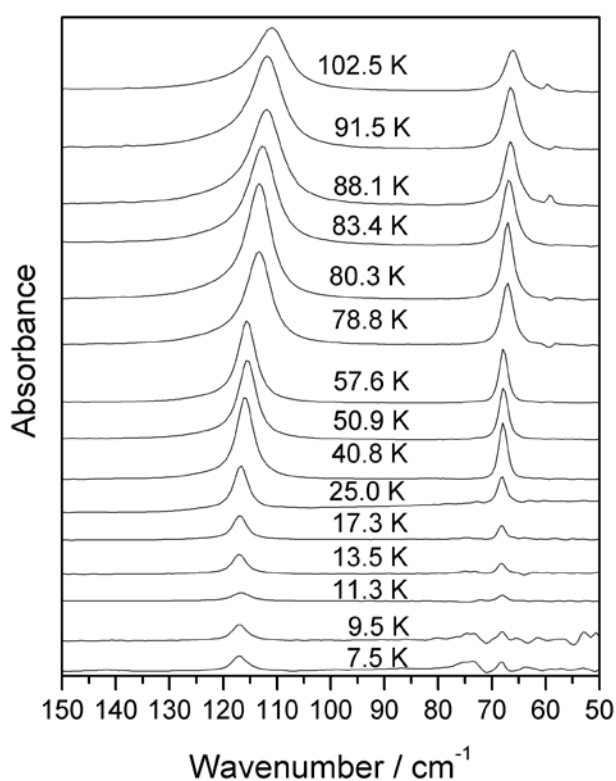


Figure 7: Far infrared spectrum of carbon dioxide particles produced by pulsing a 60 mL sample at 270 kPa into the cell containing $\approx 15 \text{ mol/m}^3$ of helium buffer gas at various temperatures. Note that the small feature $\approx 60 \text{ cm}^{-1}$ is a noise artefact. These spectra were recorded with the storage ring in decay mode whereby the injections were made two times per day up to a current of 202 mA which decayed over 12 hours to $\approx 150 \text{ mA}$.

Experiments under similar conditions were performed in the mid infrared ($700\text{-}8000 \text{ cm}^{-1}$) at temperatures between 78-110 K and they showed a large amount of scattering at 1000 cm^{-1} we therefore estimate the particle size to be larger than $10 \mu\text{m}$ at 80 K. Since nucleation rates change with temperature, particle size will also vary, with smaller particles produced at colder temperatures. Unlike a previous study [58] on nano-sized water aerosols the positions of the peaks shown in Figure 6 compare well with thin film transmission studies. The incongruity in the results of water particles was attributed to a lack of scattering effect due to the size of the particles. The consistency of this work with previous CO₂ data suggests the particles are in a similar size regime to the thin films ($2\text{-}30 \mu\text{m}$). While most data points from previous work are compatible with the present work the improved accuracy and range of these measurements suggests that the

previously assumed linear dependence [64] in the temperature versus peak position trend either has a discontinuity near 60 K where the trend changes gradient or the trend is quadratic in nature.

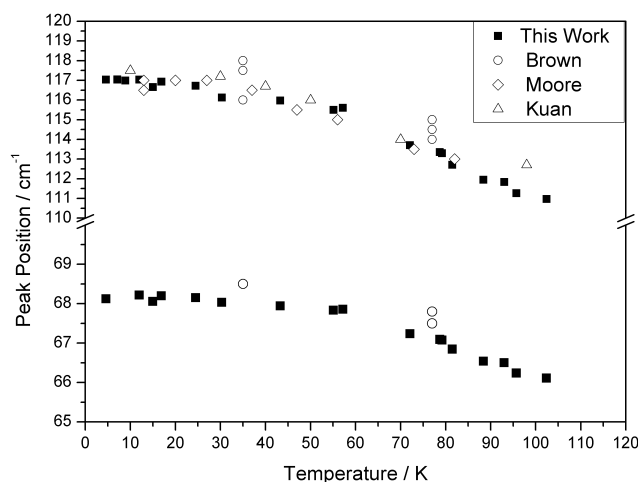


Figure 6: Peak position of the far-infrared translational lattice modes of carbon dioxide particles.

Conclusions

The performance and capabilities of the Far-Infrared beamline at the Australian Synchrotron are described. For high resolution studies the synchrotron source provides an advantage in signal to noise up to 1700 cm^{-1} . We also report the coupling of a collisional/enclosive flow cooling cell to the spectrometer at the high resolution FTIR and far infrared beamline at the Australian Synchrotron and adapted it for use in the far-IR. This cell is capable of operating between 4-400 K for high resolution spectroscopy as well as for investigations of aerosol particles formed *in situ*. We report the first far-infrared spectra of pure carbon dioxide particles in the aerosol phase between 8 K and 110 K.

References

1. McKellar, A., *High-resolution infrared spectroscopy with synchrotron sources*. Journal of Molecular Spectroscopy, 2010. **262**(1): p. 1-10.
2. Nelander, B., *Beam-line for infrared spectroscopy at Max-lab*. Vibrational Spectroscopy, 1995. **9**(1): p. 29-41.
3. Roy, P., M. Rouzières, Z. Qi, and O. Chubar, *The AILES Infrared Beamline on the third generation Synchrotron Radiation Facility SOLEIL*. Infrared Physics & Technology, 2006. **49**(1–2): p. 139-146.
4. May, T.E., *Infrared facility at the Canadian light source*. Infrared Physics and Technology, 2004. **45**(5–6): p. 383-387.
5. Lerch, P., L. Quaroni, J. Wambach, J. Schneider, D.B. Armstrong, D. Rossetti, F.L. Mueller, P. Peier, V. Schlott, L. Carroll, P. Friedli, H. Sigg, S. Stutz, and M. Tran, *IR beamline at the Swiss Light Source*. Journal of Physics: Conference Series, 2012. **359**(1): p. 012003.
6. Creagh, D., M. Tobin, A. Broadbent, and J. McKinlay, *An Infrared Beamline at the Australian Synchrotron*. AIP Conference Proceedings, 2007. **879**(1): p. 615-618.
7. Boldeman, J. and D. Einfeld, *The physics design of the Australian synchrotron storage ring*. Nuclear Instruments and Methods in Physics Research Section A: Accelerators, Spectrometers, Detectors and Associated Equipment, 2004. **521**(2): p. 306-317.
8. Carr, G.L., M.C. Martin, W.R. McKinney, K. Jordan, G.R. Neil, and G.P. Williams, *High-power terahertz radiation from relativistic electrons*. Nature, 2002. **420**(6912): p. 153-156.
9. May, T., J. Bergstrom, L. Dallin, and D. Appadoo. *Coherent synchrotron radiation measurements in the THz region at the CLS far infrared beamline*. in *Infrared, Millimeter and Terahertz Waves, 2008. IRMMW-THz 2008. 33rd International Conference on*. 2008: IEEE.

10. Evain, C., J. Barros, A. Loulergue, M.A. Tordeux, R. Nagaoka, M. Labat, L. Cassinari, G. Creff, L. Manceron, J.B. Brubach, P. Roy, and M.E. Couprie, *Spatio-temporal dynamics of relativistic electron bunches during the micro-bunching instability in storage rings*. EPL (Europhysics Letters), 2012. **98**(4): p. 40006.
11. Barros, J., L. Manceron, J.B. Brubach, G. Creff, C. Evain, M.E. Couprie, A. Loulergue, L. Nadolski, M.A. Tordeux, and P. Roy. *Toward highly stable Terahertz Coherent Synchrotron Radiation at the synchrotron SOLEIL*. in *Journal of Physics: Conference Series*. 2012: IOP Publishing.
12. Lerch, P., P. Dumas, T. Schilcher, A. Nadji, A. Luedeke, N. Hubert, L. Cassinari, M. Boege, J.-C. Denard, L. Stingelin, L. Nadolski, T. Garvey, S. Albert, C. Gough, M. Quack, J. Wambach, M. Dehler, and J.-M. Filhol, *Assessing noise sources at synchrotron infrared ports*. Journal of Synchrotron Radiation, 2012. **19**(1): p. 1-9.
13. Bane, M.K., E.G. Robertson, C.D. Thompson, C. Medcraft, D.R.T. Appadoo, and D. McNaughton, *High-resolution Fourier-transform infrared spectroscopy of the Coriolis coupled ground state and nu [sub 7] mode of ketenimine*. The Journal of Chemical Physics, 2011. **134**(23): p. 234306-6.
14. Bane, M.K., C.D. Thompson, E.G. Robertson, D.R.T. Appadoo, and D. McNaughton, *High-resolution FTIR spectroscopy of the [small nu]8 and Coriolis perturbation allowed [small nu]12 bands of ketenimine*. Physical Chemistry Chemical Physics, 2011. **13**(15).
15. Bane, M.K., E.G. Robertson, C.D. Thompson, D.R.T. Appadoo, and D. McNaughton, *High-resolution Fourier-transform infrared spectroscopy of the nu [sub 6] and Coriolis perturbation allowed nu [sub 10] modes of ketenimine*. The Journal of Chemical Physics, 2011. **135**(22): p. 224306-6.
16. Bane, M.K., C.D. Thompson, D.R.T. Appadoo, and D. McNaughton, *Synchrotron far infrared spectroscopy of the ground, nu5, and nu15 states of thiirane*. The Journal of Chemical Physics, 2012. **137**(8): p. 084306-084306-6.
17. Bane, M.K., C. Jones, S.L. Choong, C.D. Thompson, P.D. Godfrey, D. McNaughton, and D.R.T. Appadoo, *High-resolution FTIR spectroscopy of the nu7 and nu8 bands of 1-phosphapropyne*. Journal of Molecular Spectroscopy, 2012.
18. Chimdi, T., E.G. Robertson, L. Puskar, C.D. Thompson, M.J. Tobin, and D. McNaughton, *High resolution synchrotron FTIR spectroscopy of the far infrared nu10 and nu11 bands of R152a (CH3CHF2)*. Chemical Physics Letters, 2008. **465**(4-6): p. 203-206.
19. Chimdi, T., E.G. Robertson, L. Puskar, C.D. Thompson, M.J. Tobin, and D. McNaughton, *Ro-vibrational analysis of the nu9 and nu16 bands of R152a*. Journal of Molecular Spectroscopy, 2008. **251**(1-2): p. 256-260.
20. McNaughton, D., E.G. Robertson, C.D. Thompson, T. Chimdi, M.K. Bane, and D. Appadoo, *Overview of High-Resolution Infrared Measurement and Analysis for Atmospheric Monitoring of Halocarbons†*. Analytical chemistry, 2010. **82**(19): p. 7958-7964.
21. Appadoo, D.R.T., E.G. Robertson, and D. McNaughton, *High resolution FTIR spectroscopic study of the [nu] 4 band of CH3CHF2 enclosed in a flow of cold N2 gas*. Journal of Molecular Spectroscopy, 2003. **217**(1): p. 96-104.
22. McNaughton, D., I. Aleksic, D.R.T. Appadoo, C.D. Thompson, and E.G. Robertson, *Decongestion of high-resolution FTIR-spectra and assignment of CHF2CF3*. Vibrational Spectroscopy, 2004. **36**(1): p. 123-128.
23. Herman, M., R. Georges, M. Hepp, and D. Hurtmans, *High resolution Fourier transform spectroscopy of jet-cooled molecules*. International Reviews in Physical Chemistry, 2000. **19**(2): p. 277-325.
24. Snels, M., V. Horká-Zelenková, H. Hollenstein, and M. Quack, *High-Resolution FTIR and Diode Laser Spectroscopy of Supersonic Jets*, in *Handbook of High-resolution Spectroscopy*. 2011, John Wiley & Sons, Ltd.
25. McNaughton, D., D. McGilvery, and E.G. Robertson, *High-resolution FTIR-jet spectroscopy of CCl2F2*. J. Chem. Soc., Faraday Trans., 1994. **90**(8): p. 1055-1060.
26. Petry, R., S. Klee, M. Lock, B.P. Winnewisser, and M. Winnewisser, *Spherical mirror multipass system for FTIR jet spectroscopy: application to the rovibrationally resolved spectrum of OC5O*. Journal of Molecular Structure, 2002. **612**(2): p. 369-381.

27. Georges, R., G. Durry, M. Bach, R. Pétrisse, R. Jost, and M. Herman, *Multinozzle supersonic expansion for Fourier transform absorption spectroscopy*. Chemical Physics Letters, 1995. **246**(6): p. 601-606.
28. Amrein, A., M. Quack, and U. Schmitt, *High-resolution interferometric Fourier transform infrared absorption spectroscopy in supersonic free jet expansions: carbon monoxide, nitric oxide, methane, ethyne, propyne, and trifluoromethane*. The Journal of Physical Chemistry, 1988. **92**(19): p. 5455-5466.
29. Barnes, J.A. and T.E. Gough, *Fourier transform infrared spectroscopy of supersonic jets: observation of clusters containing sulphur hexafluoride*. Chemical Physics Letters, 1986. **130**(4): p. 297-300.
30. Arno, J. and J.W. Bevan, *Jet Spectroscopy and Molecular Dynamics*, ed. J.M. Hollas and D. Phillips. 1995, Edinburgh: Blackie.
31. Chandrasekaran, V., L. Biennier, E. Arunan, D. Talbi, and R. Georges, *Direct Infrared Absorption Spectroscopy of Benzene Dimer*. The Journal of Physical Chemistry A, 2011. **115**(41): p. 11263-11268.
32. Luckhaus, D., M. Quack, U. Schmitt, and M.A. Suhm, *On FTIR Spectroscopy in Asynchronously Pulsed Supersonic Free Jet Expansions and on the Interpretation of Stretching Spectra of HF Clusters*. Berichte der Bunsengesellschaft für physikalische Chemie, 1995. **99**(3): p. 457-468.
33. Devlin, J.P., M. Farnik, M.A. Suhm, and V. Buch, *Comparative FTIR spectroscopy of HX adsorbed on solid water: Ragout-jet water clusters vs ice nanocrystal arrays*. Journal of Physical Chemistry A, 2005. **109**(6): p. 955-958.
34. Häber, T., U. Schmitt, and M.A. Suhm, *FTIR-spectroscopy of molecular clusters in pulsed supersonic slit-jet expansions*. Phys. Chem. Chem. Phys., 1999. **1**(24): p. 5573-5582.
35. Larsen, R.W., F. Hegelund, and B. Nelander, *Studies of intermolecular vibrations in hydrogen-bonded molecular complexes for the gas phase using a synchrotron radiation source*. Molecular Physics, 2004. **102**(16-17): p. 1743-1747.
36. Larsen, R.W., F. Hegelund, A. Engdahl, P. Uvdal, and B. Nelander, *High-resolution infrared study of collisionally cooled trans-1,2-dichloroethylene*. Journal of Molecular Spectroscopy, 2007. **243**(1): p. 99-102.
37. Chernin, S.M. and E.G. Barskaya, *Optical multipass matrix systems*. Appl. Opt., 1991. **30**(1): p. 51-58.
38. Ulenikov, O., E. Bekhtereva, S. Albert, S. Bauerecker, H. Hollenstein, and M. Quack, *High resolution infrared spectroscopy and global vibrational analysis for the CH₃D and CHD₃ isotopomers of methane*. Molecular Physics, 2010. **108**(7-9): p. 1209-1240.
39. Bauerecker, S., M. Taraschewski, C. Weitkamp, and H.K. Cammenga, *Liquid-helium temperature long-path infrared spectroscopy of molecular clusters and supercooled molecules*. Review of Scientific Instruments, 2001. **72**(10): p. 3946-3955.
40. Bauerecker, S., F. Taucher, C. Weitkamp, W. Michaelis, and H.K. Cammenga, *Spectral simplification by enclosive flow cooling I - FT-IR spectroscopy of supercooled gases at 100 K*. Journal of Molecular Structure, 1995. **348**(0): p. 237-241.
41. Taucher, F., C. Weitkamp, H.K. Cammenga, and S. Bauerecker, *Infrared spectroscopy and enclosive flow cooling: concept of an integrated multireflection optics*. Spectrochimica Acta Part A: Molecular and Biomolecular Spectroscopy, 1996. **52**(8): p. 1023-1027.
42. Kunzmann, M.K., R. Signorell, M. Taraschewski, and S. Bauerecker, *The formation of N₂O nanoparticles in a collisional cooling cell between 4 and 110 K*. Physical Chemistry Chemical Physics, 2001. **3**(17): p. 3742-3749.
43. Kunzmann, M.K., S. Bauerecker, M.A. Suhm, and R. Signorell, *Spectroscopic characterization of N₂O aggregates: From clusters to the particulate state*. Spectrochimica Acta - Part A: Molecular and Biomolecular Spectroscopy, 2003. **59**(12): p. 2855-2865.
44. Dartois, E. and S. Bauerecker, *Infrared analysis of CO ice particles in the aerosol phase*. The Journal of Chemical Physics, 2008. **128**(15): p. 154715-10.
45. Buch, V., S. Bauerecker, J. Paul Devlin, U. Buck, and J.K. Kazimirski, *Solid water clusters in the size range of tens–thousands of H₂O: a combined computational/spectroscopic outlook*. International Reviews in Physical Chemistry, 2004. **23**(3): p. 375-433.

46. Bauerecker, S., A. Wargenau, M. Schultze, T. Kessler, R. Tuckermann, and J. Reichardt, *Observation of a transition in the water-nanoparticle formation process at 167 K*. The Journal of Chemical Physics, 2007. **126**(13): p. 134711-6.
47. Bauerecker, S. and E. Dartois, *Ethane aerosol phase evolution in Titan's atmosphere*. Icarus, 2009. **199**(2): p. 564-567.
48. Signorell, R. and D. Luckhaus, *Aerosol Spectroscopy of Dihydroxyacetone: Gas Phase and Nanoparticles*. The Journal of Physical Chemistry A, 2002. **106**(19): p. 4855-4867.
49. Signorell, R. and M.K. Kunzmann, *Isotope effects on vibrational excitons in carbon dioxide particles*. Chemical Physics Letters, 2003. **371**(3-4): p. 260-266.
50. Signorell, R. and M. Jetzki, *Vibrational exciton coupling in pure and composite sulfur dioxide aerosols*. Faraday Discussions, 2008. **137**: p. 51-64.
51. Jetzki, M., A. Bonnamy, and R. Signorell, *Vibrational delocalization in ammonia aerosol particles*. The Journal of Chemical Physics, 2004. **120**(24): p. 11775-11784.
52. Robertson, E.G., C. Medcraft, L. Puskar, R. Tuckermann, C.D. Thompson, S. Bauerecker, and D. McNaughton, *IR spectroscopy of physical and chemical transformations in cold hydrogen chloride and ammonia aerosols*. Physical Chemistry Chemical Physics, 2009. **11**(36).
53. Medcraft, C., E.G. Robertson, C.D. Thompson, S. Bauerecker, and D. McNaughton, *Infrared spectroscopy of ozone and hydrogen chloride aerosols*. Physical Chemistry Chemical Physics, 2009. **11**(36).
54. Signorell, R., M. Jetzki, M. Kunzmann, and R. Ueberschaer, *Unraveling the Origin of Band Shapes in Infrared Spectra of N₂O-¹²CO₂ and ¹²CO₂-¹³CO₂ Ice Particles*. Journal of Physical Chemistry A, 2006. **110**: p. 2890-2897.
55. Signorell, R., *Verification of the vibrational exciton approach for CO₂ and N₂O nanoparticles*. The Journal of Chemical Physics, 2003. **118**(6): p. 2707-2715.
56. Taraschewski, M., H.K. Cammenga, R. Tuckermann, and S. Bauerecker, *FTIR Study of CO₂ and H₂O/CO₂ nanoparticles and their temporal evolution at 80 K*. Journal of Physical Chemistry A, 2005. **109**(15): p. 3337-3343.
57. Bauerecker, S., *Self-Diffusion in Core-Shell Composite ¹²CO₂/¹³CO₂ Nanoparticles*. Physical Review Letters, 2005. **94**: p. 033404.
58. Medcraft, C., D. McNaughton, C.D. Thompson, D. Appadoo, S. Bauerecker, and E.G. Robertson, *Size and Temperature Dependence in the Far-IR Spectra of Water Ice Particles*. The Astrophysical Journal, 2012. **758**(1): p. 17.
59. Hu, R., K. Cahoy, and M.T. Zuber, *Mars atmospheric CO₂ condensation above the north and south poles as revealed by radio occultation, climate sounder, and laser ranging observations*. J. Geophys. Res., 2012. **117**(E7): p. E07002.
60. Forget, F. and R.T. Pierrehumbert, *Warming early Mars with carbon dioxide clouds that scatter infrared radiation*. Science, 1997. **278**(5341): p. 1273.
61. Mischna, M.A., J.F. Kasting, A. Pavlov, and R. Freedman, *Influence of carbon dioxide clouds on early Martian climate*. Icarus, 2000. **145**(2): p. 546-554.
62. Gerakines, P.A., D.C.B. Whittet, P. Ehrenfreund, A.C.A. Boogert, A.G.G.M. Tielens, W.A. Schutte, J.E. Chiar, E.F.v. Dishoeck, T. Prusti, F.P. Helmich, and G. Th. de, *Observations of Solid Carbon Dioxide in Molecular Clouds with the Infrared Space Observatory*. The Astrophysical Journal, 1999. **522**(1): p. 357.
63. Ron, A. and O. Schnepf, *Lattice Vibrations of the Solids N₂, CO₂, and CO*. The Journal of Chemical Physics, 1967. **46**(10): p. 3991-3998.
64. Moore, M.H. and R.L. Hudson, *Far-infrared spectra of cosmic-type pure and mixed ices*. Astronomy and Astrophysics Supplement Series, 1994. **103**: p. 45-56.
65. Brown, K.G. and W. King, *Infrared Intensities of the Lattice Modes of Solid Carbon Dioxide*. The Journal of Chemical Physics, 1970. **52**: p. 4437.
66. Kuan, T.S., *PhD Thesis*. 1969, University of Southern California.

Declaration for Thesis Chapter 2.2

Declaration by candidate

In the case of Chapter 2.2 the nature and extent of my contribution to the work was the following:

Nature of contribution	Extent of contribution (%)
Initiation, key ideas, experimental, development and writing up	80%

The following co-authors contributed to the work. Co-authors who are students at Monash University must also indicate the extent of their contribution in percentage terms:

Name	Nature of contribution	Extent of contribution (%) for student co-authors only
W. Fuss	Experiments, analysis and initiation	
D.R.T. Appadoo	Experimental Assistance	
D. McNaughton	Initiation and key ideas	
C.D. Thompson	Initiation and key ideas	
E.G. Robertson	Initiation and key ideas	

Candidate's
Signature

	Date
--	-------------

Declaration by co-authors

The undersigned hereby certify that:

- (1) the above declaration correctly reflects the nature and extent of the candidate's contribution to this work, and the nature of the contribution of each of the co-authors.
- (2) they meet the criteria for authorship in that they have participated in the conception, execution, or interpretation, of at least that part of the publication in their field of expertise;
- (3) they take public responsibility for their part of the publication, except for the responsible author who accepts overall responsibility for the publication;
- (4) there are no other authors of the publication according to these criteria;
- (5) potential conflicts of interest have been disclosed to (a) granting bodies, (b) the editor or publisher of journals or other publications, and (c) the head of the responsible academic unit; and
- (6) the original data are stored at the following location(s) and will be held for at least five years from the date indicated below:

Location(s)

Monash University, School of Chemistry

[Please note that the location(s) must be institutional in nature, and should be indicated here as a department, centre or institute, with specific campus identification where relevant.]

Signature 1

	Date
--	-------------

Signature 2

--	--

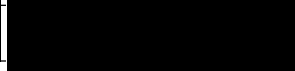
Signature 3

--	--

Signature 4

--	--

Signature 5

	3-12-2012
---	-----------

Structural, vibrational, and rovibrational analysis of tetrafluoroethylene

C. Medcraft,¹ W. Fuss,^{2,a)} D. R. T. Appadoo,³ D. McNaughton,¹ C. D. Thompson,¹
 and E. G. Robertson^{4,b)}

¹School of Chemistry, Monash University, Wellington Rd., Clayton, Victoria 3800, Australia

²Max-Planck-Institut für Quantenoptik, 85748 Garching, Germany

³Australian Synchrotron, 800 Blackburn Rd, Clayton, Victoria 3168, Australia

⁴Department of Chemistry, La Trobe Institute of Molecular Sciences, La Trobe University, Bundoora, Victoria 3086, Australia

(Received 23 August 2012; accepted 6 November 2012; published online 3 December 2012)

High resolution FTIR spectra of ¹³C enriched tetrafluoroethylene (C₂F₄) were measured at 150 K at the Australian Synchrotron. Rovibrational transitions were assigned in the *a*-type symmetric and *b*-type antisymmetric CF₂ stretches of ¹²C¹³CF₄ and ¹³C₂F₄ near 1170 cm⁻¹ and 1300 cm⁻¹, respectively. Ground vibrational state spectroscopic constants for both molecules were determined in addition to the upper state constants for ν_{11} and ν_9 of ¹³C₂F₄ and ν_{11} , $\nu_2+\nu_6$, and ν_5 of ¹²C¹³CF₄. The ground state constants, along with those determined for the ¹²C₂F₄ isotopologue from previously published data, were used to determine a semi-experimental *r_e* structure $r_{CC} = 132.36 \pm 0.37$ pm, $r_{CF} = 131.11 \pm 0.23$ pm, $\alpha_{FCC} = 123.3 \pm 0.3^\circ$ in excellent agreement with *ab initio* structures. Lower resolution FTIR spectra were measured between 100 and 5000 cm⁻¹ at room temperature and band centres obtained for all modes of the three isotopologues; although only 5 out of 12 modes in ¹²C₂F₄ and ¹³C₂F₄ are infrared (IR) active, the others were inferred from combination and hot-band positions. A number of modes are observed to be infrared active only in the ¹²C¹³CF₄ isotopologue due to its lower symmetry. Most notably, decoupling of the antisymmetric CF₂ motions in the two halves of ¹²C¹³CF₄ results in 2 strongly IR active modes that involve motion at one carbon or the other. © 2012 American Institute of Physics. [<http://dx.doi.org/10.1063/1.4768417>]

I. INTRODUCTION

Tetrafluoroethylene is used industrially in the production of various fluoropolymers, most notably polytetrafluoroethylene, Teflon. Rapid oxidation by hydroxyl radicals leads to an atmospheric lifetime of 1.9 days, therefore, the global warming potential is minimal (0.070 over 20 years) despite strong absorptions in the appropriate infrared windows.¹ Vibrational assignments of ¹²C₂F₄ date back to an infrared study in 1945² and a combined IR and Raman study in 1950;³ the lowest-wavenumber IR active band was measured in 1954 and the IR and Raman inactive torsion vibration estimated from thermodynamic data.⁴ These assignments were summarised by Shimanouchi.⁵

In earlier work by Robertson *et al.*⁶ using a sample with natural isotopic abundance cooled to 160 K, high resolution spectra of the intense symmetric (ν_{11}) and antisymmetric (ν_9) CF₂ stretches in the mid-infrared region were measured.⁶ The rovibrational data were used to generate ground state combination differences (GSCD) which were fitted to provide ground vibrational state rotational and centrifugal distortion constants not available from rotational spectroscopy since ¹²C₂F₄ does not possess a permanent dipole moment. The upper vibrational state spectroscopic constants for ν_9 and ν_{11} were also determined in that study. The ground state constants were used to produce estimated equilibrium constants

by subtracting computationally derived vibrational and electronic contributions. However, there was insufficient information to determine a definitive molecular structure because one set of rotational constants linked by the planarity relation provides only two geometric constraints but there are three structural parameters ($r_{C=C}$, r_{CF} , and α_{FCC}). An earlier electron diffraction study reported a thermal equilibrium structure (r_g),⁷ but rotational constants calculated from this r_g structure are significantly different to both the fitted ground state constants and the semi-experimental equilibrium constants presented in Ref. 6. Improvements in the structural parameters of tetrafluoroethylene require the isotopic substitution method of Kraitchman.⁸

A recent *ab initio* study by Feller *et al.* performed a number of geometry optimizations on tetrafluoroethylene using high level coupled cluster theory with large correlation consistent basis sets.⁹ This study also included corrections for core/valence interactions and relativistic effects which had been shown to produce structures in excellent agreement with experimental equilibrium structures of difluoroethylenes.¹⁰

In the present study, we first improve the normal mode assignments and include assignments for the two ¹³C isotopologues. A number of vibrational modes are found to be IR active only in the ¹²C¹³CF₄ isotopologue due to its different (*C_{2v}*) symmetry. Second, in order to simplify the spectrum the high resolution FTIR spectrum of ¹³C enriched C₂F₄ has been measured in a long path cell¹¹ cooled to 150 K. This technique provides spectra that are more amenable to analysis and has been used successfully by this

^{a)}Permanent address: Weidachstr. 12, 85748 Garching, Germany.

^{b)}Author to whom correspondence should be addressed. Electronic mail: E.Robertson@latrobe.edu.au.

TABLE I. Vibrational wavenumber values (cm^{-1}) for the three isotopologues of C_2F_4 .

Mode	Description	Previous work ^a		$^{12}\text{C}_2\text{F}_4$		$^{12}\text{C}^{13}\text{CF}_4$		$^{13}\text{C}_2\text{F}_4$
ν_1	C=C str	1872	A_g	1873.8 ^b	A_1	1840.4 ^b	A_g	1806.3 ^b
ν_2	CF_2 sym str	778	A_g	776.1 ^b	A_1	773.5 ^b	A_g	769.7 ^b
ν_3	CF_2 scissor	394	A_g	395.1 ^b	A_1	395.1 ^c	A_g	395.1 ^c
ν_4	CF_2 twist	190	A_u	193.7 ^b	A_2	193.7 ^d	A_u	193.7 ^d
ν_5	CF_2 asym str	1340	B_{2g}	1337.7 ^b	B_1	1300.1 ^e	B_{2g}	1285.8 ^b
ν_6	CF_2 rock	551	B_{2g}	550.0 ^b	B_1	548.8 ^b	B_{2g}	547.0 ^b
ν_7	CF_2 wag	406	B_{2u}	405.2 ^f	B_2	398.8 ^f	B_{2u}	393.4 ^f
ν_8	CF_2 wag	508	B_{3g}	509.8 ^b	B_2	501.4 ^b	B_{3g}	483.3 ^b
ν_9	CF_2 asym str	1340	B_{3u}	1340.0 ^a	B_1	1340 ^{f,g}	B_{3u}	1305.0 ^e
ν_{10}	CF_2 rock	218	B_{3u}	210.0 ^{b,f}	B_1	209.7 ^c	B_{3u}	209.3 ^c
ν_{11}	CF_2 sym str	1187.6	B_{1u}	1187.6 ^a	A_1	1173.0 ^e	B_{1u}	1160.0 ^e
ν_{12}	CF_2 scissor	558	B_{1u}	555.3 ^f	A_1	553.6 ^f	B_{1u}	551.9 ^f

^a ν_9 and ν_{11} are from high resolution FTIR,⁶ other modes are as reported in Shimanouchi.⁵

^bBand assigned from combination modes (see Table II).

^cShift in band position from $^{12}\text{C}_2\text{F}_4$ is calculated from MP2 calculations (see Table III).

^dSymmetry dictates that there is no shift in band position with isotopic substitution.

^eMeasured by high resolution spectroscopy (the number presented is truncated).

^fMeasured directly at low resolution (see Figure 2).

^gDetermined via spectral subtraction, see Figure 6.

group for the study of a number of different halocarbons large enough to make their room temperature spectra difficult or impossible to assign.^{12–17} The cold cell is now located at the high resolution infrared and far-IR beamline at the Australian Synchrotron which has been used in previous studies to provide a higher signal to noise ratio than thermal sources.^{17–20} This combination of synchrotron and collisional cooling cell optimized the prospects of assigning mixed isotopologue spectra in this work.

II. EXPERIMENTAL

Isotope enrichment was achieved by the selective dissociation of CHClF_2 to generate CF_2 by CO_2 laser photolysis.²¹ The final products of this process (C_2F_4 and HCl) were separated from the remaining precursor by low temperature distillation and HCl was then removed by contact with moist KOH . The resulting ratio of isotopologues in the process is 1:2:1 for $^{12}\text{C}_2\text{F}_4$: $^{12}\text{C}^{13}\text{CF}_4$: $^{13}\text{C}_2\text{F}_4$ as measured by mass spectrometry and confirmed by infrared spectroscopy.

High resolution FTIR spectra of the symmetric and antisymmetric stretch bands were recorded at the far-IR beamline of the Australian Synchrotron using a cell designed for enclosive flow cooling (EFC) which has been described in Ref. 11. The stainless steel vacuum chamber of the EFC cell is located inside a large vacuum insulated glass Dewar where a flow of cold nitrogen gas cools the sample chamber to 150 ± 10 K, as measured by K-type thermocouples and an iron rhodium thermistor inside the vacuum chamber. By reducing the thermal population of excited vibrational states the congestion caused by hot bands was reduced significantly because at room temperature only $\approx 22\%$ of the molecules are in the ground vibrational state while at 150 K this increases to 69%. At this temperature the Doppler width of the rovibrational lines is also reduced by approximately 30% resulting in measured line widths close to the instrumental line width.

The cooling cell, set to a 2.5 m optical path length, was fitted with calcium fluoride windows and coupled to a Bruker IFS125HR spectrometer equipped with a KBr beamsplitter and an external mercury-cadmium-telluride detector. Sample pressure was maintained at 0.1 mbar and 148 co-added scans were recorded at a nominal resolution of 0.00096 cm^{-1} . Far infrared spectra ($100\text{--}600 \text{ cm}^{-1}$) were also measured at 0.1 cm^{-1} spectral resolution using a 10 cm room temperature cell with polyethylene windows; the sample pressure was ≈ 50 mbar. The Bruker IFS125HR was equipped with a liquid helium cooled silicon bolometer and a $6 \mu\text{m}$ Mylar beamsplitter.

Low-resolution spectra (0.2 cm^{-1}) were also recorded at the Max Plank Institute in Garching using 10 cm and 1 m path length gas cells with KBr windows and coupled to a Perkin-Elmer FTIR 2000 spectrometer equipped with a KBr beamsplitter and a DTGS detector to measure the region $400\text{--}4000 \text{ cm}^{-1}$. These spectra used a variety of higher sample pressures (400–2000 mbar) in order to allow assignment of the combination and overtone bands.

III. RESULTS AND DISCUSSION

A. Vibrational assignment

The two monoisotopic species of C_2F_4 have D_{2h} symmetry while the mixed isotopologue ($^{12}\text{C}^{13}\text{CF}_4$) has C_{2v} symmetry. Previous studies on the $^{12}\text{C}_2\text{F}_4$ isotopologue^{5,6} have used the III' representation $(x,y,z) = (a,b,c)$ for the symmetry assignments and corresponding vibrational mode number labels. However, the $^{12}\text{C}^{13}\text{CF}_4$ isotopologue cannot be properly described by C_{2v} symmetry in this representation since the carbon-carbon bond lies along the C_2 axis which, by convention, is the z -axis. Here, we present the vibrational assignments for all three isotopologues with symmetries designated in the conventional I' representation with the z -axis along the C=C bond and the y -axis perpendicular to the plane of the

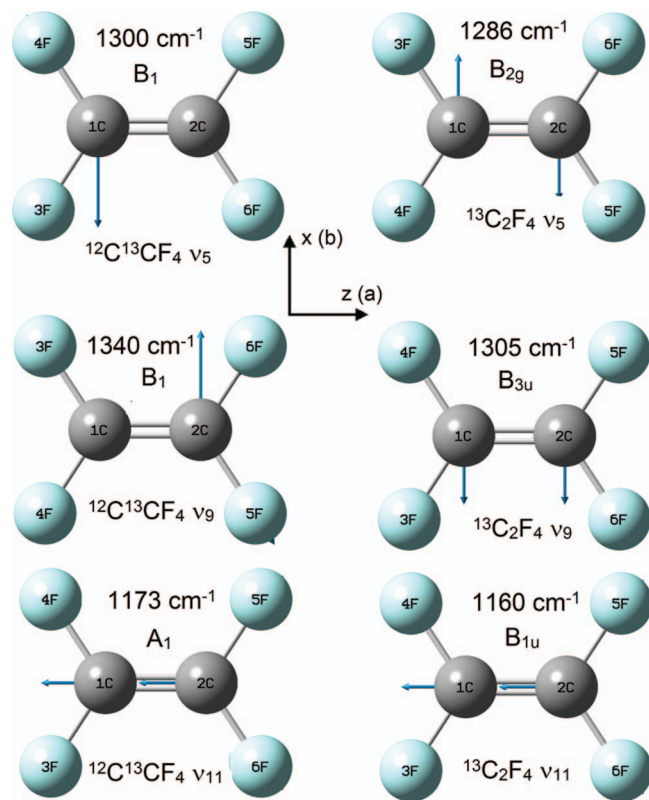


FIG. 1. Atomic displacement vectors from GaussView²³ from MP2/cc-pDVZ calculations using GAUSSIAN03.²⁴ The symmetric and antisymmetric CF₂ stretches of ¹²C¹³CF₄ (left) and ¹³C₂F₄ (right, identical for ¹²C₂F₄) are shown, with experimentally assigned band positions. ν_5 in the monoisotopic species (top right) is not infrared active. Note that for ¹²C¹³CF₄ the 1C atoms are ¹³C and the 2C are ¹²C. The potential energy distributions of all modes can be found in the VIBCA output files in the supplementary material.⁴⁶

molecule (Table I). Vibrational symmetry was assigned with the aid of atomic displacement vectors taken from MP2 calculations. Three of the more interesting modes corresponding with those measured at high resolution are shown in Figure 1. Vibrational modes with B_{1u}/A₁ symmetry produce *a*-type IR bands, those with B_{3u}/B₁ symmetry *b*-type bands and those with B_{2u}/B₂ symmetry *c*-type bands with the modes of other symmetry IR inactive. For consistency, the vibrational mode number labels have not been changed from the previous assignments for ¹²C₂F₄. The mode numbers for ¹²C¹³CF₂ are designated to correspond with the equivalent mode in the monoisotopic species. The calculated atomic displacements for the vibrational modes are analogous within the isotopologues with the exception of the two antisymmetric CF₂ stretches, ν_5 and ν_9 , discussed in detail in Sec. III F. Interestingly, 7 of 12 modes are IR forbidden in the parent species, but only one vibrational mode of the ¹²C¹³CF₄ isotopologue is infrared inactive by symmetry (the A₂ symmetry CF₂ twist \approx 194 cm⁻¹); all other modes have some infrared intensity. This pattern is more obvious in the analogous ethylene isotopologue (¹²C¹³CH₄) due to the greater difference in reduced masses compared with its parent.²² The nuclear spin statistical weightings for the rotational levels also change between isotopologues, for ¹²C₂F₄ the ground vibrational state weightings ee:oe:eo:oo ($K_a K_c$) are 7:3:3:3 while ¹²C¹³CF₄ has 6:3:6:3 and ¹³C₂F₄ has 16:12:24:12.

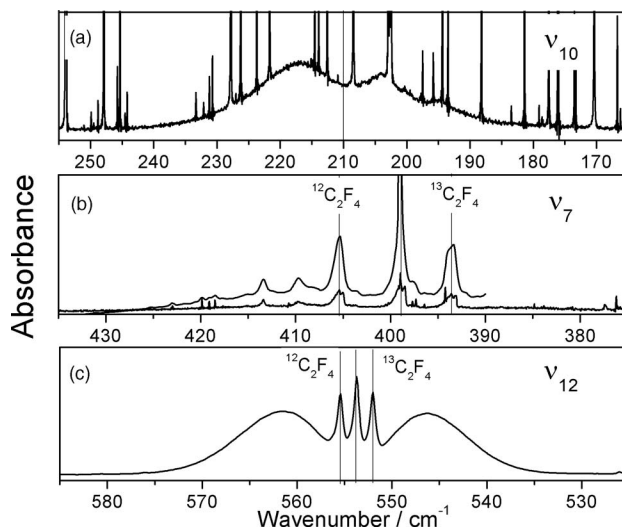


FIG. 2. Low-resolution IR spectra of the low wavenumber fundamentals of a 1:2:1 mixture of ¹²C₂F₄:¹²C¹³CF₄:¹³C₂F₄. The sharp, saturated lines in the top spectrum are due to water vapour. The absorbance has been scaled for clarity, however, the relative intensities for each mode are approximately equal. The ν_{10} spectrum and the lower spectrum of ν_7 were recorded at the Australian Synchrotron, the ν_{12} spectrum and the upper spectrum of ν_7 were recorded at the Max Planck Institute, Garching. The band centres of ν_7 and ν_{12} of ¹²C₂F₄ and ¹³C₂F₄ have been labelled, the ¹²C¹³CF₄ band centre lies in between these.

Of the 6 modes of ¹²C¹³CF₄ that become IR allowed as the symmetry changes from D_{2h} to C_{2v}, most have very weak infrared intensity and were not observed. A notable exception is ν_5 at 1300 cm⁻¹ which was measured at high resolution (see details in Secs. III E and III F). The ν_1 C=C stretching mode may also have been observed at low resolution in an absorption near 1840 cm⁻¹. The band centre for the ν_{11} symmetric CF₂ stretch near 1175 cm⁻¹ was determined with high accuracy from high resolution spectra. Other infrared active modes measured at lower resolution (0.2 cm⁻¹) were the ν_9 antisymmetric CF₂ stretch near 1340 cm⁻¹, the ν_{12} CF₂ rocking mode near 550 cm⁻¹ (Figure 2(c)) and the ν_7 CF₂ wagging mode near 400 cm⁻¹ (Figure 2(b)) which both contained intense Q-branches which allowed for the bands centres from all three isotopologues to be determined to within 0.1 cm⁻¹. The ν_{10} CF₂ rocking mode near 210 cm⁻¹ (Figure 2(a)) has less separation between isotopologues and the shifts were derived from MP2 calculations (see Sec. III B).

The infrared inactive modes were derived indirectly from a number of combination and difference bands; these are listed in Table II and the bands used for the ν_8 assignment are shown in Figure 3 along with a survey spectrum. Whereas difference bands do not need any anharmonic correction to extract the fundamental wavenumber values, sum bands do and the appropriate anharmonic constants were determined from observed hot bands and subtracted in order to give the band centre of the fundamental. The shifts in the combination band positions between isotopologues were in general found to be a linear combination of the shifts of the component fundamentals. Assignment of a number of combination and difference bands resulted in a consistent set of isotopic shifts for all fundamental modes with the exception of ν_3 and ν_{10} where the combination modes were too weak and the isotopic

TABLE II. Summary of overtone and combination bands used to indirectly determine the fundamental band positions of $^{12}\text{C}_2\text{F}_4$.

Mode	Observed band(s)	Observed position (cm^{-1})	Anharmonic correction (cm^{-1})	Calculated position (cm^{-1})
ν_1	$\nu_1 - \nu_7$	1468.6	...	1873.8
ν_2	$(\nu_8 + \nu_{11}) - (\nu_8 + \nu_{11} - \nu_2)$	1696.1 and 920.0	...	776.1
ν_3	$\nu_3 + \nu_{12}$ and $\nu_3 + \nu_7$	951.2 and 788.85	$x_{3,12} = +0.85, x_{3,7} = -1.45$	395.1
ν_4	$\nu_5 - \nu_4$ and $\nu_5 + \nu_4$	1144.0 and 1528.2	$x_{4,4} = +1.65, x_{5,4} = -3.4$	193.7
ν_5	$\nu_5 - \nu_4$ and $\nu_5 + \nu_4$	1144.0 and 1528.2	$x_{4,4} = +1.65, x_{5,4} = -3.4$	1337.7
ν_6	$\nu_{11} - \nu_6$ and $\nu_9 - \nu_6$	637.8 and 789.5	...	550.0
ν_8	$\nu_8 + \nu_{12}$ and $\nu_7 + \nu_8$	1065.6 and 913.4	$x_{8,12} = +0.5, x_{7,8} = -1.6$	509.8
ν_{10}	$2\nu_{10} + \nu_{11}$	1607.4	$x_{10,10} = +1.0, x_{10,11} = -0.7$	210.0

shifts too small to be observed. In these cases, the shift was calculated from anharmonic MP2/cc-pVTZ calculations. These calculations were generally found to be accurate to within $\approx 0.5 \text{ cm}^{-1}$ for other modes and are in agreement with shifts calculated using the Teller-Redlich product rule.²⁵ Table II shows a summary of the combination and difference bands used to determine band centres for the fundamentals. A full table of all observed combination modes is included in Table S1 of the supplementary material.⁴⁶

B. Quantum mechanical calculations

The vibrational assignment was aided by a number of harmonic wavenumber calculations performed with the GAMESS code²⁶ using the B3LYP hybrid density functional or MP2 theory. The basis sets used included Pople's triple split (6-311),²⁷ the Dunning-type correlation consistent (cc-pVnZ),²⁸ and Ahlich's contracted Gaussians (nZV)²⁹ with various diffuse and polarisation functions added. Anharmonic calculations were also performed, using GAUSSIAN03 (C.02)²⁴ at the MP2 level and using the Dunning type basis sets. The cc-pVTZ basis set, chosen as the best compromise between accuracy and computational cost, was used to calculate shifts in vibrational wavenumber values from $^{12}\text{C}_2\text{F}_4$ for the two ^{13}C isotopologues which are compared to the experimentally determined shifts in Table III.

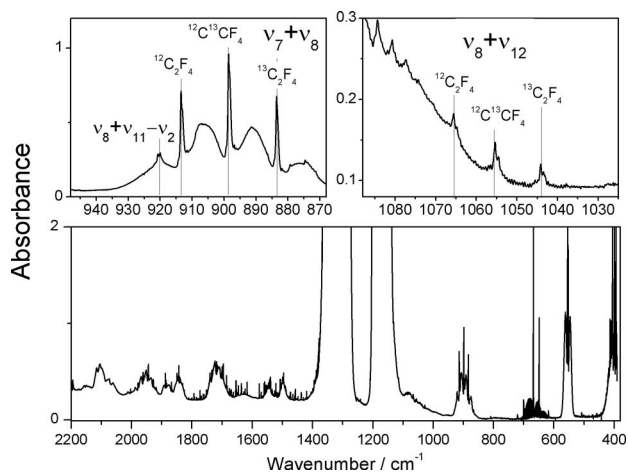


FIG. 3. Infrared spectra of the isotopically enriched sample showing many of the bands with moderate IR intensity (lower panel), and expanded to show selected combination modes that were used to determine band centres of the IR inactive modes (upper panels).

Generally shifts in vibrational frequency with isotopic substitution are caused only by the nuclear kinetic energy terms in the Hamiltonian and indicate the amplitude of motion of the substituted atom. The calculated shifts are very close to the observed shifts except in the case of ν_2 , the symmetric CF_2 stretch, and the ν_5/ν_9 antisymmetric CF stretching modes. The ν_2 symmetric CF_2 stretch has A_g symmetry and is entangled via Fermi resonances with a number of interacting levels: ($2\nu_7 \approx 810 \text{ cm}^{-1}$, $2\nu_3 \approx 790 \text{ cm}^{-1}$, $\nu_3 + 2\nu_4 \approx 782 \text{ cm}^{-1}$, $4\nu_4 \approx 775 \text{ cm}^{-1}$). The anharmonic calculations indicate the magnitude of some of the relevant Fermi terms ($W_{2,33} = 4.5 \text{ cm}^{-1}$ and $W_{3,44} = 2.9 \text{ cm}^{-1}$ for each isotopologue), but the computed energies of these levels relative to ν_2 are not quite right and so neither are the computed isotopic shifts in consequence. Similarly, discrepancies in the antisymmetric CF_2 stretch shifts may be attributed to the strong Fermi resonance interactions which are discussed in detail in Sec. III F.

The poor prediction of these modes should not affect the assignment of the shifts in ν_3 and ν_{10} which were too small to be observed in the spectrum; the calculated shifts are $< 1 \text{ cm}^{-1}$ and the Teller-Redlich product rule²⁵ also predicts shifts of near zero in both cases.

The GAMESS Hessian output files from these calculations were used as an input for the harmonic force field analysis program VIBCA³⁰ which generates rotational and centrifugal distortion constants and Coriolis zeta parameters. These were used to aid the rovibrational analyses presented in Secs. III E and III F. The optimized geometries that were used in these calculations also aided the structural analysis (Sec. III D), however, none of the *ab initio* structures improved on those presented previously.^{6,10}

C. Ground vibrational states

The *a*-type symmetric stretches (ν_{11} of $^{13}\text{C}_2\text{F}_4$ at 1160.0 cm^{-1} and ν_{11} of $^{12}\text{C}^{13}\text{CF}_4$ at 1173.0 cm^{-1}) were measured at high resolution and a total of 1658 and 1719 rovibrational transitions were assigned for the modes, respectively. The *b*-type antisymmetric stretching region was more complex with three observed bands for $^{12}\text{C}^{13}\text{CF}_4$, ν_9 at 1340 cm^{-1} (for which rovibrational transitions were not assigned), $\nu_2 + \nu_6$ at 1321.1 cm^{-1} , and ν_5 at 1300.1 cm^{-1} ; 1366 and 754 transitions were assigned in these latter two bands. The $^{13}\text{C}_2\text{F}_4$ molecule had one *b*-type mode, ν_9 at 1305.0 cm^{-1} , and 933 transitions were assigned. Transitions from the *a*-type bands were used to generate qS type

TABLE III. Calculated and experimental shifts in vibrational wavenumber from $^{12}\text{C}_2\text{F}_4$ for each ^{13}C isotopologue.

Mode	$^{12}\text{C}_2\text{F}_4$		$^{12}\text{C}^{13}\text{CF}_4$		$^{12}\text{C}^{13}\text{C}_2\text{F}_4$		$^{13}\text{C}_2\text{F}_4$	
	Exp. (cm^{-1})	Calc. (cm^{-1}) ^a	Exp. shift (cm^{-1})	Calc. shift (cm^{-1})	IR intensity ^b	Exp. shift (cm^{-1})	Calc. shift (cm^{-1})	IR intensity ^b
ν_1	1873.8	1862.2	-33.4	-33.8	0.95	-67.5	-67.9	...
ν_2	776.1	773.8	-2.6	-1.4	0.008	-6.4	-3.3	...
ν_3	395.1	392.0	^c	0.0	0.0001	^c	0.0	...
ν_4	193.7	199.2	0.0	0.0	...	0.0	0.1	...
ν_5	1337.7	1346.1	-37.6	-56.0	191.9	-51.9	-64.7	...
ν_6	550.0	545.7	-1.2	-1.8	0.0018	-3.0	-3.5	...
ν_7	405.2	418.9	-6.4	-6.7	3.19	-11.8	-12.3	3.12
ν_8	509.8	526.6	-8.4	-8.9	0.025	-18.1	-18.9	...
ν_9	1340.0	1331.9	0	6.9	194.7	-35.0	-34.9	375.4
ν_{10}	210	208.4	^c	-0.3	4.49	^c	-0.6	4.50
ν_{11}	1187.6	1179.8	-14.6	-14.5	354.7	-27.6	-27.4	346.2
ν_{12}	555.3	549.5	-1.7	-1.7	2.98	-3.4	-3.4	3.18

^aCalculated in GAUSSIAN03 using MP2/cc-PVTZ, scaled by a factor of 0.986.

^bIR intensity as calculated in MP2/cc-PVTZ calculation in units of km mol^{-1} .

^cThe “experimental” position for these bands was determined from the calculated shifts.

($\Delta J = 2$, $\Delta K_a = 0$, $\Delta K_c = 2$) GSCD pseudotransitions while the b -type bands generated both qS and sS ($\Delta J = 2$, $\Delta K_a = 2$, $\Delta K_c = 0$) type GSCDs. The GSCDs for all three isotopologues were combined and fitted to Watson’s A -reduced Hamiltonian³¹ in the I' representation using Pickett’s SPFIT program.³² The rotational constants (A , B , C) were fitted independently for each molecule while the centrifugal distortion constants were fitted with fixed ratios to those of $^{12}\text{C}_2\text{F}_4$. The ratios for each centrifugal distortion constant were determined from the MP2/TZV+(3df) calculation described above; these ratios varied by less than 0.1% between basis sets and levels of theory. Fitting the constants in this manner reduced the uncertainties in the rotational constants by a factor of ≈ 2 . The transitions in the present experiments were assigned an uncertainty of 0.00028 cm^{-1} ($0.0002 \text{ cm}^{-1} \times \sqrt{2}$), transitions of $^{12}\text{C}_2\text{F}_4$ from the previous study⁶ were assigned an uncertainty of 0.00042 cm^{-1} ($0.0003 \text{ cm}^{-1} \times \sqrt{2}$). The fitted r_0 constants are shown in Table IV along with semi-experimental equilibrium rotational constants.

D. Geometry

The geometry of tetrafluoroethylene can be fully described by three parameters, r_{CC} , r_{CF} , α_{FCC} . In previous work on this molecule, Robertson *et al.*⁶ used the ground state constants of $^{12}\text{C}_2\text{F}_4$ and subtracted both the vibration-rotation contributions calculated from a MP2 harmonic force field and the small contribution from out-of-plane π electrons to obtain an inertial defect of $-0.0002 \text{ u}\text{\AA}^2$. The resulting rotational constants were assumed to be close to the equilibrium constants and by fixing one of the structural parameters (α_{FCC}), the remaining two parameters could be fitted to the rotational constants; three such self-consistent structures were reported and the intermediate one is listed in Table V.

Now, the isotopic substitution of the carbon atoms allows for the calculation of the C=C bond distance directly from the three sets of ground state rotational constants via Kraitchman’s equations.⁸ This calculation found the r_s/r_0 bond distance to be $131.3 \pm 0.4 \text{ pm}$, the error arises from propagation of the errors in the rotational constants and includes the

Costain error.⁴³ The remaining two structural parameters (r_{CF} and α_{CFE}) were fitted to the ground vibrational state rotational constants and are shown in Table V as the r_s/r_0 structure. It compares very well with the r_g electron diffraction structure. Both r_s and r_g structures include the effects of nuclear motion, and so neither is directly comparable to the equilibrium structures from *ab initio* calculations: the C=C bond distances are shorter and the C-F bond distances longer than the theoretical values.

TABLE IV. Ground state rotational and centrifugal distortion constants from a combined fit of the three $^{12}\text{C}/^{13}\text{C}$ isotopologues of tetrafluoroethylene.

Parameter	$^{12}\text{C}_2\text{F}_4$	$^{12}\text{C}^{13}\text{CF}_4$	$^{13}\text{C}_2\text{F}_4$
A_0 (MHz)	5512.7893(110) ^a	5513.0430(104)	5513.2587(299)
B_0 (MHz)	3237.893(28)	3228.993(41)	3220.123(53)
C_0 (MHz)	2038.4977(49)	2035.0737(43)	2031.5337(51)
Δ_J (kHz)	0.4462(53)	0.4426 ^b	0.4389 ^b
Δ_{JK} (kHz)	-0.7111(211)	-0.6981	-0.6854
Δ_K (kHz)	2.1507(165)	2.1418	2.1329
δ_J (kHz)	0.17608(260)	0.17440	0.17273
δ_K (kHz)	0.5407(159)	0.5417	0.5427
Exp. Δ_0 ($\text{u}\text{\AA}^2$)	+0.1608(15)	+0.1519(21)	+0.1571(27)
Calc. Δ_0 ($\text{u}\text{\AA}^2$) ^c	+0.1652	+0.1661	+0.1657
IR RMS (cm^{-1})	0.00026	0.00023	0.00016
RMS deviation		0.663	
No. of transitions	2117	942	804
sS type	1326	355	19
qS type	791	587	785
A_e (MHz) ^c	5537.0704	5537.0897	5537.0707
B_e (MHz) ^c	3251.860	3242.704	3233.574
C_e (MHz) ^c	2048.6810	2045.1152	2041.4317
Exp. Δ_e ($\text{u}\text{\AA}^2$)	+0.0009	-0.0075	-0.0020

^aNumbers in parenthesis are 1 standard deviation of least-squares fit in units of least significant figure.

^bValues of the centrifugal distortion constants were determined using fixed ratios to the $^{12}\text{C}_2\text{F}_4$ constants, with the ratios derived from MP2/TZV+(3df) calculations.

^cSemi-experimental r_e constants, with $1/2 \Sigma \alpha$ corrections derived from anharmonic MP2/cc-pVTZ calculations, and electronic corrections for one pair of π electrons assumed to be $\Delta I_a = 0.0028$, $\Delta I_b = 0.0025$, $\Delta I_c = 0.0002 \text{ u}\text{\AA}^2$ by comparison with formaldehyde following the approach of Oka and Morino.³³

TABLE V. Molecular geometries for C₂F₄ and other fluoroethylenes.

Geometry	r_{CC} (pm)	r_{CF} (pm)	α_{FCC} (°)	Ref.	C=C str. (cm ⁻¹)
Tetrafluoroethylene					
r_e^{SE}	132.36(37)	131.11(23)	123.29(16)	a	1874
r_s/r_0	131.34(39)	131.85(25)	123.57(16)	a	
Previous r_e^{SE} with fixed α_{FCC}	132.6(15)	131.5(5)	123.3(3)	b	
Electron diffraction ^c					
Limit 1	130.7	132.0	123.8		
r_g	131.1(7)	131.9(2)	123.76(15)		
Limit 2	132.2	131.7	123.5		
<i>Ab initio</i> structures					
CCSD(T)/TVP+(3df)	132.78	131.61	123.34	d	
MP2/cc-pVTZ	132.50	131.47	123.24	e	
MP2/cc-pVQZ	132.29	131.24	123.25	e	
MP2/cc-pV5Z	132.26	131.19	123.24	e	
MP2/cc-pV6Z	132.26	131.19	123.24	e	
MP2/TVP+(3df)	132.52	131.30	123.28	d	
Feller <i>et al.</i> ^f					
CCSD(T)(FC)/CBS(aVQ56)	132.42	131.29	123.31		
CCSD(T)-F12b/VDZ-F12	132.61	131.43	123.29		
CCSD(T)-F12b/VTZ-F12	132.44	131.32	123.30		
CCSD(T)-F12b/VQZ-F12	132.40	131.26	123.31		
“Composite method”	132.21	131.13	123.3		
Other fluoroethylenes					
(r_g) C ₂ H ₃ F	133.3(7)	134.8(4)		c	1654 ^g
(r_0) 1,1-C ₂ H ₂ F ₂	131.3(3)	132.5(2)		h	1729 ⁱ
(r_g/r_z) 1,1-C ₂ H ₂ F ₂	134.0(6)	131.5(3)		j	
(r_e^{SE}) 1,1-C ₂ H ₂ F ₂	131.75(4)	131.57(2)		k	
(r_s/r_0) <i>trans</i> -C ₂ H ₂ F ₂	131.8	135.1		l	1694 ^m
(r_e^{SE}) <i>trans</i> -C ₂ H ₂ F ₂	132.4(1)	133.9(1)		l	
(r_s) <i>cis</i> -C ₂ H ₂ F ₂	132.4	133.9		l	1715 ^m
(r_e^{SE}) <i>cis</i> -C ₂ H ₂ F ₂	132.3(1)	133.4(1)		l	
(r_g) C ₂ F ₃ H	130.9(6)			c	1788 ⁱ
(r_g) C ₂ F ₃ H	134.1(12)			n	
(r_e) C ₂ H ₄	133.05(10)			o	1623 ^m
(r_g) C ₂ Cl ₄	135.4(3)			p	
(r_g) C ₂ I ₄	136.3(15)			p	

^aUncertainty arises from the propagation of errors in the rotational constants shown in Table IV and includes Costain's error, without this the uncertainty is 0.2 pm.

^bA range of structures were presented by Robertson *et al.*,⁶ where the FCC angle was fixed to three plausible values (123.0°, 123.3°, and 123.6°) and the two bond distances were fitted to yield corresponding values for r_{CC} (134.00, 132.57, and 131.13 pm) and r_{CF} (131.00, 131.45, and 131.90 pm).

^cElectron diffraction structures of C₂F₄ from Carlos *et al.*,⁷ including the set of mutually compatible upper and lower bound limits for atom positions determined by 99% confidence intervals. The errors in parentheses for the r_g structure represent 1/2 the total change at the 99% confidence level.

^dPerformed in GAMESS.

^ePerformed in GAUSSIAN03.

^fReference 10.

^gReference 41.

^hReference 34.

ⁱReference 42.

^jReference 35.

^kReference 36.

^lReference 37.

^mReference 5.

ⁿReference 38.

^oReference 39.

^pReference 40.

Semi-experimental equilibrium rotational constants (Table IV) were determined by subtracting *ab initio* vibration-rotation corrections from MP2/cc-pVTZ anharmonic calculations, and the small electronic contributions. The inertial defects, $\Delta = I_c - I_a - I_b$, from the r_0 constants have non-zero, positive values of ca. +0.16 uÅ², suggesting a

greater contribution from in-plane vibrations than out-of-plane ones. The corrected r_e^{SE} inertial defects are close to zero, as expected for a planar equilibrium structure. A further indication that the r_e^{SE} constants are sensible is the comparable values of A_e obtained for each isotopologue; they should be the same given that the carbon atoms lie along the *a*-axis

in C_2F_4 . The r_e^{SE} constants were used to find the equilibrium coordinates of the substituted carbon atoms and hence the C=C bond distance. The C=C bond distance. The C-F bond distance and the bond angle were then fitted to the equilibrium rotational constants using Kisiel's fitting program STRFIT.⁴⁴ This structure, with $r_{\text{CC}} = 132.36 \pm 0.37$ pm, $r_{\text{CF}} = 131.11 \pm 0.23$ pm, and $\alpha_{\text{FCC}} = 123.26 \pm 0.16^\circ$, is shown in Table V as r_e^{SE} . Significantly, all three geometric parameters agree within experimental uncertainty with most *ab initio* calculations including the high level "composite" method which attempts to account for the small core/valence interaction effect on carbon-carbon bond distance (≈ 0.3 pm) as well as other deficiencies and performed very well with difluoroethylenes.⁹

Uncertainties in the structural parameters may be reduced by improving the rotational constants via microwave measurements of $^{12}\text{C}^{13}\text{CF}_4$ which is predicted to have a small permanent dipole moment. Rotationally resolved far IR or improved mid-IR measurements may also be able to provide an increased range of ground state combination differences. Improved equilibrium rotational constants may also necessitate the use of a higher level of theory (e.g., coupled-cluster singles and doubles plus perturbative triples (CCSD(T))) or larger basis sets for the calculation of the vibration-rotational constants.

E. Rovibrational analysis: Symmetric stretches

1. $^{13}\text{C}_2\text{F}_4$ ν_{11}

The *a*-type ν_{11} mode (B_{1u} symmetry) of the $^{12}\text{C}_2\text{F}_4$ isotopologue at 1187.6 cm^{-1} (Figure 4) was found to be essentially unperturbed,⁶ however, a simple fit of the assigned lines of ν_{11} of the $^{13}\text{C}_2\text{F}_4$ isotopologue (1160 cm^{-1}) show local perturbations centred around transitions with $K_c' = 47$. The pattern of the perturbation (see the residuals plots in Figure 5) suggests a Coriolis interaction with another vibrational state along either the *a*- or *b*-axis with its energy levels approaching from below ν_{11} and crossing over ν_{11} at $K_c' = 47$. Symmetry considerations restrict possible states to A_u or B_{2u} symmetry. The most likely candidate for this is the ($\nu_2 = 1; \nu_7 = 1$) level, which would give rise to a *c*-type IR combination band $\nu_2 (\text{A}_g, 769\text{ cm}^{-1}) + \nu_7 (\text{B}_{2u}, 393\text{ cm}^{-1})$, though with inten-

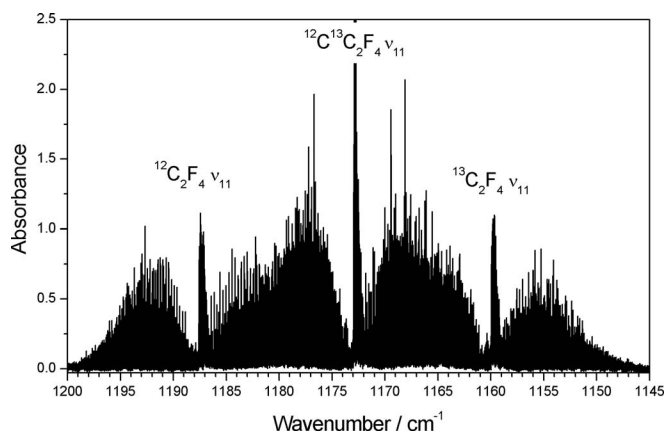


FIG. 4. *a*-type bands from the symmetric CF_2 stretch of C_2F_4 .

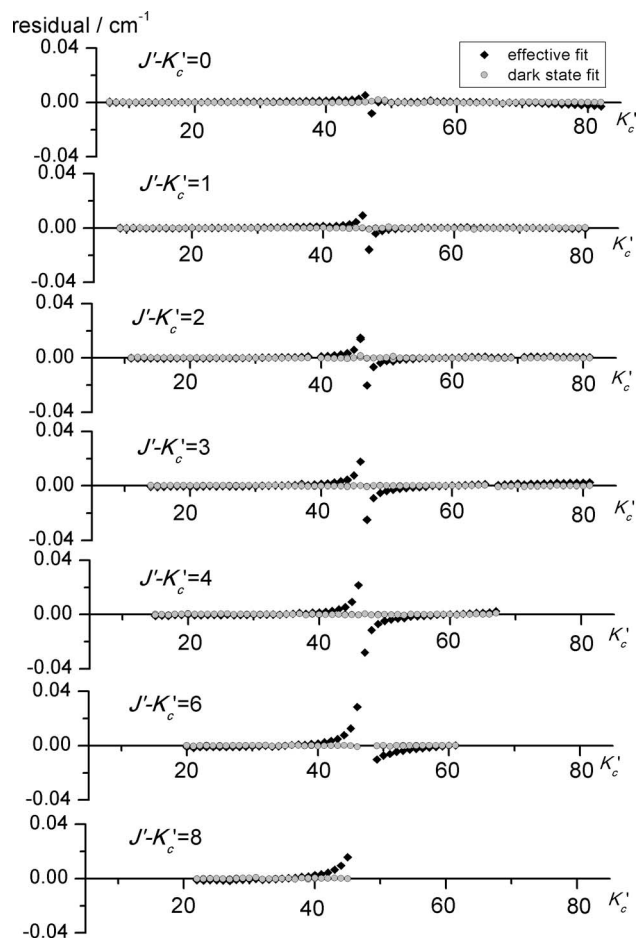


FIG. 5. Residuals (obs-calc) of the assigned transitions of the ν_{11} (symmetric CF_2 stretch) of $^{13}\text{C}_2\text{F}_4$. A single state effective fit is shown in black, while the fit with an interacting dark state is shown in gray.

sity very much weaker than the ν_{11} fundamental. By including this "dark" state with interaction via $\nu_{11} (J', K_c') \leftrightarrow \text{dark state} (J', K_c' + 1)$ a satisfactory fit is achieved with a rms error of 1.31 with a *b*-axis Coriolis coupling constant $Z^b = 106$ MHz, as detailed in Table VI.

2. $^{12}\text{C}^{13}\text{CF}_4$ ν_{11}

A simple two state fit of the ν_{11} symmetric stretch of $^{12}\text{C}^{13}\text{CF}_4$ reveals (in Figure S1 of the supplementary material⁴⁶) a similar pattern in the residuals to that seen in the analogous mode of $^{13}\text{C}_2\text{F}_4$ (ν_{11}) with a number of important differences. First, no avoided level crossing is observed for $J - K_a' = 0$ and the residuals are negative for values of J' below the level crossings and positive for those above it. This leads to the assumption that the interacting state approaches from above ν_{11} rather than below. Second, the value of K_c' for these crossings changed markedly for different values of $J - K_c'$ whereas the crossing occurred at consistent K_c' values in the $^{13}\text{C}_2\text{F}_4$ band. As a consequence, only three such crossings could be located with any certainty while seven such crossings were observed in the analogous band in the $^{13}\text{C}_2\text{F}_4$ molecule. While several dark state fits were trialed (see note accompanying Figure S1), these characteristics of the avoided crossings proved insurmountable hence the constants presented in

TABLE VI. Fitted spectroscopic constants for ν_{11} of $^{13}\text{C}_2\text{F}_4$ and $^{12}\text{C}^{13}\text{CF}_4$.

	$^{13}\text{C}_2\text{F}_4$ effective fit	$^{13}\text{C}_2\text{F}_4$ Dark state fit	$^{12}\text{C}^{13}\text{CF}_4$ effective fit
Parameter	ν_{11}	ν_{11}	ν_{11}
ν_0 (cm^{-1})	1159.963151(19) ^a	1159.963124(20)	1172.973352(21) ^a
A (MHz)	5500.467(77)	5498.684(81)	5498.619(55)
B (MHz)	3216.5199(220)	3216.7655(230)	3225.8971(151)
C (MHz)	2026.05752(58)	2026.09581(60)	2029.56173(81)
$(B+C)/2$ (MHz)
$(B-C)/4$ (MHz)
Δ_J (kHz)	0.436097(110)	0.439105(112)	0.443520(180)
Δ_{JK} (kHz)	-0.3574(48)	-0.6812(49)	-0.8446(58)
Δ_K (kHz)	1.2468(301)	2.1903(307)	4.458(32)
δ_J (kHz)	0.1727 ^c	0.1727 ^c	0.1744 ^c
δ_K (kHz)	0.5427 ^c	0.5427 ^c	0.5417 ^c
Exp. Δ ($\text{u } \text{\AA}^2$)	+0.4405(17)	+0.4180(18)	+0.4357(12)
Calc. Δ ($\text{u } \text{\AA}^2$)		+0.4216	+0.4277
Z^B (MHz)		106.35(24) ^d	...
RMS Error	20.6	1.31	9.74
Number of transitions		1658	1461
J max		84	77
Exp./Calc. α^A (MHz)		14.575/14.463	14.424/14.575
Exp./Calc. α^B (MHz)		3.358/3.122	3.096/3.358
Exp./Calc. α^C (MHz)		5.438/5.275	5.512/5.438

^aNumbers in parenthesis are 1 standard deviation of least-squares fit in units of least significant figure.

^bThese parameters could only be fitted as $(B+C)/2$ and $(B-C)/4$.

^cValue fixed to that of the ground state.

^d $\langle v_S | \hat{H} | v_x \rangle = i Z^B \hat{J}_B$.

^eFrom anharmonic MP2/cc-pVTZ calculations. The dark state values are for $\nu_2 + \nu_7$, obtained by adding the corresponding α values from each fundamental.

Note: The ground state constants were held to the values in Table IV in the fitting procedure.

Table VI are effective constants, fitted by excluding the transitions in the vicinity of the perturbation. An expanded section of the spectrum in the ν_{11} region, with simulations of the $^{12}\text{CF}_2$ $^{13}\text{CF}_2$ and $^{13}\text{C}_2\text{F}_4$ transitions is shown in Figure S2 of the supplementary material.⁴⁶

F. Antisymmetric stretches

Our isotopically enriched sample was observed to produce five overlapping b -type bands between 1300 cm^{-1} and 1340 cm^{-1} as shown in Figure 6. The interpretation of this region was aided by comparison of spectra, by ground state constants from rovibrational analysis and by computed vibrational properties as follows. The previous study of C_2F_4 in natural abundance established that only one of the

observed bands was from $^{12}\text{C}_2\text{F}_4$: the ν_9 mode at 1340 cm^{-1} . The monoisotopic species each have two antisymmetric CF_2 stretches at approximately equal wavenumber values, but only one is IR active in each case. These modes involve the concerted motion of both carbon atoms. The carbon atoms displace in the same direction in the IR active mode (ν_9 , B_{3u}) and in opposite directions in the Raman active mode (ν_5 , B_{2g}), see Figure 1. The ν_9 band of $^{13}\text{C}_2\text{F}_4$ at $\approx 1305 \text{ cm}^{-1}$ was readily identified by its complete absence from natural abundance spectra measured at high pressure, and the isotopic form confirmed by analysis of the rotational constants as described below.

Due to the different masses of the displaced atoms in $^{12}\text{C}^{13}\text{CF}_4$ the antisymmetric CF_2 motions in the two halves of the molecule are decoupled and mainly one carbon atom or

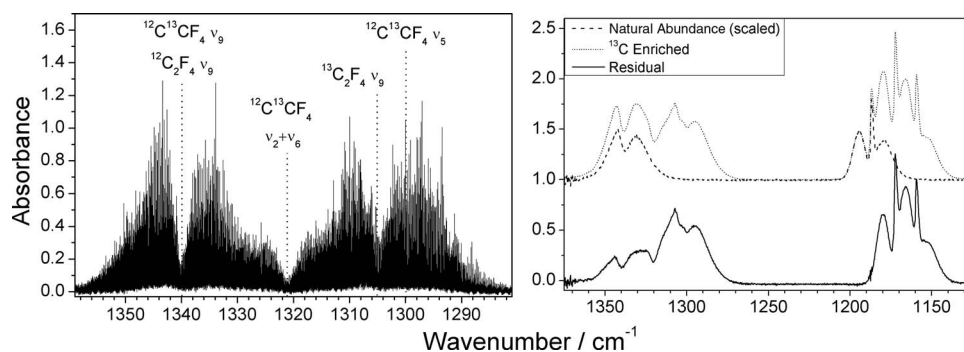


FIG. 6. (Right panel) A spectrum of C_2F_4 in natural abundance, scaled using the ν_{11} band of the $^{12}\text{C}_2\text{F}_4$ formed at 1188 cm^{-1} , is subtracted from a spectrum of the isotopically enriched sample. The residual spectrum reveals an additional b -type band centered at 1340 cm^{-1} . (Left panel) Antisymmetric C-F stretching region of ^{13}C enriched C_2F_4 at 150 K measured at high resolution.

the other moves in the two strongly IR active modes with B_1 symmetry that result. However, experimental spectra of the enriched sample show three additional b -type bands of comparable intensity, rather than two. One band near 1340 cm^{-1} was revealed when a scaled spectrum of a sample with natural abundance was subtracted from the spectrum of the isotopically enriched sample (see Figure 6). A band at 1300 cm^{-1} is clearly evident as a trace feature in natural abundance spectra indicating that it is not due to $^{13}\text{C}_2\text{F}_4$ and the rotational analysis described below confirms that this band, along with another centred at 1321 cm^{-1} share a common set of ground state rotational constants consistent with the $^{12}\text{C}^{13}\text{CF}_4$ isotopologue. According to a wide range of harmonic and anharmonic *ab initio* calculations (see Sec. III B), the two antisymmetric CF_2 stretch fundamentals of $^{12}\text{C}^{13}\text{CF}_4$ will be $40\text{--}50\text{ cm}^{-1}$ apart, with the higher wavenumber ν_9 vibration predicted to be close to the ν_9 band of $^{12}\text{C}_2\text{F}_4$. The positions of the highest (1340 cm^{-1}) and lowest (1300 cm^{-1}) wavenumber bands are thus broadly consistent with the expected isotopic shifts for the ν_9 and ν_5 modes, respectively. The middle band (at 1321 cm^{-1}) is attributed to a combination band from $\nu_2+\nu_6$. This mixed vibrational state is expected to occur at the right energy ($773.5 + 548.8 = 1322.3\text{ cm}^{-1}$) and has the required B_1 symmetry to interact via Fermi resonance with ν_5 and ν_9 . Anharmonic calculations (MP2/cc-pVDZ, performed using GAUSSIAN03²⁴) indicate that a significant Fermi resonance does occur between the ν_5 and the $\nu_2+\nu_6$ states of $^{12}\text{C}^{13}\text{CF}_4$, with an off-diagonal interaction term of magnitude 9.0 cm^{-1} . A similar interaction must be inferred between ν_9 and $\nu_2+\nu_6$, given the comparable nature and symmetry of ν_5 and ν_9 in $^{12}\text{C}^{13}\text{CF}_4$. Fermi resonance of this magnitude results in significantly mixed vibrational wavefunctions, enhancing the

intensity of the combination band, but leaving its central position relatively unchanged, while shifting the fundamentals by ca. $4\text{--}5\text{ cm}^{-1}$ away from their “unperturbed” energy levels.

In the monoisotopic species, the B_{3u} state ν_9 is uncoupled, but the MP2/cc-pVDZ anharmonic calculations predict a 14.5 cm^{-1} Fermi resonance term between the IR inactive B_{2g} states ν_5 and $\nu_2+\nu_6$ of $^{13}\text{C}_2\text{F}_4$, and 15.1 cm^{-1} for the corresponding term in $^{12}\text{C}_2\text{F}_4$. In $^{12}\text{C}_2\text{F}_4$, this pushes the ν_5 level higher, and the $\nu_2+\nu_6$ level lower. Comparison of various combinations and hot bands involving $\nu_2+\nu_6+\nu_x$ states suggest an anomalously large anharmonic constant, $x_{26} \approx -10\text{ cm}^{-1}$, consistent with this model. In $^{13}\text{C}_2\text{F}_4$, the energy ordering of the ν_5 and $\nu_2+\nu_6$ states is reversed so ν_5 is depressed and $\nu_2+\nu_6$ elevated by the interaction. This Fermi resonance model explains why the observed shift in ν_5 between $^{12}\text{C}_2\text{F}_4$ and $^{13}\text{C}_2\text{F}_4$ of -52 cm^{-1} is greater than the computed harmonic shifts which are consistently ca. -43 cm^{-1} . The calculated anharmonic shifts vary (e.g., -65 cm^{-1} for MP2/cc-pVTZ, -57 cm^{-1} for MP2/cc-pVDZ), being sensitive to the computed relative energies of the interacting ν_5 and $\nu_2+\nu_6$ levels.

1. $^{12}\text{C}^{13}\text{CF}_4$ ν_5 and $\nu_2+\nu_6$

The rovibrational assignment of $\nu_2+\nu_6$ (1321 cm^{-1}) was relatively straightforward as the band centre is in an uncongested region. A total of 1366 transitions were assigned, 924 of which belonged to series of equal $J'-K'_a$ and 442 from series with constant $J'-K'_c$. These rovibrational transitions were fitted to the rotational constants and the quartic centrifugal distortion constants shown in Table VII with a RMS error of 1.16. An expanded section of the spectrum showing $\nu_2+\nu_6$

TABLE VII. Effective rotational and centrifugal distortion constants for the b -type antisymmetric CF_2 stretching modes of $^{12}\text{C}^{13}\text{CF}_4$.

Parameter	$^{12}\text{C}^{13}\text{CF}_4$ $\nu_2+\nu_6$	$^{12}\text{C}^{13}\text{CF}_4$ ν_5	$^{13}\text{C}_2\text{F}_4$ ν_9
ν_0 (cm^{-1})	1321.068199(17) ^a	1300.050213(37)	1304.952414(31) ^b
A (MHz)	5513.6635(38)	5504.9526(60)	5503.94665(302)
B (MHz)	3225.5336(46)	3222.6190(72)	3209.8543(46)
C (MHz)	2035.34313(71)	2031.33256(299)	2027.33414(117)
Δ_J (kHz)	0.39100(288)	0.44199(160)	-0.437315(295)
Δ_{JK} (kHz)	-0.4541(114)	-0.5387(126)	-2.5001(46)
Δ_K (kHz)	2.0131(98)	2.0587(147)	3.7346(52)
δ_J (kHz)	0.13638(145)	0.1744 ^b	0.1727 ^b
δ_K (kHz)	0.4501(69)	0.5417 ^b	0.5427 ^b
Exp. Δ ($\text{u}\text{\AA}^2$)	-0.0385(2)	+0.1578(5)	+0.0162(3)
Calc Δ ($\text{u}\text{\AA}^2$)	+0.3084	+0.1386	-0.0039
RMS Error	1.16	2.51	6.85
Number of transitions	1366	754	933
J max	65	43	64
K_a max	31	33	41
K_c max	65	43	64
Exp./Calc. α^A (MHz)	-0.620/-11.683	8.090/10.470	9.312/9.410
Exp./Calc. α^B (MHz)	3.459/3.595	6.374/8.420	10.269/10.830
Exp./Calc. α^C (MHz)	-0.269/0.986	3.741/4.547	4.200/4.218

^aNumbers in parenthesis are 1 standard deviation of least-squares fit in units of least significant figure—value fixed to that of the ground state.

^bThese values are fixed to the ground state values.

Note: The ground state constants were held to the values in Table IV in the fitting procedure.

transitions and simulations is shown in Figure S3 of the supplementary material.

The ν_5 mode (1300 cm^{-1}) on the other hand was much more difficult to assign due to its band centre occurring at the same position as the most intense lines of the P-branch of ν_9 of $^{13}\text{C}_2\text{F}_4$ and a possible perturbation of levels with low K_a' ; only 754 lines could be assigned. When fitted with all quartic centrifugal distortion constants, the fit converged to non-physical values. By fixing δ_J and δ_K to the ground state values a fit with a RMS standard deviation of 2.51 was achieved. Small J dependent trends remain in the residuals of transitions with $K_a' < 6$ indicating that there may be a perturbation from an interacting state affecting the upper state levels. Possible dark states include ν_2 (773.5 cm^{-1}) + ν_{12} (553.6 cm^{-1}) which would interact via b -axis Coriolis resonance or states such as $2\nu_3$ (395.1 cm^{-1}) + ν_8 (501.4 cm^{-1}) or $2\nu_7$ (398.8 cm^{-1}) + ν_8 (501.4 cm^{-1}) with the right symmetry for a -axis Coriolis resonance. However, there is not enough information about the interacting state to allow either to be included in the fit and therefore the constants shown in Table VII are effective constants, predicting the line positions included in the fit to within 0.002 cm^{-1} .

The ν_9 band of $^{12}\text{C}^{13}\text{CF}_4$ lies underneath the stronger $^{12}\text{C}_2\text{F}_4$ ν_9 band at 1340 cm^{-1} . A number of rovibrational transitions not associated with $^{12}\text{C}_2\text{F}_4$ were observed in this vicinity, but no unambiguous assignment was possible.

2. $^{13}\text{C}_2\text{F}_4$ ν_9

The antisymmetric stretch of the $^{13}\text{C}_2\text{F}_4$ isotopologue (ν_9 , 1305 cm^{-1}) also proved to be challenging to assign and to fit. The two overlapping bands of $^{12}\text{C}^{13}\text{CF}_4$ resulted in a congested spectrum where assignment was difficult. When the spectrum was displayed vertically in MACLOOMIS,⁴⁵ a Loomis-Wood spectral analysis program, considerable overlap was observed between adjacent series of transitions, both those with constant $J - K_a'$ and those with constant $J' - K_c'$. This limited the number of transitions that could be firmly assigned to 933. Furthermore, avoided crossings were detected for both types of series suggesting a dark state originating below ν_9 that interacts via Coriolis resonance along the b -axis. However, no fit that included such a state successfully converged with meaningful rotational constants. Table VII shows an effective fit that predicts line positions in the quantum number range given to within 0.005 cm^{-1} . Residual plots that show the avoided crossings (and details of the possible dark states) are given in Figure S4 of the supplementary material.⁴⁶ The values of the centrifugal distortion constants, particularly Δ_{JK} and the large RMS error of the fit (6.85) clearly show that this fit isn't representing the system physically however it may still be useful in predicting line positions. The α values are consistent with those from the corresponding $^{12}\text{C}_2\text{F}_4$ band, and in excellent agreement with the calculated set. In general, the anharmonic MP2/cc-pVTZ alpha values for the fundamentals in Tables VI and VII closely match experiment and support the assignments. For the combination levels, the α_A values happen to be poorly predicted, probably because of a -axis Coriolis interactions that are not properly accounted for

by the approximation of adding alphas from the constituent fundamentals.

Additional figures, a full table of all observed combination modes, details of ground and excited state fits of rovibrational transitions from SPFIT, the fitted geometry from STRFIT, and vibration-rotation data from VIBCA are supplied as the supplementary material.⁴⁶

IV. DISCUSSION AND CONCLUSIONS

High resolution FTIR spectra of carbon-13 enriched C_2F_4 were used to determine ground vibrational state rotational constants for $^{12}\text{C}^{13}\text{CF}_4$ and $^{13}\text{C}_2\text{F}_4$ for the first time. These were used, along with rotational constants for $^{12}\text{C}_2\text{F}_4$ to determine a r_s/r_0 substitution structure very much in line with the previous r_g electron diffraction structure. Removing the effect of nuclear motion, anharmonic vibration rotation parameters were used to compute semi-experimental r_e^{SE} rotational constants and thus evaluate the equilibrium C=C bond distance to be $132.36 \pm 0.37\text{ pm}$ via Kraitchman's substitution equations. This bond distance allowed the remaining two equilibrium structural parameters to be determined. Table V shows a comparison with available structures for related halo-substituted ethenes. Some caution is required when comparing different types of structures, and in particular the r_g parameters are not always consistent with spectroscopic ones (e.g., 1,1- $\text{C}_2\text{H}_2\text{F}_2$) or indeed with other electron diffraction determinations (e.g., $\text{C}_2\text{H}_3\text{F}$). Nevertheless, the data points to the C=C bond distance of ethene decreasing slightly with fluorine substitution. It is interesting that C_2F_4 and both isomers of 1,2- $\text{C}_2\text{H}_2\text{F}_2$ have essentially the same C=C equilibrium bond distance while 1,1- $\text{C}_2\text{H}_2\text{F}_2$ has a significantly shorter bond distance. In contrast, substitution with other halogens results in a slight increase in the C=C bond distance. The differences in C-F equilibrium bond distance are more pronounced, decreasing from 133.9 pm in *trans*- $\text{C}_2\text{H}_2\text{F}_2$ to 131.57 pm in 1,1- $\text{C}_2\text{H}_2\text{F}_2$ and 131.11 pm in C_2F_4 .

Table V also includes wavenumber values for C=C stretch vibrations of the substituted ethylenes. A clear trend is seen for large increases from 1623 cm^{-1} in C_2H_4 through to an exceptionally high 1874 cm^{-1} for C_2F_4 . It is a striking result that perfluoro substitution decreases the bond distance by less than 1.5% while the vibrational frequency increases by 15%. The large wavenumber shifts have been noted previously by Kurbakova *et al.*⁴⁷ and attributed to increasing localisation of the C=C coordinate in the normal mode, from just 53% of the potential energy in ethylene to 80% in C_2F_4 (or 73% according to our MP2/TVP+(3df) calculations). They also noted that these shifts could be exploited to identify and quantify mixtures of fluoroethylenes.

The upper state rotational and centrifugal distortion constants for ν_{11} of $^{13}\text{C}_2\text{F}_4$ and $\nu_2 + \nu_6$ of $^{12}\text{C}^{13}\text{CF}_4$ were determined along with effective constants for ν_{11} and ν_5 of $^{12}\text{C}^{13}\text{CF}_4$ and for ν_9 of $^{13}\text{C}_2\text{F}_4$. These bands in the CF stretch region dominate the IR spectrum of tetrafluoroethylene, having intensities far greater than any of the other fundamentals. Substitution of a single ^{13}C in $^{12}\text{C}^{13}\text{CF}_4$ leads to dramatic changes in the spectrum of the ν_5 and ν_9 antisymmetric CF stretch modes. The nuclear motions are reconstituted such that

both fundamentals are symmetry allowed rather than just ν_9 , and both of them have strong IR intensity. Furthermore, these fundamentals share their IR transition strength with a third, $\nu_2 + \nu_6$ combination level via strong Fermi resonance induced mixing. The ν_1 band may also have been observed in low-resolution spectra (with interference from another band) in the mixed isotopic species.

Also, the wavenumbers of the fundamentals extracted from the low-resolution IR spectra are improved over previous values, even where they were deduced from combination bands, because the necessary anharmonic corrections were able to be applied. A value was derived for the torsional vibration (ν_4), which is neither IR nor Raman active and was previously only estimated from thermodynamic data.⁴ A much better contour than previously reported⁴ was measured for the lowest-wavenumber IR active band (ν_{10}) and its band origin (confirmed by a combination band); whereas the band origin is near the minimum of this contour, a satellite maximum at 195 cm^{-1} might be due to a Coriolis resonance with ν_4 , transferring some intensity to this torsional vibration as suggested already in Ref. 4 and further supported by the high calculated coupling constant reported by Castro.⁴⁸

ACKNOWLEDGMENTS

This work was generously supported by the Australian Synchrotron through beam-time access and an Australian Synchrotron Postgraduate Award (C.M.). Financial support from the Australian Government through an Australian Postgraduate Award to C.M. is also gratefully acknowledged. The quantum chemical calculations performed in this work were supported by computational resources on the NCI Australia National Facility through the National Computational Merit Allocation Scheme.

- ¹G. Acerboni, J. A. Beukes, N. R. Jensen, J. Hjorth, G. Myhre, C. J. Nielsen, and J. K. Sundet, *Atmos. Environ.* **35**(24), 4113 (2001).
- ²P. Torkington and H. Thompson, *Trans. Faraday Soc.* **41**, 236 (1945).
- ³J. R. Nielsen, H. H. Claassen, and D. C. Smith, *J. Chem. Phys.* **18**(6), 812 (1950).
- ⁴D. Mann, N. Acquista, and E. K. Plyler, *J. Res. Natl. Bur. Stand.* **52**(2), 67 (1954).
- ⁵T. Shimanouchi, *J. Phys. Chem. Ref. Data* **6**(3), 993 (1977).
- ⁶E. G. Robertson, C. D. Thompson, D. Appadoo, and D. McNaughton, *Phys. Chem. Chem. Phys.* **4**(20), 4849 (2002).
- ⁷J. L. Carlos, R. R. Karl, and S. H. Bauer, *J. Chem. Soc., Faraday Trans. 2* **70**, 177 (1974).
- ⁸J. Kraitchman, *Am. J. Phys.* **21**(1), 17 (1953).
- ⁹D. Feller, N. C. Craig, P. Groner, and D. C. McKean, *J. Phys. Chem. A* **115**(1), 94 (2011).
- ¹⁰D. Feller, K. A. Peterson, and D. A. Dixon, *J. Phys. Chem. A* **115**(8), 1440 (2011).
- ¹¹S. Bauerecker, M. Taraschewski, C. Weitkamp, and H. K. Cammenga, *Rev. Sci. Instrum.* **72**(10), 3946 (2001).
- ¹²D. R. T. Appadoo, E. G. Robertson, and D. McNaughton, *J. Mol. Spectrosc.* **217**(1), 96 (2003).
- ¹³D. McNaughton, I. Aleksic, D. R. T. Appadoo, C. D. Thompson, and E. G. Robertson, *Vib. Spectrosc.* **36**(1), 123 (2004).

- ¹⁴C. D. Thompson, E. G. Robertson, and D. McNaughton, *Phys. Chem. Chem. Phys.* **5**(10), 1996 (2003); *Mol. Phys.* **102**(14-15), 1687 (2004); *Chem. Phys.* **279**(2-3), 239 (2002).
- ¹⁵C. D. Thompson, E. G. Robertson, C. J. Evans, and D. McNaughton, *J. Mol. Spectrosc.* **218**(1), 48 (2003).
- ¹⁶C. D. Thompson, E. G. Robertson, I. Aleksic, and D. McNaughton, *J. Mol. Spectrosc.* **230**(2), 133 (2005).
- ¹⁷M. K. Bane, E. G. Robertson, C. D. Thompson, D. R. T. Appadoo, and D. McNaughton, *J. Chem. Phys.* **135**(22), 224306 (2011).
- ¹⁸M. K. Bane, E. G. Robertson, C. D. Thompson, C. Medcraft, D. R. T. Appadoo, and D. McNaughton, *J. Chem. Phys.* **134**(23), 234306 (2011).
- ¹⁹M. K. Bane, C. D. Thompson, E. G. Robertson, D. R. T. Appadoo, and D. McNaughton, *Phys. Chem. Chem. Phys.* **13**(15), 6793 (2011).
- ²⁰C. Medcraft, C. D. Thompson, E. G. Robertson, D. R. T. Appadoo, and D. McNaughton, *ApJ* **753**(1), 18 (2012).
- ²¹W. Fuss, J. Göthel, M. Ivanenko, W. Schmid, P. Hering, K. Kompa, and K. Witte, *Isotopes Environ. Health Stud.* **30**(2-3), 199 (1994).
- ²²J. M. Flaud, W. J. Lafferty, R. Sams, and V. M. Devi, *J. Mol. Spectrosc.* **259**(1), 39 (2010).
- ²³R. Dennington, T. Keith, and J. Millam, GaussView, Version 5, Semichem Inc., Shawnee Mission, KS, 2009.
- ²⁴M. J. Frisch, G. W. Trucks, H. B. Schlegel *et al.*, GAUSSIAN03, Revision C.02, Gaussian, Inc., Wallingford, CT, 2004.
- ²⁵G. Herzberg, *Molecular Spectra and Molecular Structure, Vol. 2: Infrared and Raman Spectra of Polyatomic Molecules* (Van Nostrand Reinhold, New York, 1945).
- ²⁶M. W. Schmidt, K. K. Baldrige, J. A. Boatz, S. T. Elbert, M. S. Gordon, J. H. Jensen, S. Koseki, N. Matsunaga, K. A. Nguyen, and S. Su, *J. Comput. Chem.* **14**(11), 1347 (1993).
- ²⁷R. Krishnan, J. Binkley, R. Seeger, and J. A. Pople, *J. Chem. Phys.* **72**, 650 (1980).
- ²⁸T. H. Dunning, Jr., *J. Chem. Phys.* **90**, 1007 (1989).
- ²⁹A. Schäfer, H. Horn, and R. Ahlrichs, *J. Chem. Phys.* **97**, 2571 (1992).
- ³⁰P. W. Fowler and Z. Kisiel, VIBCA, Version 26.III.1999, Polish Academy of Sciences, Warsaw, see <http://www.ifpan.edu.pl/~kisiel/vibr/vibr.htm>.
- ³¹J. K. G. Watson, *Mol. Phys.* **15**(5), 479 (1968).
- ³²H. M. Pickett, *J. Mol. Spectrosc.* **148**(2), 371 (1991).
- ³³T. Oka and Y. Morino, *J. Mol. Spectrosc.* **11**, 349-367 (1963).
- ³⁴V. W. Laurie and D. T. Pence, *J. Chem. Phys.* **38**(11), 2693 (1963).
- ³⁵F. C. Mijlhoff, G. H. Renes, K. Kohata, K. Oyanagi, and K. Kuchitsu, *J. Mol. Struct.* **39**(2), 241 (1977).
- ³⁶D. C. McKean, M. M. Law, P. Groner, A. R. Conrad, M. J. Tubergen, D. Feller, M. C. Moore, and N. C. Craig, *J. Phys. Chem. A* **114**(34), 9309 (2010).
- ³⁷N. C. Craig, P. Groner, D. C. McKean, and M. J. Tubergen, *Int. J. Quantum Chem.* **95**(6), 837 (2003).
- ³⁸V. Mom, P. A. G. Huisman, F. C. Mijlhoff, and G. H. Renes, *J. Mol. Struct.* **62**, 95 (1980).
- ³⁹N. C. Craig, P. Groner, and D. C. McKean, *J. Phys. Chem. A* **110**(23), 7461 (2006).
- ⁴⁰T. G. Strand, *Acta Chem. Scand.* **21**(8), 2111 (1967).
- ⁴¹L. M. Sverdlov, M. A. Kovner, E. P. Krainov, *Vibrational Spectra of Polyatomic Molecules* (Wiley, New York, 1974).
- ⁴²H. Jiang, D. Appadoo, E. Robertson, and D. McNaughton, *J. Comput. Chem.* **23**(13), 1220 (2002).
- ⁴³C. C. Costain, *J. Chem. Phys.* **29**(4), 864 (1958).
- ⁴⁴Z. Kisiel, *J. Mol. Spectrosc.* **218**(1), 58 (2003).
- ⁴⁵D. McNaughton, D. McGilvery, and F. Shanks, *J. Mol. Spectrosc.* **149**(2), 458 (1991).
- ⁴⁶See supplementary material at <http://dx.doi.org/10.1063/1.4768417> for a list of observed combination modes, details of ground and excited state fits of rovibrational transitions from SPFIT, the fitted geometry from STRFIT, and vibration-rotation data from VIBCA.
- ⁴⁷A. P. Kurbakova, L. A. Leites, L. S. German, and M. A. Kurykin, *J. Fluorine Chem.* **77**(2), 169 (1996).
- ⁴⁸J. B. Castro and J. R. Anaconda, *J. Mol. Struct.: THEOCHEM* **304**(3), 273 (1994).

Declaration for Thesis Chapter 2.3

Declaration by candidate

In the case of Chapter 2.3 the nature and extent of my contribution to the work was the following:

Nature of contribution	Extent of contribution (%)
Initiation, key ideas, experimental, development and writing up	80%

The following co-authors contributed to the work. Co-authors who are students at Monash University must also indicate the extent of their contribution in percentage terms:

Name	Nature of contribution	Extent of contribution (%) for student co-authors only
C.D. Thompson	Experimental assistance, Initiation and key ideas	
E.G. Robertson	Initiation and key ideas	
D.R.T. Appadoo	Experimental assistance	
D. McNaughton	Initiation and key ideas	

Candidate's
Signature

	Date
--	------

Declaration by co-authors

The undersigned hereby certify that:

- (1) the above declaration correctly reflects the nature and extent of the candidate's contribution to this work, and the nature of the contribution of each of the co-authors.
- (2) they meet the criteria for authorship in that they have participated in the conception, execution, or interpretation, of at least that part of the publication in their field of expertise;
- (3) they take public responsibility for their part of the publication, except for the responsible author who accepts overall responsibility for the publication;
- (4) there are no other authors of the publication according to these criteria;
- (5) potential conflicts of interest have been disclosed to (a) granting bodies, (b) the editor or publisher of journals or other publications, and (c) the head of the responsible academic unit; and
- (6) the original data are stored at the following location(s) and will be held for at least five years from the date indicated below:

Location(s)

Monash University, School of Chemistry
--

[Please note that the location(s) must be institutional in nature, and should be indicated here as a department, centre or institute, with specific campus identification where relevant.]

Signature 1

Signature 2

Signature 3

Signature 4

	3-12-2012

THE FAR-INFRARED ROTATIONAL SPECTRUM OF ETHYLENE OXIDE

CHRIS MEDCRAFT¹, CHRISTOPHER D. THOMPSON¹, EVAN G. ROBERTSON², DOMINIQUE R. T. APPADOO³, AND DON MCNAUGHTON¹

¹ School of Chemistry, Monash University, Wellington Road, Clayton, Victoria 3800, Australia; donald.mcnaughton@monash.edu

² Department of Chemistry, La Trobe Institute of Molecular Sciences, La Trobe University, Bundoora, Victoria 3086, Australia

³ Australian Synchrotron, 800 Blackburn Road, Clayton, Victoria 3168, Australia

Received 2012 March 21; accepted 2012 April 20; published 2012 June 11

ABSTRACT

High-resolution FTIR spectra of ethylene oxide have been measured in the far-infrared region using synchrotron radiation. A total of 1182 lines between 15 and 73 cm⁻¹ were assigned, with $J_{\max} = 64$, expanding upon previous studies that had recorded spectra up to 12 cm⁻¹, $J_{\max} = 49$. All available data were co-fitted to provide greatly improved rotational constants for the ground vibrational state that are capable of predicting transitions up to 73 cm⁻¹.

Key words: Infrared: ISM – ISM: molecules – methods: laboratory – molecular data

Online-only material: color figure, machine-readable table

1. INTRODUCTION

Ethylene oxide or oxirane (*c*-C₂H₄O) is a widely used industrial chemical used in hospitals as a disinfectant and as an industrial reagent, primarily in the formation of ethylene glycols. Ethylene oxide is a cyclic isomer of ethenol (vinyl alcohol) and ethanal (acetaldehyde). The strained three-membered ring makes *c*-C₂H₄O higher in energy than the other two; however, it is kinetically stable in laboratory conditions. All three species have been detected in the interstellar medium (Turner & Apponi 2001; Matthews et al. 1985; Dickens et al. 1997) and knowledge of their relative abundances will provide information on reaction pathways. Rotational lines between 1 and 9 cm⁻¹ (34 and 262 GHz) have been used to detect ethylene oxide in Sgr B2N (Dickens et al. 1997). Subsequently, it was detected in a number of other “hot-core” sources (Nummelin et al. 1998) and in more varied environments (Ikeda et al. 2001) as well as in the “central molecular zone” (Requena-Torres et al. 2008). It is also a candidate as the carrier of some unidentified infrared bands (Bernstein & Lynch 2009). Although production mechanisms are not fully understood laboratory experiments conducted on graphite surfaces have shown that ethylene oxide is readily formed via the impact of oxygen atoms on ethene (Ward & Price 2011). Reaction barriers were found to be an order of magnitude lower than that for the gas-phase reaction whereby precursor molecules such as methanol are synthesized on grain surfaces and then enter the gas phase and react further (Millar et al. 1991; Blake et al. 1987).

Ground vibrational state rotational constants, first reported by Cunningham (1951), were improved upon by Hirose (1974) and Creswell & Schwendeman (1974) using lines up to 4.1 cm⁻¹ (123 GHz). These constants were further refined by Pan et al. (1998) in a millimeter wave study including lines up to 12 cm⁻¹ (368 GHz). Vibrationally excited state parameters for ν_3 were first reported by Russell & Wesendrup (2003), and these were improved upon by Flaud et al. (2012) who also reported constants for two Coriolis coupled systems (ν_2 , ν_{10}) and (ν_5 , ν_{12} , ν_{15}).

In this work, we use high-resolution far-infrared spectra to extend the range to 73 cm⁻¹ (2.2 THz). This was accomplished with the aid of a synchrotron source which we have used previously to measure the ground and vibrationally excited state parameters of another molecule of astrophysical interest, ketenimine (Bane et al. 2011a, 2011b, 2011c).

2. EXPERIMENTAL

The high-resolution FTIR spectra were measured at the far-infrared and high-resolution beamline of the Australian Synchrotron. The synchrotron provides a continuous source that is brighter than thermal sources offering a signal-to-noise advantage of 3–4 below 200 cm⁻¹. The synchrotron radiation beam enters a Bruker IFS125/HR spectrometer with a maximum resolution of 0.00096 cm⁻¹; with a 75 μ m beam splitter and a silicon bolometer (equipped with a 1 mm thick quartz cold filter over coated with Garnet powder). This provided an optical bandwidth of 15–120 cm⁻¹ (0.45–4 THz) with a gap around 43 cm⁻¹ due to the beamsplitter, as is apparent in Figure 1. The ethylene oxide sample (Sigma-Aldrich, >99.8%) was introduced into a multipass gas cell (path length of 8.8 m) without purification. Two sets of measurements were taken, one at higher pressure (178 co-added scans at 5.3 Pa) and one at lower pressure (226 scans at 1.3 Pa; Figure 1).

3. RESULTS AND DISCUSSION

Residual water lines were used to calibrate the spectrum to within 0.00006 cm⁻¹ (rms). A spectral analysis program, MacLoomis (McNaughton et al. 1991), was used to help assign the spectral lines by vertically stacking lines with the same K_a or K_c values. A total of 1182 lines were assigned between 15 and 73 cm⁻¹. Oxirane is an oblate asymmetric top ($\kappa = 0.41$) with C_{2v} symmetry, as the molecular dipole moment is along the *b*-axis (see Figure 2) all rotational transitions are *b*-type in character, i.e., $\Delta K_a = \pm 1$, $\Delta K_c = \pm 1$.

The assignment was aided by a simulation of the spectrum using the rotational constants in Pan et al. (1998). For low values of K_c (<25) these constants predict line positions to within the experimental uncertainty; however, as K_c becomes larger the simulation is increasingly poor as shown by the residuals in Figure 3 where values >0.04 cm⁻¹ (1.2 GHz) are encountered. The maximum residual observed was 4.0 cm⁻¹ (120 GHz) for the transition 64_{3,62}–63_{2,61} (not shown in Figure 3). These transitions are predicted much better by a fit found on the Cologne Database for Molecular Spectroscopy (Müller et al. 2001, 2005). This fit uses the lines from Pan’s study but changes the representation from III¹ to I¹. In this representation the fit converges with much fewer constants, only 14 were needed as opposed to the 25 used in Pan’s fit. This fit predicts the

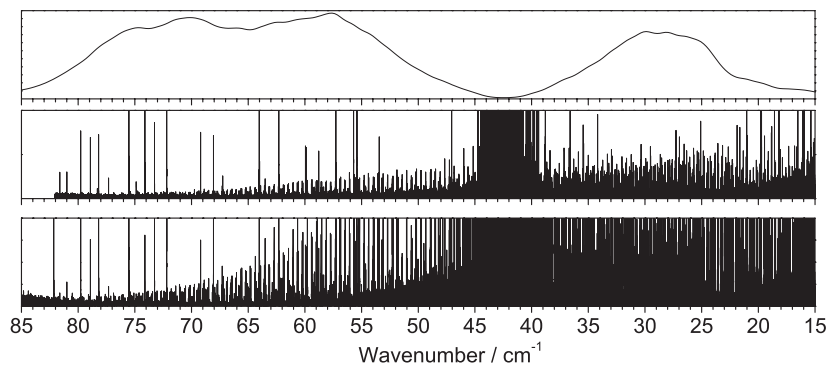


Figure 1. Far-infrared spectrum of ethylene oxide at 5.3 Pa (bottom), at 1.3 Pa (middle), and the background spectrum (top). Due to the 75 μm beamsplitter there is no optical throughput between 40 cm^{-1} and 45 cm^{-1} .

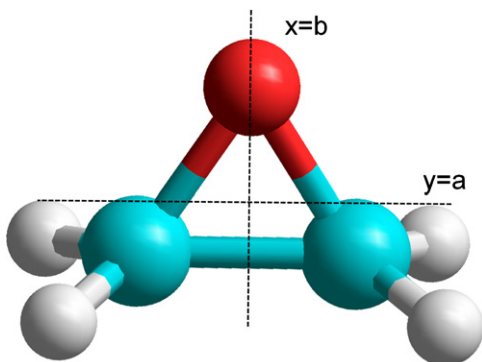


Figure 2. Ethylene oxide molecule with molecular axes labeled ($z = c$ is perpendicular to the page).

(A color version of this figure is available in the online journal.)

line positions of the far-IR transitions remarkably well; the maximum residual is 0.0015 cm^{-1} (44 MHz).

No vibrational satellite lines were observed because the lowest energy vibrational mode in this strained cyclic molecule is found at 808 cm^{-1} (Flaud et al. 2012). The measured lines, along with the previously assigned microwave and millimeter wave lines were fitted to a Watson A-reduced Hamiltonian using Pickett’s SPFIT least-squares fitting program (Pickett 1991) with the fitted constants shown in Table 1. Uncertainties of 0.05 MHz (Hirose 1974) and 0.01 MHz (Creswell & Schwendeman 1974) were used for the microwave lines, 0.15 MHz for the mil-

limeter wave lines (Pan et al. 1998) and 0.0002 cm^{-1} (6 MHz) for the far-IR/THz lines. The observed and calculated frequencies of these transitions are listed in Table 2.

Although the set of constants reported in Pan et al. (1998) are able to fit the observed mm-wave transitions, the extraneous constants needed to fit the data in the III¹ representation result in poor predictions of transitions outside of the range of the observed quantum numbers. The fit found on the CDMS Web site extrapolates much more accurately and only required one more constant (ϕ_J) in order to fit our far-IR data. This fit used a total set of 1848 transitions over a much wider range of quantum numbers than previous studies and provides accurate line positions from the microwave to the far infrared. Approximately half of the assigned lines belonged to series of transitions with constant K_a while the other half had constant K_c . The fitted centrifugal distortion constants in Table 1 are compared with those from an anharmonic vibrational frequency calculation using density function theory with the B3LYP function and the 6–31 + G(d) basis set (Frisch et al. 2009). The excellent agreement suggests that the fit has converged to physically realistic values.

A recent paper reported rotational and centrifugal distortion constants for a number of mid-IR vibrational levels from a high-resolution FTIR (0.0019 cm^{-1}) study (Flaud et al. 2012). We were able to use their reported line assignments to generate a set of 3503 ground state combination difference pseudo transitions. Our constants were able to predict the position of all of these pseudo transitions to within 0.003 cm^{-1} . However,

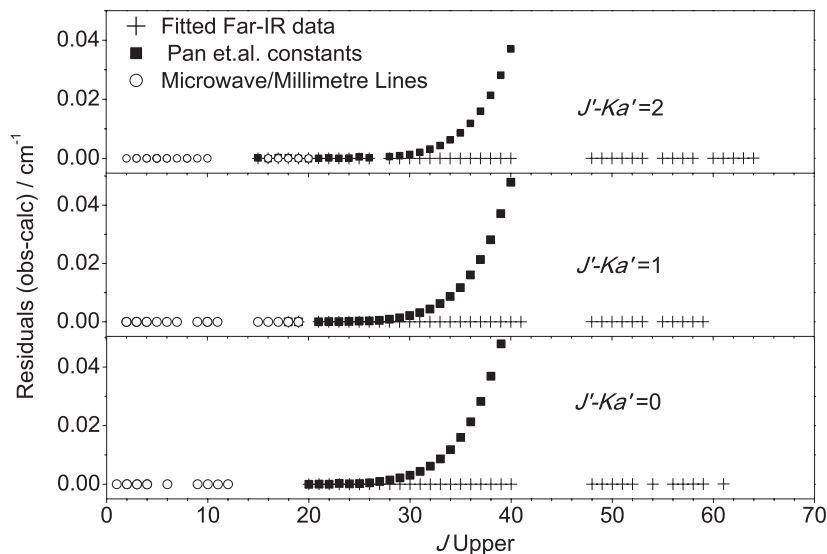


Figure 3. Residual (observed–calculated) vs. quantum number from the left-hand fit of Table 1, and from the constants of Pan et al. (1998).

Table 1
Spectroscopic Parameters for the Ground Vibrational State of Ethylene Oxide

Parameter	Fitted Value ^a		CDMS Fit ^b		B3LYP/6-31 + G(d)
<i>A</i> (MHz)	25483.86060	(96)	25483.86064	(108)	25314
<i>B</i> (MHz)	22120.87122	(88)	22120.87128	(101)	21795
<i>C</i> (MHz)	14097.82440	(55)	14097.82432	(63)	13929
ΔJ (kHz)	20.68572	(77)	20.68629	(117)	19.73
ΔJK (kHz)	20.91000	(216)	20.91427	(216)	19.65
ΔK (kHz)	27.59143	(275)	27.58826	(281)	27.81
δJ (kHz)	6.210757	(211)	6.211239	(299)	5.954
δK (kHz)	18.10778	(120)	18.10539	(122)	17.04
ΦJK (Hz)	0.61135	(302)	0.63010	(420)	0.3622
ΦKJ (Hz)	-2.5999	(68)	-2.6325	(108)	-1.984
ΦK (Hz)	2.2142	(50)	2.2308	(73)	1.847
ϕJK (Hz)	0.27716	(153)	0.26790	(213)	0.1887
ϕK (Hz)	-0.3297	(43)	-0.3187	(56)	-0.3354
ϕJ (mHz)	-1.324	(179)	-1.096
<i>IK</i> (mHz)	-0.01010	(243)	-0.01040	(245)	...
Number of transitions	1848		666		
<i>J</i> _{max}	64		49		
<i>K</i> _{a,max}	42		35		
<i>K</i> _{c,max}	62		21		
σ^c	0.826		1.039		

Notes.

^a Numbers in parentheses are one standard deviation according to the least-squares fit, in units of the last digit. *I*^f representation was used.

^b Details of this database can be found in Müller et al. (2001, 2005), the entry for this molecule can be found at <http://www.astro.uni-koeln.de/site/vorhersagen/catalog/archive/c-C2H4O/>.

^c Weighted standard deviation of the fit (dimensionless).

Table 2
Observed and Predicted Transition Frequencies of Ethylene Oxide in the Ground Vibrational State

<i>J'</i>	<i>K</i> _{a'}	<i>K</i> _{c'}	<i>J''</i>	<i>K</i> _{a''}	<i>K</i> _{c''}	Observed (cm ⁻¹)	Calculated (cm ⁻¹)	Obs-Calc (cm ⁻¹)
44	37	7	43	36	8	71.060031	71.060038	-0.000007
44	37	8	43	36	7	71.060031	71.060038	-0.000007
43	41	2	42	40	3	71.392322	71.392297	0.000026
43	41	3	42	40	2	71.392322	71.392297	0.000026
43	42	1	42	41	2	71.786231	71.786326	-0.000095
43	42	2	42	41	1	71.786231	71.786326	-0.000095
44	40	4	43	39	5	72.254536	72.254581	-0.000045
44	40	5	43	39	4	72.254536	72.254581	-0.000045
45	38	7	44	37	8	72.713712	72.713754	-0.000042
45	38	8	44	37	7	72.713712	72.713754	-0.000042

(This table is available in its entirety in a machine-readable form in the online journal. A portion is shown here for guidance regarding its form and content.)

these transitions were not included in our final fit mainly because they do not offer more information to the fit in terms of quantum number range. When included in the fit these pseudo transitions did not alter the constants significantly nor do they improve the uncertainties of them. The improved constants reported here provide essential information for future ro-vibrational studies of this molecule as well as an improved set of rotational constants for predicting interstellar transitions up to and beyond the measured range of frequencies.

The authors thank the Australian Government for financial support through an Australian Postgraduate Award (C.M.). The Australian Synchrotron is also acknowledged for beamtime access and financial support via an Australian Synchrotron Postgraduate Award (C.M.). Quantum chemistry calculations

were carried out using Australia's National Computational Infrastructure National Facility (NCI-NF).

REFERENCES

- Bane, M. K., Robertson, E. G., Thompson, C. D., Appadoo, D. R. T., & McNaughton, D. 2011a, *J. Chem. Phys.*, **135**, 224306
- Bane, M. K., Robertson, E. G., Thompson, C. D., et al. 2011b, *J. Chem. Phys.*, **134**, 234306
- Bane, M. K., Thompson, C. D., Robertson, E. G., Appadoo, D. R. T., & McNaughton, D. 2011c, *Phys. Chem. Chem. Phys.*, **13**, 6793
- Bernstein, L. S., & Lynch, D. K. 2009, *ApJ*, **704**, 226
- Blake, G. A., Sutton, E. C., Masson, C. R., & Phillips, T. G. 1987, *ApJ*, **315**, 621
- Creswell, R. A., & Schwendeman, R. H. 1974, *Chem. Phys. Lett.*, **27**, 521
- Cunningham, J. G. L., Boyd, A. W., Myers, R. J., Gwinn, W. D., & I. Le Van, W. 1951, *J. Chem. Phys.*, **19**, 676
- Dickens, J. E., Irvine, W. M., Ohishi, M., et al. 1997, *ApJ*, **489**, 753
- Flaud, J. M., Lafferty, W. J., Kwabia Tehana, F., Perrin, A., & Landsheere, X. 2012, *J. Mol. Spectrosc.*, **271**, 38
- Frisch, M. J., Trucks, G. W., Schlegel, H. B., et al. 2009, Gaussian 09, Revision A.1 (Wallingford, CT: Gaussian, Inc.)
- Hirose, C. 1974, *ApJ*, **189**, L145
- Ikeda, M., Ohishi, M., Nummelin, A., et al. 2001, *ApJ*, **560**, 792
- Matthews, H. E., Friberg, P., & Irvine, W. M. 1985, *ApJ*, **290**, 609
- McNaughton, D., McGilvery, D., & Shanks, F. 1991, *J. Mol. Spectrosc.*, **149**, 458
- Millar, T. J., Herbst, E., & Charnley, S. B. 1991, *ApJ*, **369**, 147
- Müller, H. S. P., Schlöder, F., Stutzki, J., & Winnewisser, G. 2005, *J. Mol. Struct.*, **742**, 215
- Müller, H. S. P., Thorwirth, S., Roth, D. A., & Winnewisser, G. 2001, *A&A*, **370**, L49
- Nummelin, A., Dickens, J. E., Bergman, P., et al. 1998, *A&A*, **337**, 275
- Pan, J., Albert, S., Sastry, K. V. L. N., Herbst, E., & Lucia, F. C. D. 1998, *ApJ*, **499**, 517
- Pickett, H. M. 1991, *J. Mol. Spectrosc.*, **148**, 371
- Requena-Torres, M. A., Martín-Pintado, J., Martín, S., & Morris, M. R. 2008, *ApJ*, **672**, 352
- Russell, D. K., & Wesendrup, R. 2003, *J. Mol. Spectrosc.*, **217**, 59
- Turner, B. E., & Apponi, A. J. 2001, *ApJ*, **561**, L207
- Ward, M. D., & Price, S. D. 2011, *ApJ*, **741**, 121

Declaration for Thesis Chapter 2.4

Declaration by candidate

In the case of Chapter 2.4 the nature and extent of my contribution to the work was the following:

Nature of contribution	Extent of contribution (%)
Experimental assistance	5%

The following co-authors contributed to the work. Co-authors who are students at Monash University must also indicate the extent of their contribution in percentage terms:

Name	Nature of contribution	Extent of contribution (%) for student co-authors only
M.K. Bane	Initiation, key idea, development, writing up	80%
C.D. Thompson	Initiation and key ideas	
E.G. Robertson	Initiation and key ideas	
D.R.T. Appadoo	Experimental assistance	
D. McNaughton	Initiation and key ideas	

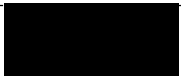
Candidate's Signature		Date
-----------------------	--	------

Declaration by co-authors

The undersigned hereby certify that:

- (1) the above declaration correctly reflects the nature and extent of the candidate's contribution to this work, and the nature of the contribution of each of the co-authors.
- (2) they meet the criteria for authorship in that they have participated in the conception, execution, or interpretation, of at least that part of the publication in their field of expertise;
- (3) they take public responsibility for their part of the publication, except for the responsible author who accepts overall responsibility for the publication;
- (4) there are no other authors of the publication according to these criteria;
- (5) potential conflicts of interest have been disclosed to (a) granting bodies, (b) the editor or publisher of journals or other publications, and (c) the head of the responsible academic unit; and
- (6) the original data are stored at the following location(s) and will be held for at least five years from the date indicated below:

Location(s) **Monash University, School of Chemistry**

Signature 1		3-12-2012
Signature 2		
Signature 3		3-12-2012
Signature 4		
Signature 5		

High-resolution Fourier-transform infrared spectroscopy of the Coriolis coupled ground state and ν_7 mode of ketenimine

Michael K. Bane,¹ Evan G. Robertson,² Christopher D. Thompson,¹ Chris Medcraft,¹ Dominique R. T. Appadoo,³ and Don McNaughton^{1,a)}

¹*School of Chemistry, Monash University, Wellington Rd., Clayton, Victoria 3800, Australia*

²*Department of Chemistry, La Trobe University, Bundoora, Victoria 3086, Australia*

³*Australian Synchrotron, 800 Blackburn Rd, Clayton, Victoria 3168, Australia*

(Received 3 April 2011; accepted 15 May 2011; published online 16 June 2011)

High resolution FTIR spectra of the short lived species ketenimine have been recorded in the regions 390–1300 cm^{-1} and 20–110 cm^{-1} using synchrotron radiation. Two thousand six hundred sixty transitions of the ν_7 band centered at 693 cm^{-1} and 126 far-IR rotational transitions have been assigned. Rotational and centrifugal distortion parameters for the ν_7 mode were determined and local Fermi and b -axis Coriolis interactions with $2\nu_{12}$ are treated. A further refinement of the ground state, ν_{12} and ν_8 parameters was also achieved, including the treatment of previously unrecognized ac -axis and ab -axis second order perturbations to the ground state. © 2011 American Institute of Physics. [doi:10.1063/1.3597775]

I. INTRODUCTION

The short lived molecule ketenimine (CH_2CNH , Fig. 1) was tentatively identified in a cold matrix by Jacox and Milligan¹ and its identity confirmed using low resolution matrix isolation vibrational and electronic spectroscopic techniques by Jacox.² In the gas phase, it was characterized first by microwave spectroscopy^{3,4} and subsequently by photoelectron spectroscopy.⁵ Since ketenimine is a structural isomer of acetonitrile, a known interstellar molecule, it was predicted to be a probable chemical component of the interstellar medium. In 2006, ketenimine was located by Lovas *et al.*⁶ in the star forming region Sagittarius B2(N) by observing microwave emissions predicted from rotational constants determined by the previous microwave study.⁴

The microwave assignment of Rodler *et al.*,³ was subsequently revised in a later rotation-inversion study by Rodler *et al.*⁴ and those rotational constants have recently been improved by incorporating combination differences from the ν_8 mode into the ground state (G.S.) least-squares fit.⁷ A small inversion splitting was observed in the microwave study of Rodler *et al.*,⁴ however, in this work we assume the symmetry of the molecule to be C_s since inversion splitting was not resolved, and therefore the normal modes have A' and A'' symmetry.

The low frequency modes of ketenimine and molecules of similar structure, such as ketene,⁸ thioketene,⁹ methyleneimine,¹⁰ formaldehyde,^{11,12} and thioformaldehyde,¹³ have been shown to exhibit a high degree of Coriolis coupling and consequently complex ro-vibrational structure. The strongly Coriolis coupled ν_{12} and ν_8 modes of ketenimine were analyzed in our previous high-resolution FTIR study,⁷ which uncovered an a -axis Coriolis interaction of sufficient strength that the rotational constants of the

very weak ν_{12} mode were determined purely by analyzing transitions with intensities enhanced via Coriolis intensity stealing. A table of all fundamental modes is available in Ref. 7. Perturbations were also located during the analysis of the ν_6 mode of ketenimine in a very recent high resolution (0.005 cm^{-1}) FTIR study by Ito *et al.*,¹⁴ however, due to the complexity of the ro-vibrational structure a satisfactory set of molecular constants for ν_6 could not be derived.

In this work, we present the assignment and analysis of the G.S. and ν_7 mode of ketenimine. Both are perturbed by resonances with the previously studied ν_{12} and ν_8 system of strongly Coriolis coupled modes, and/or their overtones and combination bands (which are also strongly coupled). In order to derive an improved set of ground state, $\nu_{12} = 1$ and $\nu_8 = 1$ rotational constants to adequately fit the new data, we have refitted the microwave data together with the observed pure rotational transitions in the far-IR and ground state combination differences (GSCD) from both this study and the previous high-resolution IR study.⁷

II. EXPERIMENTAL

The transient species ketenimine was generated by flow pyrolysis of 3-hydroxypropionitrile as described previously.⁷ Under the experimental conditions formaldehyde, hydrogen cyanide, carbon monoxide, and acetonitrile are also present in varying concentrations depending on the precise experimental conditions. Acetonitrile is present from the rapid tautomerization of ketenimine, a reaction studied theoretically by Doughty *et al.*¹⁵ whilst the other species are the side products of the pyrolysis. From the microwave studies the half-life of ketenimine in the cell was <1 s and our flow experiments are consistent with a similar half life. The optimum experimental conditions were found to be an oven temperature of ~ 1100 °C, to ensure the precursor was completely decomposed, whilst pumping the products through the multi-pass

^{a)} Author to whom correspondence should be addressed. Electronic mail: donald.mcnaughton@monash.edu.

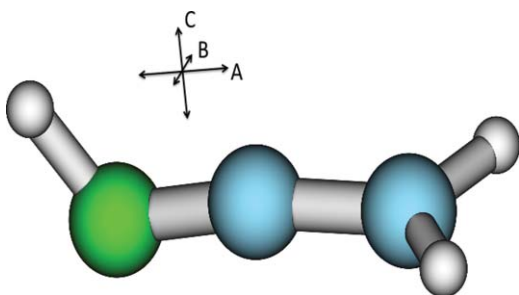


FIG. 1. Ketenimine molecule with axes labeled. Geometry optimized via B3LYP/cc-pVTZ calculations. Note: in the I' representation $z = a$, $x = b$, and $y = c$.

White cell at a rate high enough to ensure that the amount of the more stable acetonitrile conformation was minimized.

The experiments were performed at the Australian synchrotron, using the infrared synchrotron edge radiation continuum source and a Bruker IFS 125HR spectrometer capable of achieving a nominal resolution of 0.001 cm^{-1} . The spectrum was recorded in two separate spectral regions, between 770 and 390 cm^{-1} (region 1) which utilized the synchrotron source and between 1300 and 700 cm^{-1} (region 2) using an internal source. Both regions were recorded using a KBr beam-splitter. A silicon-boron bolometer equipped with a cold filter cutoff at 770 cm^{-1} was used for region 1 and a mercury cadmium telluride detector for region 2. For region 1 an aperture of 3.15 mm was used, which is wide enough for the already highly collimated synchrotron beam to pass through unimpeded, whereas for region 2, a 1.5 mm aperture was used. Both regions were scanned at a speed of 40 kHz . The pressure within the cell was maintained at $\sim 0.3 \text{ mbar}$, with optical path-lengths between 8 and 18 m and the temperature in the cell was assumed to be 300 K for simulations. Overall 58 and 19 spectra were recorded in regions 1 and 2, respectively, separately averaged then apodized using a 4P function and post-zero filled by a factor of 8 . Region 1 was recorded at the highest spectral resolution of the instrument, thus, requiring $\sim 12 \text{ h}$ of continuous flow pyrolysis to obtain the data. Region 2 was recorded at a spectral resolution of 0.002 cm^{-1} and required significantly less recording time.

The pure rotational structure was also recorded using the synchrotron source in the far-IR region between 20 and 110 cm^{-1} (region 3). The experimental conditions were identical to the recording of regions 1 and 2, however, the spectrometer was equipped with a $75 \mu\text{m}$ mylar beam-splitter and silicon bolometer. An aperture of 12.5 mm was used and spectra were scanned at a speed of 40 kHz . Overall 83 scans were recorded at the instrument's highest spectral resolution and averaged. This was then apodized using a 4P function and post-zero filled by a factor 8 to produce the final far-IR spectrum. All spectra were calibrated by comparison with water line positions from the HITRAN database.¹⁶

Density functional calculations were performed using GAMESS (Ref. 17) at the B3LYP/cc-pVTZ level of theory and were input into the harmonic force-field analysis program VIBCA (Ref. 18) as described in the previous study.⁷ The primary objective of the calculations was to determine the values for the derivatives of the component of the recipro-

cal moment of inertia tensor, α_i , which are a measure of the strength of Coriolis interactions between the G.S. and mode i . These calculations were also used to predict the G.S. rotational and quartic (D and d) centrifugal distortion parameters. GAUSSIAN (Ref. 19) DFT calculations at the same level of theory provided a prediction of the sextic (H) centrifugal distortion parameters.

Spectral simulation data are achieved by inputting the parameters obtained from the fits into Pickett's prediction software SPCAT.²⁰ The resulting calculated transitions were then convolved with a Gaussian line shape, with appropriate FWHM ($\sim 0.002 \text{ cm}^{-1}$) to produce a simulated spectrum.

III. RESULTS/DISCUSSION

The section of region 1 containing the ν_7 mode of ketenimine is shown in Fig. 2(a) ($\sim 83\%$ of the assigned transitions were picked from this region). The spectrum is contaminated with the ν_2 mode of HCN,²¹ an undesired by-product of the pyrolysis, centered about 712 cm^{-1} . Since HCN is a linear rotor with simple ro-vibrational structure, transitions attributed to this molecule introduced little complication to the analysis.

ν_7 , a CH_2 wag with A' symmetry has predominantly c -type character with selection rules $oe \leftrightarrow ee$ and $eo \leftrightarrow oo$

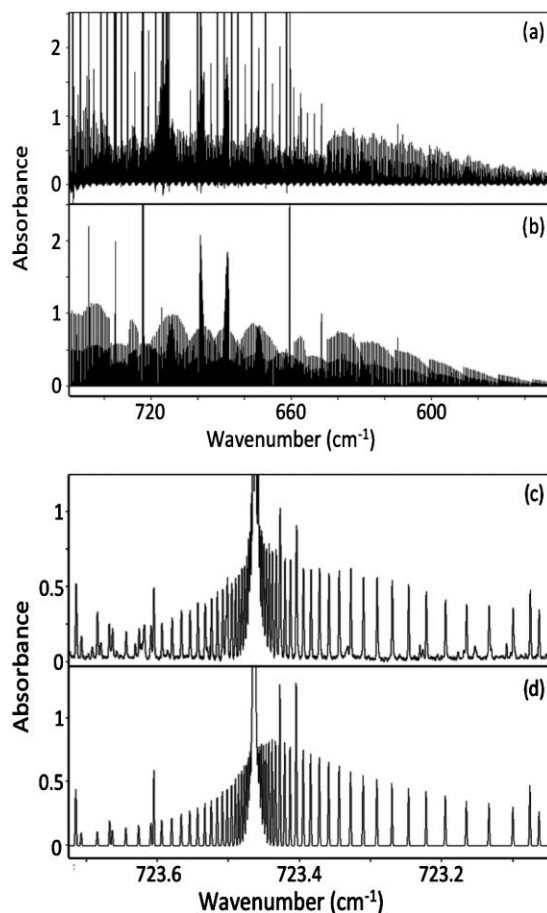


FIG. 2. (a) Experimental, survey spectrum of ν_7 (region 1) and (b) corresponding simulation. The expanded experimental (c) and simulated (d) sections illustrate the agreement between the two. (a) Intense transitions attributed to the ν_2 mode of HCN centered about 712 cm^{-1} which do not appear in the simulation. (c) Weak hot-band structure which does not appear in the simulation. Further additional lines are due to residual water.

($\Delta K_a = \pm 1, \pm 3, \dots$, $\Delta K_c = 0, \pm 2, \dots$). The ν_7 spectra were peak-picked and presented in the Loomis-Wood format using MacLoomis,²² which groups regularly spaced lines, such as those differing in J but sharing constant K_a , into approximately vertical series of constant K_a . Presenting the spectra in this way allowed series up to K_a (max) = 9 to be assigned quantum numbers, with J (max) = 52. Overall, 2660 ro-vibrational P , Q , and R branch transitions were assigned to this mode, and given an uncertainty of 0.0002 cm^{-1} (10% of the FWHM of the peak) in the fitting procedure. These assignments were confirmed by comparison of the experimentally determined ground state combination differences with those generated from the known ground state constants. The assigned transitions were least-squares fitted to Watson's S -reduced rotor Hamiltonian in the I' representation using Pickett's SPFIT.²⁰ The S -reduced Hamiltonian was used for consistency and comparison with the previous work. From the resultant high residual errors in this fit, it was apparent that the system contains perturbations.

A. Fit and treatment of perturbations to the G.S.

Prior to a successful fitting of the ν_7 mode, the G.S. parameters needed to be improved because the previous study incorporated GSCD up to K_a (GS) = 7 only, and the resultant constants were inaccurate for the range of K_a (GS) recorded in this study. The ν_7 mode contains GSCD up to K_a (GS) = 10, and a least squares fit to these, the observed transi-

tions from the microwave study⁴ and the GSCD from the ν_{12} and ν_8 modes from the previous IR study⁷ was performed. It was found that only combination differences involving states with K_a (GS) ≤ 8 could be accurately fitted with low residual error and it was apparent that the K_a (GS) = 9 and 10 states are perturbed. Consequently, it was necessary to fit the ground state together with the coupled low frequency modes to obtain a satisfactory fit. Although it is rare for the G.S. to be perturbed, the iso-electronic molecule thioketene has also been shown to exhibit this same property in a previous study by McNaughton *et al.*⁹

The DFT calculations determined that the most significant interactions between the G.S. and excited states were ac -axis and ab -axis second order Coriolis interactions with the lowest energy modes ν_{12} (409 cm^{-1}) and ν_8 (466 cm^{-1}), respectively. Parameters describing these interactions were introduced to the fit, and the microwave transitions,³ the GSCD from the ν_{12} , ν_8 , and ν_7 modes and the IR ro-vibrational transitions of ν_{12} and ν_8 were co-fitted (see below for weightings).

The resulting co-fit obtained improved G.S. parameters, which were used to simulate the μ_a and μ_c components of the pure rotational spectrum in an attempt to locate and assign transitions that occur in far-IR spectrum above 20 cm^{-1} . The dipole moments used in the simulation were $\mu_a = 0.434 \text{ D}$ and $\mu_c = 1.371 \text{ D}$ as determined by the microwave study.³ The experimental far-IR spectrum contained a large number of lines from other products of the pyrolysis, as well as regions of high noise. The simulation did, however, locate with high

TABLE I. Band parameters fitted to Watson's S -reduced I' Hamiltonian for the G.S., ν_8 , and ν_{12} system of coupled modes of ketenimine. Presented in the frequency units for consistency with previous work.

Constant	G.S. ^a	G.S. ^b	G.S. ^c	ν_{12}	ν_8
Band center (cm^{-1})				409.036624 (63) ^d	466.454164 (23)
A (MHz)	204523.235	201445.422 (30)	201445.279 (28)	195260. (160)	204290. (160)
B (MHz)	9744.0295	9663.14123 (93)	9663.1593 (10)	9697.170 (79)	9671.280 (12)
C (MHz)	9555.0030	9470.12039 (79)	9470.1547 (10)	9483.557 (85)	9492.265 (12)
D_J (kHz)	2.8260	2.98288 (70)	2.98672 (66)	3.0558 (17)	3.02893 (88)
D_{JK} (kHz)	235.76	232.178 (77)	130.52 (60)	56.3 (18)	508.8 (16)
D_K (kHz)	9866.	10126.3 (20)	10218.0 (11)	3290. (290)	21750. (290)
d_J (kHz)	-0.0586	-0.06870 (30)	-0.06785 (30)	-0.06785 ^e	-0.05088 (84)
H_{JK} (kHz)	0.00150	0.001043 (35)	0.000957 (31)	0.000957 ^e	0.000957 ^e
H_{KJ} (kHz)	1.714	-0.24223 (29)	...	-1.447 (19)	1.075 (31)
H_K (kHz)	3.0975	2.516 (28)	2.1782 (77)	...	2.1782 ^e
L_{KKJ} (kHz)	...	-0.000983 (37)	-0.00690 (20)
				η_{12}^{ac} (MHz) = 491.7 (49)	η_8^{ab} (MHz) = 705.0 (64)
				$G_{12,8}^a$ (MHz) = 306320. (450)	
				$G_{12,8}^{ak}$ (MHz) = -100.6 (33)	
				$F_{12,8}^{bc}$ (MHz) = 1.943 (47)	
J (max)		54	54	49	54
K_a (max)		8	10	7	7
Number trans.		5675 ^f	5761 ^f	666	1359
rms _{dev}		0.872		0.877	

^a A , B , C , D , and d parameters determined by B3LYP/cc-pVTZ GAMESS (Ref. 17) calculation and VIBCA (Ref. 18). H parameters determined by GAUSSIAN (Ref. 19) calculation at same level of theory.

^bEffective G.S. parameters for the fit to the unperturbed levels (up to K_a (GS) = 8).

^cG.S. fitted by combined treatment with ν_8 and ν_{12} .

^dFigures in parentheses are one standard deviation according to the least squares fit in units of the least significant figure quoted.

^eParameter forced during the fit to be equal to the G.S. value.

^fThe set of G.S. transitions includes 29 published microwave transitions, 126 far-IR rotational transitions and combination differences from the ν_8 , ν_{12} , and ν_7 bands. Note that η_{12}^{ac} has the same form as F_{12}^{ac} .

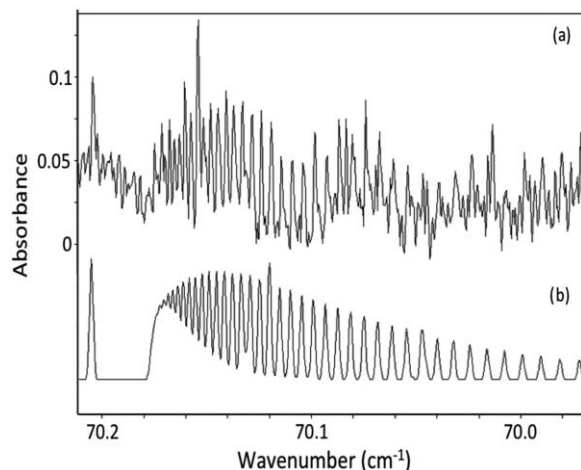


FIG. 3. (a) A section of the recorded far-IR spectrum containing the weak $K_a = 5-6$ Q -branch transitions and (b) simulation based on parameters presented in Table I. The simulation also contains an accurate prediction of the $20_{5,15} \leftarrow 19_{4,15}$ R -branch rotational transition, which is not explicitly fitted, centered about 70.204 cm^{-1} whilst extra transitions in the experimental spectrum attributed to impurities (probably water, ammonia, or methyl cyanide), which do not appear in the simulation.

accuracy some weak, μ_c -type rotational structure attributed to ketenimine, which corresponded to the strongest features of the simulation. Three Q -branch heads with $K_a^{\max}(\text{G.S.}) = 8$, which were not engulfed by noise or other structure, were assigned and included into the fit, with results shown in Table I. This fit is available in the supplementary material.²³ Figure 3 shows the excellent agreement between experiment and simulation for a section of the far-IR spectrum.

The final fit of the G.S. rotational structure of ketenimine included 29 rotational microwave transitions with varying but small uncertainties taken from the original microwave work,³ 126 Q -branch far-IR rotational transitions with an uncertainty of 0.0002 cm^{-1} , 2025 IR ro-vibrational transitions with an uncertainty 0.0002 cm^{-1} to the ν_{12} and ν_8 modes and 5761 IR GSCD from the ν_{12} , ν_8 , and ν_7 modes with an uncertainty of 0.00028 cm^{-1} and resulted in a fit with root mean square (rms) deviation = 0.877. It was found during fitting that one of the few b -type microwave transitions could not be fitted to acceptable accuracy and skewed the fit. This high J transition was “weighted out” by giving it an effectively infinite uncertainty of 999 MHz.

It can be seen from Table I that the fitted G.S. parameters are of comparable value to those of previous studies and to the theoretical predictions. The centrifugal distortion parameters d and the majority of the higher order H parameters for all the three states involved in this fit were constrained to be equal to each other, but allowed to vary during the fit. d_2 was calculated by DFT to be small relative to d_1 (calculated values are $d_1 = -0.0586 \text{ kHz}$ and $d_2 = -0.0016 \text{ kHz}$ for the G.S.), and was omitted from all modes since it did not significantly improve the fit and could not be determined with acceptable accuracy. During this analysis, the ν_{12} and ν_8 parameters were also improved, particularly, by the addition of an L_{KKJ} centrifugal distortion term to the parameters describing $\nu_8 = 1$. Addition of this term significantly improved the residual error of the fit to both the ν_{12} and ν_8

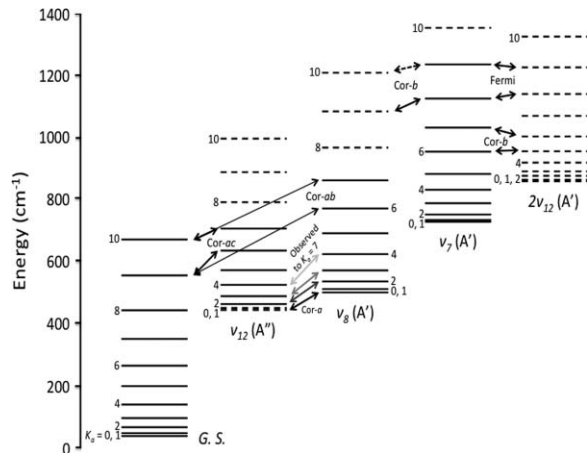


FIG. 4. Calculated energies of the $J = 10$ level for K_a up to 10 for the lowest energy modes of ketenimine. ν_7 and $2\nu_{12}$ energies calculated from parameters in Table II. G.S., ν_{12} , and ν_8 energies calculated from the parameters in Table I. Some symmetry allowed Coriolis interactions between states are indicated (note: observed $Cor-a$ interactions between ν_{12} and ν_8 continue to high K_a). Solid and dashed lines represent observed and predicted levels and interactions, respectively.

modes. Physically, the L_{KKJ} parameter is most likely “soaking up” very weak perturbations to the $\nu_8 = 1$ state not explicitly treated, such as the theoretically predicted (by GAMESS and VIBCA calculations) b -axis and c -axis interactions with $\nu_7 = 1$ and $\nu_{12} = 1$, respectively. The d_1 parameter associated with $\nu_8 = 1$ was allowed to vary freely since it greatly reduced error, particularly in the low K_a transitions, and did not deviate greatly from the expected value. The deviation from the G.S. values of the D_K and D_{JK} distortion parameters of the $\nu_{12} = 1$ and $\nu_8 = 1$ states is detailed in the previous study,⁷ however, the inclusion of L_{KKJ} substantially reduces the magnitude of this effect.

Local, second order perturbations with both modes of the ν_{12} , ν_8 strongly Coriolis coupled system were identified and treated. The fitted parameters, η_i , can be related to the calculated value of α_i by the equation in, for example, Watson.²⁴

$$\eta_i^{ab}(\text{cm}^{-1}) = -4\pi \sqrt{\frac{c}{h\omega_i}} A_i B_i q_i \alpha_i^{ab}, \quad (1)$$

where q_i is the normal co-ordinate of the mode i (Note Eq. (1) has been modified from that presented in Watson²⁴ and is presented in terms of rotational constants as opposed to rotational moments of inertia). Upon substitution of the fitted values and assuming $q_i = 1/2$ we obtain values of $\alpha_{12}^{ac} = 0.93 \text{ u}^{1/2} \text{ \AA}$ and $\alpha_8^{ab} = 1.43 \text{ u}^{1/2} \text{ \AA}$ which compares well to the theoretically calculated values of $\alpha_{12}^{ac} = 0.94 \text{ u}^{1/2} \text{ \AA}$ and $\alpha_8^{ab} = 1.31 \text{ u}^{1/2} \text{ \AA}$. The necessity to fit these second order Coriolis interaction terms explicitly arises from the high dependence of the spacing of K_a levels on A . As seen in Fig. 4, interacting $\nu_{12} = 1$ levels draw nearer with increasing K_a . Equivalent interactions, e.g., $\nu_i \leftrightarrow \nu_i + \nu_{12}$, will affect high K_a levels of every other vibrational level in ketenimine also. In addition an effective fit which does not include any of the perturbed states was performed with results also shown in Table I.

TABLE II. Band parameters fitted to Watson's S -reduced I' Hamiltonian for the system of coupled modes of ketenimine. Presented in frequency units for consistency with the previous work.

Constant	ν_7	$2\nu_{12}^a$	$\nu_{12} + \nu_8^a$	$2\nu_8^a$
Band center (cm^{-1})	692.850020 (23) ^b	823.306 (43)	875.49079	932.90833
A (MHz)	196799.844 (91)	200358. (22)	198103	207158
B (MHz)	9652.7647 (24)	9731.177	9705.288	9679.398
C (MHz)	9480.7345 (23)	9469.615	9505.668	9514.374
D_J (kHz)	2.99730 (52)	3.12400	3.09731	3.07059
D_{JK} (kHz)	208.78 (11)	17.65	434.5	886.8
D_K (kHz)	1454.8 (42)	3585	14818	33220
d_J (kHz)	-0.05799 (60)	-0.06786	-0.05010	-0.03234
H_{JK} (kHz)	0.000849 (30)	0.000922	0.000922	0.000922
H_{KJ} (kHz)	-0.1773 (45)
H_K (kHz)	1.161 (45)
L_{KKJ} (kHz)	-0.002060 (56)
$G_{7,12+12}^b$ (MHz)	640.1 (20)			
Fermi $_{7,12+12}$ (MHz)	13708 (56)			
		$G_{12+12,12+8}^a$ (MHz) = $G_{12+8,8+8}^a$ (MHz) = 434976 ^a		
$J(\text{max})$	52			
$K_a(\text{max})$	9			
Number trans.	2660			
rms $_{\text{dev}}$	0.718			

^a Band centers determined by Eq. (1) A, B, C, D, d , and H parameters determined by Eq. (2). Coriolis interaction parameters determined by Eq. (3). Calculation based on parameters from Table I.

^b Figures in parentheses are one standard deviation according to the least squares fit in units of the least significant figure quoted.

These parameters now more accurately describe the G.S. (as well as the ν_{12}, ν_8 system), and an accurate fit of ν_7 up to the recorded limit of K_a is now possible.

B. Fit and treatment of perturbations to $\nu_7 = 1$

The most probable candidate for an interaction with $\nu_7 = 1$ is $\nu_{12} = 2$ ($\sim 818 \text{ cm}^{-1}$) since it is the closest in energy and strong Coriolis interactions with the next state up ($\nu_8 + \nu_{12}$) result in a very small effective A rotational constant for $2\nu_{12}$ compared with that of $\nu_7 = 1$. Because no $2\nu_{12}$ transitions were observed, (ν_{12} itself has a very low predicted IR intensity of $0.008 \text{ D}^2 \text{ \AA}^{-2} \text{ amu}^{-1}$ and the overtone would be expected to be weaker still), this state must be introduced into the fit as a dark state, and we rely purely on theory to describe it since no experimental data is available. The band centers, ω , of the overtones and the combination bands were predicted using the harmonic approximation

$$\begin{aligned}\omega_{2\nu_8} &\approx 2\omega_{\nu_8} \\ \omega_{\nu_8+\nu_{12}} &\approx \omega_{\nu_8} + \omega_{\nu_{12}}.\end{aligned}\quad (2)$$

Calculations to determine anharmonic contributions to ω proved unreliable, and the harmonic approximation was considered sufficient. The rotational and centrifugal distortion parameters for overtones and combination bands can be calculated using the following approximation:

$$\begin{aligned}A_{2\nu_8} &\approx -A_{GS} + 2A_{\nu_8} \\ A_{\nu_8+\nu_{12}} &\approx -A_{GS} + A_{\nu_8} + A_{\nu_{12}}.\end{aligned}\quad (3)$$

$\nu_{12} = 2$ is itself strongly coupled directly to $\nu_{12} = 1 + \nu_8 = 1$ and indirectly to $\nu_8 = 2$. Equation (4) adapted from the theory presented in, for example, Nakagawa and

Morino¹¹ shows the parameter in the fit describing the a -axis Coriolis interaction, G_a , between these dark states can be approximated by

$$G_{2\nu_{12}, \nu_{12}+\nu_8}^a = G_{2\nu_8, \nu_{12}+\nu_8}^a = \sqrt{2}G_{\nu_8, \nu_{12}}^a. \quad (4)$$

As can be seen in Table I, the value of $G_a^{\nu_8, \nu_{12}}$ is large, and the interactions between the combination and overtone states cannot be ignored when attempting to describe these modes.

Equations (2)–(4) describe all of the parameters required to approximate the location of the energy levels of the three dark-states, from parameters presented in Table I. $2\nu_{12}$ has A' symmetry implying Fermi and b -axis Coriolis interactions with ν_7 are symmetry allowed, and the parameters describing these were introduced to the fit. With the introduction of the dark state system and the interactions between ν_7 and $2\nu_{12}$, along with the improved G.S. parameters, a satisfactory fit was achieved, with the resultant rotational parameters shown in Table II. All parameters describing the strongly Coriolis coupled dark-states system, except the band center and the A rotational parameter of $\nu_{12} = 2$, were constrained to their values calculated using Eqs. (2), (3), and (4) during the fit. This fit is also available in the supplementary material.²³

The ν_7 fit incorporated 2661 ro-vibrational transitions with an uncertainty of 0.0002 cm^{-1} and delivered a fit with rms $_{\text{dev}} = 0.748$. Again, d_2 was omitted since it did not significantly improve the fit and could not be determined with acceptable accuracy. The fitted band center of ν_7 (692.9 cm^{-1}) compares well to the value calculated by DFT calculations in previous work⁷ of 692.0 cm^{-1} . The band center and A rotational constants of $2\nu_{12}$ were allowed to vary since this greatly reduced the rms $_{\text{dev}}$ of the fit and the values obtained did not vary greatly from the predicted values. The band center and A of $2\nu_{12}$ were fitted to $\sim 1\%$ and 5% , respectively, of their

theoretical values. All other rotational, centrifugal distortion, and interaction parameters associated with the dark-states were constrained to their theoretical value (except the Coriolis interaction between ν_7 and $2\nu_{12}$). Although the dark state system treats the perturbations in ν_7 well, it is a theoretical model that contains small errors, and such small deviations from calculated values are expected.

For the same reasons as outlined previously, an L_{KKJ} term associated with $\nu_7 = 1$ was introduced, which significantly reduced the rms_{dev} of the fit. This term “soaked up” a very small but anomalous J -dependant deviation of the residual error at $K_a = 8$, which could be attributed to a very weak b -axis Coriolis resonance with $\nu_8 = 1$ (see Fig. 4).

Figure 4 gives an insight into the complex nature of the ro-vibrational structure of ketenimine. The symmetry of the ν_7 and $2\nu_{12}$ modes implies that both Fermi and b -axis Coriolis interactions are allowed between them. b -axis Coriolis interactions primarily occur between the states with $\Delta K_a = \pm 1$, and it can be seen that the $K_a = 6$ and 7 states of $\nu_7 = 1$ are very close in energy to the $K_a = 5$ and 6 states of $\nu_{12} = 2$. Similarly, Fermi interactions primarily occur between states with $\Delta K_a = 0$, and Fig. 4 shows that the $K_a = 8$ and 9 states of $\nu_7 = 1$ are very close in energy to the $K_a = 8$ and 9 states of $\nu_{12} = 2$. It is important to note that the states with $K_a = 6$ and 7 can be satisfactorily fitted by introducing only the b -axis Coriolis interaction, implying that both interactions are local and primarily perturb only the states outlined in Fig. 4.

IV. CONCLUSION

Ro-vibrational transitions within the Coriolis coupled ν_7 mode of ketenimine have been assigned and fitted to determine rotational, centrifugal distortion, and Coriolis interaction parameters. Local b -axis Coriolis and Fermi interactions have been treated between ν_7 and the $2\nu_{12}$ dark state. Introduction of the $\nu_8 + \nu_{12}$ and $2\nu_8$ dark-states proved necessary in the theoretical model describing $2\nu_{12}$. Second, the G.S. parameters have been improved by incorporating GSCD up to $K_a(\text{GS}) = 10$ in the G.S. fit. Ketenimine is one of the relatively few molecules where resonance perturbations are evident in the rotational levels of the ground vibrational state. Local perturbations at high $K_a(\text{GS})$, attributed to interactions with the ν_{12} , ν_8 system of strongly coupled modes, have been accounted for. The fitted values of α_{12}^{ac} and α_8^{ab} are in agreement with B3LYP/cc-pVTZ calculations. The parameters describing ν_{12} and ν_8 have also been refined during the G.S. analysis. It can be seen from Figs. 2 and 3 that there is a good agreement between the observed and simulated spectra.

ACKNOWLEDGMENTS

The authors would like to thank Dr. Danielle Martin of the Australian synchrotron for assistance in recording the spectra. This research was undertaken on the high resolution infrared beamline at the Australian Synchrotron, Victoria, Australia. M.B. is supported by a Monash science faculty Dean’s scholarship.

- ¹E. Jacox and D. E. Milligan, *J. Am. Chem. Soc.* **85**, 278 (1963).
- ²M. E. Jacox, *Chem. Phys.* **43**, 157 (1979).
- ³M. Rodler, R. D. Brown, P. D. Godfrey, and L. M. Tack, *Chem. Phys. Lett.* **110**, 447 (1984).
- ⁴M. Rodler, R. D. Brown, P. D. Godfrey, and B. Kleibömer, *J. Mol. Spectrosc.* **118**, 267 (1986).
- ⁵H. W. Kroto, G. Y. Matti, R. J. Suffolk, J. D. Watts, M. Rittby, and R. J. Bartlett, *J. Am. Chem. Soc.* **112**, 3779 (1990).
- ⁶F. J. Lovas, J. M. Hollis, A. J. Remijan, and P. R. Jewell, *Astrophys. J.* **645**, L137 (2006).
- ⁷M. K. Bane, C. D. Thompson, E. G. Robertson, D. R. T. Appadoo, and D. McNaughton, *Phys. Chem. Chem. Phys.* **13**, 6793 (2011).
- ⁸L. Nemes, D. Luckhaus, M. Quack, and J. W. C. Johns, *J. Mol. Struct.* **517–518**, 217 (2000).
- ⁹D. McNaughton, E. G. Robertson, and L. D. Hatherley, *J. Mol. Spectrosc.* **175**, 377 (1996).
- ¹⁰G. Duxbury and M. L. Le Lerre, *J. Mol. Spectrosc.* **92**, 326 (1982).
- ¹¹T. Nakagawa and Y. Morino, *J. Mol. Spectrosc.* **38**, 84 (1971).
- ¹²H. H. Blau and H. H. Nielsen, *J. Mol. Spectrosc.* **1**, 124 (1957).
- ¹³P. H. Turner, L. Halonen, and I. M. Mills, *J. Mol. Spectrosc.* **88**, 402 (1981).
- ¹⁴F. Ito and T. Nakanaga, *J. Mol. Spectrosc.* **264**, 100 (2010).
- ¹⁵A. Dougherty, G. B. Bacskay, and J. C. Mackie, *J. Phys. Chem.* **98**, 13546 (1994).
- ¹⁶L. S. Rothman, I. E. Gordon, A. Barbe, D. C. Benner, P. F. Bernath, M. Birk, V. Boudon, L. R. Brown, A. Campargue, J. P. Champion, K. Chance, L. H. Coudert, V. Dana, V. M. Devi, S. Fally, J. M. Flaud, R. R. Gamache, A. Goldman, D. Jacquemart, I. Kleiner, N. Lacome, W. J. Lafferty, J. Y. Mandin, S. T. Massie, S. N. Mikhailenko, C. E. Miller, N. Moazzen-Ahmadi, O. V. Naumenko, A. V. Nikitin, J. Orphal, V. I. Perevalov, A. Perrin, A. Predoi-Cross, C. P. Rinsland, M. Rotger, M. Simecková, M. A. H. Smith, K. Sung, S. A. Tashkun, J. Tennyson, R. A. Toth, A. C. Vandaele, and J. Vander Auwera, *J. Quant. Spectrosc. Radiat. Trans.* **110**, 533 (2009).
- ¹⁷M. W. Schmidt, K. K. Baldrige, J. A. Boatz, S. T. Elbert, M. S. Gordon, J. H. Jensen, S. Koseki, N. Matsunaga, K. A. Nguyen, S. Su, T. L. Windus, M. Dupuis, and J. A. Montgomery, Jr., *J. Comput. Chem.* **14**, 1347 (1993).
- ¹⁸See <http://info.ifpan.edu.pl/~kisiel/vibr/vibr.htm#vibca> for information on VIBCA and FCONV.
- ¹⁹M. J. Frisch, G. W. Trucks, H. B. Schlegel *et al.*, GAUSSIAN 09, Revision A.1, Gaussian, Inc., Wallingford, CT, 2009.
- ²⁰H. M. Pickett, *J. Mol. Spectrosc.* **148**, 371 (1991).
- ²¹V. K. Wang and J. Overend, *Spectrochim. Acta, Part A.* **29**, 687 (1973).
- ²²D. McNaughton, D. McGilvery, and F. Shanks, *J. Mol. Spectrosc.* **149**, 458 (1991).
- ²³See supplementary material at <http://dx.doi.org/10.1063/1.3597775> for transition lists and final least squares fits.
- ²⁴J. K. G. Watson, in *Vibrational Spectra and Structure*, edited by J. R. Durig (Elsevier, New York, 1977), Vol. 6.

CHAPTER 3.0

FTIR SPECTROSCOPY OF AEROSOLS

3.1.1 INTRODUCTION

The study of molecular ices is important to a number of disciplines. The majority of solid matter in the universe is contained in interstellar dust which is thought to be composed of carbonaceous or silicate cores that are often coated by more volatile components such as water or carbon dioxide. These particles can act as reaction sites, producing more complex molecules. The dust grains also play an important role in star formation as a significant route of radiative loss in collapsing clouds.

Similarly aerosol particles play significant roles in the absorptive and reflective behaviour of planetary atmospheres. On Earth the water particles that make up clouds can vary in size, shape and phase (liquid or solid) depending on the altitudes and latitudes at which they form. Other particles can also provide nucleation sites for ice crystals, instigating cloud formation. Other molecules can form clouds in the atmospheres of other planets, for example, CO₂ on Mars or ethane and other hydrocarbons on Titan.

The majority of literature on the infrared spectroscopy of molecular ices comes from transmission or reflection studies on thin films deposited on a substrate. These are often not comparable to natural ices as surface effects can be important for small particles and scattering for large particles. Neither of these effects can be accurately modelled through thin films. The ultimate aim of our work is to produce particles that are analogous to natural particles and use infrared spectroscopy to examine the absorption and scattering behaviour. This introduction presents a brief overview of the theory and unique problems associated with the absorption and scattering of light by particles, a more thorough description can be found in Bohren & Huffman[1] or in reviews by Reid [2] or Sigurbjörnsson.[3]

There are a number of experimental methods that can be employed to generate particles, including jet expansions[4], expansions of super critical fluids[5] and acoustic levitation[6]. In this work the cooling cell was used to collisionally cool samples by injecting the sample gas into a precooled bath gas of helium or nitrogen (figure 1). The sample gas is rapidly cooled by

collisions with the bath gas and becomes supersaturated, subsequently nucleating and forming particles. This is a comparable formation mechanism to work performed on diffusive trapping type cold cells such as those described by Barnes, Gough et al. [7], Ewing & Sheng[8], Dunder & Miller[9] and Fleyfel & Devlin [10].

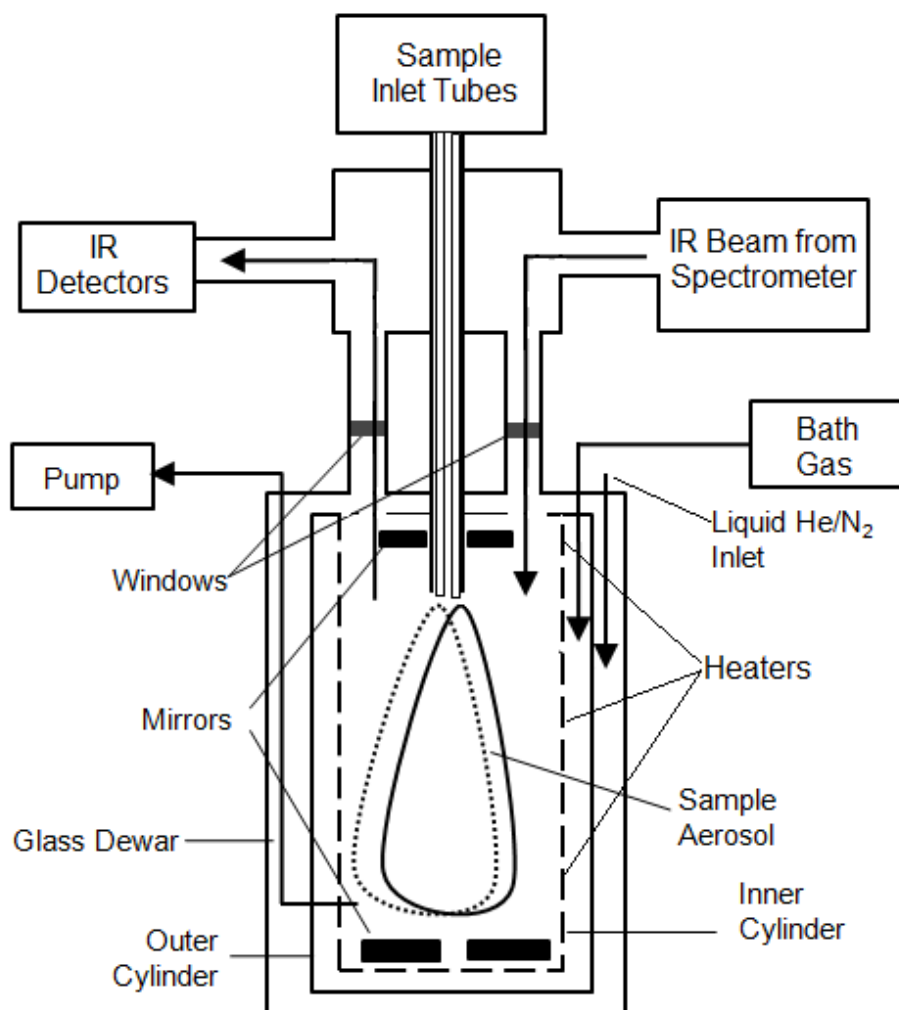


Figure 1: Experimental setup for aerosol studies

The cell used in this work was designed and built by Sigurd Bauerecker [11] and his research group as well as the group of Ruth Signorell use identical cooling cells to perform similar experiments. A summary of the current aerosol literature that used this cell design is presented in table 1. Notably different to our experiments, the group of Ruth Signorell have a setup that can produce particles outside of the cell via electrospray and independently size them before

injecting them into the cell.[12-13] This is useful in a number ways, firstly it allows for the study of less volatile compounds, such as carbohydrates[14-15]. Secondly it allows particles sizes to be controlled and measured independently of the cell temperatures.

The way in which particles nucleate and grow is an active field research and is different for every molecule. Some form liquid droplet which then become supercooled before freezing while others will form solid particles directly. An empirical relationship for determining if liquid phase may be produced in supersonic expansions was determined by Bartell et al. [16] and can be helpful for collisional cooling experiments:

$$R_c = \frac{(T_b - T_m)}{T_b} + 0.007 \left(\frac{\Delta S_m}{R} \right)^2$$

Where T_b and T_m are the boiling and melting points (in K) respectively,

ΔS_m is the change in entropy upon melting, and R is the gas constant.

If R_c is greater than 0.32 clusters are likely to be liquid, a solid will form if it is less than 0.32. Near 0.32 the phase that is formed may vary depending on other variables (e.g. temperature pressure, impurities). In the solid phase the long range order (crystal structure) can also vary depending on temperature and other formation conditions and can play an important role in the absorption spectrum.

Table 1: IR spectroscopic studies of aerosol using the Bauerecker designed Enclosive Flow Cooling Cell

Molecule	Comments	Ref
Instrument	Development and description of the EFC cell	[11, 17-18]
Review	Review of how particle properties (size, shape) can be inferred from absorption spectra	[3]
CO	Optical constants of CO generated directly from aerosol spectra	[19]
CO₂	Isotopic substitution used to determine molecular origin of absorption bands	[20]
CO₂ and H₂O/CO₂	Temporal evolution of pure CO ₂ and binary CO ₂ /H ₂ O nanoparticles	[21]
CO₂ and N₂O	Comparison of vibrational exciton calculations to experimental and DFT and MP2 calculations	[22]
¹²CO₂/¹³CO₂	Core/Shell structure of ¹² CO ₂ / ¹³ CO ₂ binary particles	[23]
¹²CO₂/¹³CO₂	Origin of band structure for 10-100 nm particles	[24]
SF₆ and SF₆/CO₂	Phase and shape behaviour of pure SF ₆ and binary SF ₆ /CO ₂ 50 nm particles	[25]
¹²CO₂/N₂O	Origin of band structure for 10-100 nm particles	[24]
NH₃, ¹²CO₂, ¹³CO₂	Calculation of refractive indices	[26]
CO₂	Temperature, size and pressure dependence	[27]
H₂O	Differential formation of water nanoparticles via Gas-Liquid-Solid and Gas-Solid transitions	[28]
H₂O	Review of the surface effects of nanosized water particles	[29]
H₂O	The effect of nitrogen absorption	[30]
H₂O	Far-IR spectra of nanosized particles. 4-200 K	[31]
H₂O	Mid-IR, size and temperature dependence	Chapter 3.3
O₃	Transition between gas phase and liquid droplets, HCl particles imbedded within O ₃ droplets	[32]
HCl	HCl particles imbedded within O ₃ droplets	[32]
N₂O	Temperature, size and pressure dependence	[27]
N₂O	Nanometre to micrometre sized particles	[33]
NH₃	Including binary NH ₃ /HCl particles	[34]
NH₃	Shape effects in pure particles and mixed NH ₃ /CO ₂ , NH ₃ /deuterated forms	[35]
NH₃	Size effects for 2-10 nm particles, crystalline and amorphous phases	[36]
SO₂	Pure particles and premixed with CO ₂ and NH ₃	[37]
CHF₃	Phase transition from liquid to crystalline	[38]
CHF₃	Investigation on the nucleation mechanism	[39]
C₂H₆	Gaseous methane prevents the freezing of ethane droplets	[40]
CH₄	Liquid/Solid phase behaviour of methane under conditions similar to Titan's atmosphere	[41]
CH₄	Phase transitions of methane particles, core and shell structure	[42]
C₂H₆	Influence of CH ₄ , C ₂ H ₂ and CO ₂ on ethane crystallisation	[43]
C₂H₆	Phase behaviour of ethane, temperature and time dependence	[44]
C₂H₂	Pure acetylene particles and binary particles of C ₂ H ₄ , C ₂ H ₆ & CO ₂	[45]
C₂H₄	Pure ethylene particles and binary particles of C ₂ H ₂ , C ₂ H ₆	[45]
C₂H₆	Pure ethane particles and binary particles of C ₂ H ₂ , C ₂ H ₄	[45]
C₂H₂	Pure acetylene particles in various crystal forms and particle shapes	[46]
C₂H₂/NH₃	Binary particles of C ₂ H ₂ and NH ₃	[47]
C₂H₆	Time dependence of liquid phase	[48]
C₂H₂/CO₂	Formation and decomposition of binary C ₂ H ₂ /CO ₂ particles	[49]
C₃H₈	Pure propane and mixed with C ₂ H ₂ , CO ₂ or H ₂ O	[50]
C₅H₁₀	Pure <i>n</i> -pentane and mixed with C ₂ H ₂ , CO ₂ or H ₂ O	[50]
Glycoaldehyde	Fermi resonance of C=O and C-C stretches reveals conformational information in small particles of pure glycoaldehyde	[15]
Dihydroxyacetone	Temperature dependence of conformational changes	[12]
Sucrose	Particles of different sizes were formed outside of the cell	[13]
Carbohydrates	A conformational change upon particle formation was monitored for pure particles of dihydroxyacetone, glyceraldehyde, fructose and glucose.	[14]

3.1.2 INFRARED ABSORPTION

Absorbance due to vibrational modes in condensed matter is quite distinct from the gas phase. Apart from the obvious fact that rotation is hindered in solids vibrational motion is greatly influenced by the intermolecular bonding. Some vibrational modes are only possible in the condensed phase, for example the librational and translational modes of water.

In highly ordered crystalline solids the infrared spectrum can be relatively simple with the vibrational modes coupling along the crystal lattice axes. However these vibrations can couple along different axis at different frequencies. A good example of this is the simple case of hydrogen chloride (see chapter 3.5) where the low temperature orthorhombic crystal phase has two strong absorptions where the displacement of atoms occurs in different directions. A more disordered form was also observed at higher temperatures whose spectrum had a single, broad absorption.

The coupling of vibrational modes can be described in terms of phonons (figure 2) which are the collective excitation of the periodically arranged particles. The phonons can be described as either acoustic or optical according to the direction of displacement of the atoms. In acoustic phonons the particles are displaced in the same direction as their neighbours while the direction of displacement alternates in optical phonons. The acoustic phonon is named as such since the displacement is similar to that of sound waves and the speed of sound in the lattice is the speed of propagation of the acoustic mode. The optical mode is so named due to it being excited in ionic crystals (such as KBr) by infrared photons. The direction of propagation of the phonon within the crystal is also a useful descriptor. Longitudinal modes propagate in the same direction as the displacement while transverse modes propagate at right angles to the displacement.

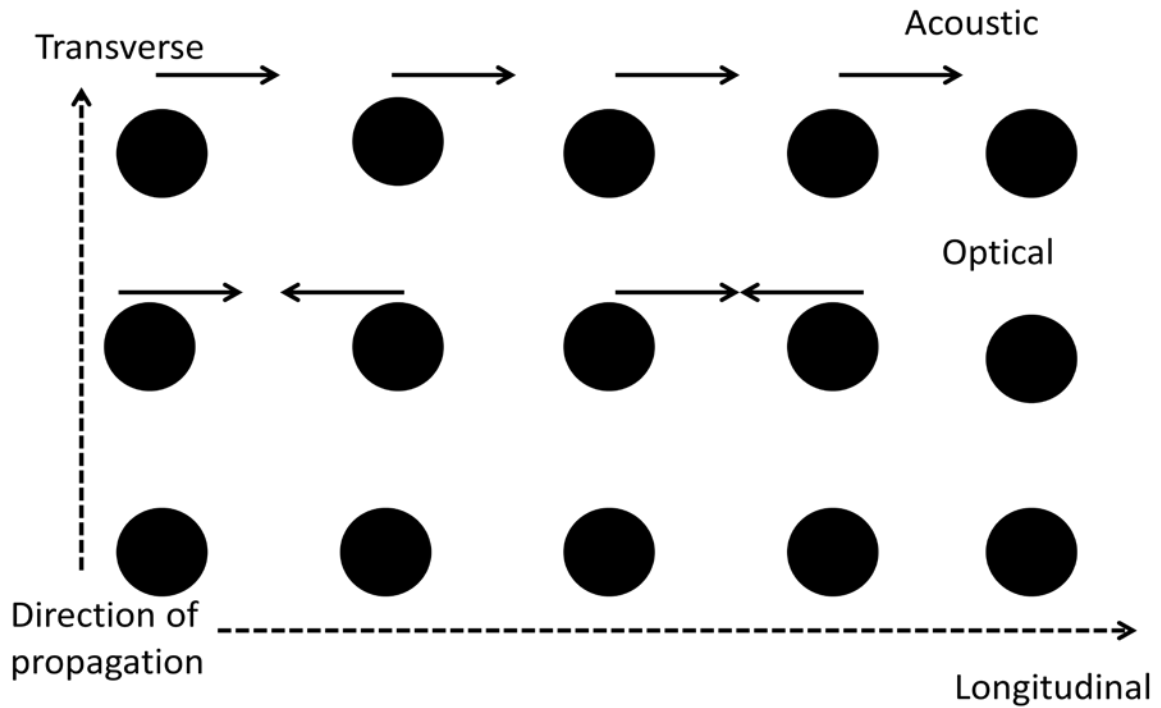


Figure 2: Description of phonon modes

The complete coupling of the vibrational modes assumes an infinite lattice, in practice there are defects in the lattice that interrupt the propagation. These defects are common on surfaces as molecules rearrange in order to minimise surface energy. This can be particularly important for particles with less than ≈ 1000 molecules where a significant proportion of molecules are on or near the surface. Such particles can be ideally suited to probing surface properties which can be distinctly different to the properties of the bulk material.

3.1.3 REFRACTIVE INDEX

The scattering (refraction) and reflective behaviour of particles is also very different to bulk material. Changing the particle sizes (figure 3) or shapes can have a dramatic influence on extinction spectrum due to different contributions from the real (n) and imaginary (k) components of the refractive index (\tilde{n}). The real component is associated with scattering/refraction while the imaginary component is the purely absorptive contribution.

$$\tilde{n} = n + ik$$

Reflectivity can also be related to the refractive index by the Fresnel equations, at a normal angle of incident this is:

$$R = \left(\frac{n_1 - n_2}{n_1 + n_2} \right)^2$$

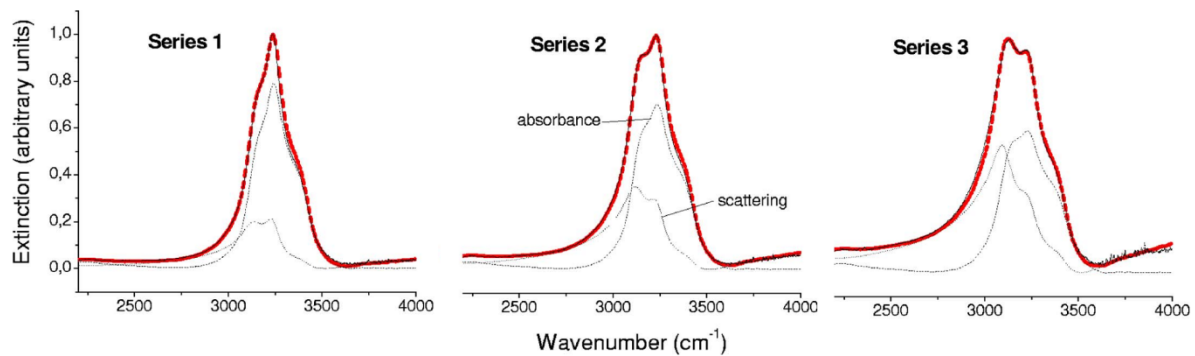


Figure 3: The absorption and scattering contributions to the extinction are shown for three different particle radii: series 1=458 nm, series 2=584 nm and series 3= 786 nm as calculated using the discrete dipole approximation. Reprinted with permission from reference [28].

The accurate calculation of refractive indices can be challenging. Even from thin film spectra the determination of refractive indices is less than straight forward. The accuracy of the determined constants is dependent on the accuracy of the thickness measurement and the purity and homogeneity of the film and may be affected by the substrate window. Determination of refractive indices from aerosol spectra is further complicated by the distribution of particle sizes and shape. The crystal phase of the particles may also be different to the bulk phase diagram due to thermodynamic or kinetic considerations.

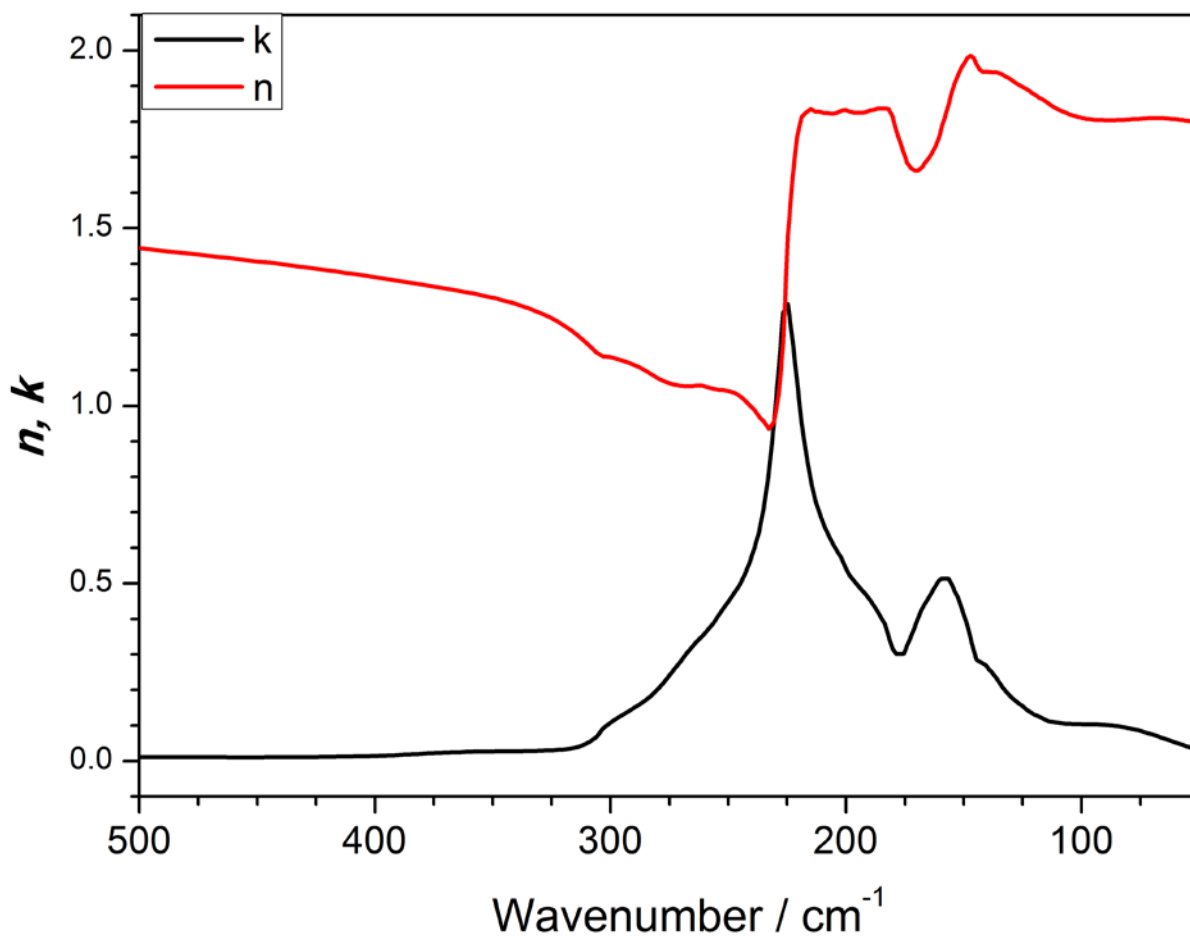


Figure 4: The real (n , red) and imaginary (k , black) components of the far-IR refractive index of crystalline I_c water ice. Data from Iwabuchi & Yang [51]

Notwithstanding these problems it has been found to be advantageous to determine refractive indices from aerosol data.[19, 52] The large temperature and spectral range available with our instrument offers the possibility of improving upon the thin film based literature refractive indices. Knowledge of the refractive indices near absorption bands is particularly important as both the real (n) and imaginary (k) components change dramatically at these points (figure 4) and inaccuracies in the data can be magnified. The interplay between absorption and refraction as shape and size changes is vitally important to the accurate modelling of natural aerosol particles. By forming particles in the laboratory under similar conditions many of these problems can be overcome and a more thorough understanding of natural systems is possible.

3.1.4 REFERENCES

1. Bohren, C.F. and D.R. Huffman, *Absorption and scattering of light by small particles*. 2008: Wiley-Vch.
2. Reid, J.P. and L. Mitchem, *Laser probing of single-aerosol droplet dynamics*. *Annu. Rev. Phys. Chem.*, 2006. **57**: p. 245-271.
3. Sigurbjörnsson, Ó.F., G. Firanescu, and R. Signorell, *Intrinsic particle properties from vibrational spectra of aerosols*. *Annual review of physical chemistry*, 2009. **60**: p. 127-146.
4. Häber, T., U. Schmitt, and M.A. Suhm, *FTIR-spectroscopy of molecular clusters in pulsed supersonic slit-jet expansions*. *Phys. Chem. Chem. Phys.*, 1999. **1**(24): p. 5573-5582.
5. Tom, J.W. and P.G. Debenedetti, *Particle formation with supercritical fluids--a review*. *Journal of Aerosol Science*, 1991. **22**(5): p. 555-584.
6. Davis, E.J., *A history of single aerosol particle levitation*. *Aerosol science and technology*, 1997. **26**(3): p. 212-254.
7. Barnes, J., T. Gough, and M. Stoer, *Diffusive trapping: An alternative to supersonic jet cooling for spectroscopic experiments?* *Review of Scientific Instruments*, 1989. **60**(3): p. 406-409.
8. Ewing, G.E. and D.T. Sheng, *Infrared spectroscopy of carbon dioxide ultrafine particles*. *The Journal of Physical Chemistry*, 1988. **92**(14): p. 4063-4066.
9. Dunder, T. and R. Miller, *Infrared spectroscopy and Mie scattering of acetylene aerosols formed in a low temperature diffusion cell*. *The Journal of Chemical Physics*, 1990. **93**: p. 3693.
10. Fleyfel, F. and J.P. Devlin, *FT-IR spectra of carbon dioxide clusters*. *The Journal of Physical Chemistry*, 1989. **93**(21): p. 7292-7294.
11. Bauerecker, S., M. Taraschewski, C. Weitkamp, and H.K. Cammenga, *Liquid-helium temperature long-path infrared spectroscopy of molecular clusters and supercooled molecules*. *Review of Scientific Instruments*, 2001. **72**(10): p. 3946-3955.
12. Signorell, R. and D. Luckhaus, *Aerosol Spectroscopy of Dihydroxyacetone: Gas Phase and Nanoparticles*. *The Journal of Physical Chemistry A*, 2002. **106**(19): p. 4855-4867.
13. Signorell, R., M. Kunzmann, and M. Suhm, *FTIR investigation of non-volatile molecular nanoparticles*. *Chemical Physics Letters*, 2000. **329**(1): p. 52-60.
14. Jetzki, M. and R. Signorell, *The competition between hydrogen bonding and chemical change in carbohydrate nanoparticles*. *The Journal of Chemical Physics*, 2002. **117**: p. 8063.
15. Jetzki, M., D. Luckhaus, and R. Signorell, *Fermi resonance and conformation in glycolaldehyde particles*. *Canadian journal of chemistry*, 2004. **82**(6): p. 915-924.
16. Bartell, L.S., L. Harsanyi, and E.J. Valente, *Phases and phase changes of molecular clusters generated in supersonic flow*. *The Journal of Physical Chemistry*, 1989. **93**(16): p. 6201-6205.
17. Bauerecker, S., F. Taucher, C. Weitkamp, W. Michaelis, and H.K. Cammenga, *Spectral simplification by enclosive flow cooling I - FT-IR spectroscopy of supercooled gases at 100 K*. *Journal of Molecular Structure*, 1995. **348**(0): p. 237-241.
18. Taucher, F., C. Weitkamp, H.K. Cammenga, and S. Bauerecker, *Infrared spectroscopy and enclosive flow cooling: concept of an integrated multireflection optics*. *Spectrochimica Acta Part A: Molecular and Biomolecular Spectroscopy*, 1996. **52**(8): p. 1023-1027.
19. Dartois, E. and S. Bauerecker, *Infrared analysis of CO ice particles in the aerosol phase*. *The Journal of Chemical Physics*, 2008. **128**(15): p. 154715-10.
20. Signorell, R. and M.K. Kunzmann, *Isotope effects on vibrational excitons in carbon dioxide particles*. *Chemical Physics Letters*, 2003. **371**(3-4): p. 260-266.
21. Taraschewski, M., H.K. Cammenga, R. Tuckermann, and S. Bauerecker, *FTIR Study of CO₂ and H₂O/CO₂ nanoparticles and their temporal evolution at 80 K*. *Journal of Physical Chemistry A*, 2005. **109**(15): p. 3337-3343.

22. Signorell, R., *Verification of the vibrational exciton approach for CO₂ and N₂O nanoparticles*. The Journal of Chemical Physics, 2003. **118**(6): p. 2707-2715.
23. Bauerecker, S., *Self-Diffusion in Core-Shell Composite ¹²CO₂/¹³CO₂ Nanoparticles*. Physical Review Letters, 2005. **94**: p. 033404.
24. Signorell, R., M. Jetzki, M. Kunzmann, and R. Ueberschaer, *Unraveling the Origin of Band Shapes in Infrared Spectra of N₂O-¹²CO₂ and ¹²CO₂-¹³CO₂ Ice Particles*. Journal of Physical Chemistry A, 2006. **110**: p. 2890-2897.
25. Firanescu, G., D. Luckhaus, and R. Signorell, *Phase, shape, and architecture of SF₆ and SF₆/CO₂ aerosol particles: Infrared spectra and modeling of vibrational excitons*. Journal of Chemical Physics, 2008. **128**(18): p. 184301-184301.
26. Bonnamy, A., M. Jetzki, and R. Signorell, *Optical properties of molecular ice particles from a microscopic model*. Chemical Physics Letters, 2003. **382**(5-6): p. 547-552.
27. Kunzmann, M.K., R. Signorell, M. Taraschewski, and S. Bauerecker, *The formation of N₂O nanoparticles in a collisional cooling cell between 4 and 110 K*. Physical Chemistry Chemical Physics, 2001. **3**(17): p. 3742-3749.
28. Bauerecker, S., A. Wargenau, M. Schultze, T. Kessler, R. Tuckermann, and J. Reichardt, *Observation of a transition in the water-nanoparticle formation process at 167 K*. The Journal of Chemical Physics, 2007. **126**(13): p. 134711-6.
29. Buch, V., S. Bauerecker, J. Paul Devlin, U. Buck, and J.K. Kazimirski, *Solid water clusters in the size range of tens-thousands of H₂O: a combined computational/spectroscopic outlook*. International Reviews in Physical Chemistry, 2004. **23**(3): p. 375-433.
30. Hujo, W., M. Gaus, M. Schultze, T. Kubař, J. Grunenberg, M. Elstner, and S. Bauerecker, *Effect of Nitrogen Adsorption on the Mid-Infrared Spectrum of Water Clusters*. The Journal of Physical Chemistry A, 2011. **115**(23): p. 6218-6225.
31. Medcraft, C., D. McNaughton, C.D. Thompson, D. Appadoo, S. Bauerecker, and E.G. Robertson, *Size and Temperature Dependence in the Far-IR Spectra of Water Ice Particles*. The Astrophysical Journal, 2012. **758**(1): p. 17.
32. Medcraft, C., E.G. Robertson, C.D. Thompson, S. Bauerecker, and D. McNaughton, *Infrared spectroscopy of ozone and hydrogen chloride aerosols*. Physical Chemistry Chemical Physics, 2009. **11**(36).
33. Kunzmann, M.K., S. Bauerecker, M.A. Suhm, and R. Signorell, *Spectroscopic characterization of N₂O aggregates: From clusters to the particulate state*. Spectrochimica Acta - Part A: Molecular and Biomolecular Spectroscopy, 2003. **59**(12): p. 2855-2865.
34. Robertson, E.G., C. Medcraft, L. Puskar, R. Tuckermann, C.D. Thompson, S. Bauerecker, and D. McNaughton, *IR spectroscopy of physical and chemical transformations in cold hydrogen chloride and ammonia aerosols*. Physical Chemistry Chemical Physics, 2009. **11**(36).
35. Jetzki, M., A. Bonnamy, and R. Signorell, *Vibrational delocalization in ammonia aerosol particles*. The Journal of Chemical Physics, 2004. **120**: p. 11775.
36. Firanescu, G., D. Luckhaus, and R. Signorell, *Size effects in the infrared spectra of NH₃ ice nanoparticles studied by a combined molecular dynamics and vibrational exciton approach*. Journal of Physical Chemistry, 2006. **125**.
37. Signorell, R. and M. Jetzki, *Vibrational exciton coupling in pure and composite sulfur dioxide aerosols*. Faraday Discussions, 2008. **137**: p. 51-64.
38. Sigurbjörnsson, Ó.F., G. Firanescu, and R. Signorell, *Vibrational exciton coupling as a probe for phase transitions and shape changes of fluoroform aerosol particles*. Physical Chemistry Chemical Physics, 2009. **11**(1): p. 187-194.
39. Sigurbjörnsson, Ó.F. and R. Signorell, *Volume versus surface nucleation in freezing aerosols*. Physical Review E, 2008. **77**(5): p. 051601.
40. Wang, C.C., E.K. Lang, and R. Signorell, *Methane Gas Stabilizes Supercooled Ethane Droplets in Titan's Clouds*. The Astrophysical Journal Letters, 2010. **712**(1): p. L40.
41. Wang, C.C., S.K. Atreya, and R. Signorell, *Evidence for layered methane clouds in Titan's troposphere*. Icarus, 2010. **206**(2): p. 787-790.

42. Signorell, R. and M. Jetzki, *Phase behavior of methane haze*. Physical Review Letters, 2007. **98**(1): p. 13401.
43. Lang, E.K., K.J. Knox, C.C. Wang, and R. Signorell, *The influence of methane, acetylene and carbon dioxide on the crystallization of supercooled ethane droplets in Titan's clouds*. Planetary and Space Science, 2011. **59**(8): p. 722-732.
44. Bauerecker, S. and E. Dartois, *Ethane aerosol phase evolution in Titan's atmosphere*. Icarus, 2009. **199**(2): p. 564-567.
45. Wang, C.C., P. Zielke, O.F. Sigurbjörnsson, C.R. Viteri, and R. Signorell, *Infrared Spectra of C₂H₆, C₂H₄, C₂H₂, and CO₂ Aerosols Potentially Formed in Titan's Atmosphere*. The Journal of Physical Chemistry A, 2009. **113**(42): p. 11129-11137.
46. Preston, T.C., G. Firanesco, and R. Signorell, *Infrared spectroscopy and vibrational exciton modeling of crystalline, polycrystalline and amorphous acetylene aerosol particles*. Physical Chemistry Chemical Physics, 2010. **12**(28): p. 7924-7933.
47. Preston, T.C. and R. Signorell, *The formation and stability of co-crystalline NH₃· C₂H₂ aerosol particles*. 2012.
48. Sigurbjörnsson, Ó.F. and R. Signorell, *Evidence for the existence of supercooled ethane droplets under conditions prevalent in Titan's atmosphere*. Phys. Chem. Chem. Phys., 2008. **10**(41): p. 6211-6214.
49. Preston, T.C., C.C. Wang, and R. Signorell, *Infrared spectroscopy and modeling of co-crystalline CO₂· C₂H₂ aerosol particles. I. The formation and decomposition of co-crystalline CO₂· C₂H₂ aerosol particles*. The Journal of Chemical Physics, 2012. **136**: p. 094509.
50. Lang, E.K., K.J. Knox, and R. Signorell, *Phase behavior of propane and *n*-pentane aerosol particles under conditions relevant to titan*. Planetary and Space Science, 2012. **http://dx.doi.org/10.1016/j.pss.2012.10.010**.
51. Iwabuchi, H. and P. Yang, *Temperature dependence of ice optical constants: Implications for simulating the single-scattering properties of cold ice clouds*. Journal of Quantitative Spectroscopy and Radiative Transfer, 2011. **112**(15): p. 2520-2525.
52. Clapp, M.L., D.R. Worsnop, and R.E. Miller, *Frequency-dependent optical constants of water ice obtained directly from aerosol extinction spectra*. The Journal of Physical Chemistry, 1995. **99**(17): p. 6317-6326.

Declaration for Thesis Chapter 3.2

Declaration by candidate

In the case of Chapter 3.2 the nature and extent of my contribution to the work was the following:

Nature of contribution	Extent of contribution (%)
Initiation, key ideas, experimental, development and writing up	80%

The following co-authors contributed to the work. Co-authors who are students at Monash University must also indicate the extent of their contribution in percentage terms:

Name	Nature of contribution	Extent of contribution (%) for student co-authors only
D. McNaughton	Initiation and key ideas	
C.D. Thompson	Initiation and key ideas	
D.R.T. Appadoo	Experimental assistance	
S. Bauerecker	Initiation and key ideas	
E.G. Robertson	Initiation and key ideas	

Candidate's
Signature

	Date
--	------

Declaration by co-authors

The undersigned hereby certify that:

- (1) the above declaration correctly reflects the nature and extent of the candidate's contribution to this work, and the nature of the contribution of each of the co-authors.
- (2) they meet the criteria for authorship in that they have participated in the conception, execution, or interpretation, of at least that part of the publication in their field of expertise;
- (3) they take public responsibility for their part of the publication, except for the responsible author who accepts overall responsibility for the publication;
- (4) there are no other authors of the publication according to these criteria;
- (5) potential conflicts of interest have been disclosed to (a) granting bodies, (b) the editor or publisher of journals or other publications, and (c) the head of the responsible academic unit; and
- (6) the original data are stored at the following location(s) and will be held for at least five years from the date indicated below:

Location(s)

Monash University, School of Chemistry
--

[Please note that the location(s) must be institutional in nature, and should be indicated here as a department, centre or institute, with specific campus identification where relevant.]

Signature 1

	Date
--	------

Signature 2

--	--

Signature 3

--	--

Signature 4

--	--

Signature 5

	3-12-2012
---	-----------

SIZE AND TEMPERATURE DEPENDENCE IN THE FAR-IR SPECTRA OF WATER ICE PARTICLES

CHRIS MEDCRAFT¹, DON McNAUGHTON¹, CHRIS D. THOMPSON¹, DOMINIQUE APPADOO²,
SIGURD BAUERECKER³, AND EVAN G. ROBERTSON⁴

¹ School of Chemistry, Monash University, Wellington Road, Clayton, Victoria 3800, Australia

² Australian Synchrotron, Blackburn Road, Clayton, Victoria 3168, Australia

³ Institut für Physikalische und Theoretische Chemie, Technische Universität Braunschweig, Hans-Sommer-Strasse 10, D-38106 Braunschweig, Germany

⁴ Department of Chemistry & La Trobe Institute of Molecular Sciences, La Trobe University, Bundoora, Victoria 3086, Australia; E.Robertson@latrobe.edu.au

Received 2012 May 1; accepted 2012 July 23; published 2012 September 20

ABSTRACT

Spectra of water-ice aerosol particles have been measured in the far-IR region using synchrotron radiation. The particles in the nanoscale size regime of 1–100 nm were formed by rapid collisional cooling at temperatures ranging from 4 to 190 K. The spectra show the characteristic bands centered near $44\ \mu\text{m}$ ($230\ \text{cm}^{-1}$) and $62\ \mu\text{m}$ ($160\ \text{cm}^{-1}$) associated with the intermolecular lattice modes of crystalline ice at all temperatures, in contrast to previous studies of thin films formed by vapor deposition where amorphous ice is generated below 140 K. The bands shift to higher wavenumber values as the temperature is reduced, consistent with the trend seen in earlier studies, but in our experiments the actual peak positions in the aerosol particle spectra are consistently higher by ca. $4\ \text{cm}^{-1}$. This finding has implications for the potential use of these spectral features as a temperature probe. The particle sizes are small enough for their spectra to be free of scattering effects, and therefore provide a means to assess imaginary refractive index values obtained through Kramers–Kronig analyses of thin film spectra.

Key words: infrared: general – ISM: molecules – radiative transfer – techniques: spectroscopic

1. INTRODUCTION

Water ice is ubiquitous throughout the universe; it has been detected in nearly every location where physical conditions permit it. The infrared (IR) spectrum of water ice varies with purity, phase, particle size and shape, and perhaps most importantly, temperature (Moore & Hudson 1994; Buch et al. 2004; Bauerecker et al. 2007). Amorphous ice is formed when deposition occurs at temperatures at or below 100 K; crystalline ice can be formed either directly by depositing above 100 K or by forming amorphous ice at temperatures lower than 100 K and then tempering to 155 K (Moore & Hudson 1992). This phase transition to crystalline ice is thermally irreversible, therefore the phase of water ice detected in astronomical bodies may provide a thermal history of sorts (Zheng et al. 2009). The near-IR bands of water have been used to gauge the temperature of Saturn’s rings and satellites (Fink & Larson 1975; Larson & Fink 1977); the mid-IR OH-stretching mode has been used to determine the temperature of a number of different protostellar nebulae (Smith et al. 1989).

The far-IR spectrum of crystalline ice has two characteristic peaks: one sharp peak near $44\ \mu\text{m}$ ($230\ \text{cm}^{-1}$, the transverse optic mode) and a broader one near $62\ \mu\text{m}$ ($160\ \text{cm}^{-1}$, the longitudinal acoustic), whereas amorphous ice has one broad peak near $45\ \mu\text{m}$ ($220\ \text{cm}^{-1}$). Additionally, both crystalline bands undergo a gradual redshift of approximately $6\ \text{cm}^{-1}$ ($1.5\ \mu\text{m}$) when cooled from 150 K to 10 K (Moore et al. 2001). These features were used to fit the emission from IRAS 09371+1212 to temperatures of 46 K indicating that significant cooling has occurred since crystallization (Omont et al. 1990).

Existing laboratory data on the far-IR spectroscopy of water ice come from studies on thin films, deposited either on a window for transmission spectra (Smith et al. 1994) or on a mirror for transmission–reflection–transmission (TRT) spectra (Moore et al. 2001). In this study, we report the far-IR spectra of nanometer-sized aerosol particles comprised of cubic (I_c) phase ice at temperatures from 5 K to 195 K.

It is important to study such particles directly, primarily because their spectroscopic properties may be distinctly different from those of bulk materials or films. As noted by Hudgins et al. (1993), this may result in a mismatch between astrophysical or atmospheric spectra and those from films. At the small particle limit, surface effects increasingly contribute to the spectral profile, particularly in the region of strong transitions. At the other end of the size scale, scattering of radiation with wavelength λ becomes significant as the dimensions of the particle approach $\lambda/2\pi$. Furthermore, analysis of IR spectra from particles smaller than this allows determination of the frequency-dependent imaginary component of the refractive index of a material, and consequently the real component also (Clapp et al. 1995; Dohm et al. 2004; Dartois & Bauerecker 2008).

Such constants are required for modeling of complex systems such as those found in planetary atmospheres. The atmospheres of Saturn and Jupiter both contain significant amounts of water (Roos-Serote et al. 2004) and, depending on the altitude, clouds of solid water, NH_3 , and NH_4SH can form (West et al. 2004; Baines et al. 2002). Various compounds such as hydrocarbons and phosphine (PH_3) are found in smaller quantities and form a complex, dynamic chemical environment (Dougherty & Esposito 2009). One of the principal aims of the CIRS mission on board the *Cassini* orbiter is the investigation of aerosols in the atmospheres of Saturn and Titan (Fouchet et al. 2009).

Saturn’s rings are primarily composed of nearly pure crystalline water-ice particles with a large distribution of particle sizes from sub-micrometer-sized dust to small moonlets (Poulet & Cuzzi 2002; Esposito 2010). Small amounts of impurities give the rings a visibly red color. The nature of these impurities is an active area of research with tholins, polyaromatic hydrocarbons, and oxidized iron (hematite) being suggested as possible absorbers (Fouchet et al. 2009).

Water-ice clouds are known to play an important role in the water cycle of Mars and influence the planet’s radiative forcing balance (Montmessin et al. 2004; Michaels et al. 2006), but

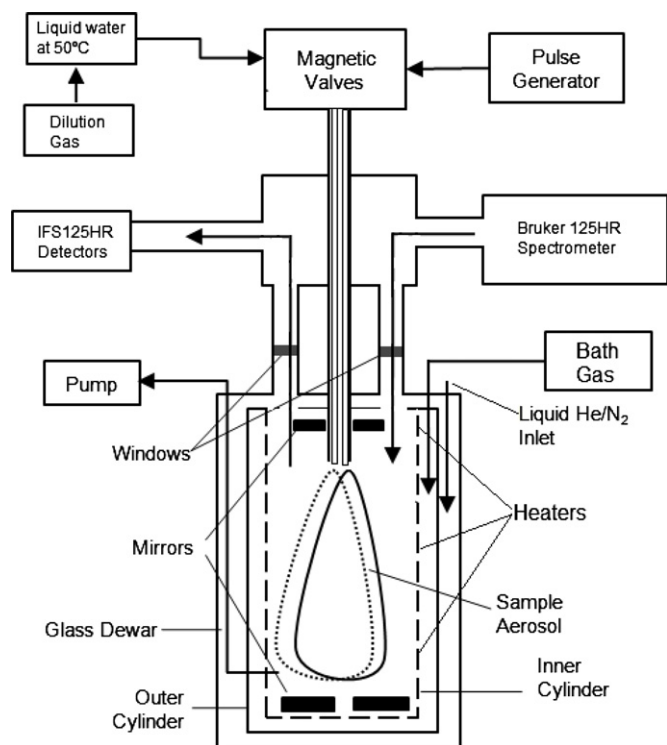


Figure 1. Schematic diagram of experimental setup.

detailed mechanisms of formation are still being established. Laboratory studies have found significant temperature-dependant barriers to ice formation by heterogeneous nucleation on mineral dust particles (Iraci et al. 2010), and recent observations suggest the frequent presence of water vapor in excess of saturation, by an amount far surpassing that encountered in Earth’s atmosphere (Maltagliati et al. 2011).

Observations in the near-IR of the exoplanet GJ1214b suggest that it contains a water-rich atmosphere where cloud formation may be possible (Berta et al. 2012). Although the expected temperature in the upper atmosphere is too high for ice formation (≈ 500 K; Miller-Ricci Kempton et al. 2012), if the atmospheres of exoplanets with lower temperatures are to be fully understood, then laboratory data are needed over a wide range of wavelengths, temperatures, and particle size. Here, we present the first laboratory far-infrared spectra of water ice in the aerosol phase.

2. EXPERIMENTAL

The aerosols were generated using an enclosive flow-cooling (EFC) cell (Bauerecker et al. 2001), shown schematically in Figure 1. A number of studies using this type of cell have demonstrated the distinct spectral properties of aerosol particles in the mid-IR region (Bauerecker 2005; Kunzmann et al. 2001; Medcraft et al. 2009; Robertson et al. 2009; Taraschewski et al. 2005; Signorell & Kunzmann 2003). Our cell has now been coupled to the Bruker IFS125HR spectrometer at the far-infrared and high-resolution infrared beamline of the Australian Synchrotron. The synchrotron provides a continuous source of light that is brighter than thermal sources and results in spectra with improved signal-to-noise ratio in the far-IR region. By selecting suitable optical components, nearly the entire infrared region is presently accessible ($10\text{--}8000\text{ cm}^{-1}$). The present far-IR experiments used a $6\text{ }\mu\text{m}$ Mylar beam splitter, high-density polyethylene (HDPE), or polymethylpentene (TPX) windows,

with a silicon bolometer detector to measure spectra in the range $50\text{--}380\text{ cm}^{-1}$. For the mid-IR region ($700\text{--}4000\text{ cm}^{-1}$), a mercury cadmium telluride detector, KBr beam splitter, and KBr cell windows were used. Wavenumber calibration is accurate to within 10^{-3} cm^{-1} . The multi-pass cell has a white design (Bauerecker et al. 2001), with an optical path length set to $5\text{--}7.5\text{ m}$ (up to 20 m maximum path length). It contained gas (N_2 or He ; see Table 1) in thermal equilibrium with the inner cooling cell wall to serve as a buffer and cool the sample via inelastic collisions. Heating was controlled via three heaters on the inner cylinder and two on the mirrors (see Figure 1) and temperature was measured via five separate thermocouples (K-type) mounted on the inner cylinder and mirrors as well as one rhodium–iron thermistor (for liquid helium temperatures). The coolant around the outer cylinder was either liquid He, liquid N_2 , or preheated N_2 vapor continually flowing from a liquid bath; see Table 1.

A diluted sample of water vapor was prepared by filling a reservoir containing distilled liquid water and heated to 50°C with ~ 3 atm of carrier gas (He or N_2). A 1 s pulse of this warm, wet sample gas at 270 kPa ($\sim 400\text{ mL}$) was injected into the central zone of the multi-pass cell containing the cold bath gas (He or N_2). Under these conditions, the sample is cooled rapidly via inelastic collisions with the bath gas until the water becomes supersaturated and particles begin to nucleate. Particle formation has been found to occur rapidly ($< 1\text{ s}$), e.g., by use of rapid-scan IR spectroscopy (Bauerecker et al. 2007) and to produce spherical nanoparticles (Bauerecker et al. 2007) of crystalline ice (Buch et al. 2004). Spectra were measured at 1 or 2 cm^{-1} resolution, over a period up to five minutes, depending on the lifetime of the aerosol. Table 1 contains a summary of the experimental conditions used to measure the spectra at different temperatures.

3. RESULTS

The spectra measured at different temperatures are shown in Figure 2. Sharp rotational lines from water monomers are visible only at temperatures at and above 173 K . The broader absorption features near $44\text{ }\mu\text{m}$ ($\approx 230\text{ cm}^{-1}$) and $62\text{ }\mu\text{m}$ ($\approx 160\text{ cm}^{-1}$), evident in all the spectra, result from intermolecular vibrations (crystal lattice modes) where the water molecule as a whole translates with respect to neighboring molecules (Bertie 1968; Bertie & Whalley 1967). These features are due to the transverse optical mode and the longitudinal acoustic mode, respectively. Their appearance and position provide clear evidence that crystalline rather than amorphous ice is formed at all temperatures down to 5 K . The spectrum of amorphous ice has only one distinct maximum that for a given temperature is found around 10 cm^{-1} lower than the 230 cm^{-1} band of crystalline ice (Moore & Hudson 1992). The production of crystalline ice under conditions of rapid collisional cooling contrasts with earlier thin film experiments in which slow deposition of water on a surface in a high-vacuum environment results in the formation of amorphous ice at temperatures below 110 K (Moore & Hudson 1992).

Distinguishing the hexagonal (I_h) or cubic (I_c) forms of ice is not so straightforward. Their mid-IR spectra are identical (Devlin & Buch 2003; Bauerecker et al. 2007) and the far-IR spectra are very similar (Bertie & Whalley 1967), except for the subtle difference reported by Bertie & Jacobs (1977) that in hexagonal ice, the 160 cm^{-1} band appears as a barely resolved doublet at 4 K . The apparent absence of such a doublet in the spectra of Figure 2 suggests the cubic form but is

Table 1
Summary of Experimental Conditions and Results

Temp (K)	Error in Temp (K)	TO Peak Position (cm^{-1})	Estimated Error (cm^{-1})	Max Abs	LA Peak Position (cm^{-1})	Estimated Error (cm^{-1})	TO:LA Abs Ratio	Estimated Diameter (nm)	Bath and Carrier Gas	Bath Pressure (mbar)	Coolant	Resolution (cm^{-1})	Optical Path Length (m)
4.9	0.1	234.6	0.7	0.04	165.9	1	4.1	1.5	He	22	LHe	2.0	5.0
5.0	0.1	234.8	0.1	0.03		1	...	1.5	He	25	LHe	2.0	5.0
5.9	0.2	234.8	0.2	0.05	171.0	1	3.5	1.6	He	28	LHe	2.0	5.0
6.8	0.2	234.8	0.5	0.05	167.0	1	4.7	1.6	He	32	LHe	2.0	5.0
10.6	0.2	233.8	0.9	0.05	168.9	1	3.7	1.7	He	1.2	LHe	2.0	5.0
18.2	0.5	233.5	0.3	0.07	167.6	1	5.1	2.0	He	32	LHe	2.0	5.0
40	2	233.1	0.5	0.09	166.0	1	5.1	3.3	He	168	LHe	2.0	5.0
50	5	232.9	0.4	0.03	168.0	1	4.1	4.2	He	50	LHe	2.0	5.0
78.0	0.1	233.1	0.2	0.25	166.0	0.5	...	7.8	He	50	LN ₂	2.0	5.0
78.4	0.1	233.2	0.1	0.40	165.3	0.5	5.9	7.9	N ₂	50	LN ₂	1.0	7.5
80.0	0.1	233.2	0.8	0.25	165.0	0.5	5.4	8.2	N ₂	50	LN ₂	1.0	7.5
92.4	0.1	232.6	0.5	0.25	166.6	0.5	4.8	10.8	N ₂	50	LN ₂	1.0	7.5
104.2	0.1	231.9	1.3	0.27	162.4	1	5.5	14.1	N ₂	50	LN ₂	1.0	7.5
113.0	0.1	231.0	0.4	0.30	163.1	0.5	5.7	17.2	N ₂	50	LN ₂	1.0	7.5
123.0	0.1	230.6	0.4	0.27	163.3	0.5	5.3	21.5	N ₂	50	LN ₂	1.0	7.5
133.0	0.1	229.9	1.3	0.23	162.8	0.5	4.6	27.0	N ₂	50	LN ₂	1.0	7.5
141.3	0.1	228.8	0.3	0.28	162.0	0.5	4.0	32.5	N ₂	50	N ₂ Gas	1.0	7.5
147.4	0.1	228.4	0.7	0.20	162.0	0.5	4.7	37.3	N ₂	50	N ₂ Gas	1.0	7.5
153.0	0.1	228.0	0.5	0.25	160.5	0.5	4.3	42.3	N ₂	50	N ₂ Gas	1.0	7.5
162.4	0.1	227.4	0.6	0.27	160.8	1	4.6	52.3	N ₂	50	N ₂ Gas	1.0	7.5
173.0	0.1	226.8	1.0	0.25	160.1	1	4.2	66.4	N ₂	50	N ₂ Gas	1.0	7.5
183.1	0.1	226.4	1.3	0.24	159.5	1	4.2	83.3	N ₂	50	N ₂ Gas	1.0	7.5
195.0	0.1	225.0	1.4	0.23	157.0	1	...	109	N ₂	50	N ₂ Gas	1.0	7.5

hardly conclusive. However, electron microscopy (Delzeit & Blake 2001) and electron diffraction studies on ice formed in supersonic expansions (Bartell 1996; Bartell & Huang 1994; Huang & Bartell 1995) have shown that cubic ice is kinetically favored over hexagonal ice. Cubic ice has a much lower interfacial free energy which reduces the barrier for formation of cubic ice cores, resulting in a much higher nucleation rate than that of hexagonal ice (Buch et al. 2004). For small ice crystals (<15 nm), there is also a thermodynamic preference for cubic ice (Johari 2005). For larger cubic-ice crystals, an irreversible conversion to hexagonal ice can occur when above 170 K, however it is extremely slow (Hallbrucker & Mayer 1987; Starr et al. 2003). We can therefore safely assume that all our particles are cubic ice, at least for the particles below 180 K.

In Figure 3, the variation of peak position with temperature in this work is compared with earlier studies. The trend of peak wavenumber value decreasing with temperature is observed in all the studies, but our data are in disagreement with the majority of the published literature values in having peak positions consistently higher by ~ 4 cm^{-1} for all but the coldest temperatures. The temperature-dependant intensity ratio of 44–62 μm bands (see Table 1) is also inconsistent with the data in Figure 3(b) of Moore et al. (2001).

3.1. Temperature

The general temperature dependence can be explained by the contraction of the hydrogen bonds between molecules as the volume of the crystalline unit cell decreases with temperature (Dougherty 1998). The reduction of absorptions occurring from thermally excited lattice energy levels also influences this shift in peak position with temperature (Whalley & Bertie 1967). The hydrogen bond length is at a minimum at approximately 73 K. Below this temperature, the intermolecular bond distance increases (Rottger et al. 1994), so the lattice vibrational modes might be expected to reflect this. Intriguingly, we do observe a

leveling in the peak positions below 80 K. Both Moore's and Schmitt's data also show this, although it went unremarked and a linear trend line was fitted to their data. In contrast, Smith's data appear to show no signs of this marked change in gradient. We note in caution that any traces of nitrogen gas introduced along with the helium in the experiments below 30 K could condense onto the particle surfaces and could have some effect on the spectrum. In the mid-IR (2600–3800 cm^{-1}), a redshift of the dangling O–H band of about 20 cm^{-1} can be observed for the OH-stretch band complex of water particles due to N₂ adsorption; the band center region is apparently not affected (Hujo et al. 2011; Sadlej et al. 1995; Devlin et al. 1994; Rowland et al. 1991). In the present experiment, we have no evidence for the presence of N₂ impurity.

At temperatures lower than 20 K, our data show a further slight increase in peak wavenumber value with decreasing temperature. These low-temperature spectra (<20 K) provide the only points that agree with the earlier literature values from Smith et al. (1994) and Bertie & Jacobs (1977) who used samples of powdered ices to obtain a peak maximum of 233 cm^{-1} at 4 K. However, in our experiments at these coldest temperatures, the small particle size (see Figure 4) becomes a critical consideration which has more bearing on the observed spectral changes than the direct effect of temperature on crystalline ice.

3.2. Particle Size

Particle size is limited by the amount of available water and the nucleation rate, which in turn depend on temperature and bath gas pressure. In order to help interpret the far-IR data, we performed a similar set of experiments in the mid-IR region. This region provides a number of markers that allow estimation of particle size; these include short wavelength scattering, the ratio of absorption intensity of surface to bulk molecules, and the shape of the H–O–H bending mode absorption (Buch et al.

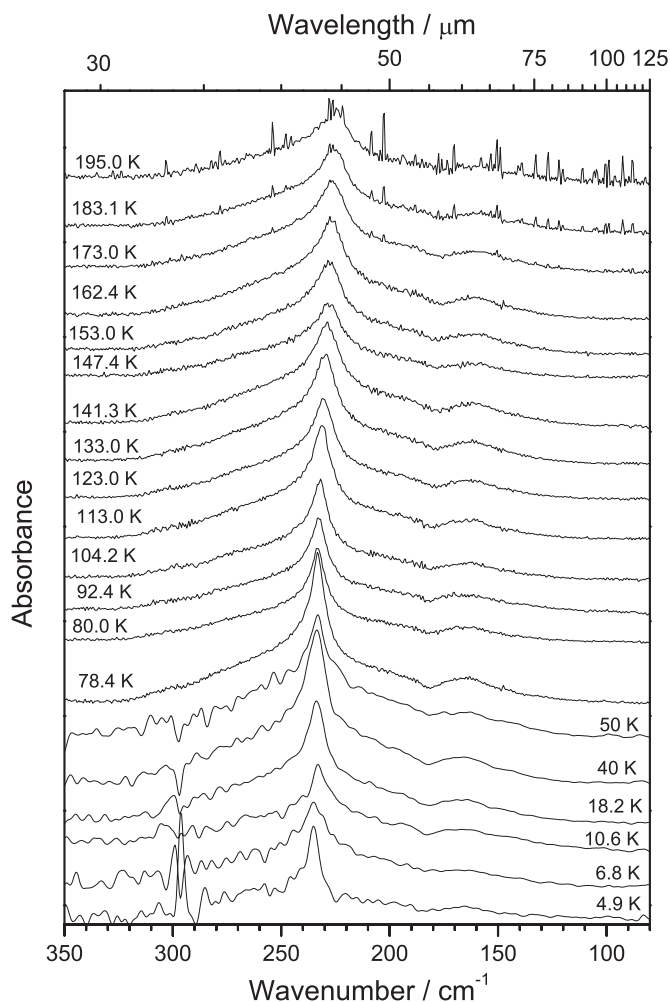


Figure 2. Far-IR spectra of water-ice aerosol at various bath gas temperatures. At temperatures above 78 K, the carrier and bath gas is N₂, below 78 K it is He. For a full set of experimental conditions for each spectrum see Table 1. Artifacts around 300 cm⁻¹ seen in the spectra below 78 K are due to absorption by TPX windows. These spectra have been scaled by a factor of seven relative to the higher temperature spectra.

2004). Estimates of particle size shown in Figure 4 and Table 1 were based on the integrated intensity ratios of the dangling-OH and bonded-OH bands: the relation to particle size is expressed in Figure 11 of Buch et al. (2004). The formation of smaller particles at colder temperature is attributed to a greater nucleation rate as the water vapor becomes more supersaturated.

Different spectral effects become significant for particles at large- and small-size scales. With smaller particles, the contribution of the more disordered surface (and subsurface) layer of water molecules is increasingly evident. In the mid-IR region, the onset of spectroscopic change occurs at a particle diameter of around 3–4 nm (Buch et al. 2004). As the size is reduced even further, the OH-stretch modes are blueshifted toward the peak absorption of amorphous ice (ca. 3304 cm⁻¹ at 10 K; Hudgins et al. 1993). The effect on the collective translational motions of the far-IR lattice modes is less predictable. The more strained and disordered intermolecular H-bonding network in smaller particles might be expected to reduce the vibrational wavenumber values, again toward the peak absorptions for amorphous ice, but it appears from Figure 3 that this is not the case. In our experiments, the 3 nm size threshold is reached

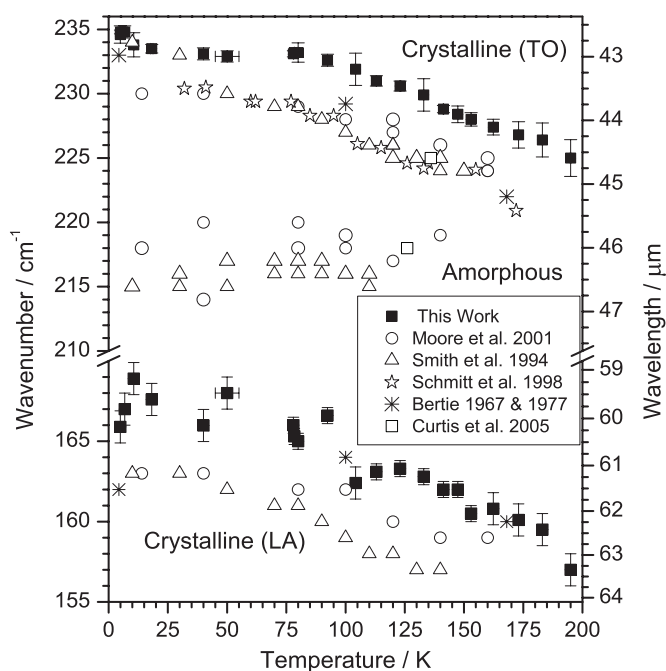


Figure 3. Peak maximum position vs. temperature for the transverse optical (TO) and longitudinal acoustic (LA) lattice modes of crystalline ice and the single peak maximum from amorphous ice. Error bars on our data are estimates of the temperature deviation during the experiment and the uncertainty of the peak center due to noise. The other peak positions were obtained from tables presented in Smith et al. (1994, series III), Moore et al. (2001, series b), Schmitt et al. (1998), Bertie & Whalley (1967), and Bertie & Jacobs (1977).

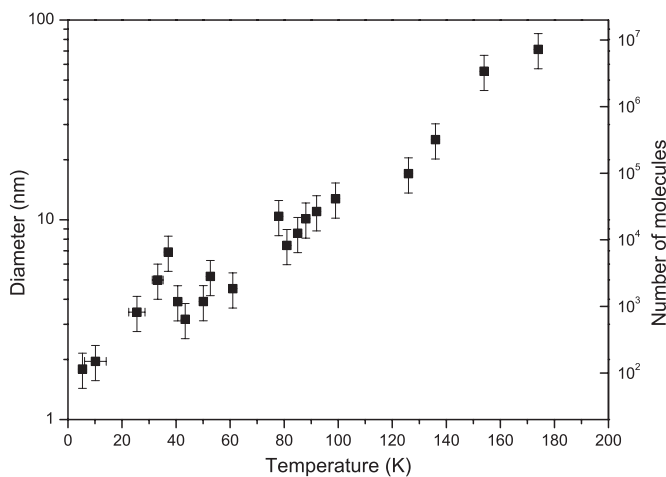


Figure 4. Plot of the estimated particle size vs. temperature, with size calculated from mid-IR spectra measured using equivalent experimental conditions of temperature and buffer gas pressure to those used for far-IR measurements. The error bars are 20% of the particle size, estimated from the propagation of errors in the measured integrated intensities of the mid-IR bands. Number of molecules is calculated assuming particles are spherical and have the density of bulk ice at each temperature.

at ca. 30 K. Below this temperature, the particles decrease to ≈ 1 nm position while the band center rises by 2 cm⁻¹.

We deduce that above 30 K, the ice aerosol particles are large enough so that surface effects only marginally influence the spectra, compare Figure 4 and Buch et al. (2004), but are also small enough to be entirely free of scattering which becomes significant as the particle dimensions approach $\lambda/2\pi$ (i.e., 7 μm for the 230 cm⁻¹ band). Thus, the measured aerosol spectra depend only on the purely absorptive component which is governed by the imaginary component of the refractive

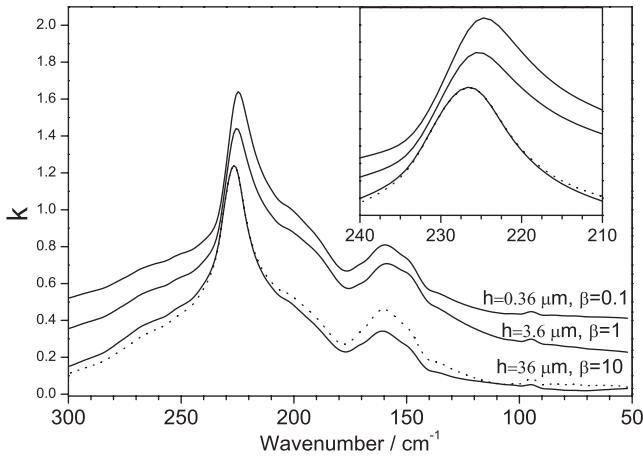


Figure 5. Absorbance curves (solid lines) calculated for crystalline water ice of three different film thicknesses, h , in vacuum without substrate, from refractive index data at 136 K (Curtis et al. 2005). The parameter $\beta = (4\pi h)/\lambda$, where λ is the wavelength at which k is a maximum. The calculated absorbance maxima are 0.064 (for $\beta = 0.1$), 0.49 (for $\beta = 1.0$), and 4.6 (for $\beta = 10$), but they have been rescaled and vertically offset for ready comparison with the trace of imaginary refractive index component, k (dotted line).

index, k , and not on scattering which is related to the real component, n .

3.3. Comparison with Thin Film Spectra

Clapp et al. (1995) point out some of the reasons why thin film spectra deposited on infrared transparent substrates may differ from aerosol spectra. One consideration is the reflections that occur at substrate/film/vacuum interfaces. These depend on the real (n) and imaginary (k) refractive indices of the materials and on the film thickness. Figure 5 illustrates one aspect of this—the effect of film thickness. Simulated absorption spectra are shown for crystalline water-ice films of different thicknesses in vacuum, based on Equations (2)–(4) of Hudgins et al. (1993). The film thickness may be characterized by the parameter $\beta = (4\pi h)/\lambda$ where λ is the wavelength at which k is a maximum. In the thick film limit where $\beta \gg 1$, the absorbance spectrum, and the peak width and peak maximum, are most similar to the plot of k , but as β approaches a value of one the peak maximum is shifted to lower wavenumber (higher wavelength) due to the sharp change in real refractive index, n , that occurs in the vicinity of a strong absorption band. This trend is in accord with the slightly higher wavenumber values at temperatures over 80 K obtained by Moore et al. (2001) for a film estimated to be $7.2 \mu\text{m}$ thick when compared to “series III” of Smith et al. (1994) with film thickness estimated at $2.9 \mu\text{m}$. However, it appears unlikely that this effect can account for the further blueshift in peak maxima for the aerosol data compared to the thin film data that are evident in Figure 3.

Other possible causes of differences between film and aerosol spectra cited by Clapp et al. (1995) include the difficulty of producing films of uniform structure and composition, and without crystal defects. There is evidence that deposition of material on a substrate can favor amorphous rather than crystalline phases, e.g., in the case of CO (Dartois & Bauerecker 2008), or even inhibit formation of a crystalline phase entirely as in nitric acid trihydrate (Berland et al. 1994). The reason may be due to the cooling velocity during the condensation and desublimation processes being normally much higher in the case of film deposits.

3.4. Other Factors

We note that the mid-IR spectra showed a trace of CO_2 indicating some contamination by air. However, this cannot account for the observed blueshift compared to thin film spectra. Above ~ 90 K CO_2 (and also N_2 and O_2) is still in the gas phase, and so is unlikely to be incorporated within or on the surface of the ice particles. Below this temperature, CO_2 might have co-condensed with the water (Taraschewski et al. 2005) but this would be expected to cause a *redshift* in the band position (Moore & Hudson 1994). We have also performed separate experiments where pure CO_2 was injected into the cell at varying time delays to the water sample injection and no shift in the far-IR water bands was observed.

4. CONCLUSIONS

The far-IR spectra of water-ice aerosol particles measured as part of this study have revealed some interesting and very significant results that may have an impact on future modeling of complex astrophysical and atmospheric systems. First, it is clear that crystalline ice is formed at all temperatures under conditions of the rapid collisional cooling, with no evidence of amorphous ice that is seen with slow vacuum deposition below 110 K. Second, at all but the coldest temperatures (below 40 K), the lattice mode bands in the aerosol particle spectra are blueshifted by ca. 4 cm^{-1} compared to those of thin films. This has implications for the potential use of the peak maximum as a temperature gauge: a 4 cm^{-1} shift is equivalent to a temperature change of ca. 60 K. Third, the present results along with those of other groups (Moore et al. 2001; Schmitt et al. 1998) hint at a change in the gradient at around 80 K, possibly associated with a minimum in the hydrogen-bond distance at 73 K (Rottger et al. 1994). Fourth, the spectra of aerosol particles in the nm size regime, being free of scattering effects associated with the real component of the refractive index, provide a means to evaluate the wavelength and temperature-dependant imaginary refractive indices. Usually, the real (n) and imaginary (k) components are correlated parameters that must be determined by iterative calculation through Kramers–Kronig analysis that relies on the film thickness being accurately known (Hudgins et al. 1993; Iwabuchi & Yang 2011).

Given that water-ice particles occur in the atmospheres of solar planets and their satellites, it is essential to characterize the size dependence and the considerable temperature dependence (Iwabuchi & Yang 2011) of their mid- and far-IR spectra in relation to potential observation. However, it is also important to be able to distinguish pure water particles from water-coated dust particles such as are found in regions of interstellar molecular clouds characterized by high atomic H abundances, where the small molecules that form polar ices are dominated by H_2O (Burke & Brown 2010). Spectral simulations for such heterogeneous particles (Prokopjeva et al. 2007), or indeed for water ice in other forms such as Martian polar CO_2 and H_2O frosts (Johnson & Atreya 1996), must rely on accurate optical constants. Surveyed across the electromagnetic spectrum, these optical constants are most uncertain in the far-IR region (Warren & Brandt 2008). Further studies will be directed toward rationalizing the observations made here, extracting optical constants and extending the study of temperature and size effects to the mid-IR region.

This work was generously supported by the Australian Synchrotron through beam-time access and an Australian

Synchrotron Postgraduate Award (C.M.). Financial support from the Australian Government through an Australian Postgraduate Award to C.M. is also gratefully acknowledged. The research was also supported by the Deutsche Forschungsgemeinschaft (Grant BA 2176/3–1).

REFERENCES

- Baines, K. H., Carlson, R. W., & Kamp, L. W. 2002, *Icarus*, **159**, 74
- Bartell, L. S. 1996, *J. Phys. Chem.*, **100**, 8197
- Bartell, L. S., & Huang, J. 1994, *J. Phys. Chem.*, **98**, 7455
- Bauerecker, S. 2005, *Phys. Rev. Lett.*, **94**, 033404
- Bauerecker, S., Taraschewski, M., Weitkamp, C., & Cammenga, H. K. 2001, *Rev. Sci. Instrum.*, **72**, 3946
- Bauerecker, S., Wargenau, A., Schultze, M., et al. 2007, *J. Chem. Phys.*, **126**, 134711
- Berland, B. S., Haynes, D. R., Foster, K. L., et al. 1994, *J. Phys. Chem.*, **98**, 4358
- Berta, Z. K., Charbonneau, D., Desert, J.-M., et al. 2012, *ApJ*, **747**, 35
- Bertie, J. E. 1968, *Appl. Spectrosc.*, **22**, 634
- Bertie, J. E., & Jacobs, S. M. 1977, *J. Chem. Phys.*, **67**, 2445
- Bertie, J. E., & Whalley, E. 1967, *J. Chem. Phys.*, **46**, 1271
- Buch, V., Bauerecker, S., Paul Devlin, J., Buck, U., & Kazimirski, J. K. 2004, *Int. Rev. Phys. Chem.*, **23**, 375
- Burke, D. J., & Brown, W. A. 2010, *Phys. Chem. Chem. Phys.*, **12**, 5947
- Clapp, M. L., Miller, R. E., & Worsnop, D. R. 1995, *J. Phys. Chem.*, **99**, 6317
- Curtis, D. B., Rajaram, B., Toon, O. B., & Tolbert, M. A. 2005, *Appl. Opt.*, **44**, 4102
- Dartois, E., & Bauerecker, S. 2008, *J. Chem. Phys.*, **128**, 154715
- Delzeit, L., & Blake, D. 2001, *J. Geophys. Res.*, **106**, 33371
- Devlin, J. P., & Buch, V. 2003, in *Water in Confining Geometries*, ed. V. Buch & J. P. Devlin (Berlin: Springer), 425
- Devlin, J. P., Silva, S. C., Rowland, B., & Buch, V. 1994, in *Hydrogenbond Networks*, ed. M. C. Bellissent-Funel & J. C. Dore (Dordrecht: Kluwer), 373
- Dohm, M. T., Potschavage, A. M., & Niedziela, R. F. 2004, *J. Phys. Chem. A*, **108**, 5365
- Dougherty, M., & Esposito, L. 2009, *Saturn from Cassini-Huygens* (Dordrecht: Springer)
- Dougherty, R. C. 1998, *J. Chem. Phys.*, **109**, 7372
- Esposito, L. W. 2010, *Annu. Rev. Earth Planet. Sci.*, **38**, 383
- Fink, U., & Larson, H. P. 1975, *Icarus*, **24**, 411
- Fouchet, T., Moses, J. I., & Conrath, B. J. 2009, in *Saturn from Cassini-Huygens* ed. M. Dougherty (Dordrecht: Springer), 83
- Hallbrucker, A., & Mayer, E. 1987, *J. Phys. Chem.*, **91**, 503
- Huang, J., & Bartell, L. S. 1995, *J. Phys. Chem.*, **99**, 3924
- Hudgins, D. M., Sandford, S. A., Allamandola, L. J., & Tielens, A. G. G. M. 1993, *A&AS*, **86**, 713
- Hujo, W., Gaus, M., Schultze, M., et al. 2011, *J. Phys. Chem., A*, **115**, 6218
- Iraci, L. T., Phebus, B. D., Stone, M. S., & Colaprete, A. 2010, *Icarus*, **210**, 985
- Iwabuchi, H., & Yang, P. 2011, *J. Quant. Spectrosc. Radiat. Transfer*, **112**, 2520
- Johari, G. P. 2005, *J. Chem. Phys.*, **122**, 194504
- Johnson, B. R., & Atreya, S. K. 1996, *Icarus*, **119**, 405
- Kunzmann, M. K., Signorell, R., Taraschewski, M., & Bauerecker, S. 2001, *Phys. Chem. Chem. Phys.*, **3**, 3742
- Larson, H. P., & Fink, U. 1977, *Appl. Spectrosc.*, **31**, 386
- Maltagliati, L., Montmessin, F., Fedorova, A., et al. 2011, *Science*, **333**, 1868
- Medcraft, C., Robertson, E. G., Thompson, C. D., Bauerecker, S., & McNaughton, D. 2009, *Phys. Chem. Chem. Phys.*, **11**, 7848
- Michaels, T. I., Colaprete, A., & Rafkin, S. C. R. 2006, *Geophys. Res. Lett.*, **33**, L16201
- Miller-Ricci Kempton, E., Zahnle, K., & Fortney, J. J. 2012, *ApJ*, **745**, 3
- Montmessin, F., Forget, F., Rannou, P., Cabane, M., & Haberle, R. M. 2004, *J. Geophys. Res.*, **109**, E10004
- Moore, M. H., & Hudson, R. L. 1992, *ApJ*, **401**, 353
- Moore, M. H., & Hudson, R. L. 1994, *A&AS*, **103**, 45
- Moore, M. H., Hudson, R. L., & Gerakines, P. A. 2001, *Spectrochim. Acta A*, **57**, 843
- Omont, A., Moseley, S. H., Forveille, T., et al. 1990, *ApJ*, **355**, L27
- Poulet, F., & Cuzzi, J. N. 2002, *Icarus*, **160**, 350
- Prokopjeva, M. S., & Il'in, V. B. 2007, *Astron. Lett.*, **33**, 699
- Robertson, E. G., Medcraft, C., Puskar, L., et al. 2009, *Phys. Chem. Chem. Phys.*, **11**, 7853
- Roos-Serote, M., Atreya, S. K., Wong, M. K., & Drossart, P. 2004, *Planet. Space Sci.*, **52**, 397
- Rottger, K., Endriss, A., Ihringer, J., Doyle, S., & Kuhs, W. F. 1994, *Acta Crystallogr. B*, **50**, 644
- Rowland, B., Fisher, M., & Devlin, J. P. 1991, *J. Chem. Phys.*, **95**, 1378
- Sadlej, J., Rowland, B., Devlin, J. P., & Buch, V. 1995, *J. Chem. Phys.*, **102**, 4804
- Schmitt, B., Quirico, E., Trotta, F., Grundy, W. M., de Bergh, C., & Festou, M. 1998, in *Solar System Ices*, ed. B. Schmitt (Dordrecht: Kluwer), 199
- Signorell, R., & Kunzmann, M. 2003, *Chem. Phys. Lett.*, **371**, 260
- Smith, R. G., Robinson, G., Hyland, A. R., & Carpenter, G. L. 1994, *MNRAS*, **271**, 481
- Smith, R. G., Sellgren, K., & Tokunaga, A. T. 1989, *ApJ*, **344**, 413
- Starr, F. W., Angell, C. A., & Stanley, H. E. 2003, *Physica A*, **323**, 51
- Taraschewski, M., Cammenga, H. K., Tuckermann, R., & Bauerecker, S. 2005, *J. Phys. Chem. A*, **109**, 3337
- Warren, S. G., & Brandt, R. E. 2008, *J. Geophys. Res.*, **113**, D14220
- West, R. A., Baines, K. H., Friedson, A. J., et al. 2004, in *Jupiter: The Planet, Satellites and Magnetosphere*, ed. F. Bagenal (Cambridge: Cambridge Univ. Press), 59
- Whalley, E., & Bertie, J. E. 1967, *J. Chem. Phys.*, **46**, 1264
- Zheng, W., Jewitt, D., & Kaiser, R. I. 2009, *J. Phys. Chem. A*, **113**, 11174

Declaration for Thesis Chapter 3.3

Declaration by candidate

In the case of Chapter 3.3 the nature and extent of my contribution to the work was the following:

Nature of contribution	Extent of contribution (%)
Initiation, key ideas, experimental, development and writing up	80%

The following co-authors contributed to the work. Co-authors who are students at Monash University must also indicate the extent of their contribution in percentage terms:

Name	Nature of contribution	Extent of contribution (%) for student co-authors only
D. McNaughton	Initiation and key ideas	
C.D. Thompson	Initiation and key ideas	
D.R.T. Appadoo	Experimental assistance	
S. Bauerecker	Experimental, Initiation and key ideas	
E.G. Robertson	Initiation and key ideas	

Candidate's Signature		Date
-----------------------	--	------

Declaration by co-authors

The undersigned hereby certify that:

- (1) the above declaration correctly reflects the nature and extent of the candidate's contribution to this work, and the nature of the contribution of each of the co-authors.
- (2) they meet the criteria for authorship in that they have participated in the conception, execution, or interpretation, of at least that part of the publication in their field of expertise;
- (3) they take public responsibility for their part of the publication, except for the responsible author who accepts overall responsibility for the publication;
- (4) there are no other authors of the publication according to these criteria;
- (5) potential conflicts of interest have been disclosed to (a) granting bodies, (b) the editor or publisher of journals or other publications, and (c) the head of the responsible academic unit; and
- (6) the original data are stored at the following location(s) and will be held for at least five years from the date indicated below:

Location(s)

[Please note that the location(s) must be institutional in nature, and should be indicated here as a department, centre or institute, with specific campus identification where relevant.]

Signature 1		Date
Signature 2		
Signature 3		
Signature 4		
Signature 5		3-12-2012

Water ice nanoparticles: size and temperature effects on the mid-infrared spectrum

Chris Medcraft,^a Don McNaughton,^a Chris D. Thompson,^a Dominique Appadoo,^b Sigurd Bauerecker,^c Evan G. Robertson^{d*}

^a School of Chemistry, Monash University, Wellington Rd., Clayton, Victoria 3800, Australia

^b Australian Synchrotron, Blackburn Rd, Clayton, Victoria 3168, Australia

^c Institut für Physikalische und Theoretische Chemie, Technische Universität Braunschweig, Hans-Sommer-Strasse 10, D-38106 Braunschweig, Germany

^d Department of Chemistry & La Trobe Institute of Molecular Sciences, La Trobe University, Bundoora, Victoria 3086, Australia

Email: E.Robertson@latrobe.edu.au

Mid-infrared spectra have been measured for cubic ice (I_c) nanoparticles (3-150 nm diameter) formed by rapid collisional cooling over a wide range of temperatures (5-209 K). Spectral diagnostics, such as the ratio of surface related dangling OH to interior H-bonded OH stretch bands, reveal the manner in which particle size depends on bath gas temperature and density, and on water molecule concentration. For particles smaller than 5 nm strained intermolecular bonds on the surface and subsurface cause the predominant OH stretch peak position to be dramatically blue shifted by up to 40 cm^{-1} . In the size regime of 8-200 nm the position of the OH stretch absorption band maximum is relatively unaffected by particle size and it is possible to measure the temperature dependence of the peak location without influences from the surface or scattering. The band maximum shifts in a linear fashion from 3218 cm^{-1} at 30 K to 3253 cm^{-1} at 209 K, which may assist with temperature profiling of ice particles in atmospheric clouds and extraterrestrial systems. Over the same temperature range the librational mode band shifts very little, from 870 to 860 cm^{-1} . In the water stretching and bending regions discrete spectral features associated with the surface or sub-surface layers have been detected in particles as large as 70 nm.

1. Introduction

Molecular ices play an important role in interstellar and atmospheric chemical processing where they can act as a reaction medium¹⁻². Their physical and chemical properties vary greatly with composition, with temperature and with particle size -the large molecular aggregates found in aerosols can behave very differently from the corresponding bulk material.³ The interactions of such aerosols with infrared radiation are significant in two major contexts. Firstly, radiative processes associated with emission and extinction are fundamental to energy transfer and considering blackbody radiation curves the IR region in particular is central in non-stellar environments such as planetary and interstellar clouds where temperatures are moderate. Secondly, infrared spectroscopy is uniquely suited to remotely probing the properties of these ices, including their temperature, and particle characteristics. Accurate laboratory data is essential to interpret such measurements.

The effect of temperature on the infrared spectrum of these ices is often inferred from laboratory studies on films of ice deposited on a substrate where the thickness of the film can be easily controlled and measured,⁴⁻⁷ but the spectra of such films often differ from those of aerosol particles. Films that are thin enough to allow sufficient optical transmission are affected by the reflections that occur at substrate/film/vacuum interfaces, which depend on both the real (n) and imaginary (k) refractive indices of the materials.⁸ Other reasons cited for these differences include the difficulty of producing thin films of uniform structure and composition, and without crystal defects.⁹ Measurements in the aerosol phase eliminate these influences and allow for investigations on how the spectrum changes with particle characteristics such as size and shape.

Experimental methods for the formation of these aerosols include collisional cooling¹⁰, supersonic jet expansion¹¹⁻¹², rapid expansion of supercritical solutions (RESS)¹³ and acoustic levitation¹⁴. In this study water ice aerosols were generated using an enclosive flow cooling cell, which is thoroughly described elsewhere¹⁵⁻¹⁷. This type of cell has been used previously to investigate the influence of temperature on aerosols of CO,

CO₂¹⁷, N₂O¹⁸⁻¹⁹, dihydroxyacetone²⁰ and small hydrocarbons²¹⁻²³, revealing that the effective “phase diagram” for aerosol formation can be very different from that of bulk material in thermal equilibrium. The size and shape of particles of NH₃ (and deuterated isotopomers), NH₃/CO₂²⁴, CO₂²⁵, N₂O²⁶, fluoroform²⁷ and acetylene²⁸ has also been studied. Similar effects have been investigated in binary particles of ¹³CO₂/¹²CO₂²⁹⁻³⁰, D₂O/H₂O³¹ and CO₂/SO₂³², O₃/HCl³³, HCl/NH₃³⁴ and CO₂/H₂O^{35,36}. Finally the nucleation and temporal evolution of particles have also been examined for particles of H₂O³⁷, CO₂/H₂O³⁵ and O₃/HCl³³.

Water ice is of particular interest because of its ubiquity. In the context of earth’s atmosphere and climate, the formation of water ice aerosols produces high altitude cirrus clouds. In this work we examine the effects of size and temperature on the mid-IR spectrum of water nanoparticles. A study on much larger aerosol particles ($\approx 1 \mu\text{m}$ diameter) at temperatures of 130-210K extracted refractive indices from aerosol particle spectra⁹. This was done by scaling the absorptive (imaginary) component directly to the spectra of clusters with diameter ≈ 600 nm, a size considered small enough for scattering to have a limited effect. The real component was obtained through Kramers-Kronig analysis of larger particle spectra affected by scattering. Similar enhanced studies have been performed in the very large close-to-reality AIDA aerosol and cloud chamber for a higher size range up to 15 μm ³⁸⁻³⁹, with among other things the goal to examine the influence of particle aspect ratio on the mid-IR extinction spectra⁶³. Further analyses were used to extend the temperature range to 230 K for ice and 273 K for liquid and supercooled liquid water.^{40,41} It is worth mentioning that water ice aerosols differ considerably from liquid and supercooled liquid water aerosols in their mid-IR spectra.⁴¹ The temperature dependence of these refractive indices has been used to remotely determine the temperature of ice in Earth’s mesosphere where particle sizes are <200 nm.⁴²⁻⁴⁴ On a size scale that is smaller still (<20 nm), a number of studies⁴⁵⁻⁵⁰ have shown that reduced particle size can have a dramatic influence on the shape and position of absorption bands, particularly for the OH stretching modes.

In this work we have measured the mid-IR spectrum (750-8000 cm^{-1}) of water ice aerosols over a wider range of temperatures (5-209 K) in a size regime (3-100 nm) where scattering effects are negligible, and where the onset of vanishing crystalline behaviour may be observed for particles smaller than around 5 nm. This work complements a related study in which the far IR spectra of ice aerosols formed under similar conditions showed shifts in the position of the intermolecular translational mode near 230 cm^{-1} compared to thin film spectra.⁸

In thin film experiments slow surface deposition of water in a high vacuum environment results in the formation of amorphous ice at temperatures below 110 K.⁵¹ In contrast, the present mid IR spectra and comparable far IR spectra⁸ provide evidence that collisional cooling produces crystalline ice even down to 5K. Particle formation has been found to occur rapidly (<0.1 s) and to produce spherical particles of cubic ice (I_c)^{37, 50}. At higher temperatures (>170 K) a transition to the hexagonal phase is possible, however the mid-IR spectra of cubic (I_c) and hexagonal (I_h) are identical.⁵² Electron diffraction^{53, 54, 55} and electron microscopy⁵⁶ studies on ice formed in supersonic expansions show the cubic ice is kinetically favoured over hexagonal. There is also a thermodynamic preference for cubic ice when particles are smaller than 15 nm⁵⁷, we are therefore confident that the particles formed are of cubic ice, at least for particles below 170 K.

2. Experimental

A gaseous mixture of water and carrier gas was prepared by filling a vacuum chamber containing distilled water kept at 50°C with ≈ 3 atmospheres of carrier gas (He or N_2). A one second pulse of this wet gas at 2.7 atm was injected into the cell containing bath gas (He or N_2) at a set temperature. The final concentration of sample in the carrier gas is difficult to quantify however it was found to be reproducibly constant throughout the experiments. Based on vapour pressure data we estimate the concentration to be of the order of 0.1-1%. The plume of sample gas is cooled rapidly via inelastic collisions with the bath gas until the water becomes supersaturated and particles begin to nucleate.

The temperature and pressure of the bath gas was varied using a combination of different coolants and heaters inside the cell. Temperatures in the range of 4-40 K were obtained with liquid helium as the coolant; at these temperatures evacuating the cell between samples was impossible due to cryopumping. Once the liquid helium had evaporated the spectra at intermediate temperatures (40-77 K) were recorded as the cell warmed up. Between 77 K and 160 K liquid nitrogen was used and above 160 K a flow of cold N_2 gas was used to provide greater temperature stability.

We have recently coupled this cell to the Bruker IFS125/HR spectrometer at the Far Infrared and High Resolution Infrared beamline of the Australian Synchrotron. By selecting various optical components nearly the entire infrared region is accessible (10-8000 cm^{-1}). In this work we used the instrument's internal source (tungsten lamp) with KBr windows and beamsplitter and an MCT detector to obtain spectra from 750-8000 cm^{-1} . This allowed for the simultaneous measurement of the fundamental vibrational modes of water as well as the intermolecular librational mode $\approx 800 \text{ cm}^{-1}$ whilst still having sufficient sensitivity to observe any scattering at high wavenumber.

The spectra that are presented in sections 3.6 and some data points in figure 7 were recorded using an identical cold cell located at the Technische Universität Braunschweig on a Nicolet Magna 550 FTIR spectrometer equipped with a Globar light

source, a KBr beamsplitter, KBr windows and an external InSb detector.

3. Results and Discussion

3.1 Temporal Evolution

Sample spectra at 4 cm^{-1} resolution were recorded continuously every ≈ 0.8 seconds (0.4 s to record and a 0.4 s wait between spectra) as the water was injected and for about 3 minutes afterwards. These were ratioed against a reference background spectrum recorded with only the cold bath gas in the cell. The absorbance in the OH-stretching region was seen to grow to a maximum over a period of approximately 2 s and then slowly decay as the particles diffuse out of the optical path. After the maximum is reached the peak location shifts to slightly lower wavenumber, at most by $\approx 5 \text{ cm}^{-1}$. This shift may be due to the particles growing in size³⁷ (see section 3.4) or due to the continued cooling of the particles (see section 3.3). No further shift occurs after approximately 4 seconds indicating that the particles have ceased changing size or temperature. The spectra presented here are averages of scans recorded after the initial shift whilst the absorbance slowly decreased. With changing temperature and pressure of the bath gas the most significant change of the temporal evolution profile was in the lifetime of the particles.

3.2 Temperature Series

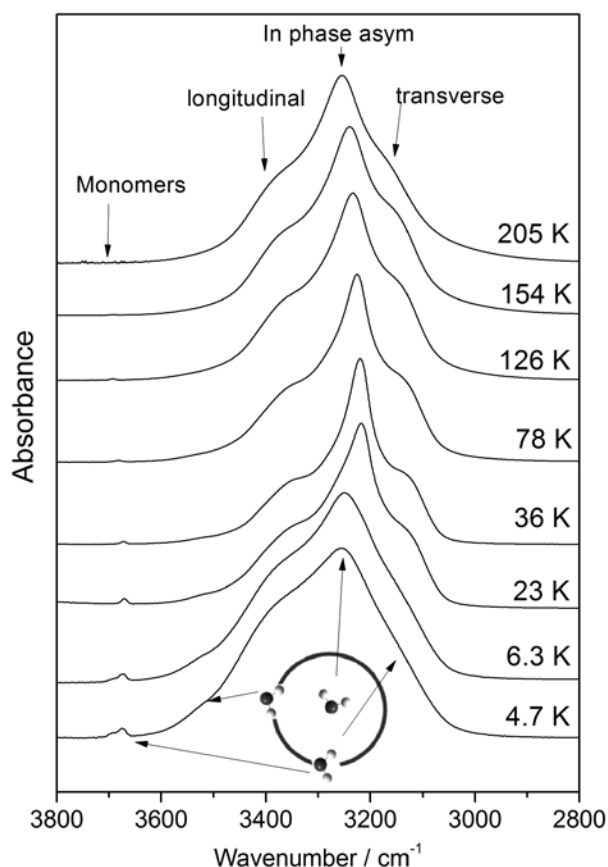


Figure 1: OH stretching region of water aerosols at various temperatures, bath gas density was between 14-27 mol m^{-3} . The maximum absorbance ranged from 0.2 to 0.7 but has been normalised here.

Figure 1 shows the OH stretching region for particles formed in various bath gas temperatures. The appearance in the warmer spectra of a central peak with two shoulders is characteristic of the H-bonded stretches in bulk crystalline ice, and these features

have been interpreted through a collective oscillating dipole model.⁴⁸ The central peak becomes sharper and shifts to lower wavenumber value as the temperature is reduced due to the reduced population of low frequency vibrational modes. Below 30 K however the central peak becomes less dominant while the signal from the dangling-OH band shows a marked increase; this is due to a decrease in particle size as well as nitrogen adsorption (see section 3.4). Above 174 K rovibrational lines associated with the water monomer are increasingly evident. The dangling OH band that is visible below this temperature may be present at higher temperatures but if so it is obscured by the monomer lines.

At the bottom of figure 1 is a schematic representation of the molecular origin of the evolving band profile which is valid for small particles (<4 nm^{47, 50}) The central peak originates from the concerted vibrations of 4-coordinate molecules in the core of the particles; the high wavenumber shoulder is from surface molecules with 'dangling' oxygen atoms that are double H-bond donors but not double acceptors. The low wavenumber shoulder originates from the hydrogen bonded side of single donor surface molecules whilst the small peak near 3700 cm⁻¹ is due to the corresponding non H-bonded, 'free' or 'dangling hydrogen' vibration.⁵⁰ These trends in the OH stretch modes of incompletely coordinated surface water molecules are evident even in clusters as small as 8 water molecules.⁵⁸

3.3 Temperature Dependence

The relationship between central peak position and temperature is summarised in figure 2. A general trend is seen in our data and the literature values where the peak position shifts to lower wavenumber at lower temperatures. Contraction of the intermolecular hydrogen bonds as the crystals cool weakens and lengthens the intramolecular bonds thus shifting the vibrational frequency lower.⁵⁹⁻⁶⁰ An approximate trend line illustrates the temperature dependence in our data.

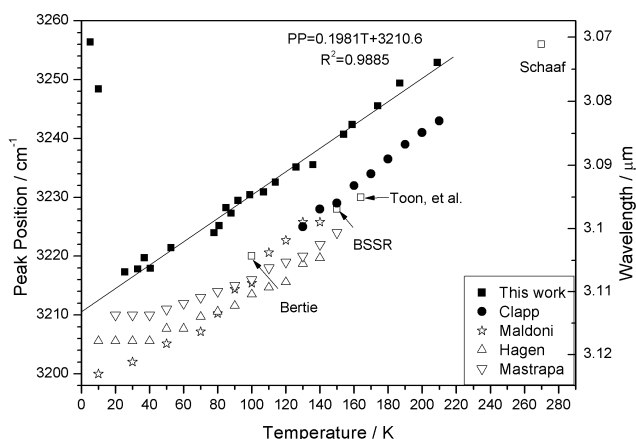


Figure 2: Peak OH-stretch position at various temperatures. Filled symbols (the present work and data from Clapp⁹) were measured in the aerosol phase; unfilled symbols are from ice deposited on various substrates. Bertie⁴Hagen⁵,Maldoni⁶ Mastrapa⁷ BSSR⁶¹Schaaf⁶²Toon⁶³. The trend line excludes the coldest two points.

Notably, our data is blue shifted by ≈ 10 cm⁻¹ compared to the literature values. Most of the literature values in figure 2 (unfilled symbols) are from thin film studies where ice is deposited onto a substrate; thicknesses ranged from 0.1-0.9 μ m. One reason for the discrepancy in peak positions is that films thin enough to allow sufficient optical transmission are affected by the reflections that occur at substrate/film/vacuum interfaces. As film thickness, h , is reduced to around $(4\pi h)/\lambda$ the peak maximum is shifted to lower wavenumber (higher wavelength) due to the sharp change in real refractive index, n , that occurs in the vicinity

of a strong absorption band.⁸ The higher peak wavenumber position in our aerosol spectra might suggest the particulate ice has some amorphous character, given that the peak of amorphous ice is also found at considerably higher wavenumber value, *ca.* 3304 cm⁻¹ at 10 K.⁶⁴ However, this possibility is ruled out by consideration of the translational mode in the far IR spectrum, where the 4 cm⁻¹ blue-shift for aerosol spectra is in the opposite direction to that expected for amorphous ice.⁸ The same argument holds for the librational mode region discussed later in section 3.7.

The series of points from Clapp⁹ were obtained from a flow through aerosol chamber instead. The particles are said to nucleate at 130 K and then flow into a secondary region where they are warmed to each of the temperatures shown. The particles are stated to be "around 0.3 μ m in radius" and were assumed to be small enough for the scattering contribution to be minimal. However, scattering of light with wavelength λ is significant for particles with dimensions approaching $\lambda/2\pi$,⁶⁴ which at 3230 cm⁻¹ (3.1 μ m) implies sizes of ≈ 0.5 μ m. This is also the approximate threshold for a size effect on the absorptive component, as the dipoles spanning the width of the particle can no longer oscillate in phase and the absorbance becomes non ideal. Discrete dipole simulations that account for both scattering and absorption indicate that spherical water ice particles of diameter 0.6 μ m have their OH stretch peak red-shifted *ca.* 8 cm⁻¹ compared to those of diameter 0.2 μ m.³⁷ As our particles are more than 10 times smaller we can be much more confident that they are free of such effects.

3.4 Determining Particle Size

Bath gas temperature affects not only the characteristic IR absorption of the material, but also the size of the particles that are formed. As a consequence, the two coldest spectra from our data set in figure 2 have peaks blue shifted by ≈ 30 cm⁻¹ from the general trend. To help interpret this shift and explore size dependence in the IR spectra, spectral features shown in figure 3 were used to estimate the particle dimensions.

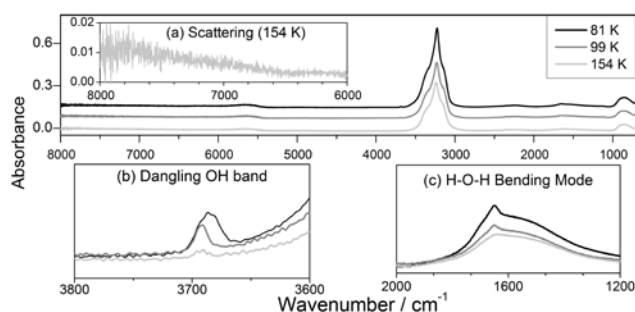


Figure 3: Summary of various particle size dependant features in the mid-IR spectrum of water aerosols. (a) the scattering at small wavelengths increases for larger particles (b) the ratio of the integrated areas dangling OH band to main OH band decreases for larger particles (c) H-O-H bending mode has extra structure for smaller particle.

First, the wavelength dependence of long wavelength scattering allows for an estimation of the particle sizes. Discrete dipole simulations³⁷ show that particles larger than 600 nm exhibit significant scattering at 4000 cm⁻¹. At higher temperatures we observed a very slight increase in the baseline around 8000 cm⁻¹ and at this wavelength (1.25 μ m) scattering becomes significant ($\lambda/2\pi$) for particle diameters of ≈ 200 nm (see figure 3a), setting an upper bound on the average particle size. Second, at temperatures below 174 K the spectra show evidence of the OH dangling bond at ≈ 3700 cm⁻¹ (figure 3b). The integrated area of this band is roughly proportional to surface area whilst the area of bonded OH band is proportional to volume. The ratio of these

two bands can therefore be used to estimate the average particle size via an empirical relationship.⁵⁰ Third, some of these estimates were confirmed by comparing spectra to those of 2-20 nm ice particles in the H-O-H bending region (figure 3c).⁶⁵ We assume that our particles have a log-normal size distribution³⁷ and the estimates in figure 4 are the mean particle size of this distribution.

Nitrogen that is adsorbed on the particles surface enhances the intensity of the dangling-OH bands, which must be accounted for when estimating particle size. This enhancement factor is 2-3 for particle diameters <3 nm and 1.5-2 for 4-10 nm particles (see figure 16 in ref⁵⁰). When N₂ is adsorbed it also causes a ≈ 20 cm⁻¹ red shift in the d-OH band⁶⁶⁻⁶⁷ which was observed in a number of our spectra below ≈ 45 K. It is assumed that N₂ was introduced along with the sample as trace amounts of air; only very small amounts of CO₂ were observed <0.01 absorbance in the ν_3 region. The low temperature size estimates in figure 4 incorporate the appropriate “self-consistent” d-OH enhancement factor, and the comparatively large uncertainty that is shown for those points reflects the uncertainty in the enhancement factor. These estimates are in accordance with a recent study where ab initio calculated spectra have been compared to experimental spectra resulting in an enhancement factor of 3 – 4 for small water particles.⁶⁷ Despite this it is clear that the strongly blue-shifted spectra observed at the coldest temperatures result from particles of around 2-5 nm where surface effects become very important (see figure 12 in reference⁵⁰).

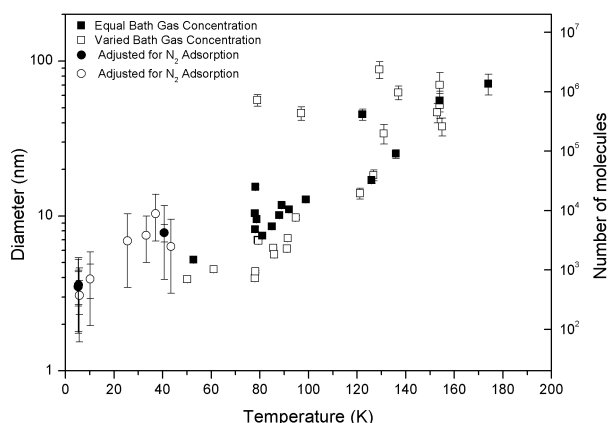


Figure 4: Size estimates of particles based on the ratio of dangling OH to bonded OH integrated intensity. The circles have been adjusted for effects of nitrogen adsorption. Solid shapes are from experiments using approximately the same bath gas concentration (25 mol m⁻³) and sample concentration while the bath gas concentration was varied for the hollow shapes.

3.5 Bath Gas Concentration†

The solid data points in figure 4 show the particle size at various temperatures where the bath gas density was equivalent. The unfilled squares are from particles formed with varying bath gas concentration. The size of particles produced in this cell is dependent on the degree of supersaturation of water vapour as it nucleates, which in turn depends on the bath gas temperature. Increasing temperature leads to decreased nucleation rate and larger particles. With sample amount and bath gas concentration kept constant, the correlation between size and temperature shown by the solid black data points in figure 4 is very strong.

†Footnote: experimentally this is measured as gas pressure however it was converted to units of mol/m³ so that comparisons could be made between different temperatures and gas types (He and N₂). The conversion used the ideal gas law which is accurate to within 0.5% under all conditions used here.

It is also clear from the hollow data points of figure 4 that bath gas concentration is a controlling variable along with temperature. Figure 5 shows spectra taken over a range of different bath gas concentrations at three different temperatures. The spectra taken around 5 K and 78 K both show an increase in particle size with increasing bath gas density. However the spectra taken at 154 K appear to show a maximum particle size at a density around 4 mol m⁻³.

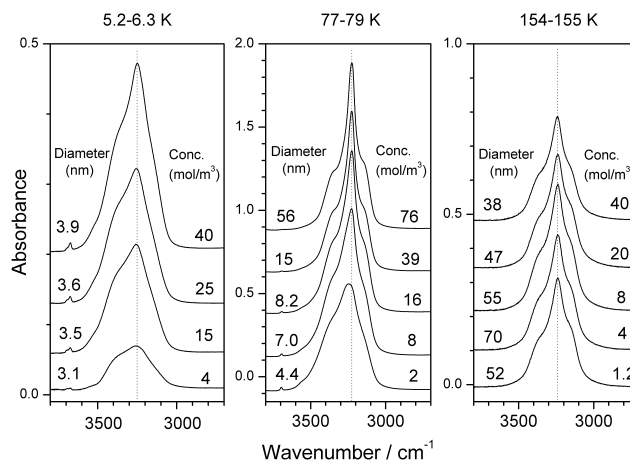


Figure 5 OH-stretching region of water aerosols at 3 different temperatures and a variety of different bath gas concentrations. The numbers on the left of the band are estimated diameters in nanometres; the numbers on the right are the concentration of the bath gas (mol/m³). The sample gas concentration has been kept constant here.

Clearly bath gas concentration has a dramatic influence on particle size. However the mechanism for particle formation is complicated by a number of confounding processes. The collision rate of sample gas to bath gas affects the cooling efficiency and diffusion rates which affect the degree of supersaturation and effective sample concentration upon nucleation. Once the particles are formed Brownian motion, agglomeration, deposition and evaporation rates (Ostwald ripening) are also likely to change with bath gas concentration. These processes are also influenced by temperature and particle size so a complete explanation on how bath gas density affects particle size is challenging. However we suggest that the most significant factor is how the plume of sample gas expands into the optical volume. When the bath gas concentration is high the plume of gas cannot expand as much as at lower densities although one has to consider the fast injection of sample gas as a merely turbulent process. The higher bath gas concentration could result in a higher local availability of water so particles are able to grow larger. The increase in intensity with bath gas concentration also suggests that more sample gas is retained in the optical volume at higher bath gas concentrations. Evaporation becomes more significant at higher temperatures and may be responsible for the more subtle trend seen at 154 K. Brownian motion driven agglomeration of bigger particles needs a quasi-liquid layer on the surface of the particles which occurs at temperatures > 245 K.⁶⁸⁻⁶⁹ This is well above the highest temperatures used in this study. So we regard this process as unlikely to play a significant role here.

The band shapes in the 5 K spectra also change significantly with changing particle size. At 3.1 nm the band has no prominent central peak while at 3.9 nm this feature is easily apparent. The reason for this change is clear when one considers the origin of the central peak coming from molecules in the core of the particles (see figure 1) and only $\approx 11\%$ of molecules in 4 nm particles (110 of 1000 molecules) are located in the core.⁵⁰ For smaller particles this core region becomes increasingly strained

and less ordered becoming entirely amorphous for particles of ≤ 6 nm.⁵⁰

Figure 5 also shows that the position of the peak absorption shifts with particle size at 78 K: there is a pronounced difference in the peak location of the 4.4 nm spectrum (3249 cm^{-1}) and the 7.0 nm spectrum (3228 cm^{-1}). In figure 2 the data points of the two coldest spectra show a similar large shift and are far above the general peak position vs temperature trend. The average particle size for both of these is less than 5 nm (figure 4). The peak positions of the spectra taken at 154 K are all $\approx 3240\text{ cm}^{-1}$ despite the large range of estimated particle sizes. This behaviour, which has been reported previously,⁵⁰ is due to the lower sensitivity of peak position at intermediate particle sizes since the crystalline core dominates the spectrum.

3.6 Sample Concentration

The concentration of water vapour in the input gas is also shown to directly affect particle size and consequently the spectra. Because the water concentration in the input gas is small for the whole sequence, the way in which the sample gas plume expands can be regarded as identical for all the spectra here, in contrast to the conditions of section 3.5. Figure 6 shows four spectra that were all recorded at 78 K and 32 mol/m^3 of helium bath gas. The concentration of water in the input helium gas (100 ml at 2 bar prepressure, 50 ms pulse) was varied by diluting a given amount of pure water (about 0.01 ml adsorbed in a porous cellulose probe which was placed in a bypass parallel to the sample gas flow) via a constantly pulsed helium flow. The concentration of water vapour in the helium carrier gas for each spectrum is shown on the left of figure 6.

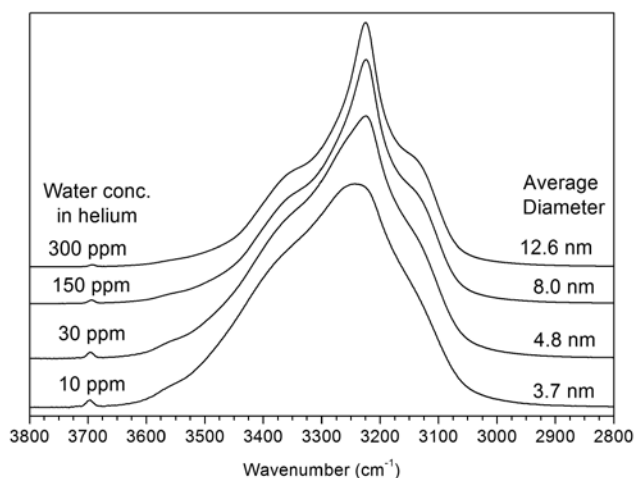


Figure 6: Spectra of the OH stretching modes at 78 K as a function of sample gas concentration. The absolute absorbance maxima were between 0.93 and 0.03 but the spectra are rescaled here for comparative purposes. The peak maximum shifts from 3224 cm^{-1} for the three upper spectra to 3241 cm^{-1} for the bottom spectrum

Decreasing the concentration of water vapour in the input gas produces a similar trend to that seen in the central panel of figure 5. At lower sample concentrations there is less water available for particle growth so therefore particles are smaller. This result supports our supposition that bath gas concentration influences particle size primarily by changing the local concentration of the sample gas.

3.7 Bending and Libration Modes

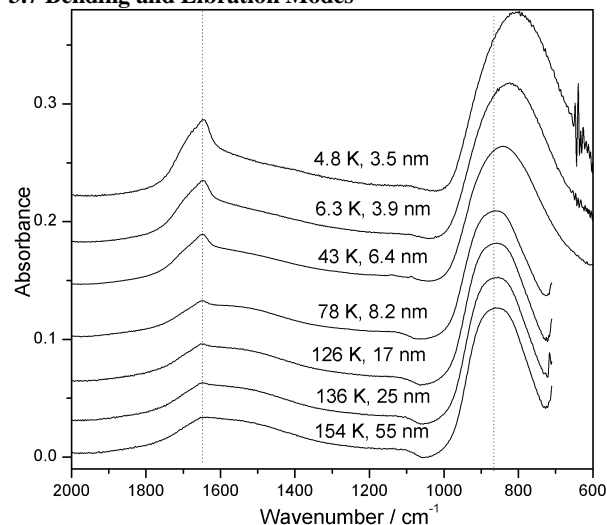


Figure 7: Spectra of the bending mode (1650 cm^{-1}) and librational mode (850 cm^{-1}) over a range of temperatures. Bath and sample gas concentrations were constant. The spectra have been normalised to the OH stretching band.

The bending mode near 1650 cm^{-1} and librational mode near 850 cm^{-1} are shown in figure 7. In the higher wavenumber region a sharp feature present near 1650 cm^{-1} is superimposed on the broad band centred around 1600 cm^{-1} which is attributed to mixing of the bend and librational overtone in crystalline ice.⁶⁵ The sharp peak has been shown to originate from the (largely unmixed) bending mode of molecules on the surface and subsurface of particles;⁶⁵ we observe this feature for sizes up to ≈ 25 nm. Despite the wide range of temperatures the band shape and position of the bending mode was found to be nearly identical to spectra of similar sized particles measured at 100 K.⁶⁵

The librational band was also observed to be insensitive to temperature. Only an indirect temperature effect is observed: colder temperatures lead to smaller particles and the librational band begins to shift to lower wavenumber position and become broader once the size is reduced beyond 7 nm, consistent with earlier results from small aerosols at 100 K.⁴⁶ This is again due to the decrease in the crystalline core component and increasing amorphous character.^{46, 70} For particles greater than 7 nm the peak position remains very consistent, shifting only slightly from 870 cm^{-1} at 36 K to 860 cm^{-1} at 209 K. Earlier thin film studies found this band maximum in cubic water to be 835 cm^{-1} at 10 K and reduced to 817 cm^{-1} at 140 K,⁷⁰ or 837 cm^{-1} at 20 K down to 825 cm^{-1} at 150 K.⁷ The trend with temperature has a similarly small, negative gradient. The significant difference (ca. 40 cm^{-1}) in band maximum between thin film and aerosol spectrum was noted in the previous aerosol work and attributed to the shape dependence of strong infrared bands of solids affecting the film spectra.⁴⁶ The difference cannot be attributed to non crystalline material in the aerosol as thin films of amorphous ice have peaks at still lower wavenumber (754 cm^{-1} at 15 K to 805 cm^{-1} at 120 K).⁷ A recent analysis of mesospheric ice temperature drew on data from different studies encompassing aerosol and thin film spectra to infer a much stronger temperature dependence for this librational band of crystalline ice and obtain a linear coefficient of $-0.7\text{ cm}^{-1}/\text{K}$ between 120 and 235 K.⁴³ That relationship is not tenable in the light of the present data, and the resultant cloud temperature determinations need re-assessment. While neither of

these bands appear to be useful as a temperature probe they may help characterise particle size or phase.

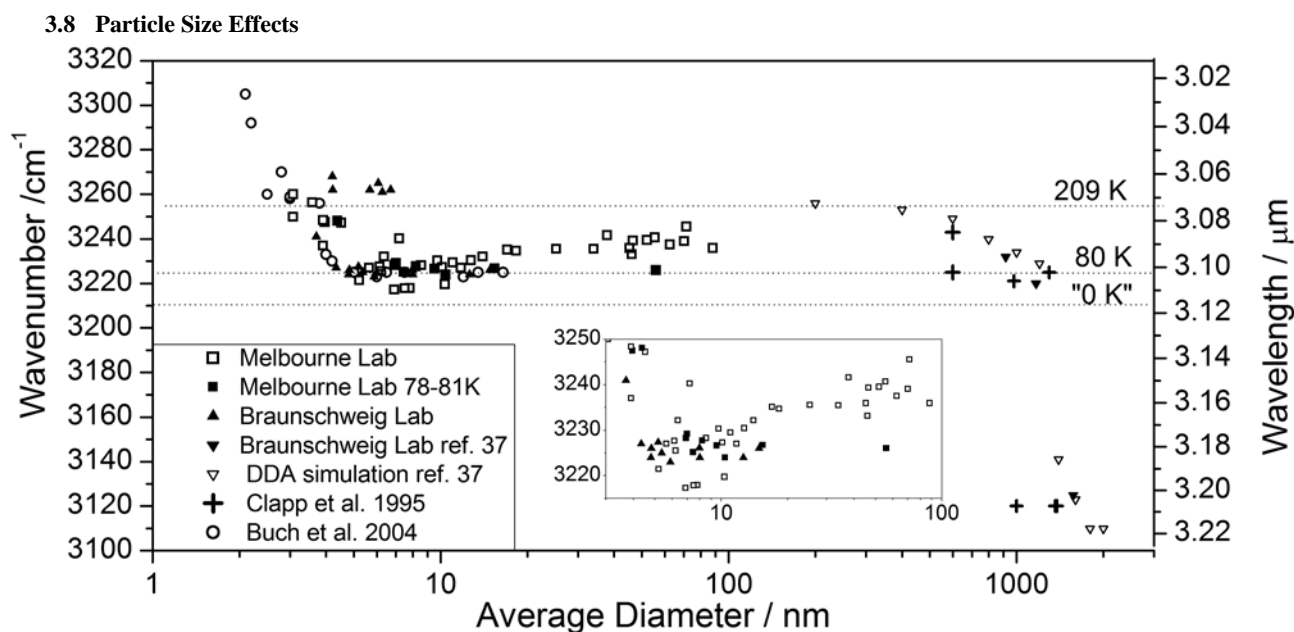


Figure 8 Peak OH stretching wavenumber as a function of particle size. The squares are for spectra taken at the Australian Synchrotron in Melbourne, with the solid filled squares all recorded around 78 K. The triangles are for spectra recorded with an identical cell located in Braunschweig. Literature values are from Buch⁵⁰ Bauerecker (experimental spectra and discrete dipole approximation (DDA) simulations)³⁷ and Clapp⁹. The three horizontal lines show the band positions expected for crystalline ice at 0 K, 80 K and 209 K from the trend line in figure 2.

Different spectral effects become significant for particles at large and small size scales, see figure 8. With smaller particles the contribution of the surface layer of water molecules is increasingly evident. In both the bending and stretching regions, distinct and relatively sharp spectral features associated with three-coordinate molecules in the top-most layer are seen. In the bending region where this band is superimposed over the broad band from the interior, the surface layer peak is evident up to a size of ≈ 25 nm. In the OH stretch region a unique band from the ‘dangling OH’ groups around 3700 cm^{-1} is fortuitously well separated from the interior band profile so that it is detectable in particles up to 70 nm where the intensity ratio is 1:10500. The top-most layer has amorphous character, but the disorder also extends further into a subsurface layer. In experiments performed at 78 K (see the solid square data points in figure 8), the position of the 3 micron water band is constant at around 3226 cm^{-1} until particles shrink to a diameter of 5 nm⁵⁰. At this point the band undergoes a blue shift of $\approx 25\text{ cm}^{-1}$. These observations have been interpreted in terms of a threshold size which allows for the presence of a crystalline core that can dictate the structure of the surface layer. As particle size is reduced even further, the more disordered state that results is characterised by weaker hydrogen bonds with greater O...O distance and more strained O...O...O angles, and the OH stretch modes are correspondingly blue-shifted towards the peak absorption of amorphous ice, *ca.* 3304 cm^{-1} at 10 K⁶⁴. Correspondingly, the librational mode band is shifted down towards the range of positions found in disordered solids at 10 K (763 cm^{-1} for microporous amorphous ice or 810 cm^{-1} for annealed amorphous ice⁷⁰).

In figure 8, the slight upward trend in OH stretch band position seen for intermediate sizes between 8 and 100 nm is solely due to the temperature variation as shown in figure 2. For sizes greater than $\lambda/2\pi$ (≈ 500 nm) scattering in the OH-stretching region becomes increasingly important. This has the effect of *red* shifting the peak absorption by as much as 100 cm^{-1} . For larger

particle sizes the particle shape must also be taken into account as spherical particles may not be favoured for some formation conditions. For example the transition from a compact shape (spherical or cubic) to an elongated shape (5:1 hexagonal column) results in a blueshift of the band centre by more than 100 cm^{-1} for water particles with a mean diameter of $1.6\text{ }\mu\text{m}$.³⁷

The trend in figure 8 is consistent except for some spectra around 5-8 nm. These spectra were all recorded at low bath gas concentration and to show a strong but broadened central peak. This suggests the particles have a significant increase in core component which has some amorphous character. This may be due to the reduced cooling rate from the lower rate of bath gas collisions. The precise dynamics of this are currently uncertain and require further investigation, an increased time resolution may be required. These spectra are presented in the supplementary data along with an expanded discussion.

5 Discussion and Conclusions

The mid infrared spectrum of water ice nanoparticles has been measured over a wide range of formation conditions using a long path collisional cooling cell. The results provide a coherent picture of two major direct influences on their spectroscopy: particle size and temperature. The former is in turn controlled by the sample gas and buffer gas concentrations and also by temperature. A size regime (8-200 nm) was found whereby the peak maximum positions of the OH stretching and librational modes were largely uninfluenced by particle size. This allowed for the measurement of the temperature dependence in the absence of scattering or surface effects. This happens to correspond to the size distribution found for mesospheric ice particles⁴²⁻⁴³, which has been exploited to model ice spectra and thereby extract ice temperatures which are found to be in the 120-160 K range. However, those studies relied on imaginary refractive index constants, *k*, derived directly from spectra of ice

aerosols of around 600 nm diameter.⁹ This present work (see figure 2) indicates that the previous data was shifted *ca.* 10 cm⁻¹ due to scattering from the moderately large sized particles. A shift of this magnitude, though apparently modest, corresponds to a temperature change of 50 K. The need to update the temperature dependant optical constants is clear. This need is reinforced by the present results concerning the librational mode, which is found to be almost invariant with temperature over the range 36-209 K and therefore unsuitable for use as a temperature probe.

While it is clear that the spectra of “large” and “small” aerosol particles can be very different from bulk material (or in practice thin films), ironically enough suitable particle spectra can help to provide the most reliable optical constants for bulk material. But what is the “Goldilocks” zone of particle size most suitable for measuring spectra that reflects the purely absorptive component of crystalline ice? In the bending mode region the lower size limit would appear to be ≈ 30 nm in diameter where the sharper surface feature around 1650 cm⁻¹ finally peters out, but it may prove necessary to employ spectral subtraction to remove this persistent surface component. In the OH stretching mode region the peak maximum is consistent for sizes over 8 nm, but for a given temperature subtle changes in the overall band profile associated with the surface and subsurface layers continue until the size reaches 15 nm, see for example figure 5. The upper particle diameter limits are dictated by the wavelength dependant onset of scattering at sizes $\approx \lambda/2\pi$, or more conservatively $\lambda/4\pi$ corresponding to 250 nm for the OH stretch region, but 500 nm and 1 μ m for the bend and libration regions. In the context of obtaining the best optical constants, control of particle size may therefore prove to be very useful.

6 Acknowledgments

This work was supported by the Australian Synchrotron through beamtime allocations and non-beamtime facility access and an Australian Synchrotron Postgraduate Award (C.M.). Financial support from the Australian Government through an Australian Postgraduate Award to C.M. is also gratefully acknowledged. The research was also supported by the Deutsche Forschungsgemeinschaft (Grant BA 2176/3-1).

7 References

1. E. Herbst and E. F. van Dishoeck, *Annual Review of Astronomy and Astrophysics*, 2009, **47**, 427-480.
2. J. Lelieveld and P. Crutzen, *Journal of Atmospheric Chemistry*, 1991, **12**, 229-267.
3. G. Firanesco, D. Hermsdorf, R. Ueberschaer and R. Signorell, *Physical Chemistry Chemical Physics*, 2006, **8**, 4149-4165.
4. J. E. Bertie, H. J. Labbe and E. Whalley, *The Journal of Chemical Physics*, 1969, **50**, 4501-4520.
5. W. Hagen, A. G. G. M. Tielens and J. M. Greenberg, *Chemical Physics*, 1981, **56**, 367-379.
6. M. M. Maldoni, R. G. Smith, G. Robinson and V. L. Rookyard, *Monthly Notices of the Royal Astronomical Society*, 1998, **298**, 251-258.
7. R. Mastrapa, S. Sandford, T. Roush, D. Cruikshank and C. Dalle Ore, *The Astrophysical Journal*, 2009, **701**, 1347.
8. C. Medcraft, D. McNaughton, C. D. Thompson, D. Appadoo, S. Bauerecker and E. G. Robertson, *The Astrophysical Journal*, 2012, **758**, 17.
9. M. L. Clapp, D. R. Worsnop and R. E. Miller, *The Journal of Physical Chemistry*, 1995, **99**, 6317-6326.
10. R. P. Blickensderfer, G. E. Ewing and R. Leonard, *Applied Optics*, 1968, **7**, 2214-2217.
11. M. Herman, R. Georges, M. Hepp and D. Hurtmans, *International Reviews in Physical Chemistry*, 2000, **19**, 277-325.
12. T. Häber, U. Schmitt and M. A. Suhm, *Phys. Chem. Chem. Phys.*, 1999, **1**, 5573-5582.
13. J. W. Tom and P. G. Debenedetti, *Journal of Aerosol Science*, 1991, **22**, 555-584.
14. E. J. Davis, *Aerosol science and technology*, 1997, **26**, 212-254.
15. S. Bauerecker, F. Taucher, C. Weitkamp, W. Michaelis and H. K. Cammenga, *Journal of Molecular Structure*, 1995, **348**, 237-241.
16. F. Taucher, C. Weitkamp, H. K. Cammenga and S. Bauerecker, *Spectrochimica Acta Part A: Molecular and Biomolecular Spectroscopy*, 1996, **52**, 1023-1027.
17. S. Bauerecker, M. Taraschewski, C. Weitkamp and H. K. Cammenga, *Review of Scientific Instruments*, 2001, **72**, 3946-3955.
18. M. K. Kunzmann, R. Signorell, M. Taraschewski and S. Bauerecker, *Physical Chemistry Chemical Physics*, 2001, **3**, 3742-3749.
19. M. K. Kunzmann, S. Bauerecker, M. A. Suhm and R. Signorell, *Spectrochimica Acta - Part A: Molecular and Biomolecular Spectroscopy*, 2003, **59**, 2855-2865.
20. R. Signorell and D. Luckhaus, *The Journal of Physical Chemistry A*, 2002, **106**, 4855-4867.
21. Ó. F. Sigurbjörnsson and R. Signorell, *Phys. Chem. Chem. Phys.*, 2008, **10**, 6211-6214.
22. S. Bauerecker and E. Dartois, *Icarus*, 2009, **199**, 564-567.
23. E. K. Lang, K. J. Knox and R. Signorell, *Planetary and Space Science*, 2012, <http://dx.doi.org/10.1016/j.pss.2012.10.010>.
24. M. Jetzki, A. Bonnamy and R. Signorell, *The Journal of Chemical Physics*, 2004, **120**, 11775-11784.
25. E. Dartois and S. Bauerecker, *The Journal of Chemical Physics*, 2008, **128**, 154715-154710.
26. R. Signorell, *The Journal of Chemical Physics*, 2003, **118**, 2707-2715.
27. Ó. F. Sigurbjörnsson, G. Firanesco and R. Signorell, *Physical Chemistry Chemical Physics*, 2009, **11**, 187-194.
28. T. C. Preston, G. Firanesco and R. Signorell, *Physical Chemistry Chemical Physics*, 2010, **12**, 7924-7933.
29. R. Signorell and M. K. Kunzmann, *Chemical Physics Letters*, 2003, **371**, 260-266.
30. S. Bauerecker, *Physical Review Letters*, 2005, **94**, 033404.
31. J. P. Devlin, *Physical Chemistry Chemical Physics*, 2011, **13**, 19707-19713.
32. R. Signorell and M. Jetzki, *Faraday Discussions*, 2008, **137**, 51-64.
33. C. Medcraft, E. G. Robertson, C. D. Thompson, S. Bauerecker and D. McNaughton, *Physical Chemistry Chemical Physics*, 2009, **11**.
34. E. G. Robertson, C. Medcraft, L. Puskar, R. Tuckermann, C. D. Thompson, S. Bauerecker and D. McNaughton, *Physical Chemistry Chemical Physics*, 2009, **11**.
35. M. Taraschewski, H. K. Cammenga, R. Tuckermann and S. Bauerecker, *Journal of Physical Chemistry A*, 2005, **109**, 3337-3343.
36. J. Devlin, C. Yinnon and V. Buch, *Physical Chemistry Chemical Physics*, 2009, **11**, 7819-7825.
37. S. Bauerecker, A. Wargenau, M. Schultze, T. Kessler, R. Tuckermann and J. Reichardt, *The Journal of Chemical Physics*, 2007, **126**, 134711-134716.

38. R. Wagner, S. Benz, O. Möhler, H. Saathoff and U. Schurath, *Atmospheric Chemistry and Physics Discussions*, 2006, **6**, 5711-5771.
39. R. Wagner, S. Benz, O. Möhler, H. Saathoff, M. Schnaiter and T. Leisner, *The Journal of Physical Chemistry A*, 2007, **111**, 13003-13022.
40. A. Y. Zasetsky, A. Khalizov, M. Earle and J. Sloan, *The Journal of Physical Chemistry A*, 2005, **109**, 2760-2764.
41. R. Wagner, S. Benz, O. Möhler, H. Saathoff, M. Schnaiter and U. Schurath, *The Journal of Physical Chemistry A*, 2005, **109**, 7099-7112.
42. S. Petelina and A. Zasetsky, *Geophysical Research Letters*, 2009, **36**, L15804.
43. S. Petelina and A. Zasetsky, *Journal of Geophysical Research*, 2011, **116**, D03304.
44. M. E. Hervig and L. L. Gordley, *Journal of Geophysical Research*, 2010, **115**, D15208.
45. J. P. Devlin and V. Buch, *The Journal of Physical Chemistry*, 1995, **99**, 16534-16548.
46. M. W. Severson, J. P. Devlin and V. Buch, *The Journal of Chemical Physics*, 2003, **119**, 4449-4457.
47. J. P. Devlin, C. Joyce and V. Buch, *The Journal of Physical Chemistry A*, 2000, **104**, 1974-1977.
48. V. Buch and J. P. Devlin, *The Journal of Chemical Physics*, 1999, **110**, 3437-3443.
49. V. Buch, L. Delzeit, C. Blackledge and J. P. Devlin, *The Journal of Physical Chemistry*, 1996, **100**, 3732-3744.
50. V. Buch, S. Bauerecker, J. Paul Devlin, U. Buck and J. K. Kazimirski, *International Reviews in Physical Chemistry*, 2004, **23**, 375-433.
51. M. H. Moore and R. L. Hudson, *The Astrophysical Journal*, 1992, **401**, 353-360.
52. J. P. Devlin and V. Buch, *Water in Confining Geometries*, Springer, Berlin, 2003.
53. L. S. Bartell and J. Huang, *The Journal of Physical Chemistry*, 1994, **98**, 7455-7457.
54. J. Huang and L. S. Bartell, *The Journal of Physical Chemistry*, 1995, **99**, 3924-3931.
55. L. S. Bartell, *The Journal of Physical Chemistry*, 1996, **100**, 8197-8199.
56. L. Delzeit and D. Blake, *J. Geophys. Res.*, 2001, **106**, 33371-33379.
57. G. P. Johari, *The Journal of Chemical Physics*, 2005, **122**, 194504-194505.
58. C. J. Gruenloh, J. R. Carney, F. C. Hagemester, C. A. Arrington, T. S. Zwier, S. Y. Fredericks, J. T. Wood III and K. D. Jordan, *The Journal of Chemical Physics*, 1998, **109**, 6601.
59. R. C. Dougherty, *The Journal of Chemical Physics*, 1998, **109**, 7372-7378.
60. K. Rottger, A. Endriss, J. Ihringer, S. Doyle and W. F. Kuhs, *Acta Crystallographica Section B*, 1994, **50**, 644-648.
61. M. S. Bergren, D. Schuh, M. G. Sceats and S. A. Rice, *The Journal of Chemical Physics*, 1978, **69**, 3477-3482.
62. J. W. Schaaf and D. Williams, *JOSA*, 1973, **63**, 726-732.
63. O. B. Toon, M. A. Tolbert, B. G. Koehler, A. M. Middlebrook and J. Jordan, *J. Geophys. Res.*, 1994, **99**, 25631-25654.
64. D. M. Hudgins, S. A. Sandford, L. J. Allamandola and A. G. G. M. A. A. A. Tielens, *The Astrophysical Journal Supplement Series*, 1993, **86**, 713-870.
65. J. P. Devlin, J. Sadlej and V. Buch, *The Journal of Physical Chemistry A*, 2001, **105**, 974-983.
66. J. Sadlej, B. Rowland, J. Devlin and V. Buch, *The Journal of Chemical Physics*, 1995, **102**, 4804.
67. W. Hujo, M. Gaus, M. Schultze, T. Kubař, J. Grunenberg, M. Elstner and S. Bauerecker, *The Journal of Physical Chemistry A*, 2011, **115**, 6218-6225.
68. S. Bauerecker and B. Neidhart, *The Journal of Chemical Physics*, 1998, **109**, 3709.
69. S. Bauerecker and B. Neidhart, *Science*, 1998, **282**, 2211-2212.
70. W. Hagen and A. G. G. M. Tielens, *Spectrochimica Acta Part A: Molecular Spectroscopy*, 1982, **38**, 1089-1094.

Declaration for Thesis Chapter 3.4

Declaration by candidate

In the case of Chapter 3.4 the nature and extent of my contribution to the work was the following:

Nature of contribution	Extent of contribution (%)
Initiation, key ideas, experimental, development and writing up	80%

The following co-authors contributed to the work. Co-authors who are students at Monash University must also indicate the extent of their contribution in percentage terms:

Name	Nature of contribution	Extent of contribution (%) for student co-authors only
E.G. Robertson	Initiation and key ideas	
C.D. Thompson	Experimental assistance, Initiation and key ideas	
S. Bauerecker	Initiation and key ideas	
D. McNaughton	Initiation and key ideas	

Candidate's
Signature

	Date
--	-------------

Declaration by co-authors

The undersigned hereby certify that:

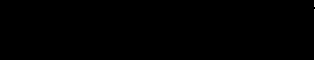
- (1) the above declaration correctly reflects the nature and extent of the candidate's contribution to this work, and the nature of the contribution of each of the co-authors.
- (2) they meet the criteria for authorship in that they have participated in the conception, execution, or interpretation, of at least that part of the publication in their field of expertise;
- (3) they take public responsibility for their part of the publication, except for the responsible author who accepts overall responsibility for the publication;
- (4) there are no other authors of the publication according to these criteria;
- (5) potential conflicts of interest have been disclosed to (a) granting bodies, (b) the editor or publisher of journals or other publications, and (c) the head of the responsible academic unit; and
- (6) the original data are stored at the following location(s) and will be held for at least five years from the date indicated below:

Location(s)

Monash, University, School of Chemistry
--

[Please note that the location(s) must be institutional in nature, and should be indicated here as a department, centre or institute, with specific campus identification where relevant.]

Signature 1

	3-12-2012
---	------------------

Signature 2

--	--

Signature 3

--	--

Signature 4

--	--

Infrared spectroscopy of ozone and hydrogen chloride aerosols

Chris Medcraft,^a Eyan G. Robertson,^{*a} Chris D. Thompson,^a Sigurd Bauerecker^b and Don McNaughton^a

Received 17th March 2009, Accepted 23rd April 2009

First published as an Advance Article on the web 2nd June 2009

DOI: 10.1039/b905424n

Aerosols of ozone have been generated in a collisional cooling cell and observed over a small temperature range *via* FTIR spectroscopy, with the phase transition from the vapour taking place in the range 80–84 K. The condensed phase bands at 1038 cm⁻¹ (ν_3) and 2105 cm⁻¹ ($\nu_1 + \nu_3$) were assigned to the liquid phase. Aerosols were also generated from mixtures of ozone and HCl. In the presence of liquid ozone aerosols, evidence of solvated HCl was observed *via* a broad IR band 2795 cm⁻¹. Notably, production of a metastable, amorphous solid phase of HCl (exhibiting a narrow band at 2780 cm⁻¹) was favoured to the extent that it could be generated in large excess over the crystalline orthorhombic form that usually dominates at 80 K.

Introduction

Atmospheric aerosols play an extremely important role in the absorptive and reflective characteristics of Earth's atmosphere.¹ Particles in the atmosphere also provide nucleation sites for water ice crystals to form (clouds).² They can also act as sites for reactions to take place, such as the catalytic destruction of ozone by chlorine oxides.^{1,3}

IR spectroscopy is widely used to monitor chemical species found in the atmosphere, both by remote detection and directly in the more controlled environments of the laboratory. FTIR spectroscopy is particularly suited for studying small particles because it is able to perform a large number of scans in a short time, enabling analysis as the particles change with time. Generation and study of condensed phase particles requires careful control of composition, temperature and pressure, such as may be afforded by a collisional cooling cell. A cell designed by one of us⁴ has been successfully employed to examine particles of CO₂,^{5–7} N₂O,^{6,8,9} H₂O,⁷ SO₂¹⁰ and ethane.¹¹ We have constructed a duplicate cell and coupled it to a high resolution FTIR instrument.

The main subject of this study, ozone, is best known for its role in shielding the Earth's surface from UV radiation, but it has even been detected on Mars,¹² on Ganymede, Jupiter's largest moon¹³ and on two icy satellites of Saturn, Rhea and Dione.¹⁴ Industrial applications include widespread usage as a disinfectant and as an oxidant. The first IR spectrum of ozone was measured over 100 years ago by Knut Ångström, son of Anders Ångström.¹⁵ Since stratospheric ozone depletion was discovered in the 1970's¹ extensive IR studies have been conducted on gaseous ozone to facilitate atmospheric monitoring.^{3,16} IR spectra have also been measured for ozone in solid phases^{14,17,18} or in cryogenic solutions^{19,20} where its low temperature reactions are of considerable interest,²¹ but

not in aerosol or neat liquid form. Here, we describe the first characterisation of liquid ozone aerosols by FTIR spectroscopy. In an accompanying paper, we have examined solid phase HCl aerosols, and the reaction with NH₃ to produce NH₄Cl.²² Here, we extended this to explore the effect of ozone aerosols on low temperature HCl particle formation.

Experimental

Aerosol particles were generated using a variable temperature collisional cooling cell coupled to a Bruker 120 HR FTIR spectrometer. The cell has been described in the accompanying paper²² and the design in much greater detail earlier.⁴ Ozone (O₃) is an unstable allotrope of oxygen and cannot be stored for any significant length of time therefore it must be produced *in situ* and used immediately. Oxygen gas (BOC industrial grade) was allowed to flow slowly through an ozone generator (Ozotech[®] Poseidon model) to produce a mixture of *ca.* 5% ozone in oxygen. Once the total pressure in the inlet gas line had reached 20 psi, a magnetic valve was activated to allow a short pulse of the ozone mixture into the cooling cell. A pulse duration of 100 ms was employed, unless otherwise specified. This was found to be sufficient time to allow enough ozone into the cell to give suitable absorbance values but not long enough to significantly exceed the particle formation times found in previous experiments using such a cell.^{6,7} The multi-pass cell, with optical path length set to 7.5 m, contained cold nitrogen gas to serve as a buffer and to cool the sample *via* inelastic collisions.

Binary particles of ozone and hydrogen chloride were also formed and analysed with HCl introduced *via* a separate inlet line, connected to a premixed cylinder of 5% (by volume) HCl in helium. The total input pressure was 15 psi and the pulse length was 60 ms.

All the spectra were taken at a resolution of 1 cm⁻¹ in coadditions of 10 scans spaced 40 s apart. It should be noted that scans were initiated manually following activation of the magnetic valves. As a consequence, the start time may vary by a few seconds (up to 2 s).

^a School of Chemistry, Monash University, Victoria 3800, Australia.
E-mail: E.Robertson@latrobe.edu.au

^b Institut für Physikalische und Theoretische Chemie,
Technische Universität Braunschweig, Hans-Sommer-Strasse 10,
D-38106 Braunschweig, Germany

Results and discussion

Ozone aerosols

Ozone is a bent triatomic molecule and hence has three fundamental vibrations. The symmetric stretch (ν_1) is observed at approximately 1103 cm^{-1} , the antisymmetric stretch (ν_3) is at 1042 cm^{-1} and the bend (ν_2) is at 701 cm^{-1} .²³

The ν_1 band is very weak and the use of calcium fluoride windows to allow water and ammonia to be introduced into the cell precluded observation of the bending mode because CaF_2 is opaque to radiation below 950 cm^{-1} . In practice only the ν_3 fundamental and the $\nu_1 + \nu_3$ combination bands could be observed under our experimental conditions and the ν_3 band was the most useful in determining the physical state of the ozone due to its greater intensity.

Fig. 1 shows the variation in IR spectra of ozone as a function of the cell temperature. Based on the IR absorbance values for the ν_3 band of gaseous ozone at 90 K, the resultant concentration of ozone is *ca.* $5\text{ }\mu\text{mol L}^{-1}$, corresponding to a partial pressure of 0.04 mbar at 90 K. Under equilibrium conditions, the lowest temperature at which this level of ozone may be maintained entirely in the vapour phase is 86 K.²⁴ Spectra from the cold cell indicate the onset of a transition from gas to condensed phase occurred at approximately 82–83 K. At and above 82 K the P, Q and R rotational branches of the ν_3 band can be clearly seen in the first spectrum taken after gas injection. Between 82 K and 79 K, this rotational sub-structure diminishes, and is replaced by a single peak. The spectra in this intermediate temperature regime may be modelled by summing contributions from gaseous ozone molecules and of condensed ozone.

The condensed phase bands at 1038 cm^{-1} and 2105 cm^{-1} have FWHM widths of 16 cm^{-1} and 11 cm^{-1} , respectively. The band centres are similar to those for ozone in liquid oxygen: 1035 cm^{-1} (width 4 cm^{-1}) and 2102 cm^{-1} (width 6 cm^{-1}),¹⁹ although the widths are greater. This is also comparable to the bands at 1037 cm^{-1} (width 9 cm^{-1}) and 2110 cm^{-1} (width 11 cm^{-1}) that Chaabouni *et al.* assigned to

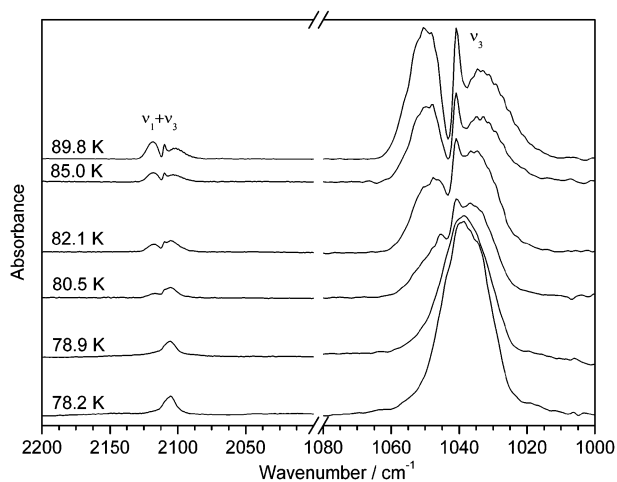


Fig. 1 Spectra of the $\nu_1 + \nu_3$ (left) and ν_3 (right) bands of ozone, labelled with the cell temperature. The pressure of cold nitrogen gas was 200 mbar. Maximum absorbance was 0.8.

an amorphous solid phase of ozone.¹⁸ This amorphous phase was produced by deposition at lower temperatures ($< 20\text{ K}$) than the crystalline phase which has bands with much smaller widths of about 2 to 3 cm^{-1} that are also shifted (ν_3 is found at 1027 cm^{-1}). The melting point of ozone is 80.7 K ,²⁵ so it is possible that solid ozone could be formed when our cell is cooled below this temperature. Based on the observations of Chaabouni *et al.* a solid formed at these temperatures would be in the crystalline phase not the amorphous phase. However, the observed band positions and widths in our aerosol spectra do not match those of the crystalline phase. The agreement with disordered amorphous solid phase spectra suggests instead that the condensed phase of ozone that we observe is a liquid (which is also disordered).

The Bartell index, R_c , is an empirical measure of the propensity of a substance to form liquid clusters in a jet expansion (and has been found to correspond well with the results of these types of experiments for other molecules).²⁶ It uses the difference in melting and boiling points and a small entropy correction term to determine this:

$$R_c = \frac{(T_b - T_m)}{T_b} + 0.007 \left(\frac{\Delta S_m}{R} \right)^2 \quad (1)$$

where T_b is the boiling point, T_m is the melting point, and ΔS_m is the entropy change associated with melting. If the R_c value for the bulk phase is greater than 0.32 then the clusters are likely to be liquid.^{11,14,26} The R_c value for ozone is calculated to be 0.54, supporting the conclusion that the condensed aerosol spectra are indeed of liquid ozone.

Fig. 2 shows how the shape of both the ν_3 and $\nu_1 + \nu_3$ bands changes with backing pressure. At the lowest pressures the bands display the PQR structure associated with the vapour phase spectra. This is the result of a slow rate of cooling with the lower pressure of buffer gas present. Loss of sample by rapid diffusion and trapping on the outer cell walls leads to the low absorbance seen in these spectra. Absorbance reaches a maximum at *ca.* 200 mbar of buffer gas, where there is little sign of the vapour component and the spectrum is dominated by the liquid phase band. At 1000 mbar, the ν_3 band is much reduced overall and the vapour phase component is slightly

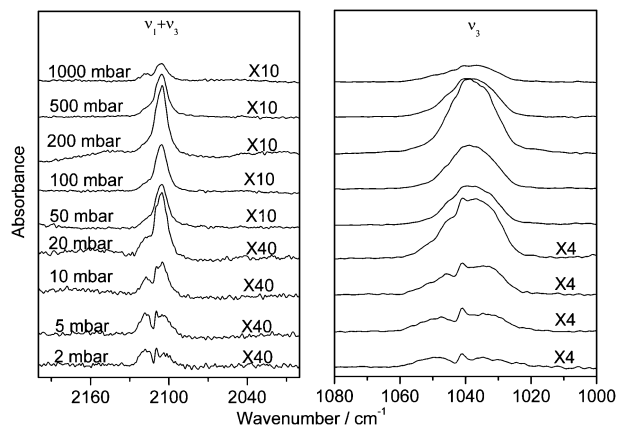


Fig. 2 Spectra of the $\nu_1 + \nu_3$ (left) and ν_3 (right) bands of ozone taken at approximately 78 K and at various pressures. The maximum absorbance in the ν_3 region was 0.8.

more prominent, superimposed on the underlying liquid phase band. A reduction in absorbance and the presence of features associated with warmer spectra are commonly observed for a range of sample molecules when high buffer pressures are used.²² Slightly reduced sample inflow and turbulent flow are just two of the factors associated with these observations.

Following injection of the sample, the spectra change over time, as illustrated in Fig. 3. It is evident that a small variation in temperature (2.2 K) creates a dramatic difference in the resultant spectra and how they evolve with time. The first spectrum at 80.4 K is dominated by the liquid phase aerosol component, but has a minor contribution from the gas phase. The liquid phase component diminishes rapidly, presumably due to evaporation and subsequent loss of the sample from trapping on the walls, leaving spectra characteristic of gaseous ozone. With slower evaporation at 78.2 K, the liquid phase appearance of the spectrum is preserved over time, and the overall absorbance declines more gradually.

Ozone–hydrogen chloride binary aerosols

Spectroscopic analyses of aerosols of hydrogen chloride alone and with water and ammonia are presented in an accompanying paper.²² In the experiments presented here, binary particles of ozone and hydrogen chloride were generated.

Fig. 4 shows spectra in the regions of the HCl fundamental and the ν_3 band of ozone. The two strong peaks at 2718 cm^{-1} and 2755 cm^{-1} are the result of the longitudinal and transverse vibrational modes of HCl in the orthorhombic crystal phase.²⁷ The presence of gaseous ozone (lower solid curve) does not influence the HCl spectrum significantly, other than to slightly increase the intensity of the 2755 cm^{-1} peak. The presence of liquid ozone (upper solid curve) gives rise to new features. The narrow peak at 2780 cm^{-1} is another solid phase, also observed previously in HCl aerosols.²²

The broad peak at 2795 cm^{-1} is observed only when liquid ozone is present and has not been seen in other experiments with HCl. Its intensity depends on the level of ozone aerosol present, governed by the amount injected into the cell, as shown in Fig. 5. It is hypothesised to be the result of HCl

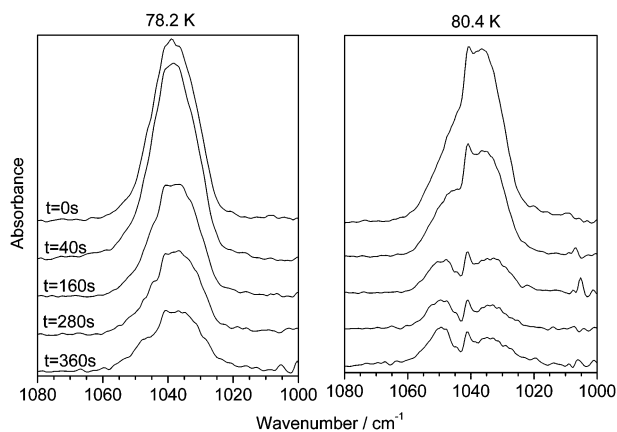


Fig. 3 Temporal evolution of the ν_3 band at 78.2 K (left) and 80.4 K (right). Successive spectra are measured approximately 30 seconds apart. The maximum absorbance was 0.50 at 78.2 K and 0.47 at 80.4 K.

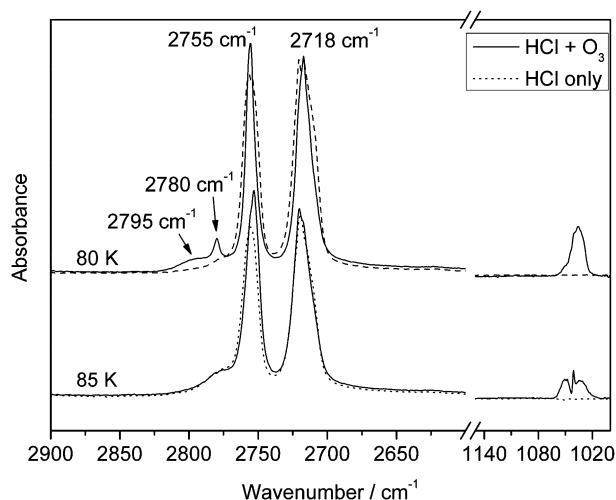


Fig. 4 Spectral comparison of ozone–HCl binary aerosol and HCl alone at 80 K (top) and at 85 K when the ozone is gaseous (bottom). Backing pressure 100 mbar, maximum absorbance = 1.9.

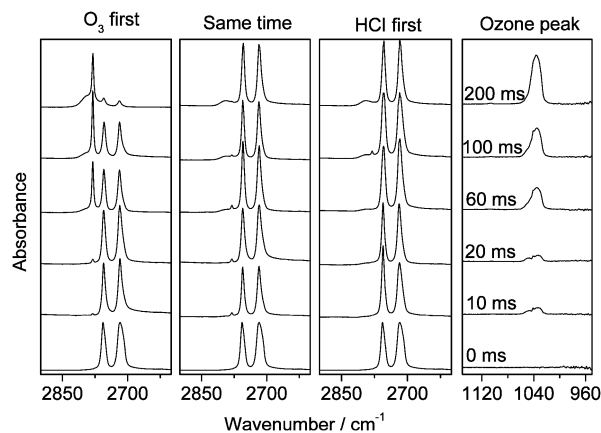


Fig. 5 Variation in O_3 –HCl spectra as a function of the amount of ozone introduced (expressed as pulse duration), and of the synchronisation of the 2 sample pulses. Cell temperature 80 K, pressure of N_2 buffer gas 200 mbar N_2 , maximum absorbance 2.1.

embedded inside liquid ozone droplets. The band position at 2795 cm^{-1} rules out isolated HCl molecules in ozone solution. The HCl monomer band in N_2 matrix, for example, is observed at 2852 cm^{-1} ,²⁸ only slightly shifted from the gas phase band centre of 2885 cm^{-1} . The liquid phase IR band of HCl however is centred at 2792 cm^{-1} .²⁹ In the accompanying paper,²² density functional theory (DFT) calculations at the B3LYP level using the 6–311+G(d,p) basis were performed on chains of HCl up to fifteen molecules long. The transverse and longitudinal stretch modes were predicted to be shifted around -150 cm^{-1} and -200 cm^{-1} , respectively, in good agreement with observation. Additional calculations on short chains of 3–5 HCl molecules with an ozone molecule H-bonded to one end suggested that the vibration closely associated with the final HCl stretch is shifted around -80 cm^{-1} from the gaseous monomer. All this suggests that HCl forms small or disordered aggregates of some kind within or on the surface of the ozone microdroplets, giving rise to the 2795 cm^{-1} band.

The narrow band at 2780 cm^{-1} , attributed to a metastable solid phase of HCl, is affected by the amount of ozone aerosol present, but also critically by the synchronisation of the sample pulses. It is greatly enhanced when ozone is injected first, as shown in the top left-hand spectrum of Fig. 5. A spectrum with comparable peak ratios is obtained when a 100 ms pulse of ozone is followed 0.2 s later by a 10 ms pulse of HCl, with ozone again in considerable excess. Presumably, with 200 mbar of N_2 buffer gas at 80 K the orthorhombic form of HCl is able to nucleate at a greater rate than that of ozone aerosol formation, so that even when the injections are simultaneous there is little HCl available to generate the metastable form by the time the ozone aerosols have condensed. In the presence of ozone aerosol, however, the metastable phase is produced in substantial quantities and persists for a few minutes, as seen in Fig. 6. The temporal evolution of the spectra shows that while the 2795 cm^{-1} band diminishes slowly in proportion to the ozone aerosol band, the orthorhombic bands ($2718, 2755\text{ cm}^{-1}$) grow at the expense of the metastable solid (2780 cm^{-1}). At the same time the IR absorbance in the high wavenumber region of the spectrum continues to increase due to scattering, indicating growth in particles to a maximum size of 500–1000 nm. In the absence of ozone, HCl particles of comparable size are generated only at elevated temperatures of 90–95 K.²² In both cases, it is slow growth in the orthorhombic crystal that allows larger particles to form.

Savoie and Anderson report a band at 2778 cm^{-1} of comparable width to that seen here.¹⁷ They assigned it to a metastable phase, noting that its intensity was not reproducible. It was particularly prominent in some crystals deposited at 10 K, and appeared to be enhanced in the presence of impurities. In considering our experiments, it is difficult to state just what processes involving ozone aerosols give rise to the enormous enhancement of the metastable solid. The initial injection of the ozone sample and its condensation could produce a small rise in temperature, but the metastable form is seen to persist for minutes. It is more likely related to the

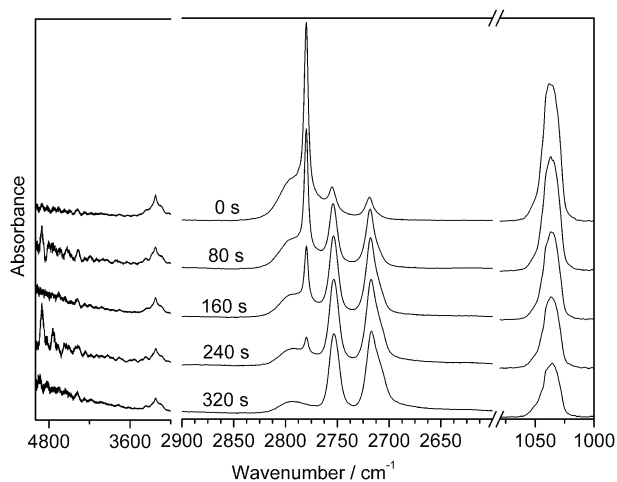


Fig. 6 Temporal evolution of the $\text{O}_3\text{-HCl}$ spectra at 200 mbar N_2 and 80 K when a 200 ms pulse from the ozone inlet is delivered 200 ms prior to a 60 ms pulse from the HCl inlet. Maximum absorbance was 1.6. The weak band at 3200 cm^{-1} is due to traces of water clusters.

solvent-like property of the liquid ozone. Rapid absorption of HCl molecules could serve to reduce the partial pressure of HCl vapour and to provide an alternative environment for aggregation.

Conclusions

With the fine control of temperature and background pressure afforded by a collisional cooling cell it has been possible to generate liquid ozone aerosols, and so observe the vapour to liquid phase transition *via* FTIR spectroscopy. These first spectra of neat liquid ozone are very similar to those of ozone in liquid oxygen solutions,¹⁹ and in its amorphous, solid phase.¹⁸

Even at low temperatures, ozone is sufficiently reactive that it can induce oxidation reactions.²¹ Here, we have shown that, acting as a solvent, it can affect the physical processes of crystallisation. In the presence of ozone aerosols, evidence of solvated HCl was observed. Notably, production of a metastable, disordered solid phase of HCl was favoured to the extent that it could be generated in large excess over the crystalline orthorhombic form that usually dominates at 80 K. Slow conversion to the orthorhombic form led to growth of much larger crystals than could be formed with HCl alone.

Acknowledgements

Financial support from the Australian Research Council and the Australian Government through an Australian Postgraduate Award (C.M.) is gratefully acknowledged. Quantum chemistry calculations were carried out using the Australian Partnership for Advanced Computing (APAC) National Facility.

Notes and references

- 1 NASA. Stratospheric Ozone. Studying Earth's Environment From Space [Online] 2000. http://www.ccpo.odu.edu/SEES/ozone/oz_class.htm.
- 2 G. P. Brasseur and S. Solomon, *Aeronomy of the middle atmosphere: chemistry and physics of the stratosphere and mesosphere*, Springer, Dordrecht, 2005. ISBN 1-4020-3284-6.
- 3 J. M. Flaud, *Atlas of ozone spectral parameters from microwave to medium infrared*, Academic Press, Boston, 1990.
- 4 S. Bauerecker, M. Taraschewski, C. Weitkamp and H. K. Cammenga, *Rev. Sci. Instrum.*, 2001, **72**, 3946.
- 5 S. Bauerecker, *Phys. Rev. Lett.*, 2005, **94**, 033404.
- 6 R. Signorell, M. Jetzki, M. K. Kunzmann and R. Ueberschaer, *J. Phys. Chem. A*, 2006, **110**, 2890.
- 7 M. Taraschewski, H. K. Cammenga, R. Tuckermann and S. Bauerecker, *J. Phys. Chem. A*, 2005, **109**, 3337.
- 8 M. K. Kunzmann, R. Signorell, M. Taraschewski and S. Bauerecker, *Phys. Chem. Chem. Phys.*, 2001, **3**, 3742.
- 9 M. K. Kunzman, S. Bauerecker, M. A. Suhm and R. Signorell, *Spectrochim. Acta, Part A*, 2003, **59**, 2857.
- 10 R. Signorell and M. Jetzki, *Faraday Discuss.*, 2008, **137**, 51.
- 11 S. Bauerecker and E. Dartois, *Icarus*, 2009, **199**, 564.
- 12 C. A. Barth, C. W. Hord and A. I. Stewart, *Science*, 1973, **179**, 795.
- 13 K. S. Noll, R. E. Johnson, A. L. Lane, H. A. Domingue and H. A. Weaver, *Science*, 1996, **273**, 341.
- 14 K. S. Noll, D. P. Roush, D. P. Cruikshank, R. E. Johnson and Y. J. Pendleton, *Nature*, 1997, **388**, 45.
- 15 K. Ångström, *Ark. Mat. Astron. Fys.*, 1904, **1**, 347–395.
- 16 C. P. Rinsland, J.-M. Flaud, A. Perrin, M. Birk, G. Wagner, A. Goldman, A. Barbe, M. R. De Backer-Barilly, S. N. Mikhailenko, VI. G. Tyuterev, M. A. H. Smith, V. Malathy Devi, D. Chris Brenner, F. Schreier, K. V. Chance,

-
- J. Orphal and T. M. Stephen, *J. Quantum Spectrosc. Radiat. Transfer*, 2003, **82**, 207.
- 17 R. Savoie and A. Anderson, *J. Chem. Phys.*, 1966, **44**, 548.
- 18 H. Chaabouni, L. Schriver-Mazzuoli and A. Schriver, *J. Phys. Chem. A*, 2000, **104**, 6962.
- 19 K. M. Bulanin, M. O. Bulanin and A. A. Tsyganenko, *Chem. Phys.*, 1996, **203**, 127.
- 20 P. F. Zittel, *J. Phys. Chem.*, 1991, **95**, 6802.
- 21 O. V. Manoilova, J. C. Lavalley, N. M. Tsyganenko and A. A. Tsyganenko, *Langmuir*, 1998, **14**, 5813.
- 22 E. G. Robertson, C. Medcraft, L. Puskar, R. Tuckermann, C. D. Thompson, S. Bauerecker and D. McNaughton, *Phys. Chem. Chem. Phys.*, 2009, **11**, DOI: 10.1039/B905425C (accompanying paper).
- 23 D. J. McCaa and J. H. Shaw, *J. Mol. Spectrosc.*, 1968, **25**, 374.
- 24 D. Hanson and K. Mauersberger, *J. Chem. Phys.*, 1986, **85**, 4669.
- 25 A. G. Streng, *J. Chem. Eng. Data*, 1971, **16**, 357.
- 26 L. S. Bartell, L. Harsanyi and E. J. Valentet, *J. Phys. Chem.*, 1989, **93**, 6201.
- 27 R. Savoie and M. Pezolet, *J. Chem. Phys.*, 1969, **50**, 2781.
- 28 K. B. Harvey and H. F. Shurvell, *Can. J. Chem.*, 1967, **45**, 2689.
- 29 P. Khatibi and H. Vu, *J. Chim. Phys. Phys.-Chim. Biol.*, 1972, **69**, 654.

Declaration for Thesis Chapter 3.5

Declaration by candidate

In the case of Chapter 3.5 the nature and extent of my contribution to the work was the following:

Nature of contribution	Extent of contribution (%)
Initiation, key ideas, experimental, development and writing up	60

The following co-authors contributed to the work. Co-authors who are students at Monash University must also indicate the extent of their contribution in percentage terms:

Name	Nature of contribution	Extent of contribution (%) for student co-authors only
E.G. Robertson	Initiation, key ideas, writing up	
L. Puskar	Experiments	
R. Tuckermann	Experiments	
C.D. Thompson	Initiation and key ideas	
S. Bauerecker	Initiation and key ideas	
D. McNaughton	Initiation and key ideas	

Candidate's
Signature

	Date
--	-------------

Declaration by co-authors

The undersigned hereby certify that:

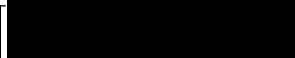
- (1) the above declaration correctly reflects the nature and extent of the candidate's contribution to this work, and the nature of the contribution of each of the co-authors.
- (2) they meet the criteria for authorship in that they have participated in the conception, execution, or interpretation, of at least that part of the publication in their field of expertise;
- (3) they take public responsibility for their part of the publication, except for the responsible author who accepts overall responsibility for the publication;
- (4) there are no other authors of the publication according to these criteria;
- (5) potential conflicts of interest have been disclosed to (a) granting bodies, (b) the editor or publisher of journals or other publications, and (c) the head of the responsible academic unit; and
- (6) the original data are stored at the following location(s) and will be held for at least five years from the date indicated below:

Location(s)

Monash University, School of Chemistry

[Please note that the location(s) must be institutional in nature, and should be indicated here as a department, centre or institute, with specific campus identification where relevant.]

Signature 1

	3-12-2012
---	------------------

Signature 2

--	--

Signature 3

--	--

Signature 4

--	--

Signature 5

--	--

Signature 6

--	--

IR spectroscopy of physical and chemical transformations in cold hydrogen chloride and ammonia aerosols

Evan G. Robertson,^{*a} Chris Medcraft,^a Ljiljana Puskar,^{ab} Rudolf Tuckermann,^c Chris D. Thompson,^a Sigurd Bauerecker^c and Don McNaughton^a

Received 17th March 2009, Accepted 23rd April 2009

First published as an Advance Article on the web 2nd June 2009

DOI: 10.1039/b905425c

Aerosol particles of hydrogen chloride corresponding to three distinct solid phases have been generated in a collisional cooling cell and observed *via* FTIR spectroscopy. The cubic phase of HCl was observed with cell temperatures of 90–100 K, while the highly ordered orthorhombic phase predominated below this temperature. The previously reported metastable phase was also observed under some conditions. Density functional theory calculations at the B3LYP/6–311 + G(d,p) level were performed on HCl clusters with a planar, zig-zag arrangement. Computed IR spectra for chain lengths up to 15 converge to show a band shape that is characteristic of the orthorhombic HCl phase. Injection of water along with HCl was found to have little influence on the formation of HCl particles. The reaction between HCl and NH₃ to produce NH₄Cl particles was also examined and found to occur over a wide range of temperatures (80–300 K). The formation of homogenous particles of HCl and NH₃ competed with this chemical reaction as the cell temperature was lowered and when higher pressures of N₂ buffer gas were used.

Introduction

Interstellar dust constitutes most of the solid matter in the universe.¹ These particles are mostly composed of carbon and silicates and it is thought that they contain many different organic molecules on their surface.¹ It is postulated that the particles act as catalysts for the formation of more complex molecules by providing a surface where smaller molecules can condense.^{2,3} The composition and structure of the particles may be understood by recording the IR spectrum of the interstellar dust with a telescope and comparing it to the results obtained in the laboratory.

The same is true for atmospheric aerosols that play an extremely important role in the absorptive and reflective characteristics of Earth's atmosphere.⁴ Atmospheric particles also provide nucleation sites for water ice crystals to form (clouds).⁵ Artificial nanoparticles have been used to promote cloud formation and rainfall in dry climates; other particles have even been suggested as a means to mitigate the effects of global warming.^{3,6}

Particles containing hydrogen chloride are of particular interest due to their possible involvement in reactions in the atmosphere,⁷ and they have also been detected in the interstellar medium.⁸ Solid HCl has been studied in detail as thin films and as single crystals⁹ and has been found to have three crystalline phases:

I. A cubic phase (I) above 120 K, where the chlorine atoms are in an ordered cubic lattice, but the hydrogen atoms

are disordered and can be found in 12 equally probable locations.¹⁰

II. A less ordered orthorhombic phase (II) above 98.4 K, where the Cl atoms are located in the same positions but with the H atom located in one of two equally probable locations ("up or down the chain").¹¹ This phase is not observed in DCl.

III. A highly ordered face centred orthorhombic phase (III) below 98.4 K, where the molecules are arranged in planar zig-zag chains (Fig. 1).¹²

The transition from the high temperature orthorhombic phase (II) to the cubic phase (I) is associated with a sudden change in chlorine positions at 120 K, as determined by crystallography. No manifestation of this phase change is evident in IR spectra, and even in Raman spectra it can be detected only by examining the polarisation ratios as there is no change in the peak positions or widths.⁹ On the other hand, the phase transition at 98 K is easily observed. The low temperature orthorhombic phase (III) shows two characteristic

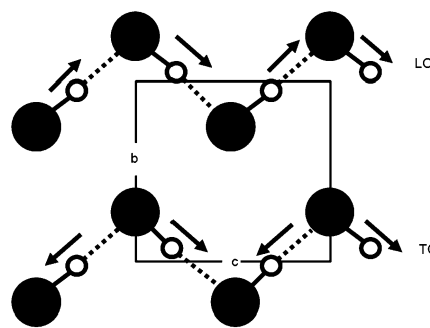


Fig. 1 The crystal structure of the low temperature orthorhombic phase (III) of HCl showing the longitudinal optic (LO) and transverse optic (TO) vibrational modes.

^a School of Chemistry, Monash University, Victoria 3800, Australia. E-mail: E.Robertson@latrobe.edu.au

^b Australian Synchrotron, 800 Blackburn Rd, Clayton, Victoria, 3168, Australia

^c Institut für Physikalische und Theoretische Chemie, Technische Universität Braunschweig, Hans-Sommer-Strasse 10, D-38106 Braunschweig, Germany

peaks in the infrared spectrum due to the symmetrically and antisymmetrically coupled vibrations^{13,14} at approximately 2710 cm⁻¹ and 2750 cm⁻¹, respectively.^{15,16} These vibrations are also described as being the longitudinal and transverse optical modes (Fig. 1).

Unlike the solid phases, HCl aerosols have received little attention. In this study a collisional cooling cell (Fig. 2) was used to generate hydrogen chloride aerosols as well as binary aerosols of hydrogen chloride with (a) water and (b) ammonia. Designed by one of the authors,¹⁷ our cell serves to generate cooled gases and aerosols through collisions with a cold buffer gas (typically N₂ or He). The cell may be operated in either a static mode or flow-through mode, allowing the analysis of transients and performing time-resolved studies. The device may be spectroscopically probed *via* multi-pass optics separated by 0.625 m, enabling an optical-path of up to 20 m, and in this instance the instrument is coupled to a high resolution FTIR spectrometer.

Experimental

Early studies using this kind of cell performed by Bauerecker *et al.* investigated spectral changes corresponding to the monomer through to crystalline clusters across the temperature descent from 300 K to 5 K for CO and CO₂. Rovibrational structure for CO was observed to slowly coalesce into broad bands once below 40 K and bands corresponding to the amorphous species could be distinguished from the crystalline phase.¹⁷ In later papers Bauerecker and Signorell *et al.* examined the nature of mixed isotopomer systems (¹²CO₂-¹³CO₂, N₂O-¹²CO₂) at 78 K.^{18,19} By injecting temporally displaced gas pulses into the cell, 'core-shell composite nanoparticles' were observed to exhibit distinct spectral

signatures for each layer of the particle. Analogous spectral features were observed in another study by Kunzmann *et al.* for N₂O, where relative intensities for bands corresponding to either core or surface vibrations were used to estimate particle-size in the sub-nm to ~50 nm range.²⁰ A number of other studies have been performed on CO₂,²¹⁻²³ N₂O,^{21,22} H₂O,²² SO₂,²⁴ and ethane.²⁵

Hydrogen chloride gas (5% in helium) at various inlet pressures (stated in figure captions) was injected into the cell in short pulses *via* an electronically controlled magnetic valve. A pulse duration of 50 ms was employed, unless otherwise specified, and a pressure of 1.7 bar was applied. The multi-pass cell, with optical-path length set to 7.5 m, contained cold nitrogen gas to serve as a buffer and to cool the sample *via* inelastic collisions. Based on the IR absorbance values for orthorhombic crystalline HCl,²⁶ the resultant HCl concentration may be evaluated as *ca.* 2.5 μmol L⁻¹, corresponding to a partial pressure of 0.02 mbar at 90 K.

Binary particles of hydrogen chloride and water or ammonia were also formed and analysed. The second gas was introduced *via* a separate inlet line, connected to premixed cylinders. The water cylinder contained 0.24% water in nitrogen (by volume), and the ammonia was 5% in nitrogen (by volume). Extensive cleaning of the cell was required following deposition of NH₄Cl. The usual precaution of venting vacuum pump exhaust outside the building was observed.

All spectra were recorded on a Bruker HR120 instrument at a resolution of 1 cm⁻¹ in coadditions of 10 scans spaced 40 s apart. It should be noted that scans were initiated manually following activation of the magnetic valves. As a consequence, the start time may vary by up to 2 s.

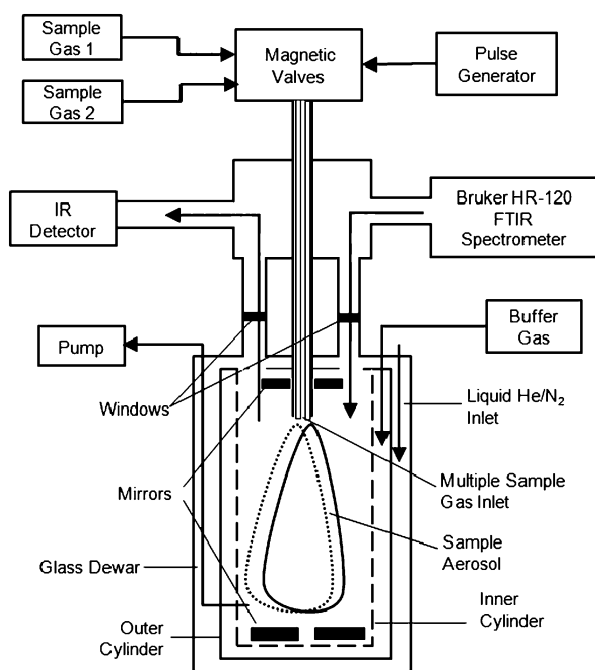


Fig. 2 Schematic drawing of the experimental set-up, modified from ref. 20.

Results and discussion

Pure hydrogen chloride aerosols

The IR spectra in Fig. 3 illustrate the effect of buffer gas temperature on the physical state of HCl, and provide evidence of different phases. The 300 K spectrum has only the rovibrational lines associated with gaseous HCl molecules. These transitions are quite intense in spectra down to 100 K, and then fall away rapidly although traces are evident even at 90 K. Equilibrium vapour pressures are not known for temperatures below 122 K, but the observation that phase transitions begin at around 105 K is consistent with a pressure of 0.02 mbar extrapolated from the Antoine parameters for 122–188 K.^{27,28}

At 80 K only the two peaks at 2755 cm⁻¹ and 2718 cm⁻¹, characteristic of the low temperature orthorhombic crystal phase (III), appear. These peaks are substantially diminished at temperatures over 90 K, but persist as weak features even to 107 K. Between 90 K and 100 K a single broad (~30 cm⁻¹) peak at 2777 cm⁻¹ emerges, characteristic of both the higher temperature crystalline phases of HCl, disordered orthorhombic (II) and cubic (I), observed in IR²⁹ and Raman⁹ spectra. As stated earlier their infrared spectra are identical so that it is difficult to determine whether the 2777 cm⁻¹ band is

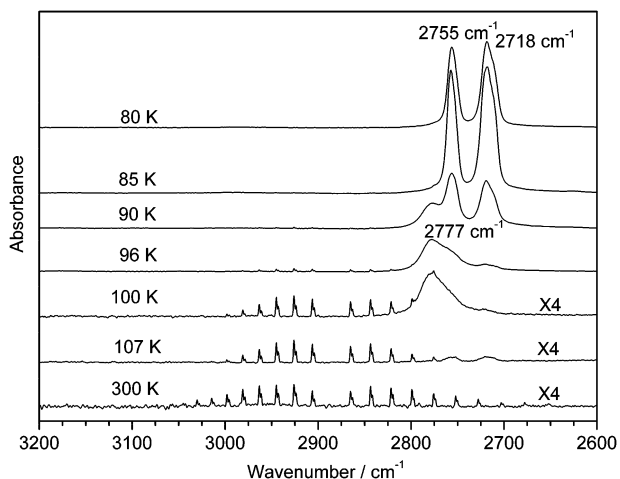


Fig. 3 IR spectra in the HCl fundamental stretching region. A 50 ms pulse of HCl at 1.7 bar positive pressure was injected into 100 mbar of dry nitrogen gas at various temperatures. The 100 K, 107 K and 300 K spectra are scaled by a factor of 4. Maximum absorbance in this set was 0.9 (85 K).

due to phase I, phase II or a mixture of both. We tentatively assign it to the more disordered cubic phase. Curiously, this band is absent at 107 K while a trace of the orthorhombic (phase III) form remains. The increase in overall absorption associated with the change from vapour to crystalline phase (III) has been noted previously, quantified as a sixfold enhancement, and attributed to the effects of H-bond formation on oscillator strength.²⁶

The spectra in Fig. 3 are measured immediately following injection of the sample, but the spectra continue to evolve over time. Fig. 4 shows the trends involving 3 different states of HCl that occur over a period of a few minutes in the spectra at 96 K. While the overall absorbance drops as sample is lost to diffusion, the gas phase spectrum is fairly constant in intensity, presumably reflecting that the equilibrium vapour pressure for that temperature is maintained as long as solid phase HCl remains. Initially, the broad peak at 2777 cm^{-1} (phase I/II) is

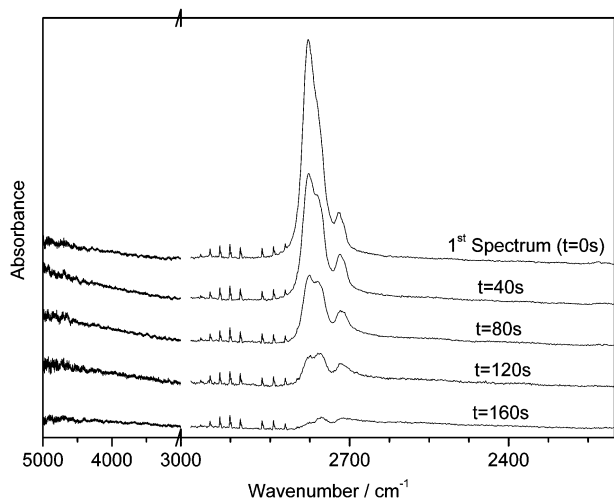


Fig. 4 Temporal evolution of HCl at 100 mbar and 96 K. Maximum absorbance was 0.6 in the first spectrum.

significantly more intense than the two orthorhombic (III) peaks, but by the end of the time sequence the relative intensities are reversed. After 40 seconds the ‘cubic’ 2777 cm^{-1} peak has declined, while a small enhancement of orthorhombic peaks is accompanied by an increase in absorbance in the high wavenumber region of the spectrum due to scattering, indicating growth in particles to a maximum size of 500–1000 nm. This suggests that conversion to phase III may occur *via* the gas phase, rather than by internal rearrangement. Vesel and Torrie noted, “It was reasonably easy to grow a single crystal in the cubic phase but impossible to cool the samples through the cubic to orthorhombic phase transition while maintaining a monocrystalline sample”.⁹ In the temporal evolution series at 100 K the 2777 cm^{-1} band disappears immediately, but there is no evidence of conversion to the orthorhombic (III) form, so the possibility that the higher temperature form is phase II cannot be ruled out. At 90 K the interconversion is rapid—consequently the ‘cubic’ form has disappeared entirely in the second spectrum (not shown here) after 40 s. At the lower temperatures, the orthorhombic form persists longer in the optical zone of the cold cell.

The pressure of N_2 buffer gas also has an effect on the spectra, as illustrated by the series measured at 80 K in Fig. 5. Firstly, a consistent pattern observed for a range of sample molecules is that overall absorbance values are highest around 100–500 mbar. At low pressures of N_2 , fewer collisions result in more rapid depletion of the sample through diffusion to the cell walls (and also less efficient cooling). At pressures well over 500 mbar the amount of sample injected into the cell is slightly less due to the smaller pressure difference between the sample line and the cell. The spectra often show features associated with warmer spectra, possibly due to pre-formation of clusters in the inlet tube between the magnetic valve and the cell (see Fig. 2), or to incomplete mixing due to turbulent flow.

Secondly, N_2 pressure affects rates of formation of various condensed phases. While the two peaks from the

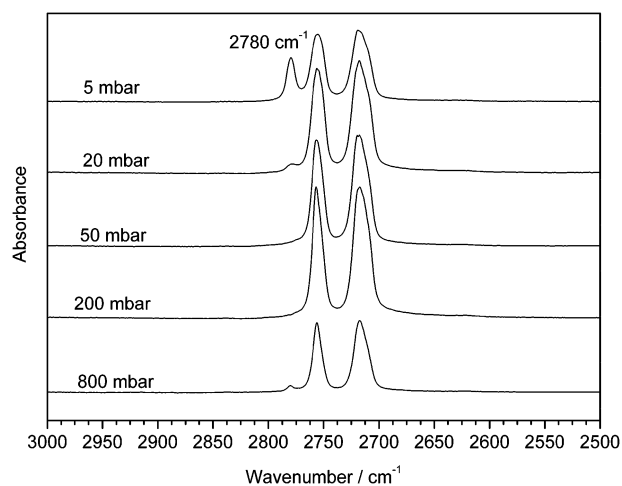


Fig. 5 HCl fundamental stretching region. A 50 ms pulse of HCl at 1.7 bar positive pressure was pulse into dry nitrogen gas at 80 K at various pressures. Maximum absorbance in this set was 1.4 (200 mbar).

orthorhombic phase (2755 cm⁻¹ and 2718 cm⁻¹) are observed at all pressures, an additional peak at 2780 cm⁻¹ is particularly prominent at the lowest N₂ pressures. Although it is located very close to the 2777 cm⁻¹ band seen at higher temperatures, we do not consider it to have the same phase I/II carrier. The

width of this peak at 80 K is much less (*ca.* 10 cm⁻¹, compared to *ca.* 30 cm⁻¹), while previous studies indicate that the phase I/II bandwidths are not very sensitive to temperature, see Table 1. In the range 98–150 K, the Raman spectral band due to phase II and then phase I shows a gradual drift in

Table 1 Vibrations of HCl in various environments

Literature	Temp/K	Position (width)/cm ⁻¹	IR or Raman
Gas H ³⁵ Cl	—	2885.3	IR ³⁵
(HCl) ₂ gas phase	Jet	2890, 2857	IR ³¹
(HCl) ₂ in He droplet	4	2888, 2852	IR ³⁰
(HCl) ₃ gas phase	Jet	2810 (4)	IR ³¹
(HCl) ₃ in He droplet	4	2808 (3)	IR ³⁰
(HCl) ₄ gas phase	Jet	2777 (3)	IR ³¹
(HCl) ₄ in He droplet	4	2808 (3)	IR ³⁰
(HCl) ₅ in He droplet	4	2768–2786	IR ³⁰
(HCl) ₆ in He droplet	4	2762–2800	IR ³⁰
(HCl) ₍₂₀₎ in He droplet	4	2780 (50)	IR ³⁰
(HCl) ₍₅₀₀₎ in He droplet	4	2775 (40)	IR ³⁰
In Ar matrix	9	2944	IR ³⁶
In Kr matrix	9	2916	IR ³⁶
In Xe matrix	9	2884	IR ³⁶
Liquid	220	2792 (100)	IR ²⁹
Metastable	10	2780 (10–12)	IR ³³
Cubic (I)	130	2778 (40)	IR ¹⁶
	100	2768 (50)	IR ¹⁵
	>98.8	2787 (75)	IR ³⁷
	130	2760 (35)	R ⁹
Orthorhombic (II)	100	2778 (60)	IR ²⁹
	110	2755 (35)	R ⁹
Orthorhombic (III)	77	2712 (12)	IR ²⁹
–LO mode	85	2708 (25)	IR ¹⁵
	79	2704 (N/A)	IR ¹⁶
	79	2709 (N/A)	R ¹⁶
	70	2708 (22)	IR ³³
	77	2705 (15)	R ³³
	10	2702 (20)	IR ³³
	10	2699 (4)	R ³³
	77	2707 (20)	IR ³⁸
	10	2705 (12)	R ³⁸
	63	2704 (25)	IR ²⁶
Orthorhombic (III)	77	2758 (20)	IR ²⁹
–TO mode	85	2747 (20)	IR ¹⁵
	79	2746 (N/A)	IR ¹⁶
	79	2759 (N/A)	R ¹⁶
	70	2749 (15)	IR ³³
	77	2748 (15)	R ³³
	10	2746 (18)	IR ³³
	10	2744 (22)	R ³³
	77	2750 (15)	IR ³⁸
	77	2748 (20)	R ³⁸
	63	2747 (15)	IR ²⁶
Experimental			
Orthorhombic – LO	80	2718 (15–19)	IR
Orthorhombic – TO	80	2755 (10–15)	IR
Metastable	80	2780 (8–11)	IR
Phase I or II	90	2777 (31)	IR
Phase I or II	95	2777 (32)	IR
Phase I or II	100	2777 (31)	IR
HCl–O ₃	80	2790 (25)	IR
Calculations			
2 × 7 HCl chains – LO	—	2770	IR
2 × 7 HCl chains – TO	—	2813	IR
2 × 9 HCl chains – LO	—	2747	IR
2 × 9 HCl chains – TO	—	2787	IR
2 × 15 HCl chains – LO	—	2707	IR
2 × 15 HCl chains – TO	—	2773	IR

position (from 2756 to 2762 cm^{-1}), but the width remains constant at 35–40 cm^{-1} .⁹ The IR band at 2778 cm^{-1} observed by Khatibi and Vu²⁹ has a width of 40 cm^{-1} at 130 K, and is even wider (*ca.* 60 cm^{-1}) at 100 K. Clusters of average size 500 HCl molecules formed in helium droplets give rise to an IR band that is also remarkably similar to the cubic form, with position 2775 cm^{-1} and width 40 cm^{-1} , despite the very low temperature.³⁰

Ruling out phases I/II, very small clusters might be considered as a possible candidate for the narrow 2780 cm^{-1} band. These have been measured in jet expansions,³¹ and in helium droplets.³⁰ The IR spectrum of the gaseous HCl tetramer in particular displays a prominent feature at 2777 cm^{-1} , with a width of just 3 cm^{-1} at low temperatures. Although DFT calculations support the notion that $n = 4$ clusters are particularly stable,³² in both jet expansions and helium droplets a range of sizes is always observed. In our cold spectra there is no evidence of additional peaks such as the trimer band at 2810 cm^{-1} .³¹ The narrow 2780 cm^{-1} band is assigned instead to a metastable state of HCl. Savoie and Anderson³³ report a band at 2778 cm^{-1} of comparable width (*ca.* 10 cm^{-1}) to that seen in our 80 K spectra. They assigned it to a metastable phase, noting that its intensity was not reproducible. It was particularly prominent in some crystals deposited at 10 K, and appeared to be enhanced in the presence of impurities. Similar features were also observed for DCl, HBr and DBr.

In temporal evolution sequences (not shown), the metastable carrier of the narrow 2780 cm^{-1} band is observed to undergo conversion into the orthorhombic phase (III), resulting in a slight increase in the 2755 cm^{-1} and 2718 cm^{-1} bands. Analysis of the high wavenumber region did not show any marked increase in scattering, so it is assumed that the particles did not significantly increase in size. At 5 mbar the peak at 2780 cm^{-1} drops to half its intensity after approximately 55 seconds, while at 800 mbar the half life is around 30 seconds. These timescales are considerably faster than those associated with the cubic to orthorhombic (III) conversion at 90 K. In an accompanying paper,³⁴ we demonstrate that the formation of the metastable phase is greatly enhanced in the presence of liquid ozone aerosols.

DFT study of zig-zag HCl chains

IR spectra measured by Skvortsov *et al.* for small HCl clusters in helium droplets agree well with spectra computed at the MP2 level of theory for clusters of the size $n = 2$ –6.³⁰ The global minimum structures for clusters with more than 5 molecules were found to be three dimensional, and the experimental spectra show convergence towards the single, broad peak associated with the cubic phase as the average cluster size increases. Here, we compute IR spectra for HCl molecules joined in the more linear, zig-zag arrangement characteristic of the orthorhombic phase (III). Density functional theory (DFT) calculations were performed at the B3LYP level using the 6-311+G(d,p) basis set. Model clusters of HCl molecules with various chain lengths were subjected to full geometry optimisation prior to vibrational analysis. The previously reported³⁹ symmetric (LO) and antisymmetric (TO) coupling

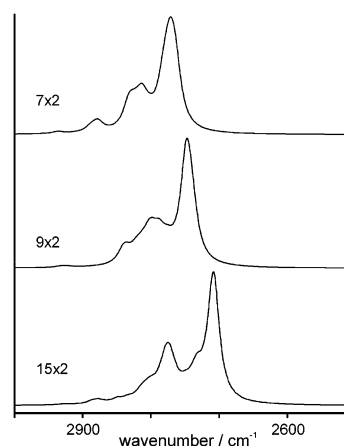


Fig. 6 Simulated spectra of two parallel chains of HCl: 7 (top), 9 (middle) and 15 (bottom) molecules long. Simulations used Lorentzian lineshapes with 20 cm^{-1} FWHM.

of the H–Cl stretches was observed along the chains. The lowest wavenumber HCl stretch vibration, corresponding to the fully symmetrically coupled mode, was the most intense. As the chains lengthen, the intensity of this mode increases and its frequency decreases, converging to around 2710 cm^{-1} (see Fig. 6). The higher wavenumber peaks are due to a number of stretches, the most intense of which is very close to the TO mode. The intensity of the antisymmetric vibrations is greatest when there are ‘nodes’[†] at every molecule so that every second molecule vibrates synchronously as in the TO mode in Fig. 1. The drop in intensity in the region between these two main peaks is due to some vibrations with less uniform coupling being much less intense (~ 10 times) than the others. If every second molecule is not a node then the individual changes in dipole moment associated with H–Cl stretching tend to cancel each other out.

These results rule out small zig-zag clusters as the carrier of the narrow 2780 cm^{-1} band, but are consistent with the observation of the two intense, sharp peaks in the experimental spectra. The peak at 2718 cm^{-1} is the result of symmetric coupling and the peak at 2755 cm^{-1} is due to antisymmetric coupling, as reported in the literature. It is notable that so few HCl molecules are required for simulations to begin to converge on the observed orthorhombic (III) band characteristics.

Hydrogen chloride–water binary aerosols

There has been considerable interest in the IR spectral characterisation of mixed HCl–water particles, with sizes ranging from a few molecules⁴⁰ to nanoparticulate ice.⁴¹ Fig. 7 shows the spectra that result when water and HCl are injected simultaneously into the cell at various temperatures. Comparison with Fig. 3 suggests that the addition of water has very little influence on the spectrum of HCl, and the converse is also true, at least in the OH stretch region. The lack of clear evidence for mixed clusters suggests that the particle

[†] In this case a ‘node’ is the chlorine atom where the direction of the vibration (lengthening or shortening) changes. In the case of the TO mode in Fig. 1 this is every chlorine atom.

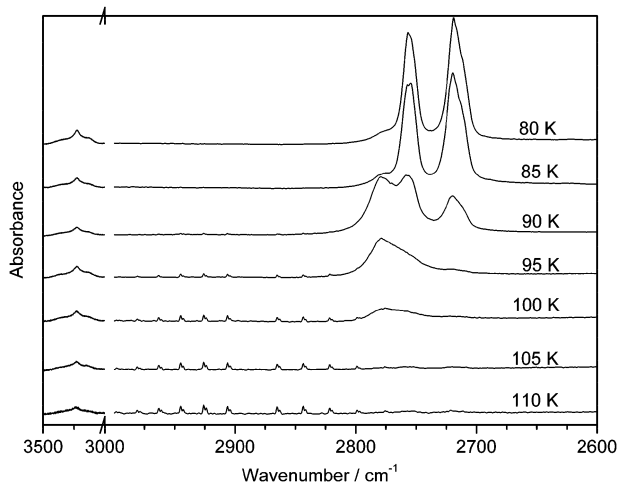


Fig. 7 Simultaneous pulses of HCl (50 ms at 1.7 bar) and H₂O (100 ms at 2.8 bar) were injected into the cell that was filled with 100 mbar of dry nitrogen gas at various temperatures. The maximum absorbance in this set was 1.4 at 80 K.

composition is not necessarily affected by the presence of different condensable gases in this temperature range. It is somewhat surprising that the two polar molecules that are capable of forming strong H-bonds and that are highly miscible in the liquid phase do not mix more in the solid phases observed here. Possibly water ice particles may form on a faster timescale than HCl particles. Like the pure HCl spectra at the same N₂ buffer pressure, these spectra show little sign of the narrow 2780 cm⁻¹ band associated with the metastable HCl phase. Savoie and Anderson had speculated previously that the metastable peak might be due to CO₂ or H₂O impurities,³³ but the present results suggest otherwise.

Hydrogen chloride–ammonia binary aerosols

A final set of experiments were performed in which both hydrogen chloride and ammonia were introduced, allowing the possibility that a low temperature chemical reaction could be observed in addition to the physical phase changes. Both chemical species are known in the atmosphere, and the reaction to produce NH₄Cl has been extensively studied at temperatures over 200 K as a model of atmospheric particle growth.^{42–46} The mechanisms involved in particle growth are complex, involving an initial nucleation stage, followed by growth by diffusion, cluster scavenging and coagulation.^{44,45}

The spectra of Fig. 8 show the reaction of gaseous ammonia and hydrogen chloride to form solid ammonium chloride at 300 K. The bands associated with ammonium chloride are clearly evident as new features in the spectrum. It is striking how much phonon resonance in the ammonium chloride particles increases the integrated intensity. The resultant sensitivity contributes to making this technique powerful for identifying the local environment of molecules even at modest concentrations.

The temperature dependence of the reaction between HCl and NH₃ can be seen in Fig. 9. Ammonium chloride particles are produced over a very wide range of temperatures, but are less prevalent at the lower temperatures. This trend is likely caused by a competition between the chemical reaction to

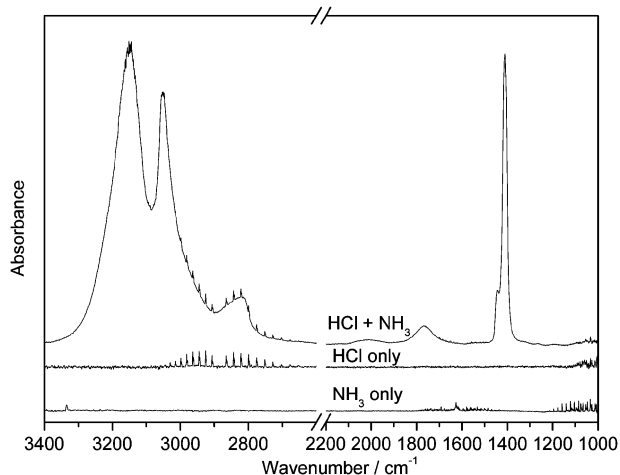


Fig. 8 IR spectra of gaseous NH₃ (bottom curve), HCl (middle) and the ammonium chloride (top) that result when they are combined at 300 K in 100 mbar of N₂ buffer gas. Both gases were pulsed for 60 ms, HCl at 1.0 bar and NH₃ at 0.7 bar. The maximum absorbance here was 1.3 for the ammonium chloride peak.

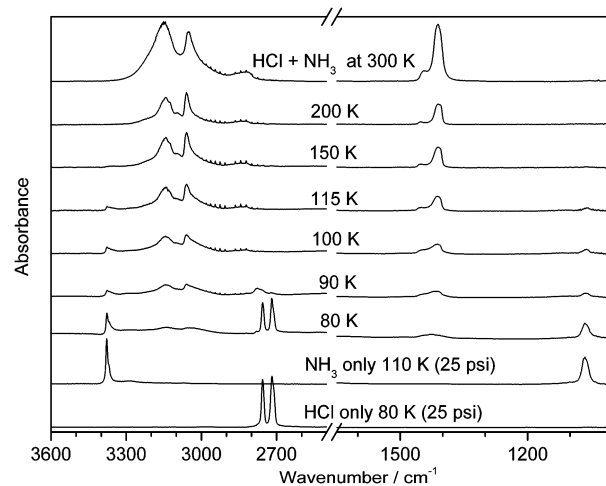


Fig. 9 Temperature dependence of particle formation. Simultaneous pulses of HCl (60 ms at 1.0 bar) and NH₃ (60 ms at 0.7 bar) were injected into the cell filled with 100 mbar of dry nitrogen gas at various temperatures. The maximum absorbance in this set was 1.3 in the 300 K spectrum.

form NH₄Cl and the physical process to form the pure clusters which is critically dependent on cold conditions. When the temperature is low enough, pure clusters are formed at a rate sufficient to compete with the chemical reaction.

Temporal evolution of the HCl–NH₃ system at 90 K is shown in Fig. 10. It can be seen that at $t = 0$ s there is a large peak from the cubic phase (ν_{\max} 2777 cm⁻¹) which decreases greatly after 40 s. The HCl peaks decrease by half after 40 s and after 80 s they have almost disappeared. It is surmised that much of the particulate HCl evaporates into the gas phase where it may be lost more rapidly to diffusion than in the case of particles. This premise is supported by the appearance of HCl monomer lines in the spectra around 2900 cm⁻¹ and the fact that at 80 K (where no HCl gas is observed) the HCl peaks have a longer half life of approximately 280 s.

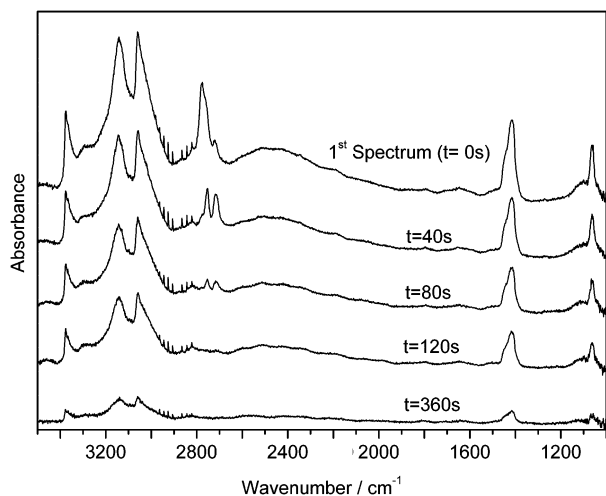


Fig. 10 Temporal evolution of HCl–NH₃ system at 100 mbar and 90 K. Maximum absorbance was 0.3 in the first spectrum.

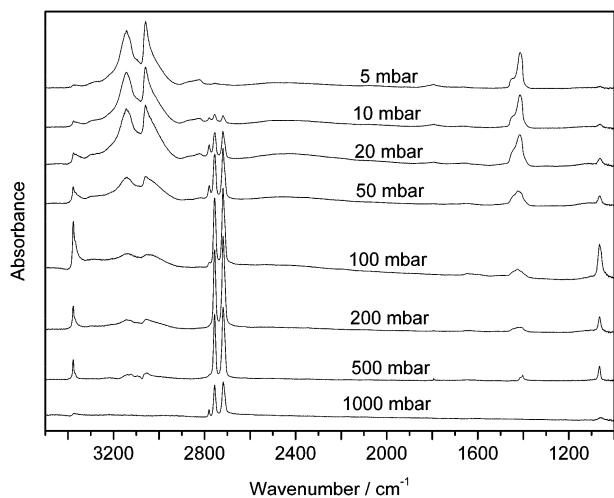


Fig. 11 Pressure dependence of particle formation. Simultaneous pulses of HCl (50 ms at 1.0 bar) and NH₃ (50 ms at 0.7 bar) were injected into the cell filled with dry nitrogen gas at 80 K at various pressures. The maximum absorbance in this set was 1.0 in the 200 mbar spectrum.

It can be seen in Fig. 11 that the formation of ammonium chloride varies dramatically with buffer gas pressure. This is because the chemical reaction to form ammonium chloride is competing with the physical process forming the pure clusters. The first step in the formation of the pure clusters has a rate that is dependent on the pressure of the buffer gas as the sample molecules need to be cooled by inelastic collisions before they can combine to form critical nuclei. This process is, in effect, a third order reaction between the two sample molecules and the cold nitrogen gas. In contrast, the chemical reaction to form ammonium chloride appears to be more independent of the buffer gas pressure.

In most mechanisms, the first step is generally assumed to be bimolecular with second order kinetics,^{42–45} and is sometimes blithely denoted as:

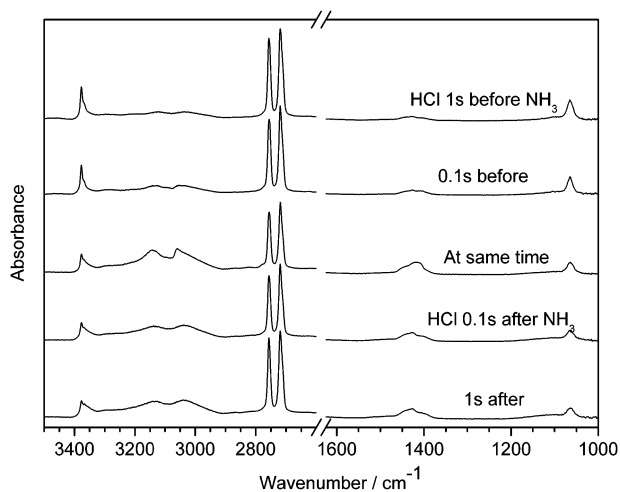


Fig. 12 Variation in NH₃–HCl spectra as a function of the synchronisation of the pulses of HCl (50 ms at 1.0 bar) and NH₃ (50 ms at 0.7 bar). The cell was filled with dry nitrogen gas at 80 K and 100 mbar. The maximum absorbance in this set was 1.1.

in spite of the fact that the gaseous monomer does not exist in the ionic form, but rather as the H-bonded dimer $\text{ClH} \cdots \text{NH}_3$.⁴⁷ While production of a single $(\text{NH}_3 \cdots \text{HCl})$ dimer is not sufficient to generate ionic NH_4Cl , Tao found in his computational study that clusters of two and four NH_3 –HCl units closely resemble the crystal structure of NH_4Cl , contain the discrete NH_4^+ and Cl^- ions, and have large binding energies.⁴⁸ Initial formation of NH_4Cl *via* these cluster forms might be expected to have a rate proportional to $[\text{NH}_3]^n[\text{HCl}]^n$, with $n \approx 2$. One empirically derived rate law for nucleation at 298 K has precisely this form, with $n = 2.7$.⁴⁷ The key point, however, is that there is no implied dependence on background gas pressure.

Fig. 12 shows spectra in which the synchronisation of the pulses of HCl and NH₃ was varied. As expected, production of NH_4Cl is optimal when reactants are pulsed simultaneously. When the pulses are offset the pure clusters begin to form before the chemical reaction can occur. Since there is a large decrease in the amount of NH_4Cl after just 0.1 seconds it can be assumed that the formation time of the pure clusters in these conditions is less than 0.1 seconds with 100 mbar of N_2 buffer pressure. This is consistent with the formation times found for other molecules analysed using this cell.^{17–25} NH_4Cl must also be formed on a comparable timescale.

Conclusions

A collisional cooling cell with fine control of temperature and background pressure was used to generate aerosols of solid hydrogen chloride and observe three distinct solid phases of HCl *via* FTIR spectroscopy. The cubic phase of HCl was observed with cell temperatures of 90–100 K while the low temperature orthorhombic phase was observed below this temperature. The previously reported metastable phase was also observed under some conditions. This study is believed to be the first on pure HCl aerosols.

Density functional theory calculations showed that it is possible to model the IR spectrum of the orthorhombic

phase (III) of HCl with small chains of HCl in an almost planar zig-zag arrangement. The simulated spectra of model clusters converge to show a band shape that is characteristic of orthorhombic HCl.

The reaction between HCl and NH₃ was also examined and found to occur over a wide range of temperatures. As the cell temperature was dropped below 100 K, it was found that the formation of homogenous clusters of HCl and NH₃ competed with the chemical reaction to form ammonium chloride. Higher pressures of buffer gas also favoured the homogenous clusters, while the chemical reaction was preferred at low background pressures. At a temperature of 80 K, NH₄Cl is formed in less than 0.1 s, with concentrations of HCl and NH₃ reactants of *ca.* 1.5 and 1.0 μmol L⁻¹, respectively.

Under conditions prevalent in the atmosphere, the reaction to produce NH₄Cl is generally assumed to occur in the presence of water vapour or *via* heterogeneous reaction on pre-existing particles⁴⁹ as the computed rates of homogeneous binary nucleation appear to be too low.⁴² The present results indicate that the reaction proceeds rapidly even at 80 K, supporting Tao's conclusion that homogeneous nucleation of NH₄Cl from pure NH₃ and HCl gases is feasible at low temperatures.

Acknowledgements

Financial support from the Australian Research Council, the Deutsche Forschungsgemeinschaft (R.T.) and the Australian Government through an Australian Postgraduate Award (C.M.) is gratefully acknowledged. Quantum chemistry calculations were carried out using the Australian Partnership for Advanced Computing (APAC) National Facility.

Notes and references

- 1 V. Abdelsayed, G. Glaspell, K. Saoud, M. Meot-Ner and M. Samy El-shall, *AIP Conf. Proc.*, 2006, **855**, 76.
- 2 A. Lipshtat and O. Biham, *Astron. Astrophys.*, 2003, **400**, 585.
- 3 L. Aigen and J. M. Greenberg, in *Solid state astrochemistry*, ed. V. Pirronello, J. Krelowski and G. Manicò, Kluwer Academic Publishers, Dordrecht, The Netherlands, 2003, pp. 7–84.
- 4 NASA. Stratospheric Ozone. *Studying Earth's Environment From Space*. [Online] 2000. http://www.ccpo.odu.edu/SEES/ozone/oz_class.htm.
- 5 G. P. Brasseur and S. Solomon, *Aeronomy of the middle atmosphere: chemistry and physics of the stratosphere and mesosphere*, Springer, Dordrecht, 2005. ISBN 1-4020-3284-6.
- 6 P. J. Crutzen, *Clim. Change*, 2006, **77**, 3–4.
- 7 P. J. Lightowers and J. N. Cape, *Atmos. Environ.*, 1988, **22**(1), 7.
- 8 G. A. Blake, J. Keene and T. G. Phillips, *Astrophys. J.*, 1985, **295**, 501–506.
- 9 J. E. Vesel and B. H. Torrie, *Can. J. Phys.*, 1977, **55**, 592.
- 10 E. Sandor and R. F. C. Farrow, *Nature*, 1967, **215**, 1265.
- 11 E. Katoh, H. Yamawaki, H. Fujihisa, M. Sakashita and K. Aoki, *Phys. Rev. B: Condens. Matter*, 2000, **61**(1), 119.
- 12 E. Sandor and R. F. C. Farrow, *Nature*, 1967, **213**, 171.
- 13 D. F. Hornig and W. E. Osberg, *J. Chem. Phys.*, 1955, **23**(4), 662.
- 14 R. Savoie and M. Pezolet, *J. Chem. Phys.*, 1969, **50**, 2781.
- 15 G. Hettner, *Z. Phys. A: Hadrons Nucl.*, 1934, **89**, 234.
- 16 E. Lee, G. B. M. Sutherland and C. K. Wu, *Nature*, 1938, **3597**, 669.
- 17 S. Bauerecker, M. Taraschewski, C. Weitkamp and H. K. Cammenga, *Rev. Sci. Instrum.*, 2001, **72**, 3946.
- 18 S. Bauerecker, *Phys. Rev. Lett.*, 2005, **94**, 033404.
- 19 R. Signorell, M. Jetzki, M. Kunzmann and R. Ueberschaer, *J. Phys. Chem. A*, 2006, **110**, 2890.
- 20 M. K. Kunzmann, S. Bauerecker, M. A. Suhm and R. Signorell, *Spectrochim. Acta, Part A*, 2003, **59**, 2857.
- 21 M. K. Kunzmann, R. Signorell, M. Taraschewski and S. Bauerecker, *Phys. Chem. Chem. Phys.*, 2001, **3**, 3742.
- 22 M. Taraschewski, H. K. Cammenga, R. Tuckermann and S. Bauerecker, *J. Phys. Chem. A*, 2005, **109**, 3337.
- 23 R. Signorell, M. Jetzki, M. K. Kunzmann and R. Ueberschaer, *J. Phys. Chem. A*, 2006, **110**, 2890.
- 24 R. Signorell and M. Jetzki, *Faraday Discuss.*, 2008, **137**, 51.
- 25 S. Bauerecker and E. Dartois, *Icarus*, 2009, **199**, 564.
- 26 H. B. Friedrich and W. B. Person, *J. Chem. Phys.*, 1963, **39**(3), 811.
- 27 D. R. Stull, *Ind. Eng. Chem.*, 1947, **39**, 517–540.
- 28 "Thermodynamics Source Database" in *NIST Chemistry WebBook, NIST Standard Reference Database Number 69*, ed. P. J. Linstrom, W. G. Mallard, National Institute of Standards and Technology, Gaithersburg, MD, 20899 <http://webbook.nist.gov> (retrieved 9 March 2009).
- 29 P. Khatibi and H. Vu, *J. Chim. Phys. Phys.-Chim. Biol.*, 1972, **69**, 654.
- 30 D. Skvortsov, M. Y. Choi and A. F. Vilesov, *J. Phys. Chem. A*, 2007, **111**(49), 12711–12716.
- 31 T. Haber, U. Schmitt and M. A. Suhm, *Phys. Chem. Chem. Phys.*, 1999, **1**, 5573–5582.
- 32 R. C. Guedes, P. C. do Couto and B. J. Costa Cabral, *J. Chem. Phys.*, 2003, **118**, 1272.
- 33 R. Savoie and A. Anderson, *J. Chem. Phys.*, 1966, **44**(2), 548.
- 34 C. Medcraft, E. G. Robertson, C. D. Thompson, S. Bauerecker and D. McNaughton, *Phys. Chem. Chem. Phys.*, 2009, **11**, DOI: 10.1039/B905424N (accompanying paper).
- 35 D. H. Rank, B. S. Rao and T. A. Wiggins, *J. Mol. Spectrosc.*, 1965, **17**, 122.
- 36 L. Young and C. B. Moore, *J. Chem. Phys.*, 1984, **81**(7), 3137.
- 37 G. L. Hiebert and D. F. Hornig, *J. Chem. Phys.*, 1957, **27**, 1216.
- 38 A. Anderson, B. H. Torrie and W. S. Tse, *J. Raman Spectrosc.*, 1981, **10**, 148.
- 39 J. F. Higgs, W. Y. Zeng and A. Anderson, *Phys. Status Solidi B*, 1986, **133**, 475.
- 40 M. Weimann, M. Fárnik and M. A. Suhm, *Phys. Chem. Chem. Phys.*, 2002, **4**, 3933–3937.
- 41 J. P. Devlin, N. Uras, J. Sadlej and V. Buch, *Nature*, 2002, **417**, 269–271.
- 42 R. J. Countess and J. Heicklen, *J. Phys. Chem.*, 1973, **77**, 444–447.
- 43 M. Luria and B. Cohen, *Atmos. Environ.*, 1980, **14**, 665–670.
- 44 R. S. Dahlin, J. Su and L. K. Peters, *AIChE J.*, 1981, **27**, 404–418.
- 45 J. F. Henry, A. Gonzalez and L. K. Peters, *Aerosol Sci. Technol.*, 1983, **2**(3), 321–339.
- 46 P. Korhonen, M. Kulmala and Y. Viisanen, *J. Aerosol Sci.*, 1997, **28**, 901.
- 47 N. W. Howard and A. C. Legon, *J. Chem. Phys.*, 1988, **88**, 4694.
- 48 Tao, *J. Chem. Phys.*, 1999, **110**(23), 11121.
- 49 J. H. Seinfeld, *Atmospheric Chemistry and Physics of Air Pollution*, Wiley, New York, 1986.

CHAPTER 4.0

CONCLUSIONS

The coupling of the enclosive flow cooling cell to the synchrotron source provides an enhanced range and sensitivity for experiments. For high resolution spectroscopy this will allow the study of a number of new molecules particularly large molecules with congested spectra. These may include bromine or iodine containing halocarbons or larger molecules of interstellar interest. Many of these molecules may be unstable and may require production from a precursor via pyrolysis or photolysis. The cooling provided by the cell can help extend the lifetime of these molecules however the sample inlet of to the cell may require significant modifications to allow the coupling of the experimental equipment required for pyrolysis or photolysis.

Further developments on the cell are also planned, mainly focussed around introducing a laser or ultraviolet radiation source into the cell. This will allow for the production of transient molecules *in situ* and possible pump probe experiments. This may require significant modifications to the top flange of the cell to allow for a safe optical path for the laser.

The extension to the far infrared has opened up a large number of possible aerosol experiments. In the immediate future a number of small hydrocarbons will be investigated. With the introduction of a laser source reaction on particle surfaces can be investigated. Reactions of this type are important to the both atmospheric and interstellar chemistry. The addition of diamond windows will greatly ease these experiments as they will allow the characterisation in both the mid and far infrared without the need to change the optical setup.

Finally, this type of cooling cell is used at a number of different laboratories; including one at a synchrotron beamline (at the Swiss Light Source) however they are all limited to the mid infrared range. The optical modifications presented in this thesis are directly applicable to any planned far-IR extensions of these cells.

